

Nano-Optics and Nanophotonics

Motoichi Ohtsu *Editor*

Progress in Nanophotonics 2



Springer

NANO-OPTICS AND NANOPHOTONICS

For further volumes:
www.springer.com/series/8765

NANO-OPTICS AND NANOPHOTONICS

The Springer Series in Nano-Optics and Nanophotonics provides an expanding selection of research monographs in the area of nano-optics and nanophotonics, science- and technology-based on optical interactions of matter in the nanoscale and related topics of contemporary interest. With this broad coverage of topics, the series is of use to all research scientists, engineers and graduate students who need up-to-date reference books. The editors encourage prospective authors to correspond with them in advance of submitting a manuscript. Submission of manuscripts should be made to the editor-in-chief, one of the editors or to Springer.

Editor-in-Chief

Motoichi Ohtsu

Department of Electrical Engineering and Informations Systems, School of Engineering
The University of Tokyo
Yayoi, Bunkyo-ku 2-11-16, 113-8656 Tokyo, Japan
ohtsu@ee.t.u-tokyo.ac.jp

Editorial Board

Gunnar Björk

Department of Electronics
KTH, Electrum 229
164 40 Kista, Sweden
gbjork@kth.se

Chennupati Jagadish

Department of Electronic Materials Engineering
Research School of Physics and Engineering
Australian National University
Canberra, ACT 0200, Australia
cxji09@rsphysse.anu.edu.au

Christoph Lienau

Institut für Physik, Fakultät V
Carl von Ossietzky Universität Oldenburg
Ammerländer Heerstraße 114-118
26129 Oldenburg, Germany
christoph.lienau@uni-oldenburg.de

Lih Y. Lin

Electrical Engineering Department
University of Washington
M414 EEL Bldg., Box 352500
Seattle, WA 98195-2500, USA
lylin@uw.edu

Erich Runge

Technische Universität Ilmenau
Curiebau, Weimarer Str. 25
98693 Ilmenau, Germany
erich.runge@tu-ilmenau.de

Frank Träger

Experimentalphysik I, Universität Kassel
Heinrich-Plett-Str. 40, 34132 Kassel, Germany
traeger@physik.uni-kassel.de

Masaru Tsukada

WPI-AIMR Center, Tohoku University
2-1-1 Katahira, Aoba-ku, Sendai, 980-8577 Japan
tsukada@wpi-aimr.tohoku.ac.jp

Please view available titles in *Nano-Optics and Nanophotonics*
on series homepage <http://www.springer.com/series/8765>

Motoichi Ohtsu

Editor

Progress in Nanophotonics 2

 Springer

Editor

Motoichi Ohtsu
Graduate School of Engineering
The University of Tokyo
Tokyo, Japan

ISSN 2192-1970
Nano-Optics and Nanophotonics
ISBN 978-3-642-35718-3
DOI 10.1007/978-3-642-35719-0
Springer Heidelberg New York Dordrecht London

ISSN 2192-1989 (electronic)
ISBN 978-3-642-35719-0 (eBook)

Library of Congress Control Number: 2011934022

© Springer-Verlag Berlin Heidelberg 2013

This work is subject to copyright. All rights are reserved by the Publisher, whether the whole or part of the material is concerned, specifically the rights of translation, reprinting, reuse of illustrations, recitation, broadcasting, reproduction on microfilms or in any other physical way, and transmission or information storage and retrieval, electronic adaptation, computer software, or by similar or dissimilar methodology now known or hereafter developed. Exempted from this legal reservation are brief excerpts in connection with reviews or scholarly analysis or material supplied specifically for the purpose of being entered and executed on a computer system, for exclusive use by the purchaser of the work. Duplication of this publication or parts thereof is permitted only under the provisions of the Copyright Law of the Publisher's location, in its current version, and permission for use must always be obtained from Springer. Permissions for use may be obtained through RightsLink at the Copyright Clearance Center. Violations are liable to prosecution under the respective Copyright Law.

The use of general descriptive names, registered names, trademarks, service marks, etc. in this publication does not imply, even in the absence of a specific statement, that such names are exempt from the relevant protective laws and regulations and therefore free for general use.

While the advice and information in this book are believed to be true and accurate at the date of publication, neither the authors nor the editors nor the publisher can accept any legal responsibility for any errors or omissions that may be made. The publisher makes no warranty, express or implied, with respect to the material contained herein.

Printed on acid-free paper

Springer is part of Springer Science+Business Media (www.springer.com)

Preface to *Progress in Nanophotonics*

As the first example, recent advances in photonic systems demand drastic increases in the degree of integration of photonic devices for large-capacity, ultrahigh-speed signal transmission and information processing. Device size has to be scaled down to nanometric dimensions to meet this requirement, which will become even more strict in the future. As the second example, photonic fabrication systems demand drastic decreases in the size of the fabricated patterns for assembling ultra-large-scale integrated circuits. These requirements cannot be met even if the sizes of the materials are decreased by advanced methods based on nanotechnology. It is essential to decrease the size of the electromagnetic field used as a carrier for signal transmission, processing, and fabrication. Such a decrease in the size of the electromagnetic field beyond the diffraction limit of the propagating field can be realized in optical near fields. Nanophotonics, a novel optical technology that utilizes the optical near field, was proposed by M. Ohtsu (the editor of this monograph series) in 1993 in order to meet these requirements. However, it should be noted that the true nature of nanophotonics involves not only its ability to meet the above requirements. It is also its ability to realize qualitative innovations in photonic devices, fabrication techniques, energy conversion, and information processing systems by utilizing novel functions and phenomena made possible by optical near-field interactions, which are otherwise impossible as long as conventional propagating light is used. Based on interdisciplinary studies on condensed-matter physics, optical science, and quantum field theory, nano-materials and optical energy transfer in the nanometric regime have been extensively studied in the last two decades. Through these studies, novel theories on optical near fields have been developed, and a variety of novel phenomena have been found. The results of this basic research have been applied to develop nanometer-sized photonic devices, nanometer-resolution fabrication, highly efficient energy conversion, and novel information processing, resulting in qualitative innovations. Further advancement in these areas is expected to establish novel optical sciences in the nanometric space, which can be applied to further progress in nanophotonics in order to support the sustainable development of peoples lives all over the world. This unique monograph series entitled *Progress in Nanophotonics* in the Springer Series in Nano-optics and Nanophotonics is being

introduced to review the results of advanced studies in the field of nanophotonics and covers the most recent topics of theoretical and experimental interest in relevant fields, such as classical and quantum optical sciences, nanometer-sized condensed matter physics, devices, fabrication techniques, energy conversion, information processing, architectures, and algorithms. Each chapter is written by leading scientists in the relevant field. Thus, this monograph series will provide high-quality scientific and technical information to scientists, engineers, and students who are and will be engaged in nanophotonics research. As compared with the previous monograph series entitled “Progress in Nano-Electro-Optics” (edited by M. Ohtsu, published in the Springer Series in Optical Science), this monograph series deals not only with optical science on the nanometer scale, but also its applications to technology. I am grateful to Dr. C. Ascheron of Springer-Verlag for his guidance and suggestions throughout the preparation of this monograph series.

Tokyo
August 2010

Motoichi Ohtsu

Preface to Volume II

This volume contains five review articles focusing on various but mutually related topics in nanophotonics written by the world's leading scientists. The first article describes near-field excitation dynamics in molecules. A generalized theoretical description of a light-matter interaction is given on the basis of the multipolar Hamiltonian. The second article is devoted to describing experimental results for wavelength up-converting a phonon-assisted excitation process with degenerate beams and non-degenerate beams in dye grains. Application to optical pulse-shape measurement is also reviewed. The third article describes a fabrication method of semiconductor quantum dots, including self-assembly of InAs quantum dots based on the Stranski-Krastanov growth mode. Fabrication and application of ultrahigh-density quantum dots by a strain compensation technique are also reviewed. The fourth article is devoted to single-nanotube spectroscopy and time-resolved spectroscopy for studying novel excitonic properties of single-walled carbon nanotubes. The striking features of excitons in the carbon nanotube, multiple-exciton states, charged exciton formation, and exciton-multiplication are reviewed. The last article describes microfluidic and extended-nano fluidic techniques. It claims that nanophotonics is used as a key technology since the space size becomes smaller than the wavelength in extended-nano space.

This volume is published with the support of Prof. Yatsui of the University of Tokyo, an associate editor. I hope that this volume will be a valuable resource for readers and future specialists in nanophotonics.

Tokyo
February 2013

Motoichi Ohtsu

Contents

1	Near-Field Excitation Dynamics in Molecules: Nonuniform Light-Matter Interaction Theory Beyond a Dipole Approximation	1
	Katsuyuki Nobusada	
1.1	Introduction	1
1.2	Theory	4
1.2.1	Multipolar Hamiltonian	4
1.2.2	A Molecule Interacting with a Nonuniform Near-Field	6
1.2.3	Near-Field Radiated from an Oscillating Dipole	8
1.2.4	Light-Matter Interaction in the Kohn-Sham DFT Approach	9
1.3	Computational Application	10
1.3.1	Time-Dependent Kohn-Sham Approach in Real Space	10
1.4	High-Harmonic-Generation Spectra Induced by the Near-Field Excitation	12
1.4.1	Molecular System and Computations	12
1.4.2	Near-Field Excitation Dynamics	13
1.4.3	Even and Odd Harmonics	18
1.4.4	Control of Harmonic Generation by Interference	19
1.4.5	Concluding Remarks	20
1.5	Near-Field Induced Optical Force in a Metal Nanoparticle and C ₆₀	21
1.5.1	Brief Review of Optical Force	21
1.5.2	Optical Force Exerted on a Particle	22
1.5.3	Model System and Computations	23
1.5.4	Optical Force on a Silver Nanoparticle	25
1.5.5	Optical Force on C ₆₀	29
1.5.6	Concluding Remarks	29
1.6	Summary	30
	References	30
2	Novel Excitonic Properties of Carbon Nanotube Studied by Advanced Optical Spectroscopy	33
	Kazunari Matsuda	

2.1	Basic Optical Properties of Carbon Nanotube	33
2.1.1	Structure of Carbon Nanotube	33
2.1.2	Electronic Structure of Graphene	34
2.1.3	Electronic Structure of Carbon Nanotube	35
2.1.4	Optical Spectroscopy of Carbon Nanotubes	37
2.1.5	Exciton State in Carbon Nanotubes	38
2.1.6	Exciton Structures in Carbon Nanotubes	39
2.2	Novel Excitonic Properties of Carbon Nanotube	40
2.2.1	Single Carbon Nanotube Spectroscopy for Revealing Exciton Structures	40
2.2.2	Singlet-Bright and -Dark Exciton Revealed by Magneto-PL Spectroscopy	42
2.2.3	Triplet and K -Momentum Dark Exciton States	45
2.2.4	Exciton-Complex in Carbon Nanotubes	49
2.3	Novel Exciton Dynamics of Carbon Nanotube	52
2.3.1	Exciton Relaxation Dynamics Between Bright and Dark State	52
2.3.2	Radiative Lifetime of Bright Exciton States	55
2.3.3	Exciton-Exciton Interaction in Carbon Nanotube	60
2.3.4	Multi-Exciton Generation in Carbon Nanotube	64
2.4	Summary	67
	References	67
3	Fabrication of Ultrahigh-Density Self-assembled InAs Quantum Dots by Strain Compensation	71
	Kouichi Akahane	
3.1	Semiconductor Quantum Dot	71
3.1.1	Self-assembled Semiconductor Quantum Dot	73
3.1.2	Fabrication of Ultrahigh-Density QDs Using Strain-Compensation Technique	75
3.1.3	Applications Using Ultrahigh-Density QDs	83
3.1.4	Summary	95
	References	95
4	Wavelength Up-Conversion Using a Phonon-Assisted Excitation Process and Its Application to Optical Pulse-Shape Measurement	97
	Hiroyasu Fujiwara	
4.1	Introduction	97
4.2	Multi-step Phonon-Assisted Processes with Degenerate Beams	98
4.2.1	Principles of Multi-step Phonon-Assisted Process	99
4.2.2	Sample Preparation	102
4.2.3	Comparison Between Fluorescence and Emitted Spectra Induced by Phonon-Assisted Process	103
4.2.4	Excitation Intensity Dependence	104
4.2.5	Lifetime of the Intermediate Excited State	105

- 4.3 Multi-step Phonon-Assisted Process with Two Nondegenerate Beams 108
 - 4.3.1 Emitted Spectra Induced by Phonon-Assisted Process with Nondegenerate Beams 109
 - 4.3.2 Excitation Intensity Dependence 111
 - 4.3.3 Dependence of the Difference in Polarization Angle Between Two Nondegenerate Beams 114
- 4.4 Application to Optical Pulse Shape Measurement 115
 - 4.4.1 Experimental Setup 116
 - 4.4.2 Experimental Results 117
- 4.5 Summary 119
- References 120
- 5 Micro and Extended-Nano Fluidics and Optics for Chemical and Bioanalytical Technology 121**

Kazuma Mawatari, Yuriy Pihosh, Hisashi Shimizu, Yutaka Kazoe, and Takehiko Kitamori

 - 5.1 Introduction 121
 - 5.2 Technology and Applications by Microfluidics 123
 - 5.2.1 Integration Methods 123
 - 5.2.2 Optical Detection Method for Single Molecule Detection . . 127
 - 5.2.3 Applications 132
 - 5.3 Extended-Nano Fluidics and Optics 136
 - 5.3.1 Introduction 136
 - 5.3.2 Optical Detection Methods 138
 - 5.3.3 Liquid and Optical Properties 147
 - 5.3.4 Applications 160
 - 5.4 Summary 162
 - References 162
- Index 165**

Contributors

Kouichi Akahane National Institute of Information and Communications Technology, Koganei, Tokyo, Japan

Hiroyasu Fujiwara Central Research Laboratories, Hamamatsu Photonics K.K., Hamamatsu, Shizuoka, Japan

Yutaka Kazoe Department of Applied Chemistry, School of Engineering, The University of Tokyo, Tokyo, Japan

Takehiko Kitamori Department of Applied Chemistry, School of Engineering, The University of Tokyo, Tokyo, Japan

Kazunari Matsuda Institute of Advanced Energy, Kyoto University, Uji, Kyoto, Japan

Kazuma Mawatari Department of Applied Chemistry, School of Engineering, The University of Tokyo, Tokyo, Japan

Katsuyuki Nobusada Department of Theoretical and Computational Molecular Science, Institute for Molecular Science, Okazaki, Aichi, Japan

Yuriy Pihosh Department of Applied Chemistry, School of Engineering, The University of Tokyo, Tokyo, Japan

Hisashi Shimizu Department of Applied Chemistry, School of Engineering, The University of Tokyo, Tokyo, Japan

Chapter 1

Near-Field Excitation Dynamics in Molecules: Nonuniform Light-Matter Interaction Theory Beyond a Dipole Approximation

Katsuyuki Nobusada

Abstract We have presented near-field excitation dynamics in molecules beyond diffraction limit of the incident visible laser field. A generalized theoretical description of a light-matter interaction taking account of nonuniformity of the light due to its intensity gradient has been developed on the basis of the multipolar Hamiltonian. The computations are demonstrated in high-harmonic generation spectra of a linear chain molecule of dicyanodiacetylene, NC_6N and also in optical forces induced by a near-field for a 1 nm-sized metal particle mimicked by a jellium model and for C_{60} .

1.1 Introduction

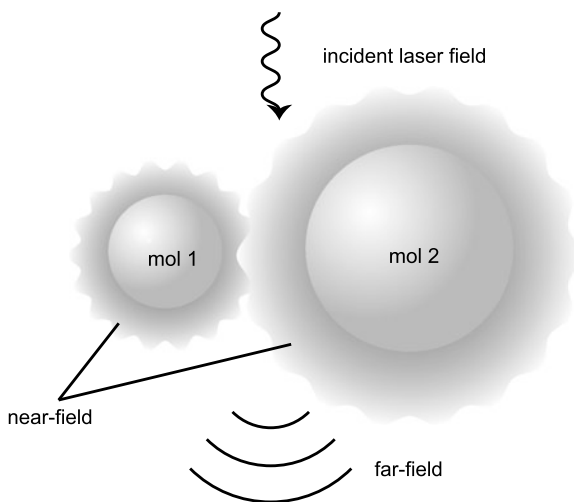
Optical response of molecules is undoubtedly essential for understanding their physicochemical properties. For example, UV-vis light is used to study electronic states of molecules, far-infrared light for molecular vibrations, microwave for molecular rotations and so forth. In these optical responses, wavelengths of the lights are usually considered to be much longer than molecular sizes. Thus, a target molecule is well approximated by a point dipole and the dipole feels an almost uniform electromagnetic field. This condition underlies the conventional dipole approximation. Furthermore, light is an external field to excite molecules and its wavelength is definitely determined by an apparatus condition. Since spatial resolution of spectroscopy is limited by the wavelength of the incident light, it is impossible to gain molecular properties in a local region shorter than the wavelength, i.e., diffraction limit. The conventional optical response mentioned above is referred here to as a far-field and matter interaction.

However, recent development of nanofabrication and nano-optical techniques requires a more general optical response theory for the following reasons. (We note that the light is considered here to be a classical wave determined by the Maxwell equations, although it should be treated in a narrow sense by resorting to the quantum electrodynamics theory.) When noninteracting or weakly-interacting nanopar-

K. Nobusada (✉)

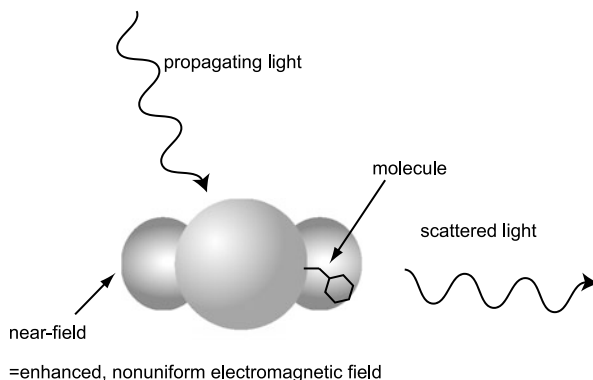
Department of Theoretical and Computational Molecular Science, Institute for Molecular Science, 38 Myodaiji-Nishigonaka, Okazaki, Aichi 444-8585, Japan
e-mail: nobusada@ims.ac.jp

Fig. 1.1 Schematic diagram of a near-field and a far-field from distant molecules 1 and 2 in the presence of an incident laser field



ticles are irradiated by an incident laser pulse, electric dipoles are induced in the nanoparticles. The induced dipoles generate local electric fields, in addition to far-fields, around the nanoparticles and then the adjacent particles can interact with each other through the local fields. This local field is often referred to as a near-field in contrast to a far-field. Figure 1.1 shows a schematic diagram of a near-field and a far-field from molecules irradiated by the incident laser field. The near-field interaction is significantly different from the far-field interaction [1–7]. If the near-field irradiates adjacent particles, the new near-field is subsequently generated around the particles. The new near-field recursively irradiates other particles and these sequential light-matter interactions between the particles persist self-consistently. As a result of the self-consistent interaction, an enhanced electric field, which is closely related to surface enhanced Raman scattering (SERS) [8–10], appears around the particles. A schematic diagram of SERS of a metallic-nanoparticle and molecule system is depicted in Fig. 1.2. Such locally enhanced electric fields have been observed experimentally [11] and intensively simulated in an effort to understand mechanisms of SERS by solving the Maxwell equations [12, 13]. SERS has currently attracted much attention in a wide range of research fields, and there is interest in both achieving a fundamental understanding of SERS itself and also in applications to engineering, biology, medical science, and pharmacology [14–16]. For example, a large enhancement in Raman intensity is expected to realize single-molecule detection [17, 18]. SERS effects are also thought to be applicable for developing ultrasensitive chemical sensors or imaging tools, especially for biomolecules [19, 20]. Second, as shown in Fig. 1.1 the near-field is a non-propagating wave rapidly decaying from the surface of a radiating-source particle, that is, the spatial variation of the near-field is of the same order of magnitude as the particle size. Thus, the near-field interaction occurs in a narrow region comparable with the size of the particle. In other words, the near-field and matter interaction, in sharp contrast to the far-field interaction, is a nonuniform one and the spatial structure of the near-field plays a crucial role.

Fig. 1.2 SERS is schematically illustrated. The *center particle* and the *right and left circles* represent a metallic nanoparticle and a near-field interaction, respectively. A molecule on the surface of the nanoparticle is exposed to the near-field and scatters the light



This means that the near-field overcomes the diffraction limit and gives in principle information about molecular properties associated with local structures even of 1-nm-sized nanoparticles or molecules. Conversely, those great advantages of the near-field interaction, that is, the self-consistency and the nonuniformity, require to describe light-matter interactions in a more general way.

Basic frameworks of optical response taking account of the full nonuniform and self-consistent light-matter interactions have so far been developed [21–23]. Although the studies were made in various molecular or nanostructure systems at different levels of theory, the authors drew essentially the same conclusion that those full light-matter interactions have a great influence on optical properties of the systems. Very recently, to confirm the importance of the full light-matter interactions in optical response, explicit computational demonstrations have been carried out in more specific nanosystems such as nanocrystals, semiconductor quantum dots, nanoparticles, and molecular compounds [12, 13, 24–28]. Every study clearly showed significant effects of the full light-matter interactions beyond the dipole approximation. An electric field enhancement due to the self-consistent light-matter interaction is a key ingredient in understanding a mechanism of SERS and its computations have been intensively demonstrated as mentioned above [12, 13]. Multipole effects concerning the nonuniform light-matter interaction were discussed in nanoparticles [25, 27], and molecular compounds [24]. Furthermore, the self-consistent and nonuniform light-matter interactions were verified in detail to play a crucial role in optical response to localized light fields generated between nanostructures [27, 28]. These explicit demonstrations have usually been done for model systems, simplifying the electronic structures of target nanostructures, for example, the nanostructures were assumed to be dielectric particles or their optical susceptibilities were given in advance. This is partly because it is computationally highly demanding to fully quantum-mechanically solve electron dynamics of the target nanosystems coupled with the electromagnetic field dynamics, in particular almost impossible for real nanostructures in a 1 nm size or more. Nevertheless, in molecular science, it is essential to calculate optical properties associated with details of electronic structures, such as geometric structures, bond characters, charge distribution, and electron correlation of target nanostructures. To describe optical response

of 1-nm-sized molecules, we split the full-light-matter interaction into the issues of self-consistency and nonuniformity. We first consider the nonuniform light-matter interaction as an initial step and leave the self-consistent interaction (i.e., solving the Maxwell-Schrödinger coupled equation) for the next. Here, a first-principles approach to treat a nonuniform light-matter interaction in real molecular systems is developed. We place special emphasis on obtaining full quantum-mechanical solutions of electron dynamics under the near-field (i.e., local field) to elucidate the nonuniform light-matter interaction at the level of molecular theory.

The conventional optical response theory is usually formulated starting from the minimal coupling Hamiltonian, and the formulation often relies on the dipole approximation. In contrast, we develop a more general theory without the dipole approximation, on the basis of the multipolar Hamiltonian derived from the minimal coupling Hamiltonian by a canonical transformation [22, 29–31]. The light-matter interaction in the multipolar Hamiltonian is described in terms of the space integral of an inner product of polarization and an electric field, whereas the minimal coupling Hamiltonian uses momentum and vector potential. The last two variables are rather inconvenient for practical calculations. Noteworthy is the fact that in the multipolar Hamiltonian approach the polarization in the integral can be treated entirely without any approximations. This means that infinite orders of multipole moments are taken into account. Therefore, the present approach is a generalization of the conventional optical response theory with the dipole approximation.

To investigate optical properties of real molecules, explicit time-evolution of electron dynamics should be solved. To this end, we have incorporated our optical response theory with the nonuniform light-matter interaction into our developed electron-dynamics simulation approach in real space [32–35] based on time-dependent density functional theory (TDDFT). The integrated TDDFT approach has been applied to and computationally solved for a test molecular system of dicyanodiacetylene (NC₆N) as an example, to elucidate the electron dynamics of 1-nm-sized molecules induced by the nonuniform near-field. Specifically, high-harmonic-generation (HHG) spectra induced by the near-field excitation are compared with those excited under the uniform light-matter interaction. The near-field excitation dynamics is also computationally demonstrated in optical forces exerted in a 1 nm-sized metal particle mimicked by a jellium model and in C₆₀.

1.2 Theory

1.2.1 Multipolar Hamiltonian

Electron dynamics in a molecule interacting with electromagnetic field is generally described by the time-dependent Schrödinger equation based on minimal coupling Hamiltonian consisting of vector potential A and scalar potential ϕ . Instead of using the minimal coupling Hamiltonian, however, we start our theoretical formulation from the multipolar Hamiltonian to include full spatial variation of an electric

field for the nonuniform light-matter interaction. The multipolar Hamiltonian can be derived from the minimal coupling Hamiltonian through a canonical transformation [29, 30]. It should be noted that in this study the electric field is considered to be a classical value and any magnetic interactions are neglected. The inter-molecular distances are assumed to be large enough so that their electronic wavefunctions do not overlap. The multipolar Hamiltonian of non-overlapping molecules interacting with an electric field is then obtained as [31]

$$\hat{H} = \hat{H}_{\text{mol}} + \hat{V}_{\text{inter}} - \int d\mathbf{r} \hat{\mathbf{P}}(\mathbf{r}) \cdot \mathbf{E}^{\perp}(\mathbf{r}, t), \quad (1.1)$$

where \hat{H}_{mol} is the Hamiltonian of the molecules and \hat{V}_{inter} is the static intermolecular Coulomb interaction. $\hat{\mathbf{P}}(\mathbf{r}) = \sum_i \hat{\mathbf{P}}_i(\mathbf{r})$ is the total polarization operator of the system with $\hat{\mathbf{P}}_i(\mathbf{r})$ being the polarization operator of the molecule i . $\mathbf{E}^{\perp}(\mathbf{r}, t)$ is the transverse part of the electric field written in the form of

$$\mathbf{E}^{\perp}(\mathbf{r}, t) = \mathbf{E}_{\text{laser}}^{\perp}(\mathbf{r}, t) + \sum_j \mathbf{E}_j^{\perp}(\mathbf{r}, t), \quad (1.2)$$

where $\mathbf{E}_{\text{laser}}^{\perp}(\mathbf{r}, t)$ is an incident laser field and $\mathbf{E}_j^{\perp}(\mathbf{r}, t)$ is the electric field radiated from the j -th molecule obtained by solving the Maxwell equations using $\mathbf{P}_j^{\perp}(\mathbf{r}', t - |\mathbf{r} - \mathbf{r}'|/c)$ as a source with c being the speed of light. The static intermolecular Coulomb interaction is given by

$$\hat{V}_{\text{inter}} = \frac{1}{\epsilon_0} \sum_{i < j} \int d\mathbf{r} \hat{\mathbf{P}}_i^{\parallel}(\mathbf{r}) \cdot \hat{\mathbf{P}}_j^{\parallel}(\mathbf{r}), \quad (1.3)$$

where $\hat{\mathbf{P}}_i^{\parallel}(\mathbf{r})$ is the longitudinal part of $\hat{\mathbf{P}}_i(\mathbf{r})$. Then, Eq. (1.1) is rewritten as

$$\hat{H} = \hat{H}_{\text{mol}} + \frac{1}{\epsilon_0} \sum_{i < j} \int d\mathbf{r} \hat{\mathbf{P}}_i^{\parallel}(\mathbf{r}) \cdot \hat{\mathbf{P}}_j^{\parallel}(\mathbf{r}) - \sum_i \int d\mathbf{r} \hat{\mathbf{P}}_i(\mathbf{r}) \cdot \mathbf{E}^{\perp}(\mathbf{r}, t). \quad (1.4)$$

The explicit form of $\hat{\mathbf{P}}_i(\mathbf{r})$ is [29–31]

$$\hat{\mathbf{P}}_i(\mathbf{r}) = \sum_{\alpha} e_{\alpha} (\hat{\mathbf{q}}_{\alpha} - \mathbf{R}_i) \int_0^1 d\lambda \delta(\mathbf{r} - \mathbf{R}_i - \lambda(\hat{\mathbf{q}}_{\alpha} - \mathbf{R}_i)), \quad (1.5)$$

where e_{α} and $\hat{\mathbf{q}}_{\alpha}$ are the charge and the position operator of the α -th electron in the molecule i , respectively, and \mathbf{R}_i is the center of mass of the molecule. The integration in Eq. (1.5) with respect to λ is introduced to express the polarization in such a compact form, instead of using multipoles explicitly.

We address here the relation between our optical response formula and the conventional approach based on a multipole expansion method. Eq. (1.5) can be expanded in a Taylor series leading to the dipole, quadrupole, octapole, and higher-

order multipole terms. The present formulation is thus a generalization of the conventional optical response theory with the dipole approximation. Applying the Taylor expansion to Eq. (1.5) and integrating the resulting equation with respect to λ , we obtain

$$\begin{aligned}
\int d\mathbf{r} \hat{\mathbf{P}}(\mathbf{r}) \cdot \mathbf{E}^\perp(\mathbf{r}, t) &= \left(\sum_\alpha e_\alpha (\hat{\mathbf{q}}_\alpha - \mathbf{R})_i \right) \cdot E_i^\perp(\mathbf{R}, t) \\
&\quad - \left(\frac{1}{2!} \sum_\alpha e_\alpha (\hat{\mathbf{q}}_\alpha - \mathbf{R})_i (\hat{\mathbf{q}}_\alpha - \mathbf{R})_j \right) \nabla_i E_j^\perp(\mathbf{R}, t) \\
&\quad + \left(\frac{1}{3!} \sum_\alpha e_\alpha (\hat{\mathbf{q}}_\alpha - \mathbf{R})_i (\hat{\mathbf{q}}_\alpha - \mathbf{R})_j (\hat{\mathbf{q}}_\alpha - \mathbf{R})_k \right) \\
&\quad \quad \times \nabla_i \nabla_j E_k^\perp(\mathbf{R}, t) \cdots \\
&\equiv \hat{\mu}_i E_i^\perp + \hat{Q}_{ij} \nabla_i E_j^\perp + \hat{O}_{ijk} \nabla_i \nabla_j E_k^\perp \cdots, \quad (1.6)
\end{aligned}$$

where $\hat{\mu}_i$, \hat{Q}_{ij} , and \hat{O}_{ijk} represent the dipole, quadrupole, and octapole moments of a molecule, respectively, and the indexes denote their (x, y, z) tensorial components. These moments are defined at the molecular center \mathbf{R} . ∇_i is the gradient operator along the i -th direction and acts on the electric field. We here use a contraction of $x_i y_i = \sum_i x_i y_i$. The dipole moment couples with the field itself, the quadrupole with the first derivative of the field, and the octapole with the second derivative of the field, and so forth. If an electric field varies slowly over a whole spatial region, the optical response can be reasonably described by only the first term of this expansion (i.e., the dipole approximation). The higher multipole effect is taken into account by including the higher terms of Eq. (1.6). However, the near-field interaction requires an infinite number of terms in the expansion because of its nonuniform spatial structure. Therefore, we use Eq. (1.5) as is, without performing the Taylor expansion of the polarization.

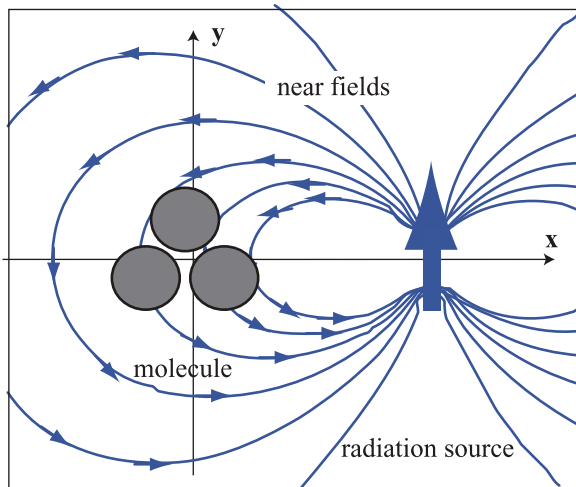
1.2.2 A Molecule Interacting with a Nonuniform Near-Field

In the previous section, we have formulated a general theory of the light-matter interaction. To demonstrate the electron dynamics in molecules interacting with a near-field, we first introduce a theoretical model consisting of two molecules irradiated by a laser light. The multipolar Hamiltonian Eq. (1.4) is rewritten for such a model system by

$$\hat{H}_{\text{mol}} + \frac{1}{\epsilon_0} \int d\mathbf{r} \hat{\mathbf{P}}_1^\parallel(\mathbf{r}) \cdot \hat{\mathbf{P}}_2^\parallel(\mathbf{r}) - \int d\mathbf{r} (\hat{\mathbf{P}}_1(\mathbf{r}) + \hat{\mathbf{P}}_2(\mathbf{r})) \cdot \mathbf{E}^\perp(\mathbf{r}, t). \quad (1.7)$$

As mentioned in the beginning of this article, the near-field is a non-propagating local field around nanostructures, generated in the presence of laser irradiation.

Fig. 1.3 Nonuniform light-matter interaction model derived from the near-field excitation process shown in Fig. 1.1. The molecule 2 is considered to be a radiation source approximated by an oscillating dipole. The near-fields, i.e., nonuniform electric fields, radiated from the oscillating dipole are shown in the *thin curves with arrows*



Although the near-field should be given by solving the Maxwell equations (or by resorting to quantum electrodynamics theory in a narrow sense), it is reasonably approximated by the short-range term of an oscillating dipole radiation [6, 36]. Then, the theoretical model given by Eq. (1.7) can be further simplified as follows. We discuss here optical response of the molecule 1 interacting only with the near-field radiated from the molecule 2, in which the molecule 2 is considered to be an oscillating dipole as shown in Fig. 1.3. This approximation means that the material Hamiltonian of the molecule 1 is solved quantum mechanically, whereas the molecule 2 is assumed to be a classical dielectric merely as a radiation source. Furthermore, we neglect the near-field induced around the molecule 1, which might affect the dielectric molecule 2 (i.e., the self-consistent effect) when the molecule 1 is electronically excited in its resonance state [27]. Since we focus on roles of the nonuniform electric field in electronic excitation of a molecule, the near-field frequency is chosen so that the resonance excitation does not occur principally. In addition, if the molecule 1 is smaller than the molecule 2, its induced polarization is also relatively smaller than that of the molecule 2. Thus, it is reasonable for the moment to neglect the induced near-field around the molecule 1. In other words, our light-matter interaction model is expected to be useful for studies about spatially-resolved local spectroscopy taking advantage of the nonuniform light-matter interaction in real molecules, because radiations from target molecules are usually weak compared to those of probe tips. For these reasons, the self-consistent effect is left for the future investigation. The incident laser field E_{laser}^{\perp} in the third term of Eq. (1.7) is required to induce the polarization associated with the oscillating dipole in the molecule 2. From our preliminary calculations, however, the incident field was found to be less important for the light-matter interaction in the near-field region because the intensity of the induced near-field is larger than that of the incident field. As a result, the electron dynamics in this region is qualitatively unaffected even if the incident laser field is neglected.

Under these conditions, Eq. (1.7) can be reduced to the form of

$$\begin{aligned} \hat{H}_{\text{mol}} - \int d\mathbf{r} \hat{\mathbf{P}}_1^{\parallel}(\mathbf{r}) \cdot \tilde{\mathbf{E}}_2^{\parallel}(\mathbf{r}, t) \\ - \int d\mathbf{r} (\hat{\mathbf{P}}_1(\mathbf{r}) + \hat{\mathbf{P}}_2(\mathbf{r})) \cdot (\tilde{\mathbf{E}}_1^{\perp}(\mathbf{r}, t) + \tilde{\mathbf{E}}_2^{\perp}(\mathbf{r}, t)), \end{aligned} \quad (1.8)$$

where the longitudinal part of the polarization operator $\hat{\mathbf{P}}_2^{\parallel}$ is replaced with the expectation (or c-number) value $-\varepsilon_0 \tilde{\mathbf{E}}_2^{\parallel}$. $\tilde{\mathbf{E}}$ represents the near-field part of \mathbf{E} . Although the far-field part of \mathbf{E} can also be included in this derivation, we only use the near-field part for simplicity. Equation (1.8) is rewritten in a more compact form of

$$\begin{aligned} \hat{H}_{\text{mol}} - \int d\mathbf{r} \hat{\mathbf{P}}_1(\mathbf{r}) \cdot \tilde{\mathbf{E}}_2(\mathbf{r}, t) \\ - \int d\mathbf{r} [\hat{\mathbf{P}}_1(\mathbf{r}) \cdot \tilde{\mathbf{E}}_1^{\perp}(\mathbf{r}, t) + \hat{\mathbf{P}}_2(\mathbf{r}) \cdot (\tilde{\mathbf{E}}_1^{\perp}(\mathbf{r}, t) + \tilde{\mathbf{E}}_2^{\perp}(\mathbf{r}, t))], \end{aligned} \quad (1.9)$$

where we used the relations of $\hat{\mathbf{P}}_1^{\parallel} \cdot \tilde{\mathbf{E}}_2^{\parallel} = \hat{\mathbf{P}}_1 \cdot \tilde{\mathbf{E}}_2^{\parallel}$ and $\tilde{\mathbf{E}}_2^{\parallel} + \tilde{\mathbf{E}}_2^{\perp} = \tilde{\mathbf{E}}_2$. Since the self-interaction term $\hat{\mathbf{P}}_1 \cdot \tilde{\mathbf{E}}_1^{\perp}$ is not important in this work and $\hat{\mathbf{P}}_2 \cdot (\tilde{\mathbf{E}}_1^{\perp} + \tilde{\mathbf{E}}_2^{\perp})$ does not act on the molecule 1, these terms can be omitted. Finally, the Hamiltonian of a molecule interacting with the near-field becomes

$$\hat{H} \equiv \hat{H}_{\text{mol}} + \hat{H}_{\text{int}}(t) = \hat{H}_{\text{mol}} - \int d\mathbf{r} \hat{\mathbf{P}}_1(\mathbf{r}) \cdot \tilde{\mathbf{E}}_2(\mathbf{r}, t). \quad (1.10)$$

This nonuniform light-matter interaction Hamiltonian is used throughout this study. Our computational model is rather oversimplified. However, it is computationally demanding to fully solved coupled Schrödinger–Maxwell equations, taking account of the properties of the self-consistency and the nonuniformity due to the light-matter interaction at the 1 nm scale. This derivation can also be applied to three or more particle systems, where only the dynamics of the molecule 1 interacting with the near-fields generated by the molecules 2, 3, ... is solved quantum mechanically in a similar way as in the two-particle system.

1.2.3 Near-Field Radiated from an Oscillating Dipole

Let us next model the near-field. The near-field is known to be a localized, non-propagating part of the light generated from a molecule when irradiated by an incident laser field (see Fig. 1.1). We describe the near-field in this article as the near-part of the electric field generated from an oscillating dipole, the simplest model for a radiation. In Fig. 1.3, the electric lines of the dipole radiation are depicted as the blue curves, the directions of which are shown by the arrows on the lines.

The analytical expression of the dipole radiation field $\mathbf{E}_{\text{dip}}(\mathbf{r}, t)$ generated by the oscillating dipole is given by [36]

$$\mathbf{E}_{\text{dip}}(\mathbf{r}, t) = \frac{k^3}{4\pi\epsilon_0} \left(\frac{[3\mathbf{n}(\mathbf{n} \cdot \boldsymbol{\mu}) - \boldsymbol{\mu}]}{(kr)^3} \right. \quad (1.11a)$$

$$\left. - i \frac{[3\mathbf{n}(\mathbf{n} \cdot \dot{\boldsymbol{\mu}}) - \dot{\boldsymbol{\mu}}]}{(kr)^2} \right. \quad (1.11b)$$

$$\left. + \frac{[\mathbf{n} \times \ddot{\boldsymbol{\mu}} \times \mathbf{n}]}{(kr)} \right) e^{-i\omega t + ikr} \quad (1.11c)$$

where k is a wavenumber, ϵ_0 is the vacuum permittivity, \mathbf{n} is the unit vector of \mathbf{r}/r , $\boldsymbol{\mu}$ is a dipole moment of the source placed at the origin, and ω is a frequency of the oscillation, where $\omega = kc$ with c being the velocity of light. The radiation field is classified into three parts in terms of the radial dependencies, r^{-3} , r^{-2} , and r^{-1} . We set the distance between the target molecule and the radiation source to be several angstroms, which is comparable in size with the molecule. In this region, the dipole radiation field is dominated by the local electric field depending on r^{-3} given by Eq. (1.11a). This local field is referred to as the near-field $\tilde{\mathbf{E}}$ used in the nonuniform light-matter interaction in Eq. (1.10). We can then neglect the magnetic interacting terms because the magnetic field from the oscillating dipole, not shown here, has the r^{-2} and r^{-1} dependent terms.

Since we consider an optical interaction between very closely spaced particles, it is reasonable to use the dipole radiation field as the electric near-field $\tilde{\mathbf{E}}_2$ without distinguishing its longitudinal and transverse components. For larger systems, however, the longitudinal and transverse parts should be evaluated separately because there is a difference in time between them, i.e., the longitudinal interaction is instantaneous, whereas the transverse one is retarded. The retardation effect can be treated by solving the Maxwell equations using the time-dependent polarization as a radiation source.

1.2.4 Light-Matter Interaction in the Kohn-Sham DFT Approach

For computational applications of the present formal theory, we will derive the light-matter interaction H_{int} in the Kohn-Sham (KS) DFT form. In the following derivations, we take $e_\alpha = -1$ for simplicity. Although the KS Hamiltonian is obtained by functional derivative of the expectation value of the total energy, it is enough to consider here only the light-matter interaction term of Eq. (1.10). The expectation value of \hat{H}_{int} is expressed by

$$\begin{aligned} \langle \hat{H}_{\text{int}}(t) \rangle &= \int d\mathbf{r} \Psi^*(\mathbf{r}, t) \hat{H}_{\text{int}}(t) \Psi(\mathbf{r}, t) \\ &= - \int d\mathbf{r} d\mathbf{r}' \Psi^*(\mathbf{r}, t) \hat{\mathbf{P}}(\mathbf{r}') \Psi(\mathbf{r}, t) \cdot \tilde{\mathbf{E}}(\mathbf{r}', t) \end{aligned}$$

$$\begin{aligned}
&= \int d\mathbf{r}d\mathbf{r}'\Psi^*(\mathbf{r},t)(\mathbf{r}-\mathbf{R}) \\
&\quad \times \int_0^1 d\lambda\delta(\mathbf{r}'-\mathbf{R}-\lambda(\mathbf{r}-\mathbf{R}))\Psi(\mathbf{r},t)\cdot\tilde{\mathbf{E}}(\mathbf{r}',t) \\
&= \int d\mathbf{r}[\Psi^*(\mathbf{r},t)\Psi(\mathbf{r},t)](\mathbf{r}-\mathbf{R})\int_0^1 d\lambda \\
&\quad \times \int d\mathbf{r}'\delta(\mathbf{r}'-\mathbf{R}-\lambda(\mathbf{r}-\mathbf{R}))\tilde{\mathbf{E}}(\mathbf{r}',t) \\
&\equiv \int d\mathbf{r}\rho(\mathbf{r},t)(\mathbf{r}-\mathbf{R})\cdot\int_0^1 d\lambda\tilde{\mathbf{E}}(\mathbf{R}+\lambda(\mathbf{r}-\mathbf{R}),t) \\
&\equiv \int d\mathbf{r}\rho(\mathbf{r},t)(\mathbf{r}-\mathbf{R})\cdot\mathbf{E}_{\text{eff}}(\mathbf{r},t) \\
&\equiv \int d\mathbf{r}\rho(\mathbf{r},t)V_{\text{eff}}(\mathbf{r},t) \tag{1.12}
\end{aligned}$$

where Ψ is the ground state wavefunction of the molecule, and the electron density $\rho(\mathbf{r})$, the effective electric field \mathbf{E}_{eff} , and the effective potential V_{eff} are given by

$$\rho(\mathbf{r},t)\equiv\Psi^*(\mathbf{r},t)\Psi(\mathbf{r},t), \tag{1.13a}$$

$$\mathbf{E}_{\text{eff}}(\mathbf{r},t)\equiv\int_0^1 d\lambda\tilde{\mathbf{E}}(\mathbf{R}+\lambda(\mathbf{r}-\mathbf{R}),t), \tag{1.13b}$$

$$V_{\text{eff}}(\mathbf{r},t)\equiv(\mathbf{r}-\mathbf{R})\cdot\mathbf{E}_{\text{eff}}(\mathbf{r},t). \tag{1.13c}$$

The λ -integration of $\tilde{\mathbf{E}}$ includes all the contributions of the spatial variation of the electric field. As is clearly seen from Eq. (1.12), the nonuniform light-matter interaction is straightforwardly calculated in the conventional KS-DFT approach if the effective potential V_{eff} is added to the external potential term in the KS equation.

1.3 Computational Application

1.3.1 Time-Dependent Kohn-Sham Approach in Real Space

In this section, the KS-DFT computational approach is explained to demonstrate the electron dynamics of nanoclusters interacting with a near-field. The time-dependent Kohn-Sham (TD-KS) approach in real space and time to electron dynamics has so far been explained elsewhere [32, 37–39]. We review the approach with particular emphasis on extending it to the optical response to a nonuniform electric field. A time-dependent N -electron interacting system is solved through a set of electronic

wave functions $\psi_j(\mathbf{r}, t)$ satisfying the following TD-KS equation

$$i\hbar\frac{\partial}{\partial t}\psi_j(\mathbf{r}, t) = \left[-\frac{\hbar^2}{2m}\nabla^2 + V_{\text{KS}}[\rho](\mathbf{r}, t) \right] \psi_j(\mathbf{r}, t), \quad (1.14)$$

where m is the electron mass and ρ is the electron density given by

$$\rho(\mathbf{r}, t) = 2 \sum_{j=1}^{N/2} |\psi_j(\mathbf{r}, t)|^2. \quad (1.15)$$

The factor of 2 indicates that each KS orbital is fully occupied (i.e., a closed shell system). The KS potential $V_{\text{KS}}[\rho](\mathbf{r}, t)$ is a functional of ρ , and it consists of four terms of an ion-electron interaction potential $V_{\text{ion}}(\mathbf{r})$, a time-dependent Hartree potential, an exchange-correlation (XC) potential $V_{\text{xc}}[\rho](\mathbf{r}, t)$, and an external potential V_{eff} as follows:

$$V_{\text{KS}}[\rho](\mathbf{r}, t) = V_{\text{ion}}(\mathbf{r}) + \frac{1}{4\pi\epsilon_0} \int \frac{\rho(\mathbf{r}', t)}{|\mathbf{r} - \mathbf{r}'|} d\mathbf{r}' + V_{\text{xc}}[\rho](\mathbf{r}, t) + V_{\text{eff}}(\mathbf{r}, t). \quad (1.16)$$

The ion-electron interaction potential $V_{\text{ion}}(\mathbf{r})$ is constructed from norm-conserving pseudopotentials of each atomic component of the system considered. Following the Troullier and Martins procedure [40], the pseudopotentials are numerically generated so that the pseudowavefunctions can imitate the all-electron atomic wave functions. The potentials depend on the angular momentum components. In this article, we use the Kleinman-Bylander separable form to represent the nonlocal (i.e., angular momentum depending) potential terms [41].

To represent the XC potential, we use the following adiabatic local density approximation (ALDA)

$$V_{\text{xc}}[\rho](\mathbf{r}, t) \approx V_{\text{xc}}^{\text{LDA}}[\rho](\mathbf{r}, t) = V_{\text{xc}}^{\text{LDA}}[\rho_0](\mathbf{r})|_{\rho_0(\mathbf{r})=\rho(\mathbf{r}, t)}, \quad (1.17)$$

where $V_{\text{xc}}^{\text{LDA}}[\rho_0](\mathbf{r})$ is the ground-state LDA XC potential given by Perdew and Zunger [42]. In ALDA, the XC potential at \mathbf{r} and t is approximated by that of the ground-state uniform electron gas having the density $\rho(\mathbf{r}, t)$. Although the ALDA XC potential does not take account of the nonlocality in both \mathbf{r} and t and more accurate exchange-correlation functionals have been developed lately, the ALDA has practically provided results for single-electron excitation processes sufficiently below the lowest ionization threshold of systems [43–45]. Furthermore, it is reasonable to use such a simple functional at this early stage of development prior to performing highly accurate calculations towards material science.

In the present theoretical model of the nonuniform light-matter interaction, the external potential V_{eff} is given by Eqs. (1.13b) and (1.13c). As mentioned above, $\tilde{\mathbf{E}}$ in Eq. (1.13b) is approximated as the oscillating dipole radiation Eqs. (1.11a)–(1.11c), the main contribution of which is given by the r^{-3} dependent term of Eq. (1.11a). We set the center of mass of the molecule to be the origin. The temporal

shape of the near-field is taken as a pulse. Finally, the effective potential Eq. (1.13c) is rewritten by

$$V_{\text{eff}}(\mathbf{r}, t) = -\mathbf{r} \cdot \mathbf{E}_{\text{eff}}(\mathbf{r}) \sin(\omega t) \sin^2\left(\frac{\pi t}{T}\right) \quad (0 < t < T), \quad (1.18)$$

where ω is the frequency of the oscillating dipole, and T determines the pulse duration. The pulse profile is approximated by $\sin^2(\frac{\pi t}{T})$ in which a few cycles of the electric fields are included. The field intensity is related to the field strength by $I = \frac{1}{2}\epsilon_0 c E^2$.

1.4 High-Harmonic-Generation Spectra Induced by the Near-Field Excitation

1.4.1 Molecular System and Computations

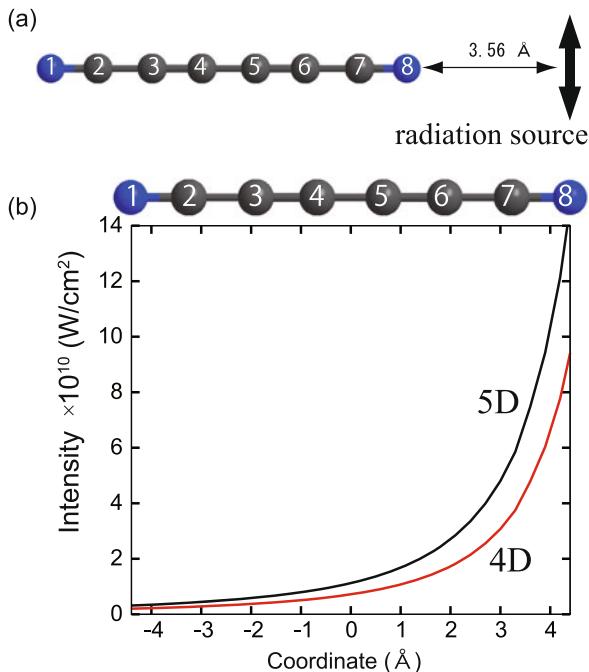
A linear chain molecule is one of the better choices to demonstrate the nonuniform light-matter interaction, in particular for such an electric field proportional to r^{-3} . We choose a dicyanodiacetylene (NC_6N) molecule [46] shown in Fig. 1.4(a) as an example of a real molecule. The geometric structure has been optimized by using the TURBOMOLE V5.10 [47, 48] package of quantum chemistry programs, employing the LDA exchange functional developed by Perdew and Wang [49] with the basis set of def-SV(P) [50] from the TURBOMOLE basis set library, which corresponds to the basis set of 6-31G*. The simplest functional LDA was chosen for consistency with the functional used in the TD-KS equation. The vibrational analysis showed no imaginary frequency. The interatomic distances of the molecule are $\text{N}_1\text{--C}_2 = 1.176 \text{ \AA}$, $\text{C}_2\text{--C}_3 = 1.354 \text{ \AA}$, $\text{C}_3\text{--C}_4 = 1.239 \text{ \AA}$, and $\text{C}_4\text{--C}_5 = 1.340 \text{ \AA}$.¹

The TDKS equation (1.14) for NC_6N is solved numerically by a grid-based method [32, 51] in a three-dimensional Cartesian-coordinate rectangular box, the lengths of which are 30 \AA along the molecular (x -) axis and 20 \AA along the y - and z -axes, utilizing uniform grids with a mesh spacing of 0.3 \AA . The Laplacian operator is evaluated by a nine-point difference formula [52]. The time-propagation of the KS orbitals is carried out with a fourth-order Taylor expansion by using a constant time step of 0.002 fs . The inner shell structures of the carbon and nitrogen atoms are approximated by effective core pseudopotentials, and then the remaining four electrons ($2s^2 2p^2$) for C and five electrons ($2s^2 2p^3$) for N are explicitly treated. In other words, we have carried out 34-electron dynamics calculations for NC_6N .

The effective potential for the dipole radiation on each grid is computed combining Eqs. (1.11a)–(1.11c), (1.13b), and (1.13c), where the main contribution in Eqs. (1.11a)–(1.11c) is its near-field part (1.11a). A point dipole $\boldsymbol{\mu}$ is placed at

¹These bond lengths remain almost unchanged (i.e., at most 0.0024 \AA for $\text{C}_3\text{--C}_4$) even if the geometry optimization was performed by using the B3LYP functional [58, 59].

Fig. 1.4 (a) Geometrical structure of NC_6N and the position of the radiation source. (b) The intensities of the effective electric fields on the molecular axis calculated from the near-field of the dipole radiation. The near-fields are generated by the oscillating dipole with its absolute value of the dipole moment being 4 D and 5 D, respectively

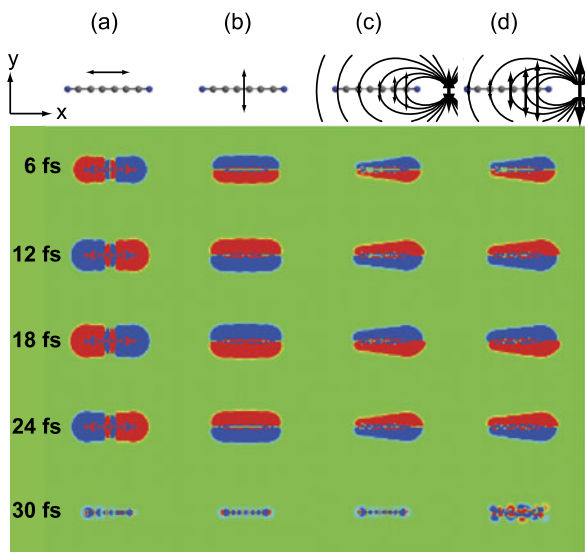


$x = 8.0 \text{ \AA}$ (i.e., the value of 3.56 \AA is the distance between the rightmost nitrogen atom N(8) and the dipole as shown in Fig. 1.4(a)) so that the nonuniform electronic excitation due to the near-field is clearly demonstrated. The dipole is assumed to be y -polarized, that is $\boldsymbol{\mu} = (0.0, \mu, 0.0)$ Debye (D), where μ is the absolute value of the dipole moment. The dipole fields generated from $\mu = 4.0 \text{ D}$ and 5.0 D are used in this study. The integral of Eq. (1.13b) is calculated numerically with a constant step of $\Delta\lambda = 0.0423 \text{ \AA}$. The contribution of the dipole radiation field at its origin to the integration is evaluated by $4\pi\mu/3$ [31]. E_{dip} is also replaced with $4\pi\mu/3$ if $|E_{\text{dip}}|$ is larger than $|4\pi\mu/3|$. This is done for a few points very close to the dipole, i.e., $|r| \sim 0.2 \text{ \AA}$. The intensity of the effective electric field varies largely as indicated in Fig. 1.4(b). The effective field intensity at the right end of the NC_6N molecule is two orders of magnitude larger than that at the left end (i.e., 10^{11} and 10^9 W/cm^2 at the right and the left ends, respectively). Thus, the molecule is nonuniformly excited by the oscillating dipole field. All the electric fields used in this study have the field frequency ω of 1 eV (the off-resonance condition). The pulse duration ($T = 30 \text{ fs}$) is short enough to avoid considering the nuclear dynamics.

1.4.2 Near-Field Excitation Dynamics

Let us first demonstrate the electron density motions in the uniform and the nonuniform electric fields. Figure 1.5 shows four snapshots of differences of the electron

Fig. 1.5 Snapshots of difference of the electron density at $t = 6, 12, 18, 24,$ and 30 fs from the initial ($t = 0$ fs) static electron density. The uniform fields ((a), (b)) and the nonuniform (oscillating dipole) fields with their dipole moments being (c) 4 D and (d) 5 D are applied to the molecule. Four schematic illustrations at the top of each snapshot display the ways of electronic excitation



densities at $t = 6, 12, 18, 24,$ and 30 fs from the initial ($t = 0$) electron density. Each snapshot indicates an increase and a decrease in the electron density, respectively. Each column of the snapshots illustrates the different time evolution of the electron density depending on the ways of electronic excitation. Four schematic illustrations at the top of the figure display how the light-matter interaction works. The uniform oscillating-electric-field with its intensity of 10^{12} W/cm² is applied to the molecule along the (a) x - or (b) y -axis, whereas the nonuniform fields radiated from the oscillating dipoles (the black bold arrows) with their dipole moments being (c) 4 D and (d) 5 D are applied to the molecule.

The electron densities in Figs. 1.5(a) and (b) oscillate uniformly and regularly along the applied field directions, keeping the molecular symmetry. However, as shown in Figs. 1.5(c) and (d), the nonuniform electric field apparently induces the symmetry-breaking time-evolution of the electron density. Such inhomogeneous electron dynamics clearly reflects the spatial distribution of the dipole field. Since the oscillating dipole is y -polarized, the generated electric field on the x -axis is also y -polarized, but its intensity sharply falls as r increases (i.e., $\propto r^{-3}$), where r is the distance from the oscillating dipole. Furthermore, only the x -component of the dipole field E_x is antisymmetric with respect to the x -axis (i.e., $E_x(x, y, z) = -E_x(x, -y, z)$), whereas E_y and E_z are symmetric. For these reasons, the time-evolved densities in Figs. 1.5(c) and (d) regularly oscillate to some extent along the y -axis, whereas those are distorted along the x -axis. The electron density distributions at 12 and 18 fs, for example, represent the antisymmetric motion along the x -axis. Specifically, the upper and lower half parts of the densities with respect to the x -axis move toward the opposite directions. These irregular motions are really due to the electronic excitation by the symmetry-breaking, nonuniform electric field. The electron density distribution at 30 fs in Fig. 1.5(d) looks

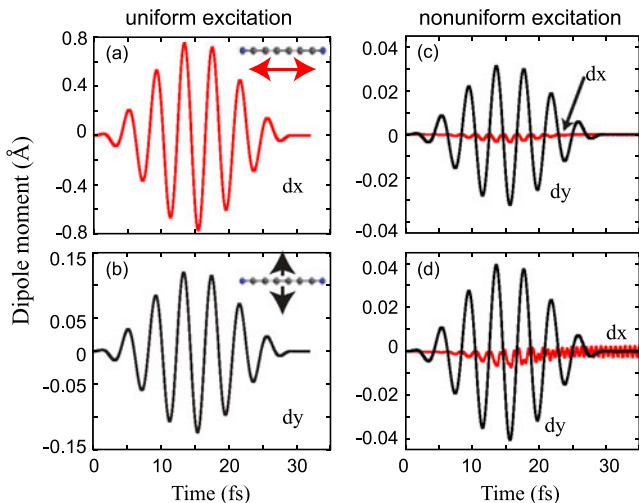
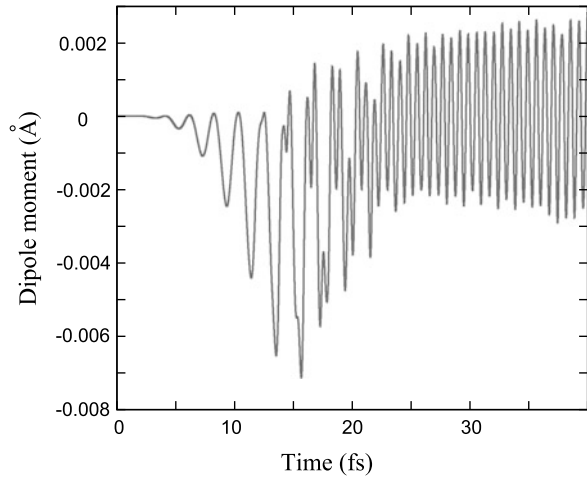


Fig. 1.6 Induced dipole moments along the x - and y -axes, d_i ($i = x, y$). The dipole moments, respectively, correspond to the time-evolutions of the density in Figs. 1.5(a)–(d). Insets in (a) and (b) are schemes of the applied field direction

rather different from the others. The electron-density-differences in Figs. 1.5(a)–(c) almost disappear at the end of the pulse of the external electric fields because the applied laser frequency considered is not in tune with any resonance frequencies. In contrast, the electron density distribution in Fig. 1.5(d), under the condition of the stronger nonuniform electric field, still persists even after the end of the pulsed near-field. This is attributed to the nonuniform excitation by the localized near-field. In this study, the near-field frequency is not tune with any dipole resonance frequencies of NC_6N . Thus, the time-evolution of the electron density should not persist after the end of the near-field radiation (see, Fig. 1.5(c)). However, higher harmonics are more easily generated by the nonuniform excitation with increasing the strength of the dipole radiation field. NC_6N has a dipole resonance frequency at 5.75 eV, which is close to the sixth harmonics (=6 eV). As the result of this, the resonance excitation accidentally occurs in the case of Fig. 1.5(d). Such a resonance excitation allows the electrons to move persistently after the end of the pulse. It should be noted that this resonance effect is due to a high-order nonlinear effect and thus is still minor in the present nonuniform light-matter interaction model, i.e., it hardly affects the radiation from the molecule 2.

Figures 1.6(a)–(d) show the induced dipole moments along the x - and y -axes, d_i ($i = x, y$), corresponding to the time evolutions of the electron densities in Figs. 1.5(a)–(d), respectively. The red and the dashed black curves represent d_x and d_y . The insets in Figs. 1.6(a) and (b) schematically draw the applied field directions. Similar overall time-profiles have been observed in d_x (Fig. 1.6(a)) and d_y (Fig. 1.6(b)) induced by the uniform field and in d_y induced by the nonuniform field. In sharp contrast, nonuniformly induced d_x s do not follow the time-profile of the applied field. To see this more clearly, we pick up d_x in Fig. 1.6(d) and plot it

Fig. 1.7 Magnification of d_x in Fig. 1.6(d)



in Fig. 1.7. In the early times until about 20 fs, d_x takes negative values owing to the sharp gradient in the field intensity. The oscillation frequency becomes much faster than that of the applied field after ~ 20 fs. Such an irregular oscillation of d_x is a consequence of the antisymmetric E_x of the dipole field that acts strongly in the right part of NC_6N . Thus, the irregular time-evolutions of the density along the x -axis in Figs. 1.5(c) and (d) were induced by the nonuniform, antisymmetric dipole radiation field. We have further confirmed that such an irregular motion cannot be induced even if we use either an electric field having a similar sharp gradient in the field intensity or an antisymmetric electric field.

We next calculate the emission spectra for each electron dynamics to analyze the uniform and nonuniform electronic excitations in an energy domain. Since the emission spectrum is associated with the dipole acceleration [53, 54], we here take the second derivative of the induced dipole moments and then perform a Fourier transform. Figure 1.8 shows the power spectra of the dipole acceleration $|\ddot{d}_i(\omega)|^2$ ($i = x, y$) in the unit of $\text{\AA}^2 \text{fs}^{-2}$ as a function of energy. We refer to the power spectra of the dipole acceleration as harmonic-generation (HG) spectra. The HG spectra in Figs. 1.8(a)–(d) correspond to the induced dipole moments in Figs. 1.6(a)–(d), respectively. The red and the dashed black curves represent $|\ddot{d}_x(\omega)|^2$ and $|\ddot{d}_y(\omega)|^2$. Comparing Figs. 1.8(a) and (b), the harmonics along the x -axis (\ddot{d}_x) seem relatively easier to generate than that along the y -axis (\ddot{d}_y). A comparatively large peak appears at around 6 eV in Fig. 1.8(a). As discussed in the time-evolution of the electron density in Fig. 1.5, this large peak is due to the fact that the sixth harmonics is accidentally close to a dipole resonance peak ($=5.75$ eV) of NC_6N . Despite the inversion symmetry of NC_6N , the nonuniform electric field, in contrast to the uniform one, causes the even harmonics in addition to the odd harmonics as shown in Figs. 1.8(c) and (d). Interestingly, the even and odd harmonics are respectively due to the induced dipole moments along the x - and y -axes. The even harmonics, therefore, have proved to be generated by the nonuniform electric field breaking the symmetry along the x -axis. Furthermore, in comparison with the

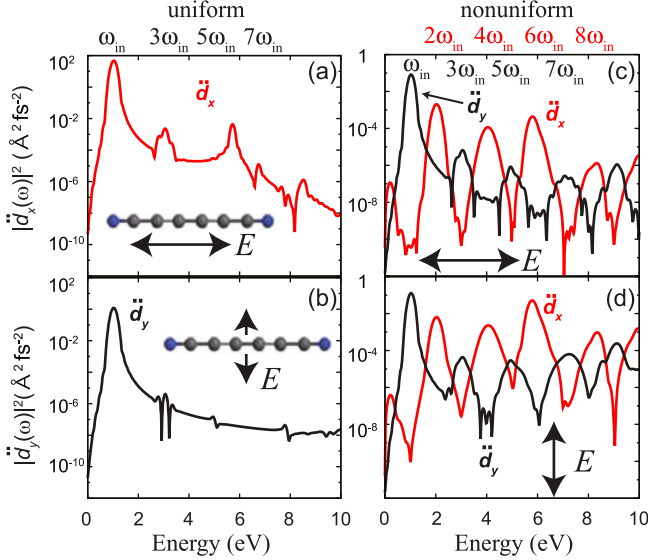


Fig. 1.8 HG power spectra of the dipole acceleration. The ways of electronic excitation correspond to those in Figs. 1.5(a)–(d) and also in Figs. 1.6(a)–(d), respectively

HG spectra by the uniform electric field, relatively higher harmonics are clearly seen in the HG spectra by the nonuniform electric field. In addition, their peak intensities do not decay linearly against the order of the harmonics.

Before ending this section, we demonstrate that the nonuniform electronic excitation also induces the quadrupole moment, which is never induced by the uniform electric field, as one of the phenomena beyond the dipole approximation. Such non-dipole excitation was observed in an experiment [55], although both nanostructure systems are different from the present one. The xy component of the quadrupole moment (Q_{xy}) for the time-evolution of Fig. 1.5(d) and its HG power spectrum are shown in Figs. 1.9(a) and (b), respectively. The quadrupole moments both in the time and the energy domains provide the structural patterns quite similar to those of the dipole ones. To verify that Q_{xy} is non-negligible in the nonuniform excitation, we consider the charge distribution that causes dipole and quadrupole moments. The calculated value of the quadrupole moment in the unit of \AA^2 is about an order of magnitude larger than that of the dipole moment in the unit of \AA . The dipole moment of two charges q and $-q$ with the inter charge distance a is $qa \text{\AA}$, whereas the quadrupole moment of two positive q' and two negative $-q'$ charges disposed at the corners of a square with its side being a is $q'a^2 \text{\AA}^2$. Then, $|Q_{xy}| \sim 10|d_y|$ (see Figs. 1.6(d) and 1.9(a)) and a is $\sim 10 \text{\AA}$ for NC_6N . Thus, we have $q \sim q'$ because $q'a^2 \sim 10 \times qa \rightarrow q'a \sim 10 \times q \rightarrow q' \sim q$. This indicates that the dipole-like and quadrupole-like charge distributions have been induced in almost the same amount as a consequence of the nonuniform light-matter interaction.

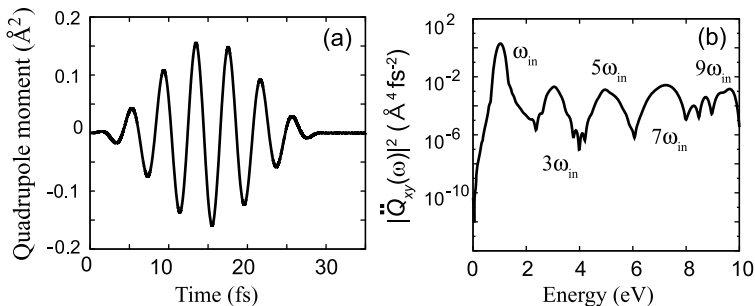


Fig. 1.9 (a) xy -component of the induced quadrupole moment as a result of the nonuniform excitation with $\mu = 5$ D and (b) its power spectrum

1.4.3 Even and Odd Harmonics

Let us next carry out a perturbation analysis of the HG power spectra generated through the nonuniform light-matter interaction. As shown in Figs. 1.8(c) and (d), the even harmonics appear despite the inversion symmetry of NC₆N. The even and odd harmonics are due to the induced dipole moments d_x and d_y , respectively. This even and odd alteration is easily understood in terms of the symmetries of the molecular wave functions and the external field.

According to the time-dependent perturbation theory [56, 57], n -th dipole moment $d_\alpha^{(n)}$ ($n = 1, 2, \dots$ and $\alpha = x, y, z$) in powers of the perturbation V_{eff} can be evaluated by the following matrix elements,

$$\langle 0|\alpha|i\rangle \underbrace{\langle i|V_{\text{eff}}|j\rangle \langle j|V_{\text{eff}}|k\rangle \cdots \langle l|V_{\text{eff}}|0\rangle}_{n \text{ brackets}}, \quad (1.19)$$

where $|0\rangle$ and $|i\rangle$ are the ground and the excited eigen states of the nonperturbative Hamiltonian of the molecule, respectively. As typical examples, $d_x^{(2)}$, $d_y^{(2)}$, $d_x^{(3)}$, and $d_y^{(3)}$ are considered. Table 1.1 summarizes the evaluation of the matrix elements of $d_x^{(2)}$ and $d_y^{(2)}$. The symmetries of the eigen states and the applied field are labeled as “ e ” for the even symmetry and “ o ” for the odd one. Since NC₆N has mirror symmetries in every direction, the eigen state $\{|i\rangle\}$ is either even or odd with respect to x -, y -, or z -axis, namely, $\psi(x, y, z) = \pm\psi(-x, y, z)$, $\psi(x, y, z) = \pm\psi(x, -y, z)$, or $\psi(x, y, z) = \pm\psi(x, y, -z)$. The effective potential V_{eff} given by Eq. (1.13c) is neither an even nor an odd function of x , an odd function of y , and an even function of z , i.e., $V_{\text{eff}}(x, y, z) \neq V_{\text{eff}}(-x, y, z)$, $V_{\text{eff}}(x, y, z) = -V_{\text{eff}}(x, -y, z)$, and $V_{\text{eff}}(x, y, z) = V_{\text{eff}}(x, y, -z)$. Thus, the brackets can be estimated by decomposing them into the integrations with respect to the x -, y -, and z -coordinates. $\int d\alpha$ ($\alpha = x, y, z$) in Table 1.1 denotes each component of the integrations. The symmetries of the ground state $|0\rangle$, the operators (x and y), and the potential V_{eff} are specified in bold characters. The symmetries of $|i\rangle$ and $|j\rangle$ are then specified so that the matrix elements have nonzero values. As a result, $d_x^{(2)}$ becomes nonzero, but

Table 1.1 Matrix elements of the second-order dipole moments along the x - and y -axes in the power of V_{eff} . e and o denote even and odd symmetries, respectively. The symmetries of the ground state and V_{eff} are indicated by bold characters

$d_x^{(2)}$	$\langle 0 x i\rangle$	$\langle i V_{\text{eff}} j\rangle$	$\langle j V_{\text{eff}} 0\rangle$	
$\int dx$	$\langle e \mathbf{o} o\rangle$	$\langle o \mathbf{e}\mathbf{o} e\rangle$	$\langle e\mathbf{o} \mathbf{e}\mathbf{o} e\rangle$	$\neq 0$
$\int dy$	$\langle e e\rangle$	$\langle e \mathbf{o} o\rangle$	$\langle o \mathbf{o} e\rangle$	$\neq 0$
$\int dz$	$\langle e e\rangle$	$\langle e \mathbf{e} e\rangle$	$\langle e \mathbf{e} e\rangle$	$\neq 0$
$d_y^{(2)}$	$\langle 0 y i\rangle$	$\langle i V_{\text{eff}} j\rangle$	$\langle j V_{\text{eff}} 0\rangle$	
$\int dx$	$\langle e e\rangle$	$\langle e \mathbf{e}\mathbf{o} e\rangle$	$\langle e\mathbf{o} \mathbf{e}\mathbf{o} e\rangle$	$\neq 0$
$\int dy$	$\langle e \mathbf{o} o\rangle$	$\langle o \mathbf{o} e\rangle$	$\langle e \mathbf{o} e\rangle$	$= 0$
$\int dz$	$\langle e e\rangle$	$\langle e \mathbf{e} e\rangle$	$\langle e \mathbf{e} e\rangle$	$\neq 0$

Table 1.2 Same as Table 1.1 but for the third-order dipole moments. As in the case of Table 1.1, $\int dx dz$ is always nonzero, and thus only $\int dy$ is summarized here

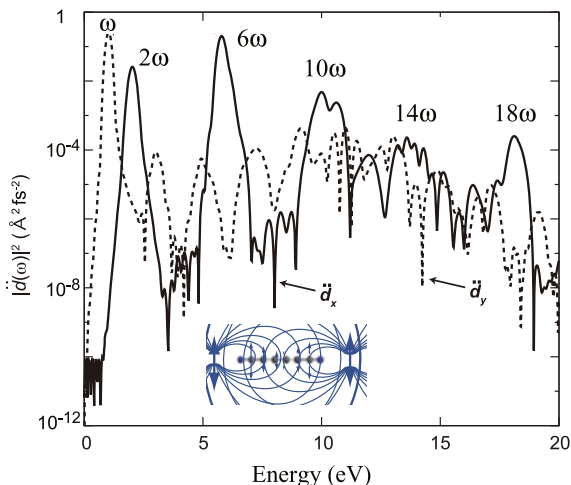
$d_x^{(3)}$	$\langle 0 x i\rangle$	$\langle i V_{\text{eff}} j\rangle$	$\langle j V_{\text{eff}} k\rangle$	$\langle k V_{\text{eff}} 0\rangle$	
$\int dy$	$\langle e e\rangle$	$\langle e \mathbf{o} o\rangle$	$\langle o \mathbf{o} e\rangle$	$\langle e \mathbf{o} e\rangle$	$= 0$
$d_y^{(3)}$	$\langle 0 y i\rangle$	$\langle i V_{\text{eff}} j\rangle$	$\langle j V_{\text{eff}} k\rangle$	$\langle k V_{\text{eff}} 0\rangle$	
$\int dy$	$\langle e \mathbf{o} o\rangle$	$\langle o \mathbf{o} e\rangle$	$\langle e \mathbf{o} e\rangle$	$\langle o \mathbf{o} e\rangle$	$\neq 0$

$d_y^{(2)}$ must be zero because the integral of $\langle j|V_{\text{eff}}|0\rangle$ with respect to the y -coordinate vanishes. The same analysis can be applied to $d_x^{(3)}$ (see, Table 1.2). Then, $d_x^{(3)}$ must be zero but $d_y^{(3)}$ becomes nonzero. The above analysis clearly explains the even-odd alteration appears in the HG power spectra obtained by the nonuniform excitation.

1.4.4 Control of Harmonic Generation by Interference

Finally, it is demonstrated that the harmonics induced by the near-field can be controlled. Figure 1.10 shows the HG power spectra obtained when both ends of the NC_6N molecule are excited by the near-fields radiated from two oscillating dipoles with different phases by $\pi/2$. The inset illustrates the schematic diagram of the near-field excitation by two radiation sources. It is clearly seen from the figure that harmonics selectively appear every $4\omega_{\text{in}}$ starting from the second harmonics ($2\omega_{\text{in}}$). The fourth and eighth harmonics ($4\omega_{\text{in}}$ and $8\omega_{\text{in}}$) completely disappear as a result of the interference between the two near-fields having different phases. We expect that this idea of the near-field excitation with different phases can control intensities and orders of HG spectra.

Fig. 1.10 Power spectra of the dipole acceleration along the x - and y -axes. Two oscillating dipole fields with different phases disposed at both ends of the molecule are applied



1.4.5 Concluding Remarks

We have presented a generalized theoretical description of optical response in an effort to understand a nonuniform light-matter interaction between a near-field and a 1-nm-sized molecule. The light-matter interaction based on the multipolar Hamiltonian, instead of the minimal coupling Hamiltonian, was described in terms of a space integral of the inner product of the total polarization of a molecule and an external electric field. Noteworthy is the fact that the polarization in the integral can be treated entirely without invoking any approximation such as a dipole approximation. Therefore, the present light-matter interaction theory allows us to understand the inhomogeneous electron dynamics associated with local electronic structures of a molecule at the 1 nm scale, although the wavelength of an incident laser pulse is much longer than the size of the molecule. For a computational application, we have studied the near-field-induced electron dynamics of NC_6N by using the TD-KS approach in real space incorporated with the present nonuniform interaction theory. The electron dynamics induced by the nonuniform light-matter interaction is completely different from that by the conventional uniform interaction under the dipole approximation. Specifically, in the nonuniform electronic excitation high harmonics were generated more easily and much more interestingly the even harmonics were also generated in addition to the odd ones despite the inversion symmetry of NC_6N . Perturbation theory clearly explained that the even harmonics were generated owing to the symmetry-breaking (nonuniform) electric field along the x -axis radiated from the oscillating dipole. It has also been found that the nonuniform fields with different phases control HG though their interference effect.

1.5 Near-Field Induced Optical Force in a Metal Nanoparticle and C₆₀

1.5.1 Brief Review of Optical Force

Optical trapping of micron-sized particles by lasers was reported in the pioneering work by Ashkin [60] and its idea was eventually realized as an innovative tool of a single-beam gradient force optical trap for dielectric particles, called “optical tweezers” [61]. In a series of papers since this seminal work, Ashkin and coworkers have succeeded in optically trapping and manipulating various types of objects [62]. The optical tweezers using force exerted by a highly focused laser-beam can trap and manipulate objects, now in practice, ranging in force up to 100–200 pN with sub-pN resolution and in size from tens of nanometers to tens of micrometers. Such laser-based optical traps have been used in a wide-range of applications [63, 64] to atoms and small molecules [62], colloidal particles [65, 66], and biological objects [67–69]. In particular, biological applications have been extensively made to study mechanical or functional properties of cells, intercellular materials, and filaments, and also to study biological motors. A large number of references of those biological applications were compiled in the resource letters [70].

Although a complete description of the laser-based optical traps needs a fully quantum-mechanical treatment, the optical force exerted on trapped objects can be derived from the Maxwell stress tensor into two limiting cases where the size of the object is much larger (i.e., infinitely extended systems) and much smaller (i.e., small particle systems) than the wavelength of an incident laser field [6]. In the limiting case of the extended systems, the net force is associated with so called optical pressure. In the other limiting case of the small particle systems, the net force considered to be a gradient force. Since in this article we study nanoparticle and light interaction, the gradient force exerted by optical field is only discussed. The gradient force is expected to be exerted more efficiently by using a near-field in optical traps because the near-field is a very short-ranged electromagnetic field with strong intensity gradient. Such a short-ranged field has the advantage of improving resolution beyond the diffraction limit. In addition, the near-field enhancement, which is a consequence of self-consistent light-matter interaction, enables to trap objects with weaker intensity of an incident laser beam. Novotny and coworkers proposed a theoretical scheme for using optical forces by the near-field close to a laser-illuminated metal tip [71]. They demonstrated that strong mechanical force and torque were exerted on dielectric particles in aqueous environments at the nanometer scale.

In recent years, laser-based optical phenomena in nanostructures including optical traps mentioned above have been intensively studied in a rapidly growing research area, referred to as “nano-optics” or “nanophotonics”. The fundamental features of those optical phenomena are understood in the more general context of light-matter interaction in optical response theory. A semiclassical approach has so far been employed to understand these phenomena because a fully quantum mechanical treatment, i.e., quantum electrodynamics theory, is almost impossible in

practice to perform for real nanostructure systems. In the semiclassical approach, an optical field is determined by the Maxwell equation and a material is described quantum mechanically, and the resulting Maxwell and Schrödinger coupled equation should be solved self-consistently [21–23]. However, it is still computationally highly demanding to carry out the coupled equation in real systems [72, 73]. Instead of treating the coupled equation rigorously, many authors employed numerically feasible approaches in which, particularly, the target objects were phenomenologically approximated by model materials such as dielectrics to avoid fully solving electronic structure calculations [71, 74–78].

Detailed electronic structures of molecules play an essential role in molecular science because they determine all the properties of materials such as geometry, bonding character, stability, functionality, reactivity, and so forth. In general, absorption spectra of molecules become discrete with many sharp peaks as the system decreases in size. Each peak is apparently associated with detailed electronic structures consisting of discrete energy levels of molecules. This is due to the fact that the light-matter interaction in such molecular systems can change drastically depending on the electronic structures. One simple and clear example is resonance effect in absorption spectra. As easily inferred from this characteristic, the optical force also strongly depends on details of the electronic structures of nanometer-sized objects. This means that we can optically trap and manipulate an object more precisely by changing the incident laser frequency or the position of the exerted force on an object. For these reasons, it is very important to analyze the optical force on nanostructures, explicitly taking account of the electronic structures of objects.

As described in the previous section, we recently reported the first-principles electron dynamics simulation approach to solving optical response fully taking account of nonuniform light and matter interaction [79]. This approach has following advantages.

- (i) Electronic structure and electron dynamics calculations are carried out at the level of density functional theory (DFT) and time-dependent (TD) DFT, respectively.
- (ii) Full nonuniform-light and matter interactions (i.e., full-multipole effects) are included.
- (iii) Electron dynamics simulation in real space and real time makes it much easier to analyze and visualize optical response of a target molecule.

We here employ this approach to understand the mechanisms of the optical force exerted on nanostructures interacting with a near-field. Special emphasis is placed on elucidating the effect of the detailed molecular-electronic-structures on the optical force.

1.5.2 Optical Force Exerted on a Particle

Optical response to the near-field has been described in the previous section. Here, we present the method of calculations of optical force exerted on a particle. The

optical force exerted on the center of mass of a nanoparticle in the time-domain can be written in the form of

$$\mathbf{F}(t) = - \int [\rho(\mathbf{r}, t) - \rho(\mathbf{r}, 0)] \mathbf{E}(\mathbf{r}, t) d\mathbf{r}. \quad (1.20)$$

It should be noted that $\rho(\mathbf{r}, t) - \rho(\mathbf{r}, 0)$ is the net or true induced charge distribution and numerically includes the full contributions of the charges screening the external electric field within the molecule, i.e., an internal electric field effect. To obtain the net force, the time-average of this quantity over the pulse duration T is taken,

$$\langle \mathbf{F} \rangle = \frac{1}{T} \int_0^T \mathbf{F}(t) dt. \quad (1.21)$$

If a target material has a complex structure unlike a sphere used in this paper, it might be useful to define local optical forces acting on each local structure of a material.

We do not consider the damping effect due to an electron-nuclear coupling or thermal relaxation on the electron dynamics. Thus, the response of the molecule could be artificially strong in the present model. Ideally, it is necessary to treat the electron dynamics in the presence of such relaxation, although it is practically almost impossible in real nanostructure systems. In an effort to accurately describe optical force exerted on molecules at the level of molecular theory, we here carry out the first-principles calculations of electron dynamics as a first step and leave the relaxation effect for future investigation.

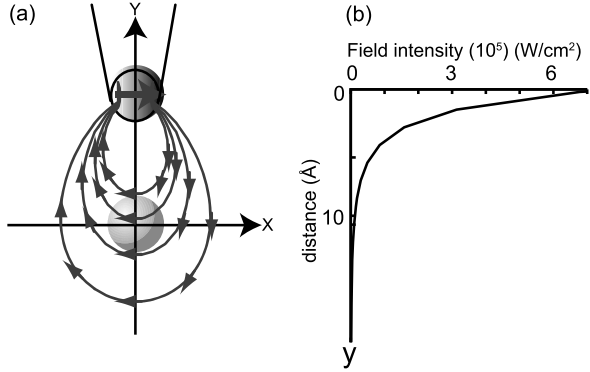
1.5.3 Model System and Computations

We consider that a nanoparticle interacts with the near-field radiated from an x -polarized oscillating dipole at 10 \AA above the molecule center, $(x, y, z) = (0, 0, 0)$, as shown in Fig. 1.11(a). The spatial distribution of the near-field is given by [36]

$$\mathbf{E}(\mathbf{r} - \mathbf{R}_{\text{dip}}) = \frac{[3\mathbf{n}(\mathbf{n} \cdot \boldsymbol{\mu}) - \boldsymbol{\mu}]}{(4\pi\epsilon_0|\mathbf{r} - \mathbf{R}_{\text{dip}}|)^3} e^{ik \cdot (\mathbf{r} - \mathbf{R}_{\text{dip}})}, \quad (1.22)$$

where \mathbf{R}_{dip} is the coordinate of the oscillating dipole, k is the wavenumber, ϵ_0 is the vacuum permittivity, \mathbf{n} is the unit vector of $(\mathbf{r} - \mathbf{R}_{\text{dip}})/|\mathbf{r} - \mathbf{R}_{\text{dip}}|$ and $\boldsymbol{\mu}$ is the dipole moment of the radiation source. We set $\mathbf{R}_{\text{dip}} = (0.0, 10.0, 0.0) \text{ \AA}$ and $\boldsymbol{\mu} = (0.01, 0.0, 0.0) \text{ Debye}$. As shown in Fig. 1.11(b), the intensities of the near-field are 7.4×10^5 , 1.2×10^4 , and $1.0 \times 10^3 \text{ W/cm}^2$ at $(x, y) = (0.0, 5.0)$, $(0.0, 0.0)$, and $(0.0, -5.0) \text{ \AA}$, respectively. The external potential V_{eff} is calculated by Eq. (1.13c) with the effective electric field Eq. (1.13b) where the electric field \mathbf{E} is given by the dipole radiation, Eq. (1.22). We set the center of mass of the molecule to be the

Fig. 1.11 (a) Schematic of a near-field fiber tip (*upper ball*) and a target particle (*lower ball*). The near-field is approximated by the radiation from an x -polarized oscillating dipole (*solid arrow*). The *thin curves with arrows* denote the electric field lines. (b) Electric field intensity as a function of distance between the tip and the particle



origin. The temporal shape of the near-field is taken as a pulse. Finally, the effective potential Eq. (1.13c) is rewritten by

$$V_{\text{eff}}(\mathbf{r}, t) = -\mathbf{r} \cdot \mathbf{E}_{\text{eff}}(\mathbf{r}) \sin(\omega t) \sin^2\left(\frac{\pi t}{T}\right) \quad (0 < t < T), \quad (1.23)$$

where ω is the frequency of the oscillating dipole, and T determines the pulse duration.

We demonstrate the TDDFT simulation of the optical force in different two systems: a metal nanoparticle and C_{60} . The metal nanoparticle is simplified by a jellium model, in which the ionic background is given by

$$V_{\text{ion}}(\mathbf{r}) = \frac{3}{4\pi r_s^3} \left[1 + \exp\left(\frac{|\mathbf{r}| - a}{w}\right) \right]^{-1}, \quad (1.24)$$

where r_s is the density parameter [80], a is the radius of the sphere and w is the smoothed out factor for the jellium surface. The jellium parameters for the metal nanoparticle are set to $r_s = 1.60$, which corresponds to a silver atom (34 electrons), $a = 0.5$ nm, and $w = 0.538$. For C_{60} , on the other hand, the ionic background $V_{\text{ion}}(\mathbf{r})$ of an atomic component C is constructed from a norm-conserving pseudopotential generated numerically following the Troullier and Martins procedure [40]. In this article, we use the Kleinman-Bylander separable form to represent the nonlocal (i.e., angular momentum depending) potential terms [41]. The C–C distances are set to be 1.457 Å for the single bond and 1.384 Å for the double bond. The inner shell structure of the carbon atom is approximated by an effective core pseudopotential, and then the remaining four electrons ($2s^2 2p^2$) are explicitly treated, i.e., 240-electron dynamics simulation in total for C_{60} . To represent the exchange-correlation potential $V_{\text{xc}}(\mathbf{r}, t)$, we use the local density approximation given by Perdew and Zunger [42] as in the previous study.

The computational approach is based on TDKS. The approach was described in the previous section. The TDKS equation (1.14) for these particles is solved numerically by a grid-based method [25, 32, 33, 35, 38, 39, 51, 52] in a three-dimensional Cartesian-coordinate cubic box. For the metal particle, the length of the cubic box is

26 Å and the uniform grids with a mesh spacing of 0.5 Å are used, while the length and the mesh spacing are 16 Å and 0.3 Å, respectively, for C₆₀. The Laplacian operator is evaluated by a nine-point difference formula [52]. The time-propagation of the KS orbitals is carried out with a fourth-order Taylor expansion by using a constant time step of 0.005 fs for the metal particle and 0.002 fs for C₆₀.

The effective potential for the dipole radiation on each grid is computed combining Eqs. (1.13b), (1.13c), and (1.22). The integral of Eq. (1.13b) is calculated numerically with a constant spacing of $\Delta\lambda = 0.0423$ Å. In the integration, \mathbf{E} is evaluated as $4\pi\boldsymbol{\mu}/3$ if $|\mathbf{E}|$ is larger than $|4\pi\boldsymbol{\mu}/3|$, including the position of the dipole [31]. This is done for a few points very close to the dipole, i.e., $|\mathbf{r} - \mathbf{R}_{\text{dip}}| \sim 0.2$ Å. The pulse duration ($T = 20$ fs) is short enough to avoid considering the nuclear dynamics and thus the ion position is fixed during the time evolution.

Before ending this section, we make comments on the validity of the theoretical model. We do not consider the self-consistent light matter interaction between the target molecule and radiation source. More specifically, we employ a theoretical model as in the case of the previous study in which the near-field is considered to be a radiation field from an oscillating dipole source and the back reaction of the electric field due to the target molecule on the source field is negligible. However, in the present theoretical model the size of the target molecule is relatively small and its induced dipole is not so strong. Thus, it can be reasonably assumed that the back reaction does not primarily affect the external source field. We need to explicitly take account of the back reaction when the target molecule becomes larger and its induced dipole is comparable with the oscillating dipole of the radiation source. The effect of the back reaction might be noticeable especially under the resonant condition and then should be treated by solving the Maxwell-Schrodinger coupled equation in a self-consistent manner. As mentioned in the beginning of this article, it is still computationally highly demanding to solve such a coupled equation in real nanostructure systems. In a model two-particle system, for instance, Govorov et al. discussed the effect of the back reaction [27].

1.5.4 Optical Force on a Silver Nanoparticle

Figure 1.12 shows the time-dependent optical force exerted on the silver nanoparticle in the y direction calculated by Eq. (1.20) at (a) $\omega = 1.0$ eV (off-resonance) and (b) $\omega = 2.7$ eV (resonance) in the unit of aN. Figure 1.12(a) clearly shows that the optical force is biased so that F_y takes the positive value during the excitation. This means that the near-field induces an attractive force on the nanoparticle. On the other hand, under the resonance condition in Fig. 1.12(b) F_y takes both positive and negative values even though the force is also biased to the positive value. Focusing on the maximum values of F_y in these excitations, the resonantly induced optical force is slightly larger than the off-resonantly induced one. The time-averaged forces calculated by using Eq. (1.21) for each excitation are (a) 16.8 aN and (b) 16.9 aN. (As a reference, the gravitation acted on the nanoparticle is of the order of 10^{-15} aN.)

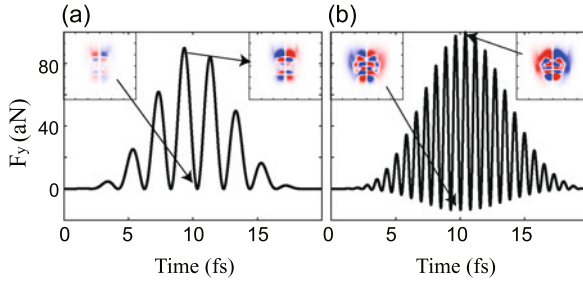


Fig. 1.12 Time dependence of optical force on a silver particle exerted by the near-field at (a) $\omega = 1.0$ eV (off-resonance) and (b) 2.7 eV (resonance). Insets are the snapshots of the induced electron densities where the red and the blue show increase and decrease in the electron density, respectively, compared to those of the ground state

This implies that the resonant condition does not necessarily significantly enhance the optical force.

The underlying mechanism of the near-field induced optical force on the nanoparticle can be schematically explained. As shown in Fig. 1.11, in the near-field region the electric field lines curve across the nanoparticle and the field intensity decreases with distance from the radiation source. When such a near-field is applied to the nanoparticle, polarization charges ($\pm Q$) are induced in accordance with the curved electric-field-lines and the electron density distribution is biased, see the schematic of the induced charges in Fig. 1.13. In addition, the screening charges ($\mp q$) are generated as counterparts of the polarization charges ($\pm Q$). The terms of the polarization and screening charges were introduced to qualitatively explain the generation mechanism of the optical force. The computed results numerically take account of full contributions of these charges by solving the TDDFT calculations. Thus, the polarization and screening charges are not calculated separately and we cannot clearly distinguish one from the other. Then, the local effective force is exerted on the polarization and screening charges, depending on both their distributions and their signs of the charge. Similar optical response is commonly found in conventional photoinduced phenomena, irrespective of whether a uniform or nonuniform electric field is applied to a nanoparticle. However, oscillating uniform electric fields, which have frequently been used in the studies of optical response under the dipole approximation, exert no net force on a time average because the uniform (or symmetric) polarization and screening charges are induced. On the other hand, since the near-field is highly localized around a radiation source and the intensity of the field decreases rapidly with distance from the radiation source, net force is induced depending on intensity gradient of the near-field and on a balance between the amounts of the polarization and screening charges. In the present system, the force acting on the polarization charges (bold arrows in Fig. 1.13) is generally larger than on the screening charges (thin arrows). As a result, the near-field induced optical force is biased so that the attractive force ($F_y > 0$) is exerted between the near-field fiber tip and the nanoparticle as shown in Fig. 1.12.

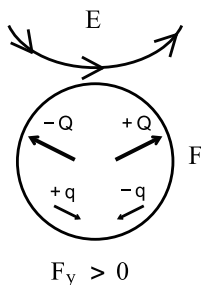


Fig. 1.13 Scheme for the optical force due to the interaction between inhomogeneously induced charges and a near-field. The *top curve with arrows* shows the electric field, the *sphere* shows a nanoparticle, and Q and q are the polarization and screening charges, respectively. The *black arrows* indicate locally induced optical forces. The net optical force in the y direction is positive

The actual electron dynamics is more complicated. The four insets in Fig. 1.12 illustrate the snapshots of time evolution of the polarization and screening charges on the xy plane, where the red and the blue indicate increase and decrease in the electron density, respectively, compared to those of the initial ground state. The charge distributions are rather complex but appear to be somewhat regular in the sense that those nodal patterns are antisymmetric to the y -axis. Although it is difficult to clearly distinguish between the polarization and screening charges in the charge distribution, the snapshots of these charges are reminiscent of the schematic in Fig. 1.13. We computationally confirmed that in the resonance excitation (Fig. 1.12(b)) the polarization charges are induced in an inner region and the corresponding screening charges are localized around the nanoparticle surface. This is mainly because in the off-resonance excitation the electrons are forced to oscillate near the radiation source, whereas in the resonance excitation the specific electrons which are strongly associated with the details of the electronic structures primarily oscillate resonantly. Thus, in the resonance excitation the optical force partly becomes negative because the net force is determined by a balance between the amounts of the polarization and screening charges.

We next discuss the energy dependence of the optical force. Figure 1.14 shows the time-averaged force (red solid curve) and the absorption spectrum (black broken curve). The force spectrum was obtained by plotting the averaged optical force, varying the frequency by 0.1 eV from 0.8 to 3.6 eV. The absorption spectrum was obtained under a dipole approximation as in a similar way of previous methods. [32, 51]. The averaged force spectrum has peaks at 1.3 eV and 2.2 eV, which are different from the resonance frequency. Although the polarization charges are significantly induced when the laser frequency is in tune with the resonance frequency, this figure proves that the resonance excitation does not necessarily maximally induce the net force. This is because the screening charges partly (and sometimes largely) cancel the polarization charges. As a result of the sensible balance between the polarization and the screening charges, several maxima and minima appear in the force spectrum. Conversely, this result indicates that we can manipulate atoms and molecules in nanostructures by controlling the strength of attractive force (and

Fig. 1.14 Absorption spectrum (*dashed curve*) of the silver nanoparticle and the time-averaged force on the particle as a function of energy

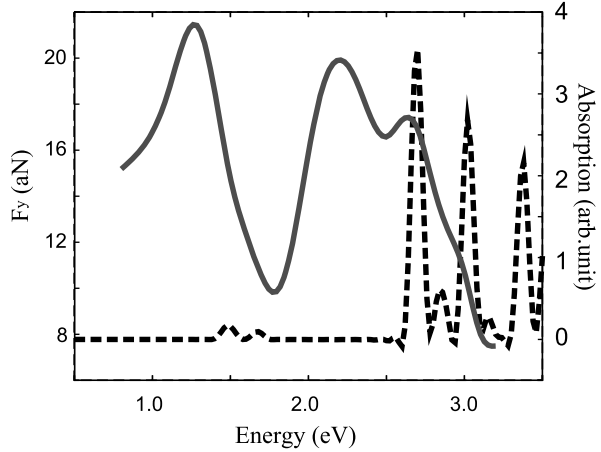
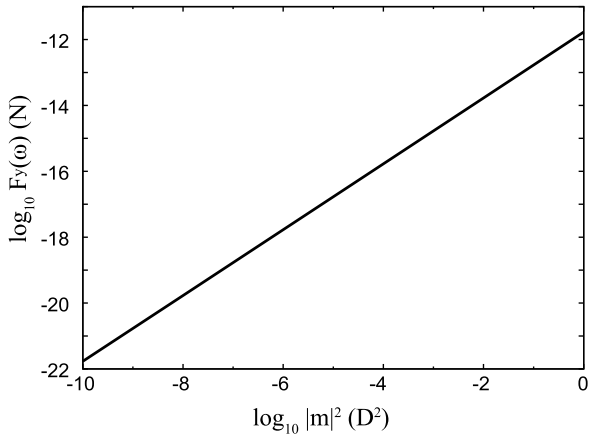


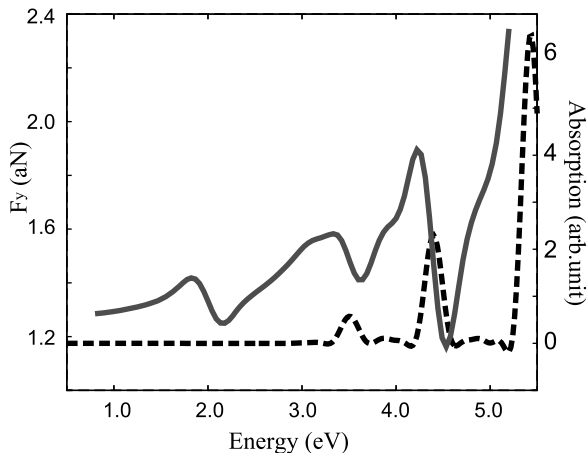
Fig. 1.15 Time-averaged force on the silver particle under the off-resonant condition (1.0 eV) as a function of the square of the dipole moment of the radiation source



possibly repulsive force), changing the laser frequency. To do that, electronic structure calculations of target nanostructures must be carried out. Our electron dynamics approach combined with nonuniform light-matter interaction theory fulfills such a requirement.

Before discussing the results of C_{60} , we show the field-intensity dependence of the optical force. Since the present near-field is approximated by the oscillating dipole in the form of Eq. (1.22), we calculated the intensity dependence by varying the dipole moment of the radiating source, which is associated with the field intensity. The laser frequency ω is set to 1.0 eV (off-resonance). Figure 1.15 shows the time-averaged optical force as a function of the square of the dipole moment of the radiation source. The x and y axes are shown in a logarithm scale with base 10. We found that the optical force is linearly proportional to the near-field intensity. The optical force amounts to 10^{-12} N when the radiation source has the moment of 1D.

Fig. 1.16 Same as Fig. 1.14 but for C_{60}



1.5.5 Optical Force on C_{60}

We have also calculated the optical force for C_{60} interacting with the near-field. Contrary to the case of the metal particle, the force on C_{60} does not become negative both for off-resonant (1 eV) and resonant (3.6 eV) conditions. This can be attributed to the hollow structure of C_{60} because there are no effective screening charges. The time-averaged forces are 1.29 aN (off-resonance condition) and 1.41 aN (resonance condition). In this case, stronger force is induced under the resonant condition than the off-resonant condition. The force on C_{60} is an order of magnitude smaller than that on the silver particle because of less mobility of the charges and of the absence of charges inside the sphere. We plot the time-averaged force (red solid curve) as a function of energy in Fig. 1.16. The absorption spectrum (black broken curve) is also drawn as a reference. The optical force has several peaks as similar to the force spectrum of the metal particle and generally increases as a function of the energy. The figure clearly demonstrates that the optical force is largely determined by the detailed electronic structures of the molecule.

1.5.6 Concluding Remarks

We have calculated the near-field induced optical forces acted on a silver particle mimicked by a jellium model and on C_{60} . The grid-based real-time and real-space time-dependent density functional theory approach combined with the nonuniform light-matter interaction formalism, recently developed by the authors, was employed to accurately calculate the inhomogeneous charge polarization induced by the full multipole interaction with the near-field. The induced force is rationally explained in terms of the polarization and screening charges. The local optical force on the silver particle in the y direction takes both positive and negative values depending

on the spatial distribution of these charges, and the net force becomes attractive as a result of a balance between the polarization and screening charges. The optical force on C_{60} is an order of magnitude smaller than that on the silver particle because of the less mobility of the electrons. The energy dependence of the optical force of these particles showed several maxima and minima, indicating that the resonance excitation does not necessarily induce the optical force most efficiently. Such a non-monotonic energy dependence of the optical force will be utilized when manipulating nanoparticles at the nanometer scale by controlling the near-field frequency. To calculate the optical forces induced by a highly nonuniform electric field in real molecules, a sensible balance of the polarization and screening charges must be determined. The present first-principles TDDFT approach taking account of full light-matter interactions can be a powerful tool for optical manipulation in nanostructures at the level of single atoms and molecules.

1.6 Summary

We have presented a generalized theoretical description of optical response in an effort to understand a nonuniform light-matter interaction between a near-field and a molecule. The present optical response theory fully taking account of the nonuniform light-matter interaction allows us to elucidate inhomogeneous electron dynamics associated with local electronic structures of a molecule at the 1 nm scale, even though the wavelength of an incident laser pulse is much longer than the size of the molecule. The near-field electron dynamics was computationally demonstrated for high-harmonic-generation and optical force. In contrast to a conventional electronic excitation process due to uniform light-matter interaction, the computed results illustrated unusual electron dynamics caused by the nonuniform light-matter interaction. We expect that the nonuniform light-matter interaction/TD-KS approach incorporated with the Maxwell equations will enable us to elucidate electron and electromagnetic field dynamics in nanostructures.

Acknowledgements This research was supported by a Grant-in-Aid (No. 21350018) and by the Next-Generation Supercomputer Project from the Ministry of Education, Culture, Sports, Science and Technology of Japan. The computation was partly performed at the Research Center for Computational Science, Okazaki, Japan.

References

1. T.W. Ebbesen, H.J. Lezec, H.F. Ghaemi, T. Thio, P.A. Wolff, *Nature* **391**, 667 (1998)
2. K. Kobayashi, S. Sangu, H. Ito, M. Ohtsu, *Phys. Rev. A* **63**, 013806 (2001)
3. S.A. Maier, P.G. Kik, H.A. Atwater, S. Meltzer, E. Harel, B.E. Koel, A.A.G. Requicha, *Nat. Mater.* **2**, 229 (2003)
4. P.N. Prasad, *Nanophotonics* (Wiley-Interscience, New York, 2004)
5. C. Girard, *Rep. Prog. Phys.* **68**, 1883 (2005)

6. L. Novotny, B. Hecht, *Principles of Nano-Optics* (Cambridge University Press, Cambridge, 2006)
7. S.A. Maier, *Plasmonics: Fundamentals and Applications* (Springer, Berlin, 2007)
8. M. Fleischmann, P.J. Hendra, A.J. McQuillan, *Chem. Phys. Lett.* **26**, 163 (1974)
9. D.L. Jeanmaire, R.P. Van Duyne, *J. Electroanal. Chem.* **84**, 1 (1977)
10. M.G. Albrecht, J.A. Creighton, *J. Am. Chem. Soc.* **99**, 5215 (1977)
11. K. Imura, H. Okamoto, M.K. Hossain, M. Kitajima, *Nano Lett.* **6**, 2173 (2006)
12. D.W. Brandl, N.A. Mirin, P. Nordlander, *J. Phys. Chem. B* **110**, 12302 (2006)
13. J. Zhao, A.O. Pinchuk, J.M. McMahon, S. Li, L.K. Ausman, A.L. Atkinson, G.C. Schatz, *Acc. Chem. Res.* **41**, 1710 (2008). And references therein
14. M. Moskovits, *Rev. Mod. Phys.* **57**, 783 (1985)
15. K. Kneipp, M. Moskovits, H. Kneipp (eds.), *Surface-Enhanced Raman Scattering* (Springer, Heidelberg, 2006)
16. R. Aroca, *Surface-Enhanced Vibrational Spectroscopy* (Wiley, New York, 2006)
17. S. Nie, S.R. Emory, *Science* **275**, 1102 (1997)
18. K. Kneipp, Y. Wang, H. Kneipp, L.T. Perelman, I. Itzkan, R.R. Dasari, M.S. Feld, *Phys. Rev. Lett.* **78**, 1667 (1997)
19. T. Vo-Dinh, K. Houck, D.L. Stokes, *Anal. Chem.* **66**, 3379 (1994)
20. Y.C. Cao, R. Jin, C.A. Mirkin, *Science* **297**, 1536 (2002)
21. K. Cho, *Prog. Theor. Phys. Suppl.* 225–233 (1991)
22. J.K. Jenkins, S. Mukamel, *J. Chem. Phys.* **98**, 7046 (1993)
23. O. Keller, *Phys. Rep.* **268**, 85 (1996)
24. D. Abramavicius, S. Mukamel, *J. Chem. Phys.* **124**, 034113 (2006)
25. K. Lopata, D. Neuhauser, R. Baer, *J. Chem. Phys.* **127**, 154714 (2007)
26. E. Lorin, S. Chelkowski, A. Bandrauk, *Comput. Phys. Commun.* **177**, 908 (2007)
27. J.Y. Yan, W. Zhang, S.Q. Duan, X.G. Zhao, A.O. Govorov, *Phys. Rev. B* **77**, 165301 (2008)
28. K. Lopata, D. Neuhauser, *J. Chem. Phys.* **130**, 104707 (2009)
29. C. Cohen-Tannoudji, J. Dupont-Roc and, G. Grynberg, *Photons and Atoms—Introduction to Quantum Electrodynamics* (Wiley-Interscience, New York, 1989)
30. D.P. Craig, T. Thirunamachandran, *Molecular Quantum Electrodynamics* (Dover, New York, 1998)
31. S. Mukamel, *Principles of Nonlinear Optical Spectroscopy*. Oxford Series on Optical and Imaging Sciences (Oxford University Press, London, 1999)
32. K. Yabana, G.F. Bertsch, *Phys. Rev. B* **54**, 4484 (1996)
33. K. Nobusada, K. Yabana, *Phys. Rev. A* **70**, 043411 (2004)
34. K. Shiratori, K. Nobusada, K. Yabana, *Chem. Phys. Lett.* **404**, 365 (2005)
35. K. Nobusada, K. Yabana, *Phys. Rev. A* **75**, 032518 (2007)
36. J.D. Jackson, *Classical Electrodynamics*, 3rd edn. (Wiley, New York, 1998)
37. E. Runge, E.K.U. Gross, *Phys. Rev. Lett.* **52**, 997 (1984)
38. F. Calvayrac, P.G. Reinhard, E. Suraud, C.A. Ullrich, *Phys. Rep.* **337**, 493 (2000)
39. M.A.L. Marques, A. Castro, G.F. Bertsch, A. Rubio, *Comput. Phys. Commun.* **151**, 60 (2003)
40. N. Troullier, J.L. Martins, *Phys. Rev. B* **43**, 1993 (1991)
41. L. Kleinman, D.M. Bylander, *Phys. Rev. Lett.* **48**, 1425 (1982)
42. J.P. Perdew, A. Zunger, *Phys. Rev. B* **23**, 5048 (1981)
43. I. Vasiliev, S. Ogut, J.R. Chelikowsky, *Phys. Rev. B* **65**, 115416 (2002)
44. A. Wasserman, N.T. Maitra and, K. Burke, *Phys. Rev. Lett.* **91**, 263001 (2003)
45. G.F. Gabriele, G. Vignale, *Quantum Theory of the Electron Liquid* (Cambridge University Press, Cambridge, 2005)
46. F. Cataldo, *Polyhedron* **23**, 1889 (2004)
47. TURBOMOLE Version 5.10, Quantum Chemistry Group, University of Karlsruhe, Karlsruhe, Germany (2008)
48. R. Ahlrichs, M. Bär, M. Häser, H. Horn, C. Kölmel, *Chem. Phys. Lett.* **162**, 165 (1989)
49. J.P. Perdew, Y. Wang, *Phys. Rev. B* **45**, 13244 (1992)
50. A. Schäfer, H. Horn, R. Ahlrichs, *J. Chem. Phys.* **97**, 2571 (1992)

51. K. Yabana, G.F. Bertsch, *Int. J. Quant. Chem.* **75**, 55 (1999)
52. J.R. Chelikowsky, N. Troullier, K. Wu, Y. Saad, *Phys. Rev. B* **50**, 11355 (1994)
53. K. Burnett, V.C. Reed, J. Cooper, P.L. Knight, *Phys. Rev. A* **45**, 3347 (1992)
54. T. Brabec, F. Krausz, *Rev. Mod. Phys.* **72**, 545 (2000)
55. S. Tojo, M. Hasuo, *Phys. Rev. A* **71**, 012508 (2005)
56. J.J. Sakurai, *Modern Quantum Mechanics* (Addison-Wesley, Reading, 1993) (revised edition)
57. R.W. Boyd, *Nonlinear Optics*, 3rd edn. (Academic Press, San Diego, 2008)
58. C.T. Lee, W.T. Yang, R.G. Parr, *Phys. Rev. B* **37**, 785 (1988)
59. A.D. Becke, *J. Chem. Phys.* **98**, 5648 (1993)
60. A. Ashkin, *Phys. Rev. Lett.* **24**, 156 (1970)
61. A. Ashkin, J.M. Dziedzic, J.E. Bjorkholm, S. Chu, *Opt. Lett.* **11**, 288 (1986)
62. A. Ashkin, *IEEE J. Sel. Top. Quantum Electron.* **6**, 841 (2000)
63. D.G. Grier, *Nature* **424**, 810 (2003)
64. K.C. Neuman, S.M. Block, *Rev. Sci. Instrum.* **75**, 2787 (2004)
65. J.C. Crocker, D.G. Grier, *Phys. Rev. Lett.* **77**, 1897 (1996)
66. B. Lin, J. Yu, S.A. Rice, *Colloids Surf. A* **174**, 121 (2000)
67. K. Svoboda, S.M. Block, *Annu. Rev. Biophys. Biomol. Struct.* **23**, 247 (1994)
68. U. Seifert, *Adv. Phys.* **46**, 13 (1997)
69. A.D. Mehta, M. Rief, J.A. Spudich, D.A. Smith, R.M. Simmons, *Science* **283**, 1689 (1999)
70. M.J. Lang, S.M. Block, *Am. J. Phys.* **71**, 201 (2003)
71. L. Novotny, R.X. Bian, X.S. Xie, *Phys. Rev. Lett.* **79**, 645 (1997)
72. E. Lorin, S. Chelkowski, A. Bandrauk, *Comput. Phys. Commun.* **177**, 908 (2007)
73. K. Lopata, D. Neuhauser, *J. Chem. Phys.* **130**, 104707 (2009)
74. K. Okamoto, S. Kawata, *Phys. Rev. Lett.* **83**, 4534 (1999)
75. P.C. Chaumet, M. Nieto-Vesperinas, *Phys. Rev. B* **61**, 14119 (2000)
76. A.I. Bishop, T.A. Nieminen, N.R. Heckenberg, H. Rubinsztein-Dunlop, *Phys. Rev. A* **68**, 033802 (2003)
77. T. Iida, H. Ishihara, *Phys. Rev. Lett.* **90**, 057403 (2003)
78. V. Wong, M.A. Ratner, *Phys. Rev. B* **73**, 075416 (2006)
79. T. Iwasa, K. Nobusada, *Phys. Rev. A* **80**, 043409 (2009)
80. N.W. Ashcroft, N.D. Mermin, *Solid State Physics* (Brooks/Cole Thomson Learning, Pacific Grove, 1976)

Chapter 2

Novel Excitonic Properties of Carbon Nanotube Studied by Advanced Optical Spectroscopy

Kazunari Matsuda

Abstract Novel excitonic properties of single-walled carbon nanotubes are studied by single-nanotube spectroscopy and time-resolved spectroscopy. Due to the enhanced Coulomb interaction, the optically generated electron-hole pair forms a strongly “bound exciton” state, analogous to the hydrogen-like state in the carbon nanotubes. The exciton properties and dynamics dominate their optical properties. The striking features of excitons in the carbon nanotube, multiple-exciton states, charged exciton (trion) formation, and exciton-multiplication are described in this chapter.

2.1 Basic Optical Properties of Carbon Nanotube

2.1.1 Structure of Carbon Nanotube

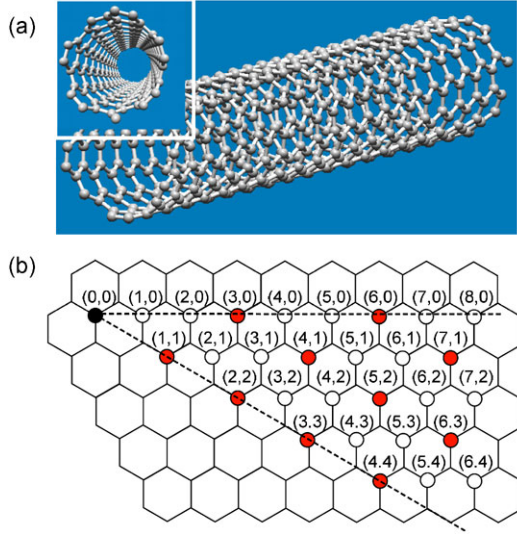
The nano-carbon materials consisting from carbon honeycomb lattice have been attracted great deal of interests from viewpoints of basic science and applications. The nano-carbon materials include varieties of materials such as fullerene (C_{60}), carbon nanotube, and graphene. In this chapter, we mainly focus on a single-walled carbon nanotube (SWNT), about 1 nm in diameter and greater than several hundred nanometers in length, is a prototypical system of one-dimensional (1D) structures [1]. SWNTs consist of a two-dimensional (2D), single-layer carbon honeycomb lattice (or graphene sheet) that has been rolled into a cylindrical structure, as shown in Fig. 2.1(a). The SWNT is characterized by the (n, m) index or chiral index (chirality), where n and m are integers [2–5]. The chiral index makes a regulation of the angle and radius, which describe the way in which the graphene sheet is rolled. Figure 2.1(b) shows the schematic of a graphene sheet. The chiral vector C in the graphene sheet can be described as

$$C = na_1 + ma_2, \quad (2.1)$$

K. Matsuda (✉)

Institute of Advanced Energy, Kyoto University, Gokasho, Uji, Kyoto 611-0011, Japan
e-mail: matsuda@iae.kyoto-u.ac.jp

Fig. 2.1 (a) Schematic of a single-walled carbon nanotube (SWNT). (b) Schematic of the chiral vector (n, m) of a carbon nanotube



where \mathbf{a}_1 and \mathbf{a}_2 are fundamental lattice vectors. The structure of SWNTs with chiral index (n, m) can be formed by connecting the origin to point (n, m) . The diameter d of SWNTs with chiral index (n, m) can be expressed as

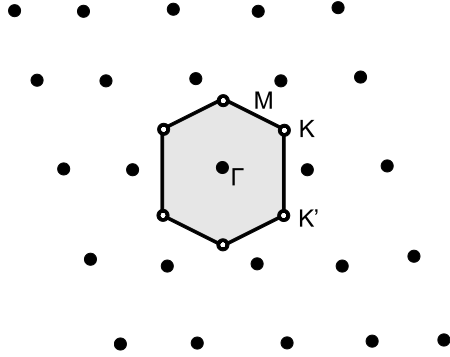
$$d = a \frac{\sqrt{n^2 + m^2 + mn}}{\pi}, \quad (2.2)$$

where $a (= |\mathbf{a}_1| = |\mathbf{a}_2|)$ is 2.46 \AA . The most striking feature of SWNTs is that the electronic properties are determined only by the structure of the carbon nanotube itself, i.e., the chiral index (n, m) , as described in the next section.

2.1.2 Electronic Structure of Graphene

At first, the electronic structure of graphene should be explained, since the electronic structure of SWNTs can be obtained by zone-folding of that of a graphene. Figure 2.2 shows the reciprocal lattice of graphene in the momentum space and its 1st Brillouin zone. The shape of 1st Brillouin zone at reciprocal space shows the hexagonal shape reflecting the hexagonal periodical lattice of graphene in the real space. The simple tight-binding approximation is useful to understand the electronic structure of the graphene as a first step, where the Coulomb interactions between the electron-electron do not be considered. The unit cell of graphene is defined by the fundamental lattice vectors of \mathbf{a}_1 and \mathbf{a}_2 . The unit cell contains two carbon atoms, and each carbon atom has four electrons in the valence band. The three of these electrons will hybridize forming σ -bonds in the hexagonal plane and one forms a π bond. The π electrons which are delocalized in the crystal, mainly dominate the

Fig. 2.2 Schematic of reciprocal lattice of graphene and 1st Brillouin zone



electronic properties. Moreover, taking account only the nearest-neighbor interaction, the energy dispersion relation of the graphene is given by

$$E_g^\pm = \pm \gamma_0 \sqrt{1 + 4 \cos \frac{\sqrt{3}k_x a_0}{2} \cos \frac{k_y a_0}{2} + 4 \cos^2 \frac{k_y a_0}{2}}, \quad (2.3)$$

where γ_0 is the nearest-neighbor transfer integral and \pm sign corresponds to the bonding (valence) and anti-bonding (conduction) bands in the k space. The energy dispersion of the bonding (valence) and anti-bonding (conduction) bands are symmetric with respect to the Fermi level. Moreover, the energy bands at the K points are degenerated at the Fermi level ($E_g = 0$), which indicates that the graphene is a zero-gap material.

2.1.3 Electronic Structure of Carbon Nanotube

Based on the electronic structure of graphene described in previous section, the zone-folding or confinement approximation of the electronic structure of graphene provides the information on the electronic band structure of SWNTs. The allowed wavevector component around the circumference of SWNTs is quantized, while the component along the nanotube axis is continuous. The zone-folding approximation consists in sectioning the graphene electronic structure as a “cutting line”, as shown in Figs. 2.3(a) and (b). Thus, the energy bands for the SWNT will be a series of 1D dispersion relations. The zone-folding approximation provides a simple scheme of the electronic properties, however it still is needed to understand that the some SWNTs have metallic electronic states and the others have semiconducting ones. This characteristic property comes from the energy band dispersion of graphene, with zero-gap at K point. If the K point is an allowed wavevector of SWNTs, i.e. the cutting line is crossed at K point as shown in Fig. 2.3(a), then the SWNTs will be metallic, as shown in the band structure of the lower panel of Fig. 2.3(a). In this case, the structure of SWNTs has a chiral index relationship of $n - m = 3m$ (m : integer). On the other hand, if the K point is not an allowed wavevector of

Fig. 2.3 Schematic of 1st Brillouin zone with the cutting lines and energy band structure in (a) metallic and (b) semiconducting carbon nanotube

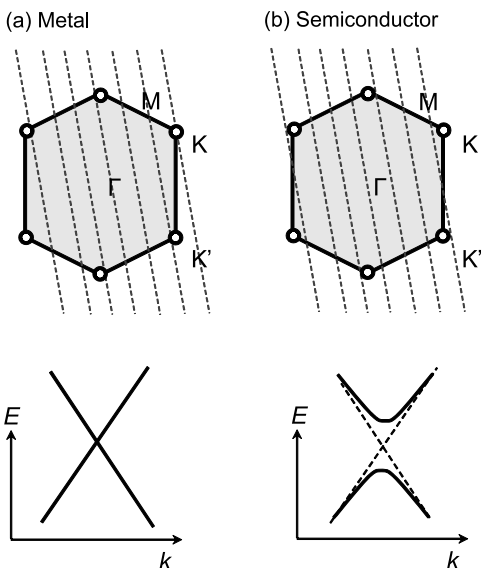
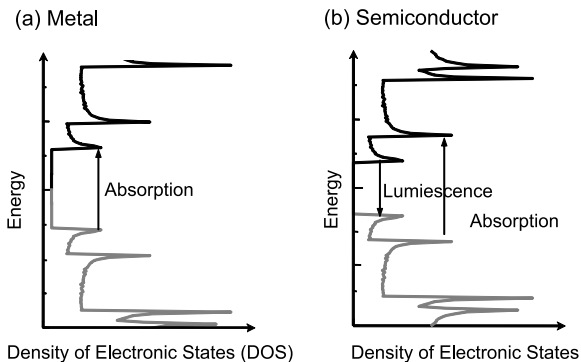


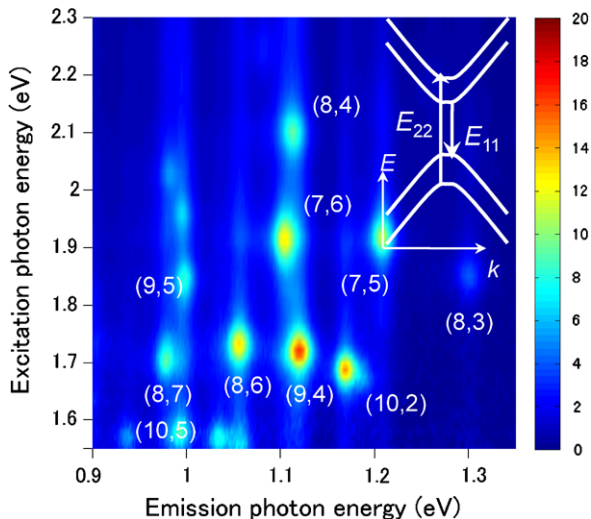
Fig. 2.4 Density of states of (a) metallic and (b) semiconducting carbon nanotube. Optical transitions of absorption and luminescence are indicated in the figure



SWNTs, i.e. the cutting line is not crossed at K point, then the SWNTs with a chiral index relationship of $n - m \neq 3m$ will be semiconducting. The chiral indices of semiconducting and metallic SWNTs are shown in Fig. 2.1(b). From this simple relationship, the 1/3 of SWNTs have metallic electronic states, while the rest have semiconducting ones.

The density of states is an useful quantity to understand the electronic structures of SWNTs. Figure 2.4 shows the schematic of the density of states (DOS) of metallic ($n - m = 3m$) and semiconducting ($n - m \neq 3m$) SWNTs. The sharp von-Hove singularity peak in the density of states arises from the 1D quantum confined electronic state in the SWNTs. The band-gap energy E_g of semiconducting SWNTs is inversely proportional to the diameter; this is predicted by the simple tight-binding calculation [6].

Fig. 2.5 Two-dimensional photoluminescence (PL) excitation map of SWNTs

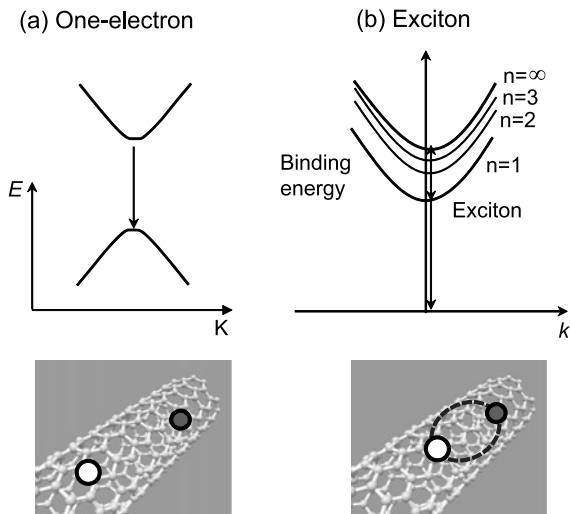


2.1.4 Optical Spectroscopy of Carbon Nanotubes

The optical properties of semiconducting SWNTs have been extensively studied since 2002 when O'Connell reported that micelle-encapsulated semiconducting SWNTs showed very clear photoluminescence (PL) [7, 8]. The observation of PL is due to the isolation of individual SWNTs that are prevented from bundling with semiconducting and metallic carbon nanotubes [7, 9]. This is because that the energy transfer between the semiconducting and metallic carbon nanotubes is occurred and optically excited carriers are non-radiatively quenched at the metallic carbon nanotubes in the bundled samples [7, 9]. Indeed, it has been reported that the isolated air-suspended carbon nanotubes fabricated between the Si pillars also showed clear PL signals [9].

Figure 2.5 shows the typical 2D PL excitation (PLE) map corresponding to the contour plot between the excitation energy (wavelength) and PL spectra of micelle-encapsulated SWNTs [8]. Several PL signals, shown as spots, are observed in the 2D PL map, which indicates the sharp resonance features of the SWNT electronic states. The photon energy of the PLE signals on the vertical axis corresponds to the optical absorption peak between the second sub-band of the conduction to valence state, as indicated by E_{22} in the inset of Fig. 2.5. In contrast, the energy of the peak on the horizontal axis corresponds to E_{11} , the PL energy corresponding to the band gap of semiconducting SWNTs. The energies E_{11} and E_{22} in (n, m) SWNTs can be calculated using the tight-binding method. From the predicted E_{11} and E_{22} energies, one can assign each peak in the 2D PLE map to (n, m) of the SWNTs, as indicated in Fig. 2.5 [10]. Most researchers in this field have believed that the PL signal from semiconducting SWNTs comes from the recombination of the optically-excited free electron in the conduction band and free hole in the valence band. In this one-electron picture, shown in Fig. 2.6(a), without consideration

Fig. 2.6 Schematic of electronic structures of SWNTs in (a) the one-electron picture without Coulomb interactions and (b) the exciton picture with Coulomb interactions



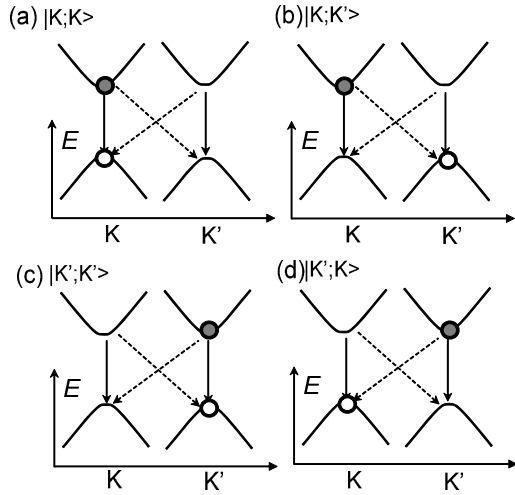
of Coulomb interactions, the resonance features of the optical spectra are attributed to the sharp electronic states corresponding to the 1D von-Hove singularity. In contrast, Ando theoretically pointed out that the Coulomb interaction between the electron and hole pair is greatly enhanced in the 1-nm cylindrical structure and, in fact, that the Coulomb interaction affects the optical spectrum of SWNTs [11], as described in the next section.

2.1.5 Exciton State in Carbon Nanotubes

The attractive Coulomb interaction between the optically excited electron and hole pair plays an important role in understanding the optically excited states in the solid. When the electron and hole are strongly confined in the 1D system such as the SWNTs with only 1 nm diameter, the attractive Coulomb interaction between the electron and hole is much enhanced in comparison with 3D bulk materials. The enhanced Coulomb interactions in 1D SWNTs lead to the formation of tightly bound electron-hole pairs, i.e., “excitons”, analogous to a hydrogen-like state in the solid, as shown in Fig. 2.6(b) [11–17]. The exciton has the series of energy structure, as similar to the hydrogen atom, $n = 1, 2, 3, \dots$, where n is the quantum number. The energy position of $n = \infty$ corresponds to the free electron and hole pair energy, i.e. band gap energy E_g . The stable energy due to formation of the exciton corresponds to the energy difference between $n = 1$, and $n = \infty$, which is defined as the exciton binding energy. The exciton binding energy in the typical bulk compound semiconductor ranges from a few to several-tenth meV.

Following theoretical studies [9–15], the optical experiments were carried out to reveal the excitons in the SWNTs. The simple tight-binding calculation without considering the Coulomb interaction predicts that the energy ratio of E_{22}/E_{11} should

Fig. 2.7 (a)–(d)
Configuration of an
electron-hole pair forming the
exciton state



be factor of 2, however it has been well known that the experimentally obtained E_{22}/E_{11} were deviated from the factor 2. This is called as “ratio problem”, which suggests the existence of “exciton” in the SWNTs. In 2005, more directly, the two-photon absorption spectroscopy was carried out to determine the exciton binding energy [18, 19]. The huge exciton binding energy of hundred meV in the SWNTs was directly evaluated from the energy difference between 1s exciton PL and two-photon 2p exciton resonance peak [18, 19]. These experimental studies verified the existence of stable excitons in SWNTs, with huge binding energies on the order of several hundred meV [18–20]. The larger binding energy than the thermal energy at room temperature (≈ 26 meV) indicates that the excitons in the SWNTs are stable even at room temperature. Moreover, noted that this exciton binding energy of several hundred meV in the SWNTs is much larger than that of several-tenth meV in the compound semiconductors. From these studies, it was found that the observed PL peak does not originate from free electron-hole pair recombination but instead from exciton recombination. This stable exciton dominates the optical properties including the optical dynamics and optical nonlinear response, even at room temperature.

2.1.6 Exciton Structures in Carbon Nanotubes

The one of the most striking features of SWNT electronic states are the two degenerate band structures at the K and K' valleys in momentum space [21]. Many configurations of the electron and hole forming the exciton are predicted due to the degeneracy of band structures. Here, the exciton configuration consists of an electron at the K valley and a hole at the K' valley, $|K; K'\rangle$, as shown in Fig. 2.7. Theoretical studies examining the exciton structure with respect to degenerate K and

Table 2.1 Table of exciton states due to the valley and spin degeneracy

Spin	Valley	Degeneracy	Selection rule
singlet	$ K; K(+)\rangle$	1	○
	$ K; K'\rangle$	1	×
	$ K; K(-)\rangle$	1	×
	$ K'; K\rangle$	1	×
triplet	$ K; K(+)\rangle$	3	×
	$ K; K'\rangle$	3	×
	$ K; K(-)\rangle$	3	×
	$ K'; K\rangle$	3	×

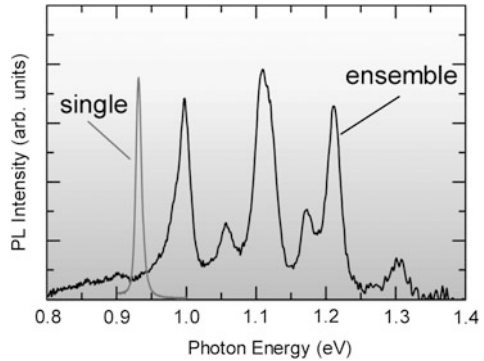
K' valleys [15–17, 21], have indicated multiple exciton states, as shown in Table 2.1 [21]. The exciton states with zero angular momentum, $|K; K\rangle$ and $|K'; K'\rangle$, are split into bonding and anti-bonding exciton states due to the inter-valley (short-range) Coulomb interaction. The bonding state is odd parity, and the anti-bonding state is even parity. Exciton states are further classified by the singlet and triplet nature of the electron-hole spin configurations. The degree of band degeneracy and spin results in 16 exciton states, as shown in Table 2.1. The optical transition from only one exciton state, denoted as $|K; K(+)\rangle$, to the ground state is a dipole-allowed transition (singlet-bright exciton), dictated by the restriction of the optical selection rule (zero-momentum, singlet state, and odd parity). The other 15 exciton states are optically forbidden (dark excitons). These exciton structures dominate the optical properties of SWNTs, such as the exciton dynamics. Thus, the exciton fine structure, including the energy separation between the bright and dark exciton states, should be clarified experimentally.

2.2 Novel Excitonic Properties of Carbon Nanotube

2.2.1 Single Carbon Nanotube Spectroscopy for Revealing Exciton Structures

Figure 2.8 shows the typical macroscopic (ensemble averaged) PL spectrum from micelle encapsulated SWNTs in D_2O solution, indicated by the black line. The many PL peaks arising from various types of SWNTs with different chiralities (n, m) are observed in the ensemble averaged PL spectrum. The optically excited electron-hole pair in SWNTs forms the exciton state due to strong Coulomb interaction described in Sect. 2.1, and recombination of exciton is the origin of the PL signals in the SWNTs. The shape of ensemble averaged PL spectrum shows the near Gaussian function, which means that each SWNT with same chiral indices is in the different environment (local strain, dielectric constant, and ...). The optical transition (absorption and PL) of each SWNT is affected from the Gaussian

Fig. 2.8 Ensemble-averaged PL spectrum (*black solid line*) and PL spectrum of a single SWNT (*gray solid line*)

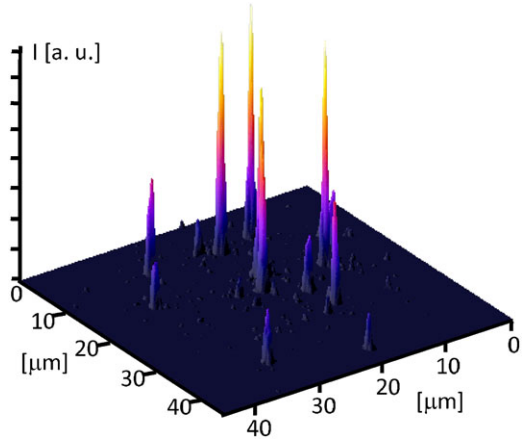


distributed inhomogeneous environment, causes fluctuation of the transition energy and broadens the optical spectrum. The PL broadening arising from the different environment is called as “inhomogeneous broadening”, which covers the intrinsic optical properties of SWNTs. In contrast, the effect of the inhomogeneous broadening is eliminated in the PL spectra from a single SWNT. The sophisticated optical spectroscopic technique, called as a single carbon nanotube spectroscopy, enables us to reveal the exciton fine structures [22–26]. Figure 2.8 also shows the PL spectrum from a single SWNT, and the PL of a single SWNT shows very clear single peak and very narrow linewidth, which provide us the fruitful information on the excitonic properties of SWNT.

The samples used for single SWNT spectroscopy were isolated SWNTs synthesized on patterned Si substrates by an alcohol catalytic chemical vapor deposition method [27]. The Si substrates were patterned with parallel grooves typically from 300 nm to a few μm in width and 500 nm in depth using an electron-beam lithography technique. The isolated SWNTs grow from one side toward the opposite side of the groove. We prepared several SWNT samples by changing the growth temperature (650–850 $^{\circ}\text{C}$) and time (30 sec–10 min). The average number density of isolated SWNTs in the sample is $0.1\text{--}1\ \mu\text{m}^{-2}$. Single SWNT PL measurements were carried out from 300 (room temperature) to 5 K using a home-built variable temperature confocal microscope setup. The SWNT samples mounted on a stage were excited with a continuous-wave He-Ne, and femtosecond pulsed Ti:Al₂O₃ laser, and the laser beam was focused on the sample surface through a microscope objective (NA 0.8). The PL signal from SWNTs was spectrally dispersed by a 30-cm spectrometer equipped with a liquid-nitrogen (LN₂)-cooled InGaAs photodiode array (spectral range: 0.78–1.38 eV), and CCD camera ($>1.22\ \text{eV}$). The spectral resolution of the system was typically less than 0.7 meV. We also obtained PL images of the luminescent SWNTs on the sample, using a Si avalanche photodiode or electron multiple (EM) CCD camera.

Figure 2.9 shows a typical PL image of isolated semiconducting SWNTs at room temperature. The monitored PL energy range is typically between 1.18 and 1.37 eV. Several spatially isolated bright spots can be observed in the 3D image. Each bright spot represents the PL signal from a single luminescent SWNT because the PL spectrum obtained just on each bright spot has only a single PL peak [26].

Fig. 2.9 Three-dimensional plots of the PL image of a SWNT at room temperature

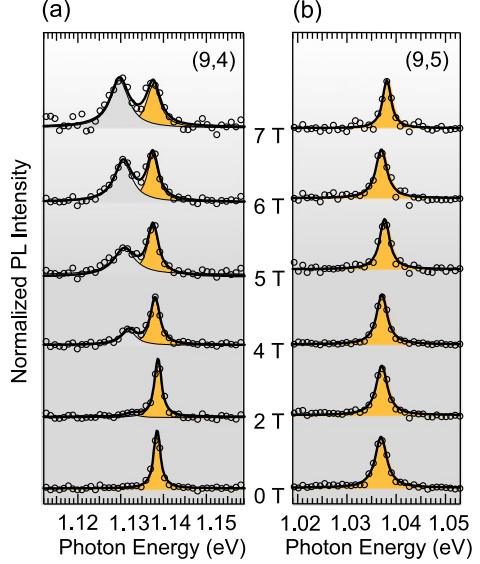


2.2.2 Singlet-Bright and -Dark Exciton Revealed by Magneto-PL Spectroscopy

Magneto optical spectroscopy is a versatile tool in order to study the exciton structures [28–33]. Here, we described low temperature magneto-PL spectroscopy of single SWNT to study the singlet exciton structures with odd $|K; K(+)\rangle$ and even $|K; K(-)\rangle$ parity due to the inter-valley Coulomb interaction [32]. In the magneto-PL measurements of a 1D SWNTs, relative angle relationship between the nanotube and magnetic field (magnetic flux) should be characterized. Magneto-PL spectroscopy was carried out under Voigt and Faraday geometry. In the Voigt geometry, in which laser light propagates perpendicular to the magnetic field, we can investigate the effect of the magnetic flux threading the nanotube axis, while in the Faraday geometry, in which the laser propagates parallel to the field, the magnetic flux is perpendicular to the tube axis.

Figure 2.10(a) shows the normalized PL spectra of a single (9,4) carbon nanotube under a magnetic field in the Voigt geometry, where the relative angle α between the tube axis and magnetic field is $\approx 9^\circ$. A single and sharp PL spectrum arising from bright exciton recombination is observed at zero magnetic field, and the shape of PL spectrum from a single SWNT is approximated by a Lorentzian function, reflects homogeneous broadening [34–36]. This single and sharp spectrum of a single carbon nanotube enables us to observe the spectral changes in detail, even under a magnetic field of several T. An additional peak is clearly observed below the bright exciton peak with an increasing field in Fig. 2.10(a). These PL spectra are fit well by summation of two Lorentzian functions and the energy positions of the two peaks can be evaluated accurately. The lower energy peak shows a redshift and the intensity relative to the higher peak increases with the magnetic field. In contrast, Fig. 2.10(b) shows the results of similar experiments on a single (9,5) nanotube performed in the Faraday geometry, where the magnetic flux is perpendicular to the nanotube axis. No spectral splitting induced by the magnetic field is observed in the

Fig. 2.10 Low temperature of PL spectra of single SWNT under a magnetic field; (a) Voigt (B//z) and (b) Faraday (B//z) configurations (Reprinted with permission from [32]. Copyright, American Physical Society)



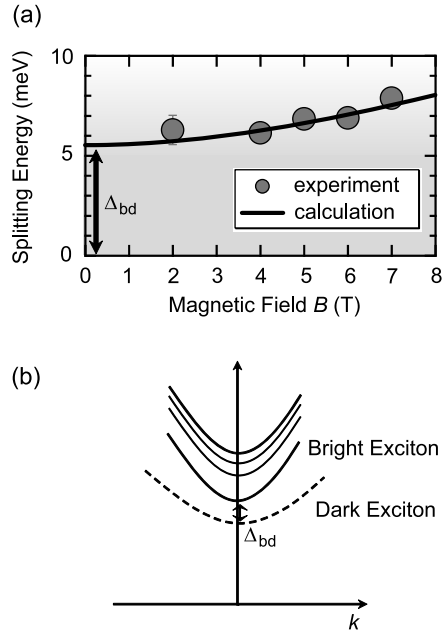
Faraday geometry, even under a magnetic field of 7 T. Note that the splitting of the PL peak occurs due to the magnetic flux parallel to the nanotube axis.

Here, we discuss the experimentally observed change of PL spectrum induced by the magnetic flux in a single carbon nanotube. The effective magnetic flux threading the nanotube is experimentally evaluated as $\phi = \pi d^2/4 \times B \cos \alpha$, where d is the nanotube diameter and B is the strength of the magnetic field. According to the theoretical calculation by Ajiki and Ando [37], the degenerated band-gaps in semiconducting carbon nanotubes at the K and K' valleys are lifted due to the Aharonov-Bohm effect. The split between the two states, Δ_{AB} , is described by

$$\Delta_{AB} = 6E_g\phi/\phi_0 \quad (\phi/\phi_0 < 1/6), \quad (2.4)$$

where $\phi_0 = ch/e$ is the magnetic quantum and E_g is the band-gap energy of the carbon nanotubes. In the excitonic picture with consideration of Coulomb interactions, two degenerated valleys create four singlet exciton states, $|K; K\rangle$, $|K; K'\rangle$, $|K'; K\rangle$, $|K'; K'\rangle$, where $|K; K\rangle$ means that the exciton consists of an electron (hole) in the K (K') valley [21]. Moreover, the singlet exciton states with zero angular momentum, $|K; K\rangle$ and $|K'; K'\rangle$, split into the bonding $|K; K(+)\rangle$ exciton state with odd parity and antibonding $|K; K(-)\rangle$ exciton states with even parity due to the short-range Coulomb interaction. The optical transition from $|K; K(+)\rangle$ ($|K; K(-)\rangle$) exciton to the ground state is dipole allowed (forbidden) and $|K; K(+)\rangle$ ($|K; K(-)\rangle$) exciton becomes bright (dark) state [21]. When the magnetic flux threads the nanotube axis, the exciton states at the K and K' valleys become independent of each other, and the singlet dark state with even parity gradually brightens as the magnetic field

Fig. 2.11 (a) Splitting of PL peak as a function of magnetic field under Voigt configuration. (b) Schematic of exciton states including single bright and dark exciton states. Splitting energy between these states is defined as Δ_{bd} (Reprinted with permission from [32]. Copyright, American Physical Society)



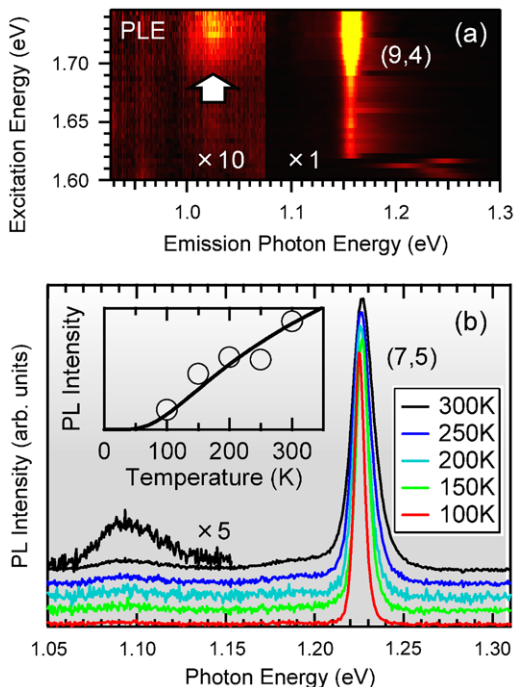
is increased. Using Eq. (2.4), the energy difference $\Delta_{bd}(B)$ between the bright and dark exciton states under magnetic field B can be described by

$$\Delta_{AB}(B) = \sqrt{\Delta_{bd}^2 + \Delta_{AB}^2}, \quad (2.5)$$

where Δ_{bd} is the energy splitting at zero magnetic field [21].

Figure 2.11(a) shows the bright and dark exciton energies estimated from the Lorentzian spectra fitting procedure as a function of magnetic field. For the evaluation of Δ_{bd} , we assumed that the Aharonov-Bohm splitting is proportional to the magnetic flux, that is, $\Delta_{AB} = \mu\phi$, where μ is a constant [21]. Figure 2.11(a) shows the experimentally observed splitting values and the theoretical curve based on Eq. (2.5) where Δ_{bd} and μ are fitting parameters. The theoretically calculated curves reproduce the experimental results well. Here the value of Δ_{bd} is about 5.5 meV under zero magnetic field and the parameter μ is 1.14 meV/T nm^2 [32]. This result indicates that the singlet dark exciton state exists about 5.5 meV below the singlet bright exciton state in the (9,4) SWNT. The Aharonov-Bohm splitting of SWNTs with various chiral indices were experimentally observed [32]. We found that the singlet dark exciton states always lie at the lower energy side of singlet-bright exciton on order of a few meV, and its energy splitting strongly depends on the tube diameter.

Fig. 2.12 (a) PLE contour map of a single (9,4) carbon nanotube. The *arrow* shows the weak satellite PL peak far below the bright exciton PL peak. (b) Temperature-dependent PL spectra of a single (7,5) carbon nanotube. The *inset* shows the temperature dependence of the PL intensity ratio of the satellite peak to the bright exciton peak. PL spectra of single SWNT with different chiral index (n, m) (Reprinted with permission from [43]. Copyright, American Physical Society)



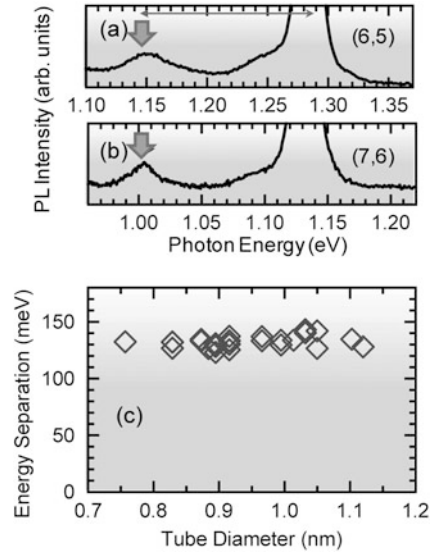
2.2.3 Triplet and K -Momentum Dark Exciton States

Recently, satellite PL peaks have been experimentally observed, with much lower energies than the singlet bright exciton peak [38–42]. Since the lower exciton states have considerable influence on the optical properties of carbon nanotubes, the origin of the low-energy PL peaks has been a matter of intense debate. Here we describe the low energy PL peaks arising from the triplet and K -momentum dark exciton states in SWNTs [43]. Figure 2.12(a) shows a typical contour map of PLE for a single (9,4) carbon nanotube with E_{11} singlet bright exciton peak at room temperature.

A sharp PL spectrum of a single SWNT provides a clear feature of the low-energy PL band below the singlet bright exciton peak. We can observe a weak low-energy PL peak ≈ 130 meV below the singlet bright exciton peak as indicated by the arrow in Fig. 2.12(a), arising from the same (9,4) nanotube.

Figure 2.12(b) shows the temperature dependence of PL spectra of a single (7,5) carbon nanotube, where each PL spectrum was normalized by the bright exciton peak intensity. With decreasing temperature, the PL intensity of the weak low-energy peak decreases. The ratio of the weak low-energy PL peak to the bright exciton peak is shown in the inset of Fig. 2.12(b) as a function of temperature. The characteristic behavior of decrease of this ratio with decreasing temperature shows that the low-energy PL peak does not come from the lower dark exciton states because the exciton population in the lower exciton states should increase and

Fig. 2.13 (a) and (b) PL spectra of single (6,5) and (7,6) carbon nanotubes, respectively. The *arrows* indicate the weak low-energy peaks. (c) Tube-diameter dependence of the energy separation between the bright exciton peak and the weak low energy peak (Reprinted with permission from [43]. Copyright, American Physical Society)



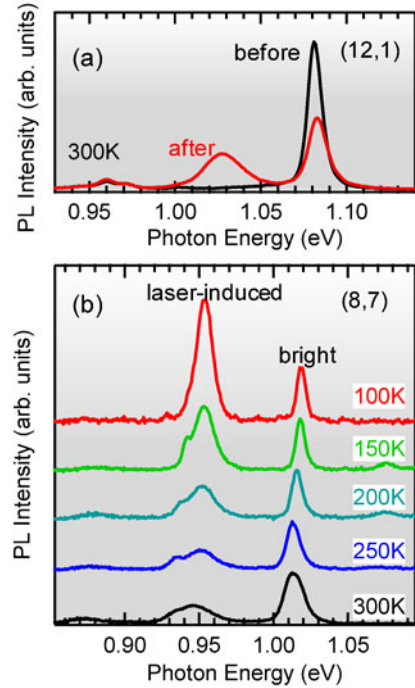
PL intensity is expected to increase at lower temperature. To evaluate the experimental data, we assumed that the low-energy peak is the phonon sideband of the K -momentum dark exciton states ($|K; K'\rangle$), emitting an in-plane TO (i TO) phonon at K -point [39, 40]. The temperature dependence of the PL intensity ratio of the phonon sideband I_{phonon} to the bright exciton state I_{bright} can be expressed as the product of the Boltzmann factor and the probability of emitting a phonon, i.e.,

$$\frac{I_{phonon}}{I_{bright}} \propto \exp\left(\frac{\Delta_K}{k_B T}\right) \times (n_{ph} + 1), \quad (2.6)$$

where Δ_K is the energy separation between the K -momentum dark and the bright exciton states, $n_{ph} = 1/[\exp(\Delta_{ph}/k_B T) - 1]$ is the phonon occupation number, and Δ_{ph} is the phonon energy. The solid curve in the inset of Fig. 2.12(b) shows the calculated result from Eq. (2.6) using $\Delta_K = 40$ meV and $\Delta_{ph} = 170$ meV and reproduces the experimental data well. These values are consistent with theoretical [14] and experimental studies [40, 44] on the phonon-mediated absorption peak ≈ 200 meV ($\approx \Delta_K + \Delta_{ph}$) above the bright exciton peak due to the K -momentum excitons. This result shows that the temperature dependence of the weak low-energy PL peak can be explained by considering the phonon sideband of the K -momentum dark exciton states.

We investigated the low-energy PL peak for many single carbon nanotubes with different chiralities shown in Figs. 2.13(a) and (b). In Fig. 2.13(c), we plotted the energy separation, Δ_1 , between the weak low-energy PL peak and the bright exciton PL peak as a function of the tube diameter. Although some of the data are slightly scattered even in the same-chirality tubes, this result indicates that $\Delta_1 = \Delta_{ph} - \Delta_K$ is about 130 meV and almost independent of the tube diameter. This is consistent with the considerations of the phonon sideband discussed above because the energy

Fig. 2.14 (a) PL spectra of a single (12,1) carbon nanotube before and after pulsed-laser irradiation. (b) Temperature dependence of PL spectra of a single (8,7) carbon nanotube after pulsed-laser irradiation (Reprinted with permission from [43]. Copyright, American Physical Society)

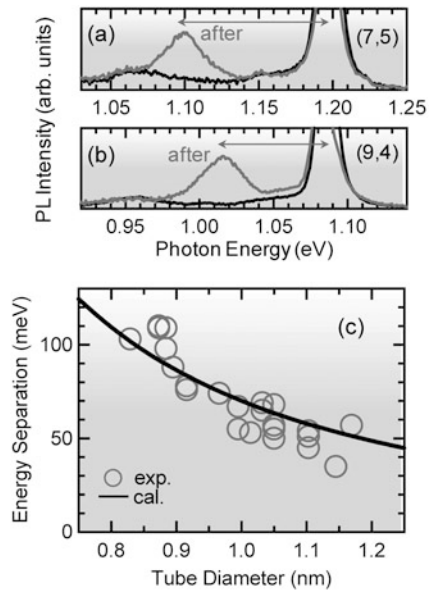


of the iTO phonon mode, Δ_{ph} , is dominant in Δ_1 , and almost independent of the tube diameter within the diameter range shown in Fig. 2.13(c). The both the temperature and diameter dependences of the weak low-energy PL peak strongly indicate that it arises from the phonon sideband of the K -momentum dark exciton states. Therefore, from these results, it was found that K -momentum dark exciton states lie above the singlet-bright exciton states above 40 meV.

Here, we also investigated the effect of the pulsed-laser irradiation to single carbon nanotubes, since the strong pulsed-laser irradiation has been reported to induce the appearance of a low-energy PL peak [41, 43]. We irradiated the femtosecond pulsed-laser with 735-nm wavelength and ≈ 2 mW to single carbon nanotubes. Figure 2.14(a) shows PL spectra of a single (12,1) carbon nanotube before/after the pulse irradiation, respectively. Additional satellite PL peak appears 70 meV below the bright exciton peak. Moreover, we also observed the weak phonon sideband simultaneously discussed above 130 meV below the bright peak.

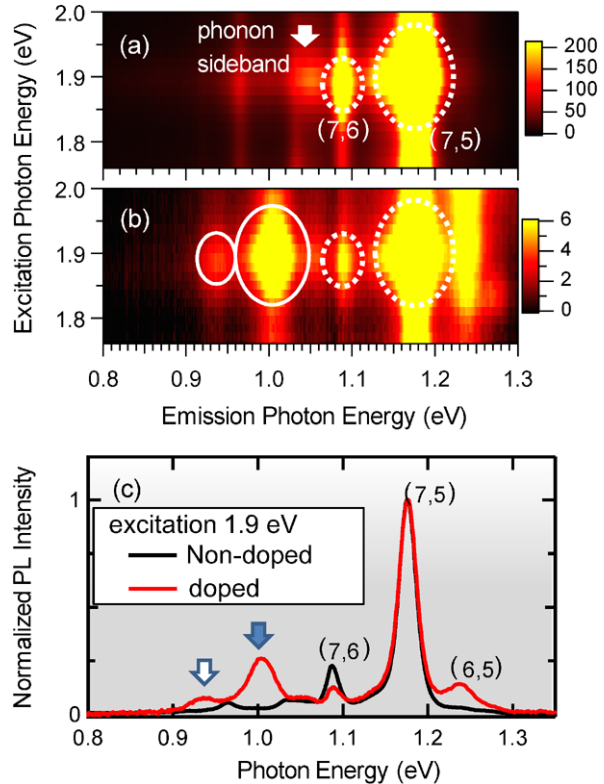
Figure 2.15(b) shows temperature dependence of the PL spectra for an (8,7) carbon nanotube after pulsed-laser irradiation. As temperature decreases, we observed that the intensity of the low-energy PL peak induced by the laser irradiation increases, in contrast with the phonon sideband at 0.87 eV, which decreases at low temperatures. This result clearly shows that the origin of the laser-induced PL peak is completely different from the phonon sideband of the K -momentum dark exciton states and that some light-emitting states lie at much lower energies than the singlet bright exciton state.

Fig. 2.15 (a) and (b) PL spectra of single (7,5) and (9,4) carbon nanotubes, respectively, before and after laser irradiation. (c) Tube-diameter dependence of the energy separation between the bright exciton and the strong low-energy peak induced by the laser irradiation. The curve shows a fit with the splitting energy proportional to $1/d^2$ (Reprinted with permission from [43]. Copyright, American Physical Society)



We investigated the laser-induced low-energy PL peak for many carbon nanotubes, as typically shown in Figs. 2.15(a) and (b), and plotted the separation energy Δ_2 between the bright exciton peak and the laser-induced peak in Fig. 2.15(c). The experimental results show that Δ_2 strongly depends on the tube diameter, with a smaller-diameter tube having a larger Δ_2 . We fit the data to $\Delta_2 = A/d^2$, where A is a coefficient and d is the tube diameter, as shown in Fig. 2.15(c), which reproduces the experimental results with $A \approx 70 \text{ meV nm}^2$. Capaz *et al.* theoretically predicted that the tube-diameter dependence of the splitting energy between the singlet and triplet exciton states is proportional to $1/d^2$ because of the tube-diameter-dependent exchange interaction [45, 46]. The calculated proportionality coefficient is $\approx 40 \text{ meV nm}^2$ for the micelle-wrapped SWNTs with a relative dielectric constant, ϵ , of ≈ 3 [47]. However, the value of proportionality coefficient ($A \approx 70 \text{ meV nm}^2$) can be well accounted with consideration of smaller dielectric constant $\epsilon \approx 1.8$ in this air-suspended SWNTs. This suggests that the origin of the laser-induced low-energy PL peak is the triplet dark exciton states. Although the spin-orbit interaction is small in carbon nanotubes and graphene due to a small mass of the carbon atoms, a recent theoretical study showed that impurities on graphene lead to a large increase of the spin-orbit coupling [48–50]. Therefore, we believe that defects created by the laser irradiation, or any impurities trapped by the defects, would result in an increase in the spin-orbit coupling, leading to the spin-flip process and PL from the triplet exciton states.

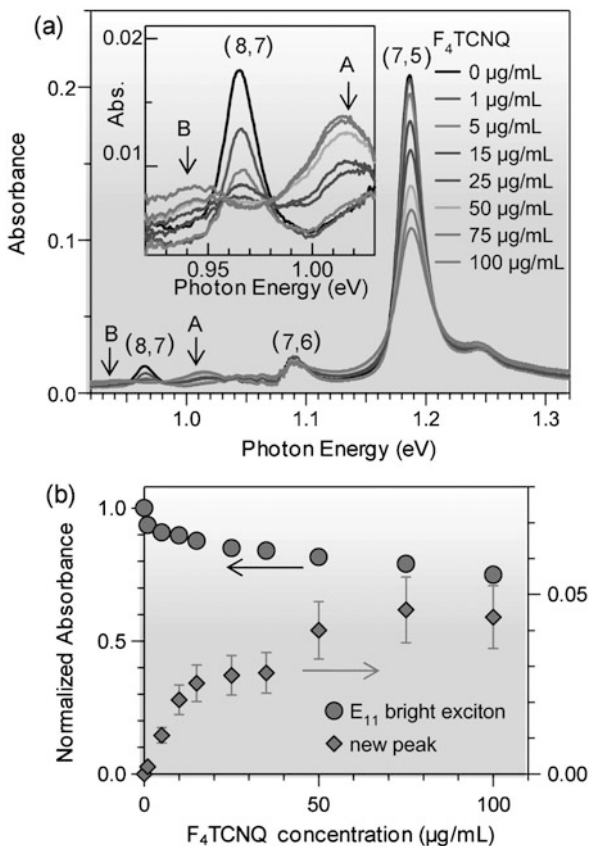
Fig. 2.16 PLE contour maps of (a) nondoped CoMoCAT-PFO nanotubes, (b) CoMoCAT-PFO nanotubes doped with F_4 TCNQ solutions. The *dotted circles* show the E_{11} bright excitons and the *solid circles* show the new PL peaks due to hole doping. (c) The normalized PL spectra of the nondoped and doped CoMoCAT-PFO nanotubes [from (a) and (b), respectively] at the excitation photon energy of 1.9 eV. The doping-induced new PL peaks of (7,5) and (7,6) nanotubes are indicated by the *solid and open arrows*, respectively (Reprinted with permission from [51]. Copyright, American Physical Society)



2.2.4 Exciton-Complex in Carbon Nanotubes

Despite the importance of many particle bound states such as exciton-exciton or exciton-electron (hole) complexes, the many particle bound states in carbon nanotubes are not yet fully understood. Here, we describe the many-particle bound states (exciton-complex) in hole-doped single-walled carbon nanotubes [51]. Figure 2.16(a) shows a contour map of PLE for non-carrier doped CoMoCAT nanotube dispersed by poly[9,9-dioctylfluorenyl-2,7-diyl] (CoMoCAT-PFO) in a toluene solution, which included many (7,5) nanotubes and a small amount of (7,6) nanotubes [52]. The dotted circles in Fig. 2.16(a) indicate the PL of the E_{11} singlet bright excitons in the (7,5) and (7,6) nanotubes. The side peak indicated by the arrow in Fig. 2.16(a) is the phonon sideband of the K -momentum dark excitons in (7,5) carbon nanotubes as described in 3-3. Figure 2.16(b) shows the PLE map after a p -type (hole) doping with 2,3,5,6-tetrafluoro-7,7,8,8-tetracyanoquinodimethane (F_4 TCNQ). At the lower energy side of singlet exciton peak, new PL peaks appears, as indicated by the solid circles in Fig. 2.16(b). These PL peaks are clearly associated with (7,5) and (7,6) carbon nanotubes. Figure 2.16(c) shows the normalized PL spectra of the non-doped and doped CoMoCAT-PFO nanotubes (Figs. 2.16(a)

Fig. 2.17 (a) The hole-doping dependence of the absorption spectra of CoMoCAT-PFO nanotubes. The inset shows an enlarged view of the lower-energy region where the new peaks appear. The new peaks indicated by the arrows A and B are associated with (7,5) and (7,6) nanotubes, respectively. (b) The hole-doping dependence of the absorption intensity of the E_{11} bright excitons (left axis) and the new peak (right axis) of (7,5) carbon nanotubes (Reprinted with permission from [51]. Copyright, American Physical Society)



and (b), respectively) at the excitation photon energy of 1.9 eV. The doping-induced new PL peaks are indicated by the arrows in Fig. 2.16(c).

Figure 2.17(a) shows the absorption spectra of CoMoCAT-PFO nanotubes with F_4TCNQ solutions added. The inset shows an enlarged view of the low-energy side. With increasing F_4TCNQ concentration, the new absorption peaks appear as indicated by the arrows A and B in Fig. 2.17(a). Compared with the new PL peaks observed in Fig. 2.17(a), we found that the absorption peaks A and B are associated with (7,5) and (7,6) nanotubes, respectively. Figure 2.17(b) shows the normalized absorption intensity of the singlet bright exciton peak (left axis) and the new peak (right axis) of (7,5) carbon nanotubes as a function of F_4TCNQ concentration. While the absorption intensity of the bright exciton decreases due to the hole-doping [53], the absorbance of the new state increases. In the same way, we also performed hole-doping to HiPco-PFO nanotubes by adding F_4TCNQ and HiPco-SDBS (SDBS: sodium dodecylbenzene sulfonate) nanotubes by adding AB (4-amino-1,1-azobenzene-3,4-disulphonic acid) solutions. Note that we observed the appearance of the same new PL and absorption peaks in the SWNTs samples with using different dispersing agents and dopant molecules. These results indicate

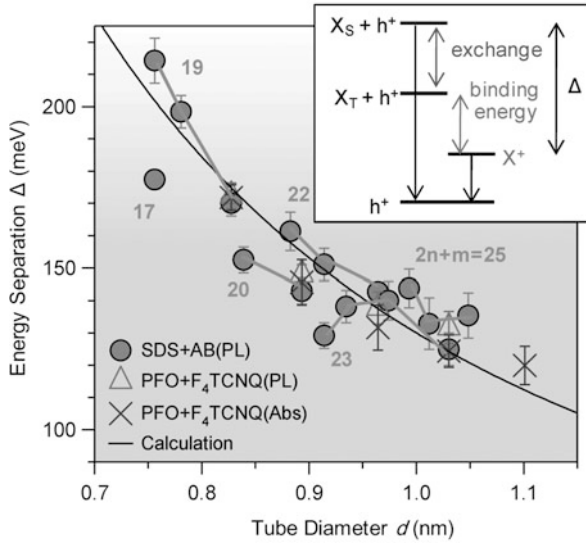


Fig. 2.18 Tube diameter d dependence of the energy separation between the bright exciton state and the new state observed in PL and absorption spectra. The *green numbers* show the value of $2n + m$ for (n, m) nanotubes. The calculated *solid curve* shows the sum of the exchange splitting of $70/d^2$ meV and the trion binding energy of $60/d$ meV. *Inset* shows the schematic of the energy levels of the singlet and triplet excitons (X_S and X_T) and the trions (X^+). A free hole is denoted as h^+ (Reprinted with permission from [51]. Copyright, American Physical Society)

that the new PL peak observed in hole-doped carbon nanotubes is independent of the dopant species, and that the new state exhibits intrinsic properties of hole-doped carbon nanotubes, rather than any chemical complex with a specific dopant.

Figure 2.18 shows the tube-diameter dependence of the energy separation Δ between the bright exciton state and the new state observed in the PL and absorption spectra. The energy separation depends strongly on the tube diameter, but not on the species of dopants. The value of Δ is about 130 meV for 1-nm diameter. This diameter dependence of the new peak is completely different from the phonon sideband of the K -momentum dark excitons or the luminescence of triplet excitons, as described in Sects. 2.2 and 2.3. The new PL and absorption peaks appear with very small Stokes shifts. In Fig. 2.18, we also show the value of $2n + m$ for each chirality with the HiPco-SDS data, where (n, m) is the chiral index. The HiPco-SDS data show clear family patterns, which are well-known optical characteristics of carbon nanotubes, similar to the exciton binding energy [46]. This result confirmed that the new state arises from the intrinsic properties of carrier-doped carbon nanotubes, rather than specific dopants.

Here, we consider the origin of the intrinsic low-energy PL and absorption peaks. Theoretical calculations have shown that stable trions (charged excitons) can exist in carbon nanotubes [54–56]. A trion binding energy is defined as the energy required for dissociating a trion into a free hole and an exciton. The calculated trion binding energy in carbon nanotubes for dielectric constant of 3.5 is about $40/d$ meV,

where d is the tube diameter (n, m), and is much larger than that in other II–VI or III–V compound semiconductors. It means that trions in carbon nanotubes are detectable even at room temperature [51, 57]. Thus, we assign the new state below the singlet excitons in hole-doped carbon nanotubes to trions, which have not been experimentally reported in carbon nanotubes so far [53].

The energy separation between the bright excitons and trions observed in our experiments for 1-nm-diameter tube was about 130 meV, which is very large value. We attribute the extremely large energy separation to the electron-hole exchange interaction originating from the short-range Coulomb interaction in carbon nanotubes, which has not been considered in the previous trion calculations [50]. The excitons in carbon nanotubes have large singlet-triplet splitting as much as several tens of meV, as described in Sects. 2.2 and 2.3. This is because the strong exchange interaction between an electron and a hole in carbon nanotubes significantly lifts up the energy level of the singlet bright exciton state. Thus, the trion binding energy corresponds to the energy separation between the trion states and the lowest triplet exciton states, as shown in the inset of Fig. 2.18. Assuming the trion binding energy of $\approx 60/d$ meV and the singlet-triplet exciton splitting of $70/d^2$ meV [43], we show the energy separation $\Delta = 70/d^2 + 60/d$ as the solid curve in Fig. 2.18. The solid curve is in good agreement with the experimental data. Thus, we concluded that the trion can be stable in hole-doped carbon nanotubes even at room temperature.

2.3 Novel Exciton Dynamics of Carbon Nanotube

2.3.1 Exciton Relaxation Dynamics Between Bright and Dark State

The exciton dynamics are important issues, which leads to the understanding of the novel excitonic properties of carbon nanotube. Here, we studied the exciton relaxation and distribution between the bright and dark states through the magnetic- and temperature-dependences of the PL spectra of single carbon nanotubes.

Figure 2.19(a) shows the temperature dependence of the magneto-PL spectra for a (7,5) nanotube in a 7 T field [58]. The two PL peaks from the dark and bright exciton states are observed, as in Fig. 2.10(a). The PL peak from the dark exciton state at the lower energy side is more clearly observed at lower temperatures. This result can be explained by the concentrating of the population in the lower dark exciton state with decreasing temperature, as the PL intensity can be represented as the product of the oscillator strength and the population of excitons.

We investigated the exciton population from the PL intensity ratio of the dark to the bright excitons, I_d/I_b . We also checked the magneto-PL spectra at various excitation laser powers, as shown in Fig. 2.19(b) and confirmed that I_d/I_b was independent of the laser power in our weak excitation conditions in Fig. 2.19(c). Figure 2.20(a) shows the temperature dependence of I_d/I_b at a magnetic field of 7 T for the (7,5) carbon nanotube shown in Fig. 2.19(a). We therefore concluded that heating of the nanotubes due to excitation laser could be neglected. While I_d/I_b (solid

Fig. 2.19 (a) Temperature-dependence of magneto-PL spectra at 7 T for a single (7,5) nanotube. (b) Magneto-PL spectra at 7 T for a (7,6) carbon nanotube under various excitation laser powers. (c) Laser-power dependence of the PL intensity ratio of the dark to the bright excitons in the (b) (Reprinted with permission from [58]. Copyright, American Physical Society)

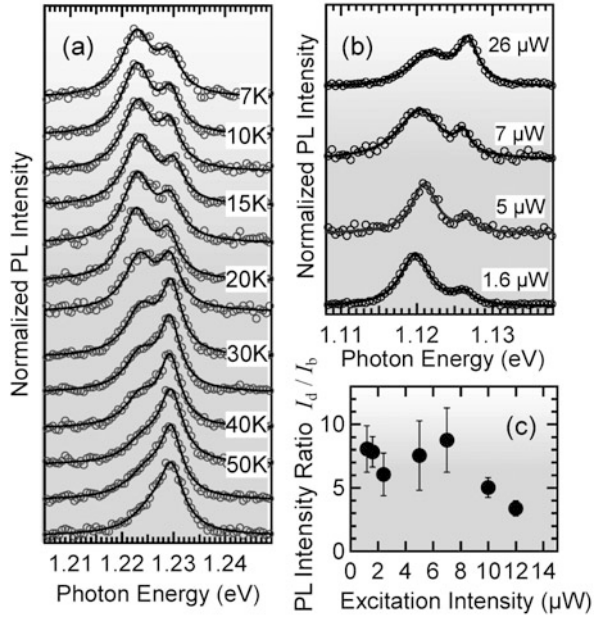
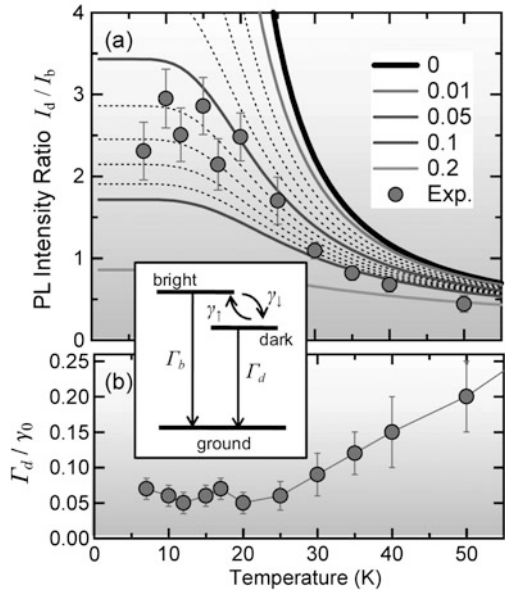


Fig. 2.20 (a) Temperature dependence of the PL intensity ratio of the dark to the bright excitons at 7 T for the (7,5) nanotube. *Solid circles* show experimental results and the lines indicate the calculated results for each Γ_d/γ_0 . (b) Temperature dependence of Γ_d/γ_0 evaluated from (a). *Inset*: Schematic of a three-level model, with the bright and dark exciton states and a ground state (Reprinted with permission from [58]. Copyright, American Physical Society)



circles) in Fig. 2.19(b) increases with decreasing temperature, it clearly saturates below 20 K. In a Boltzmann exciton distribution, I_d/I_b should diversely increase toward low temperatures (the thick solid black line in Fig. 2.20(a)) because the exci-

ton population fully concentrates on the lower dark state. However, the experimental data do not diverge as rapidly as expected for a Boltzmann distribution.

We consider the transition rates between the bright and dark exciton states at 7 T to understand the experimental results. Inset of Fig. 2.20 shows a schematic of a three-level model consisting of bright and dark exciton states with a splitting energy Δ_{bd} and a ground state [59]. The lifetimes of the bright and dark excitons are denoted as $1/\Gamma_b$ and $1/\Gamma_d$, respectively. The $\gamma_{down} = \gamma_0(n + 1)$ and $\gamma_{up} = \gamma_0 n$ represent the up and down scattering rate between the bright and dark exciton states through phonon emission and absorption processes, respectively, where $n = 1/[\exp(\Delta_{bd}/k_B T) - 1]$ is the phonon occupation number and γ_0 is the temperature-independent scattering rate. The rate equation for the dark exciton population can be expressed as

$$\frac{dN_d}{dt} = \gamma_{down} N_b - (\gamma_{up} + \Gamma_d) N_d, \quad (2.7)$$

where N_b and N_d are the populations of the bright and dark exciton states, respectively. In the steady state ($dN_d/dt = 0$), the population ratio of the dark to the bright exciton state is

$$\frac{N_d}{N_b} = \frac{\exp(\Delta/k_B T)}{1 + \frac{\Gamma_d}{\gamma_0} (\exp(\Delta/k_B T) - 1)}. \quad (2.8)$$

This equation indicates that N_d/N_b depends on the term Γ_d/γ_0 , the ratio of the dark exciton lifetime to the thermalization time between the two exciton states. If the phonon-induced exciton scattering rate γ_0 is large enough, the ratio can be neglected ($\Gamma_d/\gamma_0 \rightarrow 0$) and N_d/N_b simplifies to $\exp(\Delta/k_B T)$, a Boltzmann distribution. The thick solid black line in Fig. 2.20 shows the calculated I_d/I_b , assuming the Boltzmann distribution between the bright and dark exciton states. Here, according to the expression given in Ref. [30], we calculated the relative oscillator strength of the dark to the bright excitons at 7 T as ≈ 0.17 . The other lines correspond to the calculated results for each value of Γ_d/γ_0 . Below 20 K, the calculated line for $\Gamma_d/\gamma_0 = 0.06 \pm 0.02$ reproduces the experimental data well.

We determined the values of Γ_d/γ_0 for each temperature from the experimental data, and plotted them as a function of temperature in Fig. 2.20(d). Since γ_0 is temperature-independent, we can determine the temperature dependence of the dark exciton decay rate Γ_d , which is dominated by the non-radiative process. The Γ_d is almost constant below about 20 K, and becomes large with increasing temperature. This dependence is similar to the reported bright exciton decay rate [59]. At room temperature, up to 7 T, we could hardly observe the dark exciton PL peak. Therefore we concluded that Γ_d/γ_0 is at least larger than 1 at room temperature at 7 T. A consistent result has been recently reported by using time-resolved spectroscopy for single nanotubes [60].

Our result suggests that the phonon-induced exciton scattering between the bright and dark states does not occur rapidly as compared to the dark exciton lifetime. This means that the excitons are not fully thermalized between the two states. Theory predicts that the phonon cannot scatter excitons between these two states for ideal

carbon nanotubes because the bright and dark excitons have odd and even parities, respectively, and the phonon cannot break the symmetry [61]. Therefore, the slow phonon-induced exciton scattering between the bright and dark states leading to the non-Boltzmann distribution can be explained by different parities of the two exciton states. It means that the phonon-induced exciton scattering time between the bright and dark exciton states cannot be neglected against the dark exciton lifetime, and that PL dynamics in carbon nanotubes is under the influence of the non-Boltzmann exciton distribution between the bright and dark states.

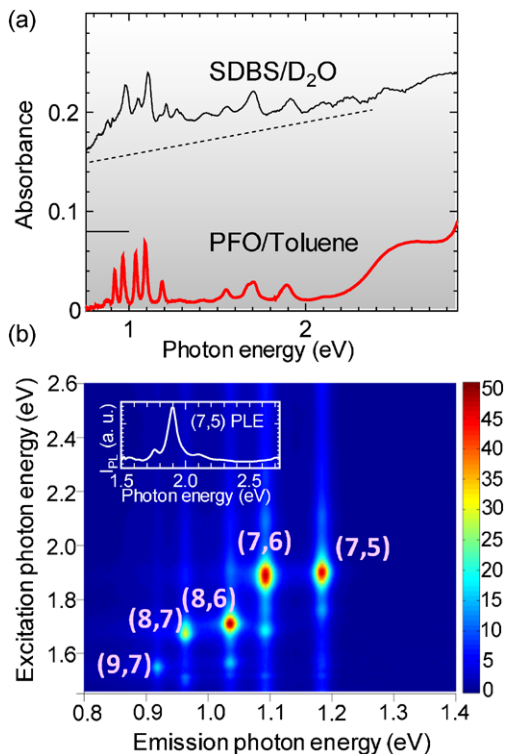
2.3.2 Radiative Lifetime of Bright Exciton States

The exciton spatial coherence volume (length) is defined as the volume from which the exciton can coherently capture the oscillator strength, and is an important parameter [62]. The exciton radiative lifetimes and the PL quantum yields (η) are therefore dominated by the coherence volumes (lengths) [62]. Moreover, the coherence lengths in SWNTs also determine whether the exciton motion can be treated as diffusive or not. This is directly related to the exciton relaxation mechanism and nonlinear optical properties. Here, we investigated the exciton radiative lifetimes of SWNTs using highly isolated SWNT ensembles with high PL quantum yields, and determined the exciton coherence lengths from the radiative lifetimes.

Figure 2.21(a) shows the absorption spectra of PFO-dispersed SWNTs and SDBS-dispersed SWNTs. The underlying background in the absorption spectrum of PFO-dispersed SWNTs is remarkably suppressed compared to that of the SDBS-dispersed SWNTs, and the absorption peaks are much more pronounced. This indicates that bundled SWNTs, residual impurities, or other amorphous and graphitic carbons were not included in the PFO-dispersed sample. Figure 2.21(b) shows the PLE map of PFO-dispersed SWNTs. The absorption spectra and PLE spectra show that only several types of chiral indices were included in the PFO-dispersed SWNTs samples. The diameters of SWNTs in the sample estimated from the absorption and PLE spectra range from ≈ 0.8 to 1.2 nm.

The η values of SWNTs were determined by comparison with those of the reference dyes (Styryl-13 and Rhodamine-6G). The η of Styryl-13 was calibrated against that of Rhodamine-6G in methanol ($\eta = 95\%$). In addition to the absorption spectrum with very low backgrounds, the small number of peaks enabled us to extract η of each (n, m) nanotube type in the PFO-dispersed sample. Figure 2.22(a) shows the absorption spectrum and the reconstructed spectrum based on the observed PLE spectrum. The reconstructed spectrum is the total of each (n, m) PLE spectrum, with only the amplitude of the peak varied as a fitting parameter. From the peak heights obtained in the fitting procedure, we determined the absorbance of each (n, m) peak at E_{22} . Figure 2.22(b) shows the evaluated η_{PL} of PFO-dispersed SWNTs as a function of tube diameter under the E_{22} resonance excitation conditions in each chiral index, where the relaxation rates from E_{22} to E_{11} were assumed to be independent

Fig. 2.21 (a) Comparison of optical absorption spectra of SWNTs dispersed with SDBS in D₂O and PFO in toluene. (b) PL excitation map of PFO-dispersed SWNTs. *Inset* shows the PLE spectrum of (7,5) SWNTs (Reprinted with permission from [52]. Copyright, American Physical Society)

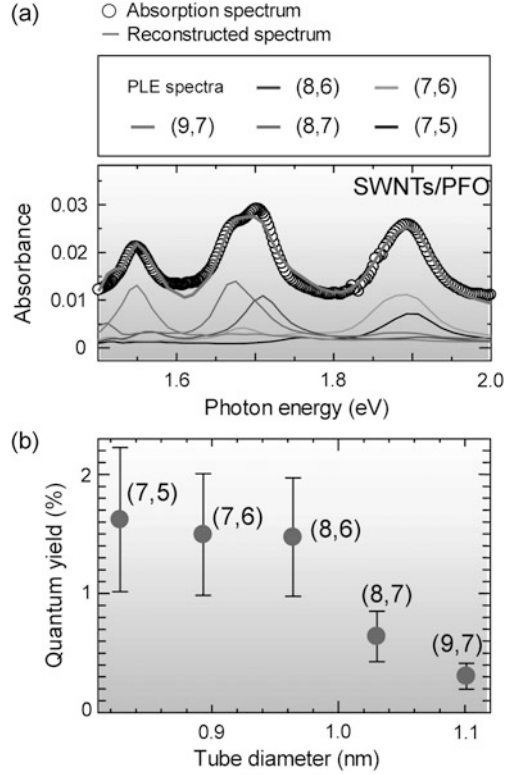


of the chirality [63]. We estimated the η_{PL} to be from $\approx 0.3\%$ to $\approx 1.6\%$, depending on the tube diameter. The relatively smaller diameter nanotubes have larger η_{PL} values, reaching $\approx 1.6\%$ for (7,5) SWNTs.

We measured the PL lifetimes using the femtosecond excitation correlation (FEC) method. The FEC method has been successfully applied to a variety of materials, including SWNTs, to measure the recombination lifetimes of excitons [64, 65]. In the FEC experiments, the SWNTs were excited with optical pulses from a Ti:sapphire laser of central wavelength 745 nm, repetition rate 80 MHz, pulse duration ≈ 150 fs, and spectral width 8 nm. The two beams separated by the delay time were chopped at 800 and 670 Hz, respectively, and collinearly focused onto the same spot (≈ 10 μm). Only the PL signal components modulated at the sum frequency (1470 Hz) were detected as FEC signals with a photomultiplier and a lock-in amplifier after dispersion of PL by a monochromator. The measurements were carried out under the excitation condition ≈ 100 $\mu\text{J}/\text{cm}^2$. For a material with efficient exciton-exciton annihilation processes, FEC signal $I_C(\tau)$ for the delay time τ can be expressed as

$$I_C(\tau) \propto \int_0^{\infty} N_1(t) dt \quad (2.9)$$

Fig. 2.22 (a) Optical (*open circles*) and decomposed (*solid lines*) absorption spectra of SWNTs with PFO in toluene using the PLE spectra of each (n, m) SWNT around the E_{22} transition. The *solid line* is the reconstructed absorption spectrum using PLE spectra of each (n, m) . (b) Measured PL quantum yields of PFO-dispersed SWNTs as a function of tube diameter (Reprinted with permission from [52]. Copyright, American Physical Society)



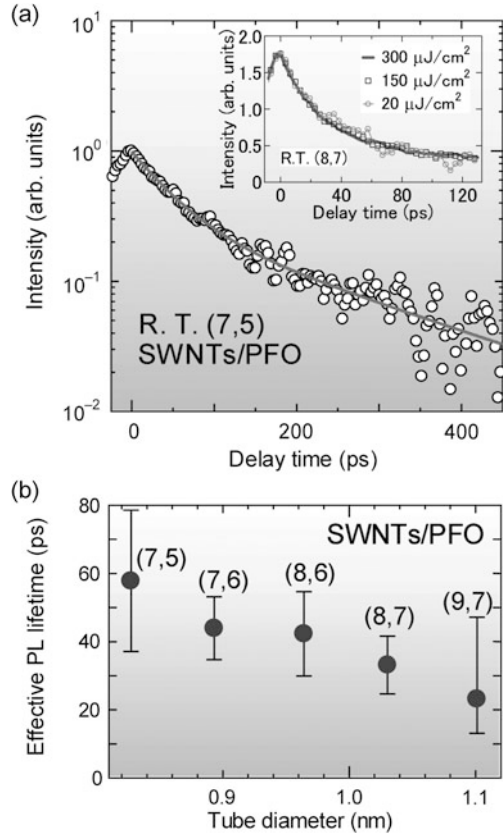
where $N_1(t)$ is the single exciton population decay. Since exciton-exciton annihilation processes occur efficiently in SWNTs [66], we are able to measure the PL lifetimes of SWNTs using the FEC technique. Detailed discussions on the PL lifetime measurement of SWNTs using FEC technique are presented in Ref. [65].

Figure 2.23(a) shows the FEC signals as a function of delay time for (7,5) SWNTs. The upward direction on the vertical axis indicates that the FEC signals have a negative sign. We checked that the FEC decay curves did not change by the excitation power density in the range from ≈ 20 to $300 \mu\text{J}/\text{cm}^2$ [see in inset of Fig. 2.23(a)]. The decay curve is closely described by a double exponential function (solid line) after subtracting the background signals. According to Eq. (2.9), the exciton population showing double exponential decay as $N_1(t) = C \exp(-t/\tau_A) + (1 - C) \exp(-t/\tau_B)$ ($0 \leq C \leq 1$, $\tau_A < \tau_B$) gives the FEC signal $I_C(\tau)$ as

$$I_C(\tau) \propto [C\tau_A \exp(-t/\tau_A) + (1 - C)\tau_B \exp(-t/\tau_B)] \quad (2.10)$$

where C is the fractional amplitude of the fast decay component. Here, we define the effective PL lifetime as $\tau_{PL} = C\tau_A + (1 - C)\tau_B$, and the ratio of the fast component as $Y_A = C\tau_A/[C\tau_A + (1 - C)\tau_B]$. For (7,5) SWNTs in Fig. 2.23(a), we obtained $Y_A \approx 0.7$, $\tau_A \approx 45$ ps, and $\tau_B \approx 200$ ps by the fitting procedure. These are similar to the recently reported values for single (6,5) SWNTs in surfactant suspension

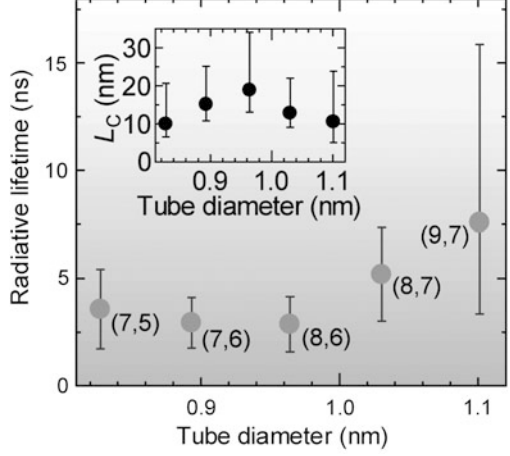
Fig. 2.23 (a) The FEC signals for the (7,5) SWNTs of the PFO-dispersed sample measured under 1.66 eV excitation at $\approx 100 \mu\text{J}/\text{cm}^2$. The *solid curve* is given by a double exponential function. *Inset* shows the excitation power dependence of FEC curves for (8,7) SWNTs from ≈ 20 to $300 \mu\text{J}/\text{cm}^2$. (b) The effective PL lifetimes τ_{PL} as a function of tube diameter in the PFO-dispersed samples. Only the τ_{PL} for the (9,7) SWNTs was measured under 1.55 eV excitation to distinguish the PL signal of the (9,7) SWNTs from that of the (8,7) SWNTs (Reprinted with permission from [52]. Copyright, American Physical Society)



[67]. The effective PL lifetime τ_{PL} is calculated as ≈ 60 ps for (7,5) SWNTs. Figure 2.23(b) shows the effective PL lifetimes of PFO-dispersed SWNTs as a function of tube diameter. SWNTs with small diameters tended to have larger values.

Figure 2.24 shows the experimentally derived radiative lifetimes τ_R of SWNTs at room temperature as a function of tube diameter. The τ_R are calculated from η_{PL} in Fig. 2.22(b) and τ_{PL} in Fig. 2.23(b) as $\tau_R = \tau_{PL}/\eta_{PL}$. We found that the evaluated τ_R are typically $\approx 3\text{--}10$ ns, and slightly increase with the tube diameter. From the obtained radiative lifetime at room temperature, the oscillator strength and the coherence length L_c of the 1D exciton states in SWNTs can be deduced. Note that the experimentally observed radiative decay rate τ_R^{-1} does not simply correspond to that of the bright $K_{ex} = 0$ exciton τ_0^{-1} , where K_{ex} is the exciton momentum. The oscillator strength of $K_{ex} = 0$ exciton is shared by all states within the finite homogeneous linewidth $\Gamma(T)$ due to the uncertainty of K_{ex} induced by dephasing process [68], and here we define the oscillator strength reduced by dephasing process as F_x . In addition, both the thermalization within each single exciton band, and the exciton distribution among bright and dark exciton states further reduce the F_x .

Fig. 2.24 (a) Determined radiative lifetimes τ_R of SWNTs as a function of tube diameter. *Inset* shows deduced coherence lengths L_c as a function of tube diameter (Reprinted with permission from [52]. Copyright, American Physical Society)



to the effective oscillator strength $F_{x,eff}$. We can obtain $F_{x,eff}$ from the measured τ_R as

$$F_{x,eff} = \frac{2\pi\epsilon_0 m_0 \hbar^2 c^3}{\tau_R n e^2 E_x^2}, \quad (2.11)$$

where n is the refractive index (≈ 1.5 for toluene), m_0 is the electron mass, and E_x is the exciton energy.

The fraction of excitons $r_S(T)$ within $\Gamma(T)$ among the thermalized excitons in the bright exciton band can contribute to radiative recombination. $r_S(T)$ is given by [68]

$$r_S(T) = \int_0^{\Delta(T)} D(E) e^{-E/k_B T} dE / \int_0^{\infty} D(E) e^{-E/k_B T} dE, \quad (2.12)$$

where $D(E)$ is the exciton density of states. For the 1D case, assuming $D(E) \propto 1/\sqrt{E}$, we obtain $r_S(T) = \text{erf}(\sqrt{\Gamma/k_B T}) \approx \sqrt{\Gamma/k_B T}$. The $T^{-1/2}$ dependence of the radiative decay rate has been observed in the temperature dependence in the PL measurements [31, 69]. As mentioned above, the exciton distribution between singlet bright and dark states decreases F_x again by a factor of [17]

$$r_M(T) = e^{-\delta_1 k_B T} / (1 + e^{-\Delta_{bd}/k_B T} + 2e^{-\Delta_K/k_B T}), \quad (2.13)$$

where Δ_{bd} and Δ_K are the energy differences of the bright exciton and higher dark excitons measured from the bottom of the lowest singlet dark exciton band, respectively. Since the relationship between $F_{x,eff}$ and F_x is expressed as $F_x = r_S^{-1} r_M^{-1} F_{x,eff}$ using $r_S(T)$ and $r_M(T)$, we thus determine the oscillator strength F_x from $F_{x,eff}$. Using experimentally obtained values of $\Delta(T) \approx 13$ meV for a single nanotube at room temperature [36], $\Delta_{bd} \approx 4$ meV [32] and $\Delta_K - \Delta_{bd} \approx 30$ meV [44], we obtain the factor $r_S^{-1}(T) r_M^{-1}(T)$ for (7,5) SWNTs.

The F_x contains information on the exciton coherence length. The exciton coherence length L_c and the exciton oscillator strength F_x are related as $L_c =$

$F_X/f_0|\phi(0)|^2$, where f_0 is the oscillator strength of a single k-state in the 1D momentum space, and $\phi(Z_e - Z_h)$ denotes the envelope function of the electron-hole relative motion. In the 1D case, $|\phi(0)|^2 \approx 1/a_X\sqrt{\pi}$, where a_X is the exciton Bohr radius (exciton size). Using the theoretical derived value of $a_X \approx 1.5$ nm [46] and evaluating $f_0 \approx 5$ according to Ref. [70], we evaluate the coherence length of excitons as $L_c \approx 10$ nm in (7,5) SWNTs.

Inset in Fig. 2.24 shows the evaluated coherence lengths for various (n, m) SWNTs. Here, we neglected the diameter dependence of $\Delta_K - \Delta_{bd}$ because of their small contribution. We found that each (n, m) type has similar values of $L_c \approx 10$ nm. These are in good agreement with the calculated values of L_c from the different formula using Γ and the exciton effective mass [71].

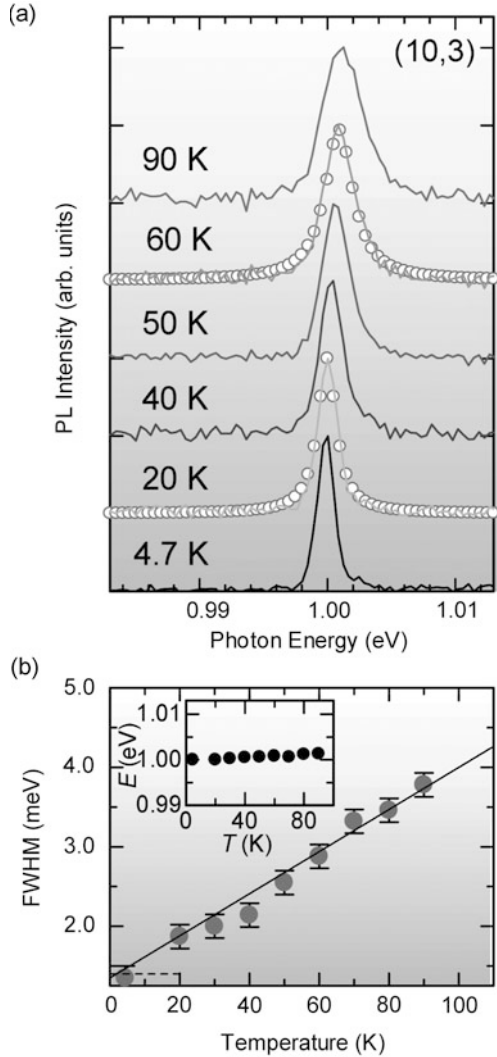
From our results, we can comment on the motion of excitons in SWNTs: The previously observed exciton excursion range of ≈ 100 nm [72, 73] is determined by the diffusive motion of the excitons because the $L_c \approx 10$ nm is much smaller than the diffusion length. The L_c also gives the saturation density N_S of excitons in SWNTs as $1/N_S \approx L_c$ [71]. From $L_c \approx 10$ nm, we get $N_S \approx 10^2$ excitons/ μm and this value is the upper limit of the exciton density in SWNTs at room temperature, which leads to the strong optical nonlinearity of SWNTs. Our experimental determination of L_c thus provides the further insight of the exciton transport and optical properties in SWNTs.

2.3.3 Exciton-Exciton Interaction in Carbon Nanotube

In the higher photoexcitation regime, the exciton-exciton interaction and multi-exciton dynamics appear in single SWNT PL spectra and their linewidths. The single carbon nanotube PL spectroscopy will provide insights into the exciton-dephasing and exciton-exciton interactions in a SWNT. Here, we examined the excitation power dependence of PL spectra from spatially isolated single SWNTs using single carbon-nanotube PL spectroscopy. In the high excitation regime, the homogeneous linewidth broadens nonlinearly with an increase in excitation intensity. Our observation suggests that the broadening of homogeneous linewidth arises from the annihilation of excitons through a rapid Auger recombination process.

Figure 2.25(a) shows the temperature dependence of the PL spectra of an isolated SWNT excited with a He-Ne laser. The spectra were measured under lower excitation conditions (less than ≈ 100 μW) from 4.7 to 90 K. The PL spectra clearly narrow when the temperature decreases [74]. As indicated by the circles in the figure, the spectral lineshapes are well fitted by Lorentzian functions. The linewidth (full-width at half-maximum, FWHM) of a single SWNT, corresponding to a homogeneous linewidth is plotted as a function of temperature in Fig. 2.25(b). The temperature dependence of the linewidth shows almost linear behavior (as indicated by a solid line) in the range of 5 to 90 K. The inset of Fig. 2.25(b) shows the temperature dependence of the PL peak energy. The energy change from 5 to 90 K (≈ 1 meV) is much smaller than that in other compound semiconductor quantum

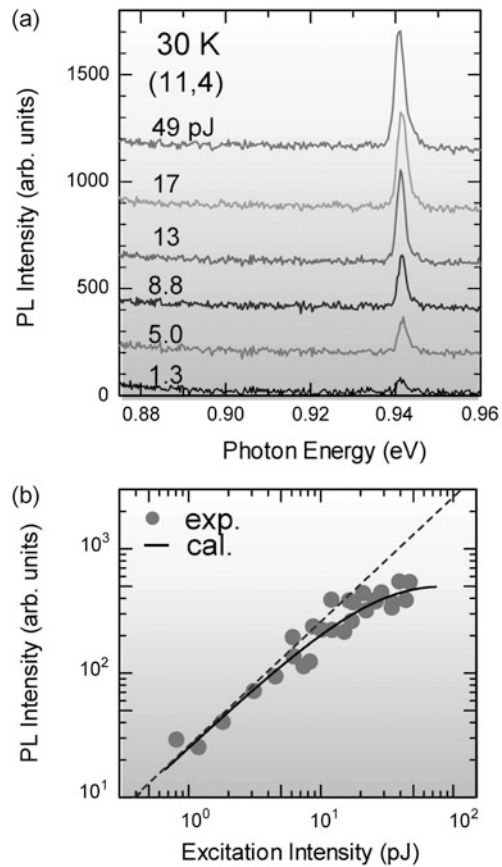
Fig. 2.25 (a) Temperature dependence of PL spectra of a single SWNT from 4.7 to 90 K excited with He-Ne laser light. *Solid circles* denote the Lorentzian function fits. (b) Spectral linewidths (full-width at half-maximum, FWHM) as a function of temperature. The *dotted line* represents the spectral resolution. The *solid line* indicates almost linear temperature dependence. *Inset* shows the temperature dependence of the PL peak energy (Reprinted with permission from [53]. Copyright, American Physical Society)



wire (12 meV from 5 to 90 K in GaAs wires) in the weak exciton-phonon coupling regime [75]. This weak temperature dependence is consistent with the experimental fact of narrow PL spectra with Lorentzian lineshape in Fig. 2.25(a).

Both the dephasing time and the lifetime of the excitons contribute to homogeneous linewidth broadening. The measured PL lifetimes of excitons are considerably longer (≥ 20 ps) from 10 to 300 K [64], and this contribution to the linewidth is negligibly small (≤ 0.01 meV) under lower excitation conditions. Thus, the temperature-dependent linewidths are determined approximately by the dephasing time of the exciton due to the exciton-phonon interactions. This linear temperature dependence implies that the very low energy phonon modes ($\ll k_B T$) dominate the exciton-

Fig. 2.26 (a) Low-temperature PL spectra obtained from a typical single SWNT [assigned chiral index: (11,4)] at various excitation intensities for 1.72-eV and 150-fs pulses. (b) Integrated PL intensity as a function of the excitation laser intensity. As indicated by the *dotted line*, under weak excitation conditions, the PL intensities show almost linear power dependence. The *solid line* corresponds to the fitted curve (Reprinted with permission from [53]. Copyright, American Physical Society)

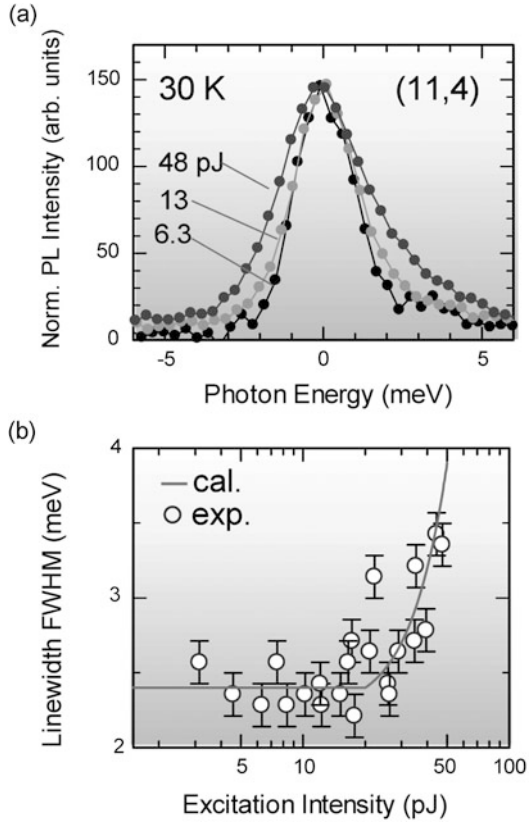


dephasing. The contributed low energy phonon to the exciton-dephasing is assigned as the TW (twisting) mode in SWNTs [26]. Based on the homogeneous linewidth, the exciton-dephasing time is evaluated from 350 fs at 90 K to more than 940 fs at 5 K.

Figure 2.26(a) shows PL spectra obtained from a typical single SWNT [assigned chiral index: (11,4)] at 30 K and at various excitation intensities of 1.72-eV and 150-fs laser pulses. Each spectrum has a single peak located at 0.941 eV. Even in the high-excitation region above about 15 pJ per pulse, the PL spectrum shows a single peak, without a change in the peak energy. Furthermore, additional spectral structures are not observed in any lower energy regions. Similarly, the PL bands due to biexcitons (M-line) and inelastic exciton scattering (P-line) are not observed in this spectral region.

Spectrally integrated PL intensities are plotted as a function of excitation laser intensity in Fig. 2.26(b). In a low excitation region below 10 pJ, the PL intensity grows almost linearly with excitation intensity (as indicated by a dotted line). Conversely,

Fig. 2.27 (a) Normalized PL spectra of a single SWNT on an expanded energy scale excited with different intensities. (b) Homogeneous linewidths as a function of excitation intensity. The *solid line* corresponds to the fitted curves considering exciton annihilation through the exciton-exciton scattering process (Reprinted with permission from [53]. Copyright, American Physical Society)



in the higher excitation intensity region (>20 pJ), saturation of the PL intensity is clearly apparent.

We show normalized PL spectra for a single SWNT, excited with different intensities, on an expanded energy scale in Fig. 2.27(a). The spectral linewidth broadens with increasing excitation intensity. The homogeneous linewidth is plotted in Fig. 2.27(b) as a function of excitation intensity, with the FWHM of the linewidth broadening nonlinearly. This broadening cannot be explained by laser heating effects because the nonlinear broadening behavior contradicts the linear temperature dependence of the linewidth broadening [see Fig. 2.25(b)]. This excitation intensity-dependent linewidth broadening indicates that the exciton dynamics are strongly affected by the multiple excitons present in a SWNT.

Under higher excitation conditions, when additional homogeneous linewidth broadening and saturation of the PL intensity occur, more than one exciton is created in a SWNT, leading to a remarkable scattering process between excitons. Exciton-exciton annihilation occurs due to the rapid Auger nonradiative recombination process through strong Coulomb interactions [66, 76, 77]. The exciton annihilation rate ($1/\tau_{ex-ex}$) is given by [66]

$$1/\tau_{ex-ex} = ALN(N - 1), \quad (2.14)$$

where A is the exciton annihilation (Auger) constant, L ($\approx 1 \mu\text{m}$) the length of the SWNT, and N the time-averaged exciton number. The exciton number should be a discrete value. However, the exciton number fluctuates at each single excitation event. Then, we might consider that the time-averaged exciton number N changes continuously in the analysis of the time-averaged PL data. Taking the radiative lifetime ($\tau_{rad} > 1 \text{ ns}$) and the nonradiative lifetime, due to the exciton trapping of the nonradiative centers ($\tau_{non-rad} \approx 40 \text{ ps}$) [64] into consideration, the PL intensity I_{PL} at the excitation power P is described by,

$$I_{PL} \propto \tau_{rad}^{-1} P / (\tau_{rad}^{-1} + \tau_{non-rad}^{-1} + \tau_{ex-ex}^{-1}). \quad (2.15)$$

The PL intensity saturation at higher excitation regions, as shown in Fig. 2.26(b), can be explained by the opening of the nonradiative relaxation path due to the exciton-exciton annihilation. The homogeneous linewidth Γ in Fig. 2.27(b) is determined by both the excitation power independent exciton-phonon interaction term Γ_{ex-ph} and the excitation power dependent Auger term $\Gamma_{ex-ex} (\propto 1/\tau_{ex-ex})$,

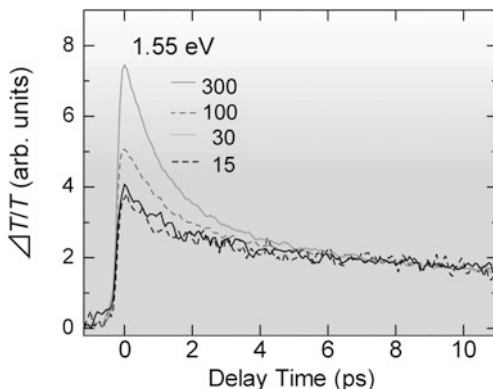
$$\Gamma = \Gamma_{ex-ph} + \Gamma_{ex-ex}. \quad (2.16)$$

The homogeneous linewidth broadening at higher excitation regions, as shown in Fig. 2.27(a), can be explained by the shortening of exciton lifetime due to the Auger process. The nonlinear behaviors of the PL intensity and the homogeneous linewidth broadening can be reproduced using Eqs. (2.14)–(2.16) as indicated by the solid lines in Figs. 2.26(b) and 2.27(b). The time-averaged exciton number N can be translated from the excitation intensity P at which the PL intensity saturates. The best fitted curves in Figs. 2.26(b) and 2.27(b) with varying the fitting parameter A reproduced the experimental results well. Then, the derived exciton-exciton annihilation constant A of $1.6 \text{ ps}^{-1} \mu\text{m}$ is almost consistent with the theoretically calculated value based on perturbation theory [66]. From this result, it was found that the multiparticle Auger process occurs very efficiently with an Auger recombination time estimated at 800 fs for $\approx 1 \mu\text{m}$ -long SWNT when two excitons are present in a SWNT. This very short time constant in comparison to bulk semiconductors, is characteristics of low-dimensional systems, including SWNTs and is comparable to the exciton-dephasing time at low temperature. These results indicate that the exciton dephasing is limited under high excitation conditions, not by the exciton-phonon interactions, but by the exciton-exciton interactions. As discussed above, the non-radiative Auger recombination process occurs efficiently at about 1 ps order. As a result, one of the two excitons nonradiatively relaxes in the ground state when two excitons are present in a SWNT. The exciton-exciton scattering rate in a SWNT is much higher than in other 1D semiconductors.

2.3.4 Multi-Exciton Generation in Carbon Nanotube

The strong enhancement of Coulomb interaction also would cause the many-body effects of excitons such as exciton multiplication (or carrier multiplication) process

Fig. 2.28 Transient absorption ($\Delta T/T$) dynamics under 1.55 eV excitation at different intensities of 15, 30, 100, and 300 $\mu\text{J}/\text{cm}^2$. Transient absorption decays with various excitation intensities normalized by the long decay component $t = 10$ ps (Reprinted with permission from [87]. Copyright, American Institute of Physics)



in SWNTs, where the exciton multiplication (or carrier multiplication) is the production process of two or more excitons (electron-hole pairs) by one high-energy photon well above the lowest exciton transition energy. In addition to the strong Coulomb interactions between excitons (carriers), the relaxation of momentum conservation in nanoscale space allows the observation of highly efficient exciton multiplication phenomena in a variety of nano-structures [78–82]. The achievement of efficient exciton multiplication in semiconductors makes it possible to produce highly efficient solar cells with conversion efficiencies that exceed the Shockley-Queisser limit of 32 % [83, 84]. Here, we describe exciton multiplication phenomena in CoMoCAT-SWNTs observed using femtosecond pump-probe spectroscopy.

Figure 2.28 shows the transient absorption decay monitored at E_{11} exciton absorption (1.2 eV) excited by 1.55 eV. It is clear that the temporal profile cannot be described by a single exponential function and that three exponential components (time constants of ≈ 1 ps, ≈ 30 ps, and ≈ 1 ns) appear. The decay times of ≈ 30 ps is consistent with those obtained using transient PL spectroscopy. These decays are determined by the trapping of excitons at defects of excitons in SWNTs. Hereafter, we focus on the transient absorption changes of the fast decay components on a picosecond time scale to clarify the exciton multiplication mechanism and fast Auger (exciton-exciton annihilation) nonradiative recombination.

Figure 2.28(a) shows the excitation intensity dependence of the transient absorption decay from 15 to 300 $\mu\text{J}/\text{cm}^2$ under 1.55 eV excitation. The observed signals correspond to absorption bleaching due to excitons in SWNTs. The decay profiles at longer delay times ($t > 10$ ps) does not depend on the excitation intensity. Then, all the data are normalized at 10 ps delay time, and the normalized signal curves provide clear information about the excitation intensity-dependence of the exciton population dynamics. The fast-decay component ($t < 5$ ps) grows at increasing excitation power densities, and this excitation dependent signal above 50 $\mu\text{J}/\text{cm}^2$ comes from the Auger (exciton-exciton annihilation) process on several picoseconds time-scale [85, 86].

Figure 2.29 shows the transient absorption dynamics under a weak excitation density at photon energies of 1.55, 3.10, and 4.65 eV, where all of the decay curves

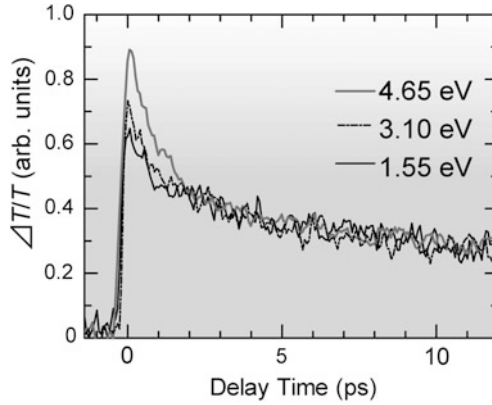


Fig. 2.29 Normalized transient absorption decays under the weak excitation regime with different excitation photon energies *black solid line*: 4.65 eV, *blue broken line*: 3.10 eV, and *red line*: 1.55 eV. This figure explains how to determine the exciton multiplication efficiency, η , which is calculated from the ratio of the transient absorption signals at zero delay (Reprinted with permission from [87]. Copyright, American Institute of Physics)

are normalized for a long time delay ($t = 10$ ps) [87]. We experimentally confirmed that in these weak intensity regions, the transient decay dynamics is independent of the excitation density. The fast-decay component due to Auger recombination does not appear in the decay curve under 1.55 and 3.10 eV excitation. Note that the decay dynamics under 4.65 eV excitation is faster than that under 1.55 eV excitation, and that the lifetime of the fast-decay component under 4.65 eV excitation is the same as the Auger recombination lifetime under intense 1.55 eV excitation. This experimental result indicates that Auger recombination occurs under 4.65 eV excitation, even in the weak-intensity region. Since the transient absorption signals of the Auger recombination process are a sign that more than two excitons are generated in a SWNT, we conclude that a single photon with an energy of 4.65 eV produces two or more excitons under weak excitation conditions, that is, exciton multiplication occurs in a SWNT [88, 89].

We can evaluate the exciton multiplication quantum efficiency (η), defined as the average number of excitons produced by one photon excitation, according to the procedures by Schaller *et al.* [89]. The $\Delta T/T$ signal amplitude is proportional to the number of excited excitons in the sample. In the ensemble experiment, the exciton density can be determined from signal amplitudes at zero delay in the time profiles normalized at a long delay time [89]. The intensity ratio of a/b at zero delay corresponds to η , where a and b are the amplitudes under 4.65 eV and 1.55 eV excitation at zero delay, respectively. In our experiment, η is estimated to be about 1.3 (130 %) under 4.65 eV excitation, while η is almost 1 within the experimental error at 3.10 eV excitation. This indicates that the novel photoelectric conversion process of exciton multiplication efficiently occurs in the SWNTs.

2.4 Summary

In this chapter, we described novel excitonic properties of carbon nanotubes revealed by single-nanotube spectroscopy and time-resolved spectroscopy. Due to the enhanced Coulomb interaction, the optically generated electron-hole pair forms a strongly bound “exciton” state, analogous to the hydrogen-like state in the carbon nanotubes. The striking properties of excitons in the carbon nanotube, such as multiple-exciton states, charged exciton (trion) formation, and exciton-multiplication were described in this chapter.

Multiple-exciton states, which affect the optical properties of carbon nanotubes, were attributed to spin degeneracy and the degenerate electronic structure of the K and K' valleys in momentum space. The singlet-bright exciton and -dark exciton, with a splitting on the order of a few meV, were revealed using the Aharonov-Bohm effect via low-temperature magneto-PL spectroscopy of a single SWNT. We identified the K -momentum dark exciton states lying approximately 40 meV above the singlet-bright exciton state from the temperature and tube-diameter dependences of the PL spectra of a single SWNT. The PL spectra showed large singlet-triplet exciton splitting, on the order of 70 meV, following pulsed-laser irradiation. We described the first observation of trions (charged excitons), three-particle bound states consisting of one electron and two holes, in hole-doped carbon nanotubes at room temperature. The unexpectedly large energy separation between the bright excitons and the trions is attributed to the strong electron-hole exchange interaction in carbon nanotubes.

The novel exciton dynamics in carbon nanotubes were revealed. We described that the very slow exciton relaxation from the bright to the dark state, and excitons are nonequilibriumly distributed between the bright and dark states due to the different parities of the wave functions. The radiative lifetimes and the 1D exciton coherence lengths in carbon nanotubes were evaluated. We found that the exciton coherence lengths in SWNTs are of the order of 10 nm, as deduced from the experimentally obtained radiative lifetimes, and they are about ten times larger than the exciton Bohr radius along the tube axis. We also observed novel exciton many body effects such as exciton (carrier) multiplication in carbon nanotubes at room temperature. These novel excitonic properties of carbon nanotube will also facilitate the future optical application based on carbon nanotubes.

References

1. S. Iijima, T. Ichihashi, *Nature (London)* **363**, 603 (1993)
2. R. Saito, G. Dresselhaus, M.S. Dresselhaus, *Physical Properties of Carbon Nanotubes* (Imperial College Press, London, 1998)
3. M.S. Dresselhaus, G. Dresselhaus, P. Avouris, *Carbon Nanotubes* (Springer, Berlin, 2001)
4. A. Jorio, G. Dresselhaus, M.S. Dresselhaus, *Carbon Nanotubes: Advanced Topics in the Synthesis, Structure, Properties, and Applications* (Springer, Berlin, 2008)
5. R. Saito, M. Fujita, G. Dresselhaus, M.S. Dresselhaus, *Appl. Phys. Lett.* **60**, 2204 (1992)

6. H. Kataura, Y. Kumazawa, Y. Maniwa, I. Umezu, S. Suzuki, Y. Ohtsuka, Y. Achiba, *Synth. Met.* **103**, 2555 (1999)
7. M.J. O'Connell, S.M. Bachilo, X.B. Huffman, V.C. Moore, M.S. Strano, E.H. Haroz, K.L. Rialon, P.J. Boul, W.H. Noon, C. Kittrell, J. Ma, R.H. Hauge, R.B. Weisman, R.E. Smalley, *Science* **297**, 593 (2002)
8. S.M. Bachilo, M.S. Strano, C. Kittrell, R.H. Hauge, R.E. Smalley, R.B. Weisman, *Science* **298**, 2361 (2002)
9. J. Lefebvre, Y. Homma, P. Finnie, *Phys. Rev. Lett.* **90**, 217401 (2003)
10. R.B. Weisman, S.M. Bachilo, *Nano Lett.* **3**, 1235 (2003)
11. T. Ando, *J. Phys. Soc. Jpn.* **66**, 1066 (1997)
12. C.L. Kane, E.J. Mele, *Phys. Rev. Lett.* **90**, 207401 (2003)
13. T.G. Pedersen, *Phys. Rev. B* **67**, 073401 (2003)
14. V. Perebeinos, J. Tersoff, Ph. Avouris, *Phys. Rev. Lett.* **92**, 257402 (2004)
15. H. Zhao, S. Mazumdar, *Phys. Rev. Lett.* **93**, 157402 (2004)
16. E. Chang, G. Bussi, A. Ruini, E. Molinari, *Phys. Rev. Lett.* **92**, 196401 (2004)
17. C.D. Spataru, S. Ismail-Beigi, R.B. Capaz, S.G. Louie, *Phys. Rev. Lett.* **95**, 247402 (2005)
18. F. Wang, G. Dukovic, L.E. Brus, T.F. Heinz, *Science* **308**, 838 (2005)
19. J. Maultzsch, R. Pomraenke, S. Reich, E. Chang, D. Prezzi, A. Ruini, E. Molinari, M.S. Strano, C. Thomsen, C. Lienau, *Phys. Rev. B* **72**, 241402(R) (2005)
20. G. Dukovic, F. Wang, D. Song, M.Y. Sfeir, T.F. Heinz, L.E. Brus, *Nano Lett.* **5**, 2314 (2005)
21. T. Ando, *J. Phys. Soc. Jpn.* **75**, 024707 (2006)
22. A. Hartschuh, H.N. Pedrosa, L. Novotny, T.D. Krauss, *Science* **301**, 1354 (2003)
23. J. Lefebvre, J.M. Fraser, P. Finnie, Y. Homma, *Phys. Rev. B* **69**, 075403 (2004)
24. K. Matsuda, Y. Kanemitsu, K. Irie, T. Saiki, T. Someya, Y. Miyauchi, S. Maruyama, *Appl. Phys. Lett.* **86**, 123116 (2005)
25. D.E. Milkie, C. Staii, S. Paulson, S. Paulson, E. Hindman, A.T. Johnson, J.M. Kikkawa, *Nano Lett.* **5**, 1135 (2005)
26. T. Inoue, K. Matsuda, Y. Murakami, S. Maruyama, Y. Kanemitsu, *Phys. Rev. B* **73**, 233401 (2006)
27. S. Maruyama, R. Kojima, Y. Miyauchi, S. Chiashi, M. Kohno, *Chem. Phys. Lett.* **360**, 229 (2002)
28. S. Zaric, G.N. Ostojic, J. Kono, J. Shaver, V.C. Moore, M.S. Strano, R.H. Hauge, R.E. Smalley, X. Wei, *Science* **304**, 1129 (2004)
29. S. Zaric, G.N. Ostojic, J. Shaver, J. Kono, O. Portugall, P.H. Frings, G.L.J.A. Rikken, M. Furis, S.A. Crooker, X. Wei, V.C. Moore, R.H. Hauge, R.E. Smalley, *Phys. Rev. Lett.* **96**, 016406 (2006)
30. J. Shaver, J. Kono, O. Portugall, V. Krstic, G.L.J.A. Rikken, Y. Miyauchi, S. Maruyama, V. Perebeinos, *Nano Lett.* **7**, 1851 (2007)
31. I.B. Mortimer, R.J. Nicholas, *Phys. Rev. Lett.* **98**, 027404 (2007)
32. R. Matsunaga, K. Matsuda, Y. Kanemitsu, *Phys. Rev. Lett.* **101**, 147404 (2008)
33. A. Srivastava, H. Htoon, V.I. Klimov, J. Kono, *Phys. Rev. Lett.* **101**, 087402 (2008)
34. K. Matsuda, T. Inoue, Y. Murakami, S. Maruyama, Y. Kanemitsu, *Phys. Rev. B* **77**, 033406 (2008)
35. K. Matsuda, T. Inoue, Y. Murakami, S. Maruyama, Y. Kanemitsu, *Phys. Rev. B* **77**, 193405 (2008)
36. K. Yoshikawa, R. Matsunaga, K. Matsuda, Y. Kanemitsu, *Appl. Phys. Lett.* **94**, 093109 (2009)
37. H. Ajiki, T. Ando, *J. Phys. Soc. Jpn.* **62**, 1255 (1993)
38. O. Kiowski, K. Arnold, S. Lebedkin, F. Henrich, M.M. Kappes, *Phys. Rev. Lett.* **99**, 237402 (2007)
39. O.N. Torrens, M. Zheng, J.M. Kikkawa, *Phys. Rev. Lett.* **101**, 157401 (2008)
40. Y. Murakami, B. Lu, S. Kazaoui, N. Minami, T. Okubo, S. Maruyama, *Phys. Rev. B* **79**, 195407 (2009)
41. H. Harutyunyan, T. Gokus, A.A. Green, M.C. Hersam, M. Allegrini, A. Hartschuh, *Nano Lett.* **9**, 2010 (2009)

42. K. Iakoubovskii, N. Minami, Y. Kim, K. Miyashita, S. Kazaoui, B. Nalini, *Appl. Phys. Lett.* **89**, 173108 (2006)
43. R. Matsunaga, K. Matsuda, Y. Kanemitsu, *Phys. Rev. B* **81**, 033401 (2010)
44. Y. Miyauchi, S. Maruyama, *Phys. Rev. B* **74**, 035415 (2006)
45. R.B. Capaz, C.D. Spataru, S. Ismail-Beigi, S.G. Louie, *Phys. Status Solidi (b)* **244**, 4016 (2007)
46. R.B. Capaz, C.D. Spataru, S. Ismail-Beigi, S.G. Louie, *Phys. Rev. B* **74**, 121401(R) (2006)
47. Y. Ohno, S. Iwasaki, Y. Murakami, S. Kishimoto, S. Maruyama, T. Mizutani, *Phys. Rev. B* **73**, 235427 (2006)
48. A.H. Castro Neto, F. Guinea, *Phys. Rev. Lett.* **103**, 026804 (2009)
49. K. Nagatsu, S. Chiashi, S. Konabe, Y. Homma, *Phys. Rev. Lett.* **105**, 157403 (2010)
50. S. Konabe, K. Watanabe, *Phys. Rev. B* **83**, 045407 (2011)
51. R. Matsunaga, K. Matsuda, Y. Kanemitsu, *Phys. Rev. Lett.* **106**, 037404 (2011)
52. Y. Miyauchi, H. Hirori, K. Matsuda, Y. Kanemitsu, *Phys. Rev. B* **80**, 081410(R) (2009)
53. K. Matsuda, Y. Miyauchi, T. Sakashita, Y. Kanemitsu, *Phys. Rev. B* **81**, 033409 (2010)
54. T.F. Rønnow, T.G. Pedersen, H.D. Cornean, *Phys. Lett. A* **373**, 1478 (2009)
55. T.F. Rønnow, T.G. Pedersen, H.D. Cornean, *Phys. Rev. B* **81**, 205446 (2010)
56. K. Watanabe, K. Asano, *Phys. Rev. B* **85**, 035416 (2012)
57. S.M. Santos, B. Yuma, S. Berciaud, J. Shaver, M. Gallart, P. Gilliot, L. Congnet, B. Lounis, *Phys. Rev. Lett.* **107**, 187401 (2011)
58. R. Matsunaga, Y. Miyauchi, K. Matsuda, Y. Kanemitsu, *Phys. Rev. B* **80**, 115436 (2009)
59. M. Nirmal, D.J. Norris, M. Kuno, M.G. Bawendi, A.L. Efros, M. Rosen, *Phys. Rev. Lett.* **75**, 3728 (1995)
60. A. Hagen, M. Steiner, M.B. Raschke, C. Lienau, T. Hertel, H. Qian, A.J. Meixner, A. Hartschuh, *Phys. Rev. Lett.* **95**, 197401 (2005)
61. V. Perebeinos, J. Tersoff, Ph. Avouris, *Nano Lett.* **5**, 2495 (2005)
62. J. Feldmann, G. Peter, E.O. Göbel, P. Dawson, K. Moore, C. Foxon, R.J. Elliott, *Phys. Rev. Lett.* **59**, 2337 (1987)
63. S. Lebedkin, F. Hennrich, O. Kiowski, M.M. Kappes, *Phys. Rev. B* **77**, 165429 (2008)
64. H. Hirori, K. Matsuda, Y. Miyauchi, S. Maruyama, Y. Kanemitsu, *Phys. Rev. Lett.* **97**, 257401 (2006)
65. Y. Miyauchi, K. Matsuda, Y. Kanemitsu, *Phys. Rev. B* **80**, 235433 (2009)
66. F. Wang, Y. Wu, M.S. Hybertsen, T.F. Heinz, *Phys. Rev. B* **73**, 245424 (2006)
67. S. Berciaud, L. Cognet, B. Lounis, *Phys. Rev. Lett.* **101**, 077402 (2008)
68. R.M. Russo, E.J. Mele, C.L. Kane, I.V. Rubtsov, M.J. Therien, D.E. Luzzi, *Phys. Rev. B* **74**, 041405(R) (2006)
69. S. Berger, C. Voisin, G. Cassabois, C. Delalande, P. Roussigno, *Nano Lett.* **7**, 398 (2007)
70. A. Grüneis, R. Saito, Ge.G. Samsonidze, T. Kimura, M.A. Pimenta, A. Jorio, A.G. Souza Filho, G. Dresselhaus, M.S. Dresselhaus, *Phys. Rev. B* **67**, 165402 (2003)
71. T. Takagahara, *Solid State Commun.* **78**, 279 (1991)
72. L. Cognet, D.A. Tsybouski, J.-D.R. Rocha, C.D. Doyle, J.M. Tour, R.B. Weisman, *Science* **316**, 1465 (2007)
73. K. Yoshikawa, K. Matsuda, Y. Kanemitsu, *J. Phys. Chem. C* **114**, 4353 (2010)
74. J. Lefebvre, P. Finnie, Y. Homma, *Phys. Rev. B* **70**, 045419 (2004)
75. A.V. Gopal, R. Kumar, A.S. Vengurlekar, T. Mélin, F. Laruelle, B. Etienne, *Appl. Phys. Lett.* **74**, 2474 (1999)
76. Y.-Z. Ma, L. Valkunas, S.L. Dexheimer, S.M. Bachilo, G.R. Fleming, *Phys. Rev. Lett.* **94**, 157402 (2005)
77. L. Huang, T.D. Krauss, *Phys. Rev. Lett.* **96**, 057407 (2006)
78. R.D. Schaller, V.I. Klimov, *Phys. Rev. Lett.* **92**, 186601 (2004)
79. R. Ellingson, M.C. Beard, J.C. Johnson, P. Yu, O.I. Micic, A.J. Nozik, A. Shabaev, A.L. Efros, *Nano Lett.* **5**, 865 (2005)
80. R.D. Schaller, M.A. Petruska, V.I. Klimov, *Appl. Phys. Lett.* **87**, 253102 (2005)

81. M.C. Beard, K.P. Knutsen, P. Yu, J.M. Luther, Q. Song, W.K. Metzger, R.J. Ellingson, A.J. Nozik, *Nano Lett.* **7**, 2506 (2007)
82. J.J.H. Pijpers, E. Hendry, M.T.W. Milder, R. Fanciulli, J.L. Herek, D. Vanmaekelbergh, S. Ruhman, D. Mocatta, D. Oron, A. Aharoni, U. Banin, M. Bonn, *J. Phys. Chem. C* **111**, 4146 (2007)
83. W. Shockley, H.J. Queisser, *J. Appl. Phys.* **32**, 510 (1961)
84. V.I. Klimov, *Appl. Phys. Lett.* **89**, 123118 (2006)
85. F. Wang, G. Dukovic, E. Knoesel, L.E. Brus, T.F. Heinz, *Phys. Rev. B* **70**, 241403(R) (2004)
86. L. Valkunas, Y.-Z. Ma, G.R. Fleming, *Phys. Rev. B* **73**, 115432 (2006)
87. A. Ueda, K. Matsuda, T. Tayagaki, Y. Kanemitsu, *Appl. Phys. Lett.* **92**, 233105 (2008)
88. S. Wang, M. Khafizov, X.M. Tu, M. Zheng, T.D. Krauss, *Nano Lett.* **10**, 2381 (2010)
89. R.D. Schaller, M. Sykora, S. Jeong, V.I. Klimov, *J. Phys. Chem. B* **110**, 25332 (2006)

Chapter 3

Fabrication of Ultrahigh-Density Self-assembled InAs Quantum Dots by Strain Compensation

Kouichi Akahane

Abstract A fabrication method of semiconductor quantum dots (QDs), which is an important fundamental technology for realizing high-performance QD optical devices, is discussed in this chapter. In the first section, we introduce self-assembly of InAs QDs based on the Stranski-Krastanov growth mode. In the second section, we discuss the fabrication of ultrahigh-density QDs by a strain compensation technique. Finally, we present applications using the ultrahigh-density QDs, in particular, various unique properties of a highly stacked InAs QD laser diode.

3.1 Semiconductor Quantum Dot

A semiconductor quantum dot (QD) is a three-dimensional nanoscale structure that confines electrons and holes. Structures that can restrict the spatial degrees of freedom of electrons and other particles are referred to as quantum structures. When the restricted spatial degrees of freedom are one-dimensional, two-dimensional, and three-dimensional, the structures are referred to as a quantum well (QW), quantum wire (QWr), and QD, respectively. As shown in Fig. 3.1, the density of states of these quantum structures—in other words, the number of states at a certain energy—changes from a parabolic shape for the bulk structure to a step shape (QW), sawtooth shape (QWr), or delta function shape (QD). Accordingly, the light absorption and emission behaviors are considered to change sequentially, which is expected to induce a change in the optical response. In QDs, the carriers are concentrated at a certain energy value, theoretically yielding laser diodes (LDs) with extremely low thresholds. Moreover, the temperature dependence of the threshold current disappears when QDs are used in semiconductor lasers; this characteristic can be attributed to the change in the density of states of QDs. In other words, the density of states changes continuously in a bulk material or in a QW structure. (The density of states of a QW changes stepwise at certain energy values but maintains a

K. Akahane (✉)

National Institute of Information and Communications Technology, 4-2-1, Nukui-Kitamachi, Koganei, Tokyo 184-8795, Japan
e-mail: akahane@nict.go.jp

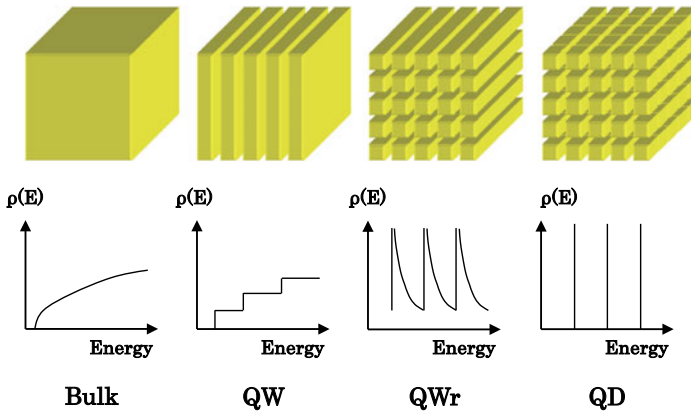


Fig. 3.1 Changes in density of states associated with decreases in structure dimensionality

constant value at others.) Therefore, when the device temperature increases, the injected carriers are redistributed, and the carrier density—which contributes to laser oscillation—decreases. As a result, new carriers need to be injected for laser oscillation. Therefore, the threshold current required for laser oscillation generally tends to increase as the temperature increases. On the other hand, a QD laser features a delta-function-like density of states; therefore, only discrete values are allowed to represent the carrier energy, even if the carriers attempt to redistribute themselves when the temperature increases. In other words, carrier redistribution is suppressed. This suppression maintains the density of carriers associated with a certain energy value before and after the temperature increases, which suppresses the increase in the threshold current that would otherwise result from the increase in temperature. Therefore, we can create a situation in an ideal QD laser in which the threshold current is completely independent of the temperature [1]. Ideal QDs are certainly difficult to fabricate and we have not yet produced a laser with a threshold current that is completely independent of temperature. Nevertheless, among the semiconductor lasers available today, a QD laser has the least temperature dependence on the threshold current. When we use QDs, we can implement a high-performance semiconductor laser that does not require a cooling mechanism, whereby the configuration of optical communication systems can be made simple and inexpensive.

Further, there are high expectations for the application of semiconductor QDs in future technologies such as quantum information processing and quantum communication. As discussed before, QDs have a three-dimensional confinement structure, and many research groups worldwide are now attempting to perform quantum information processing by using confined excitons—combined states of electrons and holes—in this confinement structure and by applying coherent control to the excitons. Attempts are also underway to apply QDs to interception-free quantum communication by controlling each of the photons generated by QDs [2]. The advantage of implementing these processes with semiconductor QDs is that such advances will enable the production of smaller devices compared to other methods. In

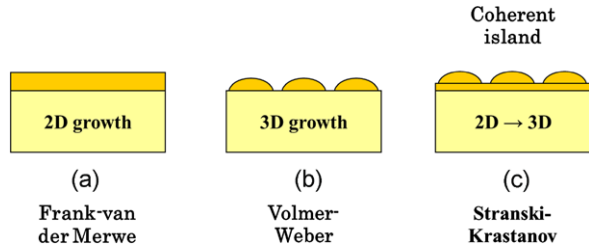
addition, applying the peculiar interaction of the optical near field is expected to enable the fabrication of a new type of photonic device with low power consumption because the QD size is less than the wavelength of light. In this chapter, we discuss the fabrication method of semiconductor QDs, which is an important fundamental technology for realizing high-performance QD optical devices. In the first section, we introduce a self-assembled QD. In the second section, we discuss the fabrication of ultrahigh-density QDs. In the third section, we present applications using ultrahigh-density QDs.

3.1.1 Self-assembled Semiconductor Quantum Dot

Quantum structures, including QDs, can be fabricated by manipulating energy band gaps in semiconductors. Specifically, by fabricating a structure in which a material with a larger energy gap surrounds a material with a smaller energy gap, electrons and holes are confined in the material with the smaller energy gap. However, to obtain sufficient quantum effects, these structures must be on the order of several tens of nanometers or even smaller. We require extremely precise techniques to fabricate arbitrary nanostructures. Recently, advanced semiconductor crystal growth technology has yielded a mature technology for fabricating semiconductor films at a precision of 1 nm or less on the basis of molecular beam epitaxy (MBE) and other techniques. Therefore, we can easily fabricate QWs, the one-dimensional carrier confinement structure. These QWs can be fabricated by precisely controlling the growth rate and growth time in semiconductor crystal growth. This technique has led to the realization of semiconductor lasers that operate at room temperature; these have been applied to various devices, including those aimed at many applications.

In contrast to the thin-film deposition technology for fabricating QWs, QD fabrication is more difficult. Because QDs require a confinement structure in all three dimensions, we now require a structure fabrication technology that can allow processes on the order of several tens of nanometers or less along directions parallel to the surface. The first attempt at fabricating QDs involved the formation of a QW, patterning of the well with electron-beam lithography equipment, and etching of the pattern. However, this top-down method cannot yield high-quality QDs because it damages the sample during etching; additionally, it cannot yield high-density QDs. In the early 1990s, a new method of QD fabrication was invented that makes use of the self-assembling nature of semiconductor crystal growth. In crystal growth in a lattice-mismatched material system, structures are self-assembled at sizes on the order of several tens of nanometers along directions parallel to the surface. The QDs obtained in this manner are referred to as self-assembled QDs [3]. Normally, in the crystal growth of a lattice-mismatched material system, defects and dislocations are formed to relax the strain energy of the growth film when the film cannot withstand the lattice strain. (When the lattice mismatch is large, three-dimensional growth, or the Volmer-Weber growth mode, occurs from the beginning, as shown in Fig. 3.2(b).) The crystal quality deteriorates because of defects and dislocations,

Fig. 3.2 Three different growth modes arise because of lattice mismatches between the underlying matrix material and the epitaxial layer

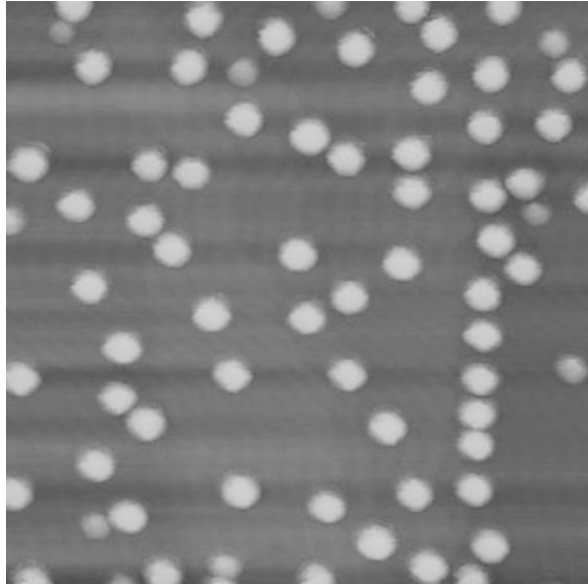


so materials with low lattice mismatching are generally selected for semiconductor crystal growth (that is, layer-by-layer growth, or the Frank-van der Merwe growth mode, as shown in Fig. 3.2(a), in which the lattice mismatch is small). In contrast, self-assembled QDs make favorable use of this strain in a lattice-mismatched system.

One of the most popular material systems for self-assembled QDs consists of a combination of GaAs and InAs. In this combination, InAs forms the QDs. GaAs and InAs have lattice constants of 5.653 Å and 6.058 Å, respectively, and the lattice mismatch between them is approximately 7%. When InAs is grown on GaAs, InAs first grows two-dimensionally and proceeds to three-dimensional growth when the layer exceeds approximately 1.5 monolayers (MLs; one ML corresponds to half the lattice constant). This type of growth mode is referred to as the Stranski-Krastanov mode (S-K mode) and is illustrated in Fig. 3.2(c) [4]. This three-dimensional growth forms InAs island structures (InAs QDs) on the sample surface, each with a diameter of approximately several tens of nanometers. When InAs is grown without interruption, defects and dislocations are formed in the crystal, as discussed earlier, and the crystal quality deteriorates. However, defects and dislocations do not arise just after the InAs QDs form; if the growth of InAs is stopped after the appropriate amount of growth and the sample is embedded in GaAs (or another material with a larger band gap than InAs), InAs QDs can be successfully produced.

As an example, Fig. 3.3 shows an atomic force microscopy (AFM) image of self-assembled InAs QDs fabricated on GaAs by MBE in our groups facilities. The fabrication procedure is as follows. First, the GaAs substrate was thermally cleaned by holding it in a growth chamber at 610 °C. After cleaning, a 150-nm-thick GaAs buffer layer was grown at a rate of 1 ML/s at 580 °C. A 2-ML InAs layer was then grown at 0.04 ML/s to fabricate the self-assembled QDs. In this sample, QDs with an average diameter of 40 nm, average height of 9 nm, and density of $2.5 \times 10^{10}/\text{cm}^2$ were obtained. The self-assembly method yields high-quality QDs without damage, as the process is completely vacuum-based; additionally, the obtained QDs exhibit a higher density than that obtained from top-down fabrication. Diverse applications using this type of QD are now under development. Among these, their use in optical communication devices is just a step away from practical application. In particular, a QD laser in the 1.3 μm band and a QD semiconductor optical amplifier (SOA) operate at a lower threshold current, depend less on temperature, and offer better high-speed signal processing performance than lasers and optical amplifiers based on QWs [5–12].

Fig. 3.3 AFM image of self-assembled InAs QDs grown on GaAs substrate (500 nm \times 500 nm)



3.1.2 Fabrication of Ultrahigh-Density QDs Using Strain-Compensation Technique

In this section, we discuss the fabrication of high-density self-assembled QDs. In an LD or SOA, QDs function as the gain medium; therefore, a method of fabricating denser QDs represents a key technology for improving device performance. However, even when simply considering how to increase the in-plane density, spatial limitations are encountered. For example, assuming that we can fabricate QDs with a diameter of 20 nm in a closely packed structure (Fig. 3.4), the surface density is limited to approximately $3 \times 10^{11}/\text{cm}^2$. Further, it is difficult to fabricate such a structure. To achieve a denser QD structure, layers comprising QDs can be stacked. However, QD fabrication based on the S-K mode uses the strain energy of a lattice-mismatched material system as the driving force in QD formation. Hence, when the density of QDs is to be increased by stacking, strain accumulation becomes problematic. This accumulation may lead to problems such as changes in the size and shape of the QDs; further, an excessive accumulation of strain generates defects and dislocations. Therefore, the number of stacked layers is generally limited to 10 or fewer.

To resolve this problem, we developed a strain compensation method of stacking that enables the stacking of multilayer QDs. Figure 3.5 shows a schematic diagram of this method. We used an InP(311)B substrate for fabricating the QDs. We used InP(311)B because, when InAs is grown on an InP(001) substrate using conventional MBE, quantum wire structures are formed along the [1-10] direction [13, 14]. As shown in Table 3.1, the lattice constant of InP is between that of GaAs or AlAs and InAs; as a result, various material systems can be grown on an InP substrate. In

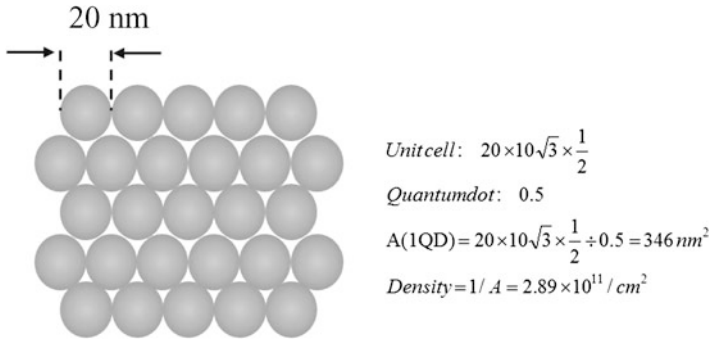
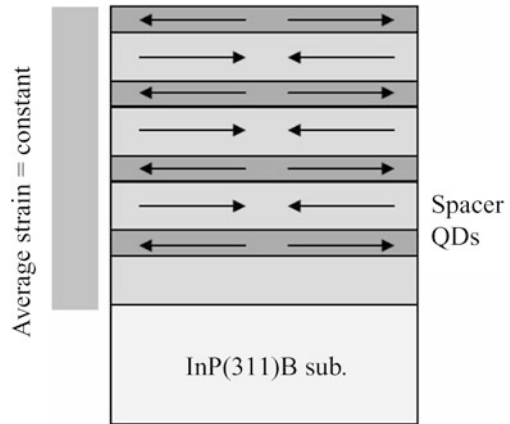


Fig. 3.4 Estimation of density limit when QDs are formed in a closely packed structure

Fig. 3.5 Schematic diagram of strain compensation



this study, we devised a structure in which InAs QDs fabricated on InP are embedded in InGaAlAs, which has a slightly smaller lattice constant than InP. In this manner, the tensile strain generated in InAs is compensated by the compressive strain in InGaAlAs, which solves the problem of accumulated strain energy when fabricating the stacked structure. We determined the conditions for strain compensation using the following equations:

$$d_{\text{QD}} \cdot \varepsilon_{\text{QD}} = -d_s \cdot \varepsilon_s$$

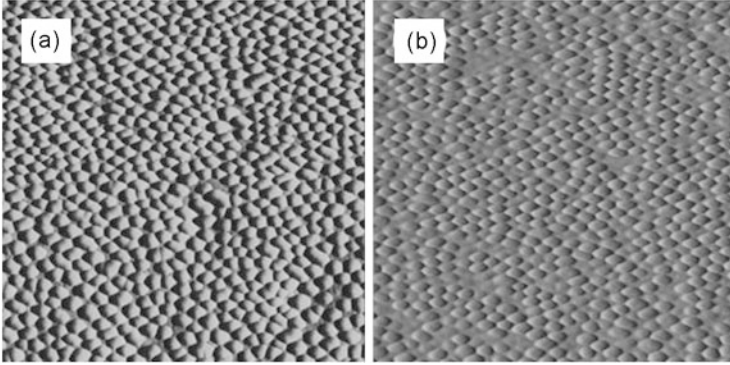
$$\varepsilon_{\text{QD}} = (a_{\text{InAs}} - a_{\text{InP}}) / a_{\text{InP}}$$

$$\varepsilon_s = (a_s - a_{\text{InP}}) / a_{\text{InP}}$$

where d_{QD} and d_s are the film thicknesses of the QD layer and strain compensation layer, respectively. Further, a_{InAs} , a_{InP} , and a_s are the lattice constants of the InAs, InP, and InGaAlAs strain compensation layers, respectively; ε_{QD} and ε_s are the strain with respect to the InP substrate in the InAs QDs and strain compensation layer, respectively. The sample was prepared as follows. The InP(311)B substrate was placed in an MBE growth chamber and thermally cleaned at 500 °C for 10 min

Table 3.1 Lattice constants of AlAs, GaAs, InP, and InAs

Material	AlAs	GaAs	InP	InAs
Lattice constant (\AA)	5.661	5.6533	5.8687	6.0583

**Fig. 3.6** Comparison of QD shapes associated with stacking: (a) single layer and (b) 20-layer stack of InAs QDs on InP ($1 \mu\text{m} \times 1 \mu\text{m}$)

to produce a clean surface. Then, a 150-nm-thick lattice-matched InAlAs buffer layer was grown. Finally, the InAs QDs and InGaAlAs strain-compensation layer were grown alternately, yielding the stacked structure.

First, to verify the effect of strain compensation, the stacked InAs QD structure was fabricated on the InP(311)B substrate. To illustrate the shapes associated with stacking, Fig. 3.6 shows AFM images of single-layer and 20-layer QDs grown on InP for comparison. Figure 3.7 shows AFM surface images of (a) single-layer, (b) 30-layer, (c) 100-layer, and (d) 150-layer stacks of InAs QDs grown on the InP(311)B substrate. We successfully increased the number of stacked QD layers to 150 without surface morphology degradation by accurately controlling the strain compensation conditions. Using this method, we can progressively increase the number of stacked layers as long as the strain compensation condition is satisfied. These results clearly indicate that strain compensation plays an important role in stacking multilayer QDs. Because the QD distribution is more uniform than that without strain compensation, we may further conclude that this method also suppresses the formation of defects and dislocations. It is also known that adding Al to the strain compensation layers suppresses In surface segregation. Therefore, it is important to use InGaAlAs, which contains Al, in the intermediate layers in order to form a uniformly stacked structure of QD layers [15].

Figure 3.8 shows the dependence of the size and density of the QDs on the number of stacked layers. The diameter, height, and density of the QDs remain almost constant regardless of the number of stacked layers, which indicates the effectiveness of the strain compensation method in fabricating a stacked structure. To confirm the absence of dislocations, we also observed a sample cross section with scanning transmission electron microscopy (STEM); Fig. 3.9 shows the results. In this

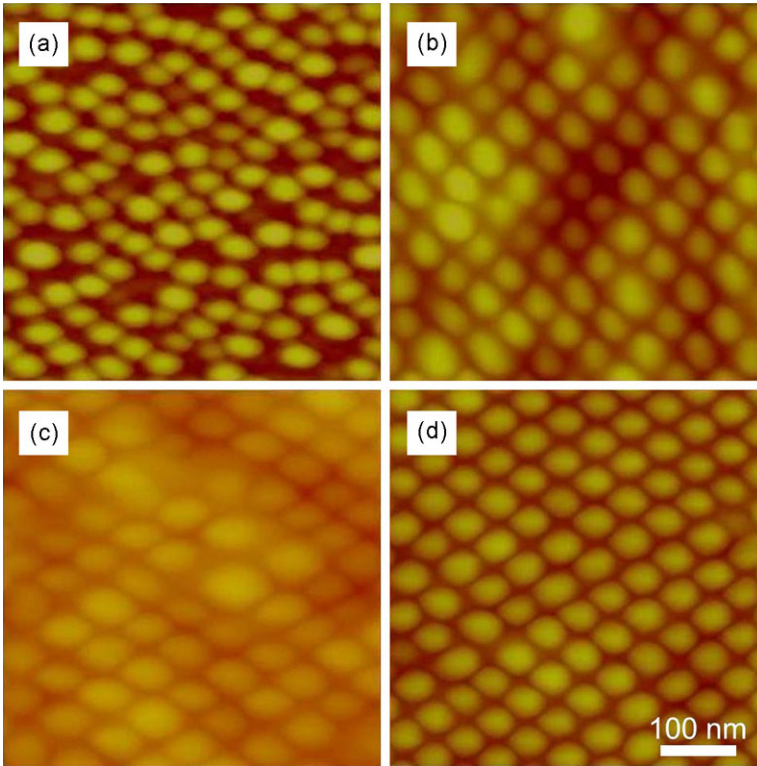


Fig. 3.7 AFM surface images of (a) single-layer, (b) 30-layer, (c) 100-layer, and (d) 150-layer stacks of InAs QDs grown on the InP(311)B substrate

sample, 150 layers are stacked with 20-nm InGaAlAs strain compensation layers, as shown in Fig. 3.7(d). Uniform QDs formed on the sample surface and cross-sectional STEM measurements did not indicate the formation of dislocations. Thus, it is clear that the creation of a stacked structure with strain compensation not only maintains the uniformity of the QDs but also suppresses the formation of dislocations, yielding high-quality QDs. The advantage of fabricating stacked structures using the strain compensation method is that the number of stacked layers is, in principle, unlimited as long as the strain compensation condition is satisfied. Hence, stacking can be repeated many times, enabling the fabrication of extremely dense QDs. If we can optimize the strain compensation condition, there should be no limit on the number of stacked layers. We investigated an increased number of layers and were able to fabricate a 300-layer InAs QD stack, as shown in the AFM image in the inset of Fig. 3.10. The QD arrays are uniform in size, and the surface morphology is not degraded. The total density of the QDs in this sample was more than $1.9 \times 10^{13}/\text{cm}^2$, which could not have been achieved using conventional QD self-assembly.

Fig. 3.8 Dependence of diameter, height, and density of QDs on the number of stacked layers

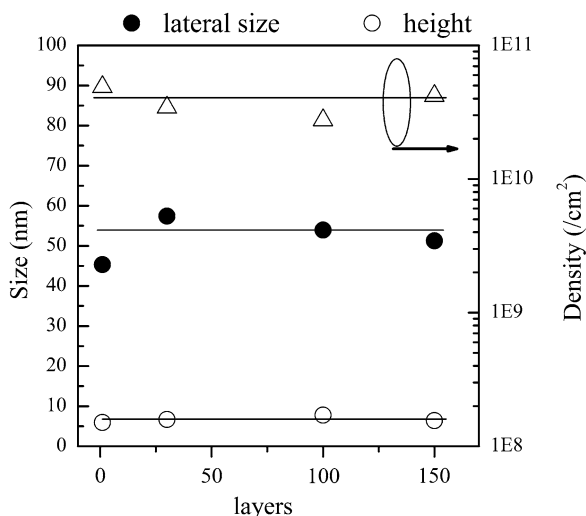


Fig. 3.9 Cross-sectional STEM image of a 150-layer stacked structure. *Inset:* Magnified pictures of vertically aligned QDs

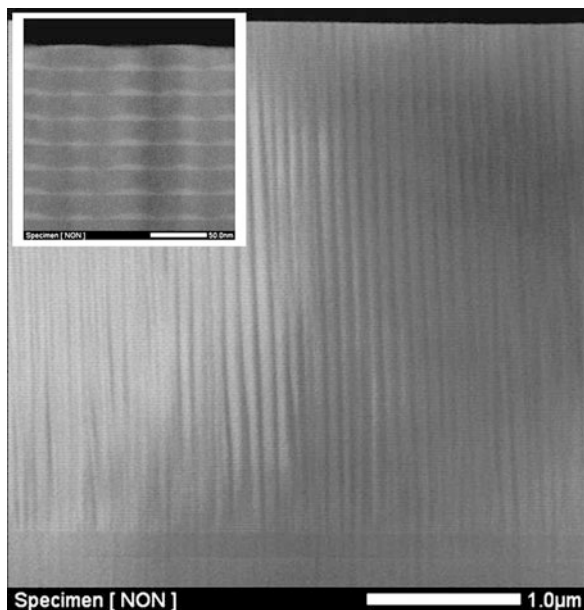


Figure 3.11 shows a two-dimensional fast Fourier transform (2DFFT) of the AFM image of a 150-layer stack (inset). Sharp sixfold peaks and several higher-order satellite peaks appear. This indicates that the lateral ordering of the QDs in this sample is well defined. The symmetry of the 2DFFT shows that the QDs were formed in a closely packed structure. Although the tendency to form an ordered structure is based on the properties of the (311)B surface [16, 17], the formation of the QD array as the number of stacked layers increases is probably due to the re-

Fig. 3.10 AFM image of 300th layer of InAs stack ($1\ \mu\text{m} \times 1\ \mu\text{m}$)

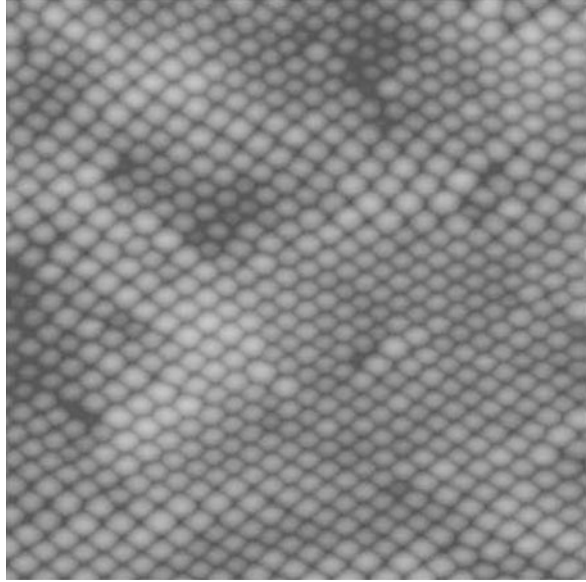
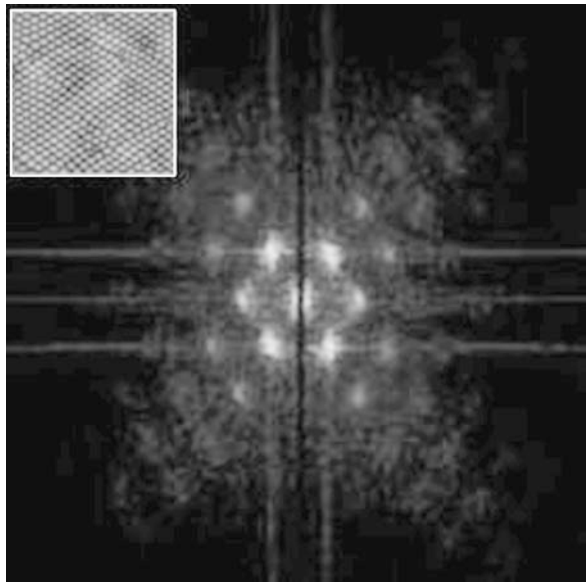
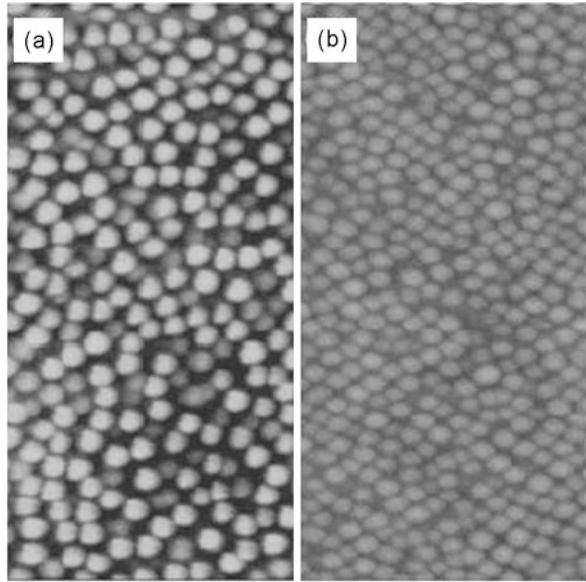


Fig. 3.11 Two-dimensional fast Fourier transform (2DFFT) of topographic image of a stack of 150 InAs QD layers



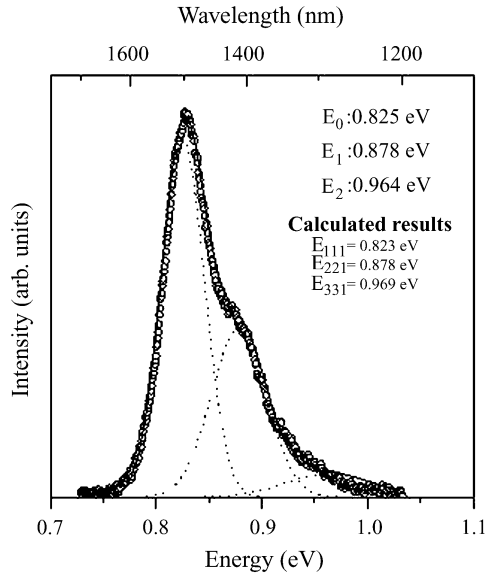
distribution of strain after the formation of each strain compensation layer. In other words, although the strain energy is counterbalanced and prevented from accumulating in the material system as a whole, a nonuniform strain is distributed on the sample surface after the growth of a strain compensation layer because of variations in the positions of the embedded QDs. The lattice constant is slightly larger di-

Fig. 3.12 Stacked 150-layer structure based on (a) 10-nm spacer layer and (b) 60-nm spacer layer ($1\ \mu\text{m} \times 0.5\ \mu\text{m}$)



rectly above the QDs, yielding dominant sites for the generation of QDs in the next layer. This phenomenon can also be confirmed in a cross-sectional STEM measurement, which shows that the QDs in the next layer are formed above the QDs of the lower layer. Because the strain compensation condition is necessarily satisfied, the lattice constant is slightly smaller at positions other than those directly above the QDs, compensating for the tensile and compressive strains in the entire system. With regard to a single QD, it is evident that a QD in a higher layer is formed above that in the lower layer, continuing the morphology of the first layer. However, the fact that array formation is promoted as the number of stacking layers increases indicates that the strain distribution formed on the spacer layer is due to the strain interactions involving the QDs in the nearby area, as well as the QDs directly below. Thus, the formation of a strain field involving multiple dots is important in the formation of QD arrays. It is easily deduced that the propagation of the strain field depends strongly on the thickness of the intermediate layer. In other words, thinner intermediate layers are more likely to facilitate QD production directly below the surrounding QDs, so the system will preserve the morphology of the first layer uninterrupted. Thicker intermediate layers involve an extremely large number of QDs in the generation of the strain field; therefore, the strain field is averaged, and the QD array may disappear. Note also that the (311)B substrate surface tends to cause the formation of QD arrays [16, 17]. This is also considered to lend additional support to the formation of a QD array structure. These phenomena have been well studied with respect to the PbSe/PbEuTe material system [18]. To investigate this topic, we also fabricated samples stacked with 150 layers including 10- or 60-nm strain compensation layers. Figures 3.12(a) and (b) show AFM images of the samples with the 10- and 60-nm strain compensation layers, respectively. As expected, the array

Fig. 3.13 PL spectrum of a 150-layer stacked structure



structure eventually dissipates with both thick and thin strain compensation layers. Thus, controlling the film thickness of the strain compensation layer is clearly an important element of QD array formation. As discussed at the outset, QDs have discrete energy levels with a delta-function-like density of states. Because the energy can be manipulated, QDs are sometimes likened to artificial atoms. By fabricating a three-dimensional array structure of QDs based on stacked QDs, we can obtain an array structure of artificial atoms—in other words, artificial crystals. Here, we consider that the following three factors will be of particular importance: stacking based on strain compensation, QD array formation based on thickness control of the intermediate layers, and control of coupled states between the QD layers.

Next, we discuss the optical properties of the stacked QDs. Strain compensation layers of 20 nm were used, and the photoluminescence (PL) of a sample consisting of 150 stacked layers was measured at room temperature. To excite the sample, the 532-nm second harmonic of a diode-pumped Nd:YVO-laser was used. A 250-mm monochromator and an electrically cooled PbS photodetector were used for spectroscopy and detection of the emitted light, respectively. Figure 3.13 shows the measurement results. The figure shows strong emission even at room temperature. These results also demonstrate the effectiveness of dislocation suppression by strain compensation and emission intensity enhancement due to the increased density. The PL spectrum has a main peak near approximately 1.5 μm and a shoulder structure on the higher-energy side. A simple calculation of quantum levels indicates that these peaks agree with the energy levels of the ground state, first excited state, and second excited state of the QDs. The corresponding values are indicated in the figure. The full width at half-maximum (FWHM) value of the ground state is approximately 40 meV. The emission wavelength of this sample corresponds to that used in fiber optic communication, and this material can be expected to be applied in

QD lasers and SOAs. The density of QDs is particularly important in these applications because it is the source of the gain. Thus, the technology used to fabricate high-density QDs in the present study has the potential to significantly improve the performance of conventional semiconductor devices. Further, InAs QDs on GaAs are subject to large compressive stress caused by the GaAs, resulting in the formation of a large band gap and a problematic restriction of emission to the 1- μm band. However, because the InP substrate has a larger lattice constant than GaAs, the compressive stress applied to InAs on an InP substrate is smaller; accordingly, we have obtained emission from the InAs QDs at the fiber optic communication wavelength. These emission characteristics can be modified by changing the volume of the InAs QDs and the barrier heights of the intermediate layers. If we combine QDs with various emission wavelengths and increase the density while satisfying the strain compensation condition, we believe it will be possible to produce SOAs with higher efficiency and broader bandwidth than those available with current products.

3.1.3 Applications Using Ultrahigh-Density QDs

Semiconductor QDs grown by self-assembly techniques in the S-K mode are expected to be used in high-performance optical devices such as QD lasers. There has been great deal of research into the development of high-performance QD lasers with characteristics such as low threshold current, temperature stability, high modulation bandwidth, and low chirp [1, 6–12, 19]. The problem with such devices is that the low number of QDs on the surface (i.e., the low surface density) causes undesirable excited-state lasing at high currents or high temperatures [6, 7, 19]. This problem can be overcome by increasing the surface density, which can be achieved by fabricating a stacked QD structure. However, in the usual stacking technique, the accumulation of strain is a problem because it limits the number of layers that can be stacked. It is difficult to overcome this problem in self-assembled QDs because strain is the main driving force for the formation of three-dimensional islands in the S-K growth mode. Therefore, the number of stacked layers in a QD laser is usually less than 10. Furthermore, Ishida et al. reported that the actual QD surface density required for high-speed direct modulation of a QD laser should be high [10].

Section 2 presented a growth technique of stacked QD layers in which InAs QDs are grown on an InP(311)B substrate under a strain compensation scheme, and spacer layers having a slightly smaller lattice constant than the substrate are used to embed the QD layers. Using this method, we successfully stacked 300 InAs QD layers without degradation of the QD quality, and we believe that there is no limit on the number of QD layers that can be stacked [20, 21]. This means that we can optimize the number of QD layers depending on the application. In this section, we describe the fabrication of a QD laser consisting of highly stacked QD layers using our strain compensation technique. The fabricated laser in this work had a stacked InAs QD structure containing up to 30 layers, and it showed ground-state laser emissions of around 1.55 μm , which is suitable for fiber optic communications systems.

All samples were also fabricated using conventional solid-source MBE. We fabricated the QD stacked structures on an InP(311)B substrate. In stacked In(Ga)As/GaAs QD structures, which are commonly used to fabricate QD lasers, the strain generated by QD growth cannot be compensated for completely after the growth of the GaAs spacer layer because the lattice constant of the GaAs spacer layer is identical to that of the substrate. This residual strain affects the formation of QDs in the next stacked layer. In addition, the average strain energy becomes high as the number of stacked layers increases, leading to the formation of defects and dislocations.

A laser structure was fabricated as a simple broad-area stripe structure. First, a buffer layer comprising a 150-nm-thick layer of lattice-matched Si-doped n-type $\text{In}_{0.52}\text{Al}_{0.48}\text{As}$ was grown. Thereafter, we consecutively grew stacks of three MLs of InAs QDs separated by 15-nm-thick $\text{In}_{0.49}\text{Ga}_{0.26}\text{Al}_{0.25}\text{As}$ spacer layers. This cycle was carried out 30 times; the Al atoms in the spacer layers prevented the segregation of In atoms and enabled the growth of high-quality spacer layers of uniform composition [15]. Then a 2000-nm-thick lattice-matched Be-doped p-type InAlAs cladding layer and a p-type InGaAs contact layer were grown. All layers were grown at 470 °C. We determined the density of the QDs in the sample without the cladding layer by AFM. The images revealed an increase in the total density of the stacked QDs to $1.02 \times 10^{12}/\text{cm}^2$ (the integrated density of the stacked structure). Such an increase cannot be achieved using the conventional method of QD stacking. Therefore, we think that this laser achieves sufficient gain for ground-state lasing. The average lateral size and height of the QDs are 66 nm and 7.5 nm, respectively. Then, 50- μm -wide Ti/Pt/Au p-contact electrodes were fabricated by a conventional photolithography lift-off process. A SiO_2 film to separate the InGaAs contact layer from the probe electrode was deposited by tetraethyl orthosilicate tetraethoxysilane chemical vapor deposition. After a Ti/Pt/Au n-contact electrode was deposited, the sample was cleaved to form cavities ranging in length from 600 to 1400 μm , and the cleaved facets were used as cavity mirrors. The light output versus injected current ($L-I$) characteristics were measured using an LD tester (AT-143; Yuasa Electronics), and the laser and electroluminescence (EL) spectra were studied using an optical spectrum analyzer (AQ6370; Yokogawa Electric Corporation).

Figure 3.14 shows a plot of the output power from one facet versus the current for a QD laser with a cavity length of 600 μm . The laser was operated in pulsed mode (1- μs pulses, 1 % duty cycle) at room temperature. The threshold current for this laser (I_{th}) is 517.5 mA, which corresponds to a threshold current density of 1725 A/cm². After lasing, the output power appeared to be proportional to the input current, and no kinks were observed. Because 30 InAs QD layers are stacked in this laser structure, the threshold current density per QD layer is only 57 A/cm². The slope efficiency from the $L-I$ plot for one facet is 0.052 W/A. Figure 3.15 shows the spectra before (dotted line) and after (solid line) lasing. The EL spectrum was measured at 500 mA. This spectrum shows a peak at 1526 nm with an FWHM of 30 meV; this spectrum is very similar to the PL spectrum (1524 nm) measured for the sample without the cladding layer. Therefore, the changes in the size and shape of the QDs that occur after growth can be ignored in our laser process. The lasing spectrum was measured at 596 mA.

Fig. 3.14 $L-I$ characteristics of laser comprising 30 InAs QD layers in pulsed mode. The threshold current obtained for this laser was 517.5 mA

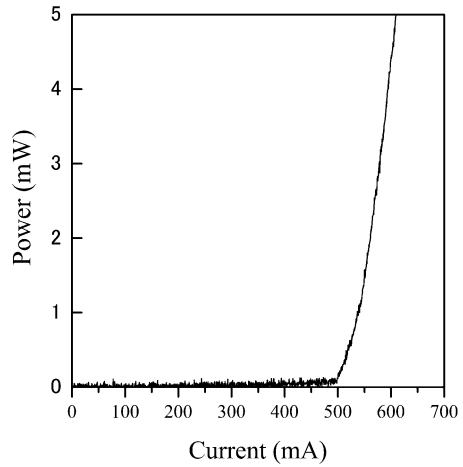


Fig. 3.15 EL and lasing spectra. Ground-state lasing was observed at 1529 nm

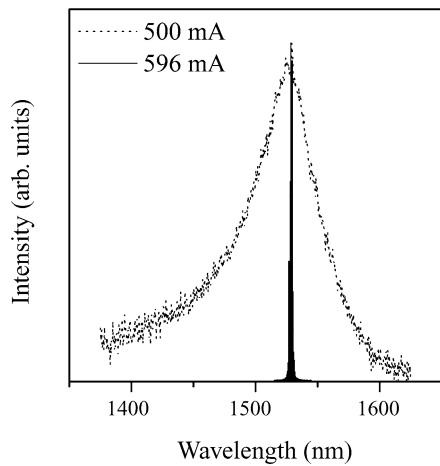


Figure 3.16 shows a magnified spectrum around the lasing wavelength, which is approximately 1529 nm. This is longer than that of the EL and PL peaks. The first excited state emission appeared at 1466 nm in the PL measurement. Therefore, this 1529-nm emission corresponds to ground-state lasing of the QDs. The periodical peaks show laser cavity mode. Our laser uses a strain compensation stack, so it has a high density of QDs. Owing to this high density, the laser has sufficient gain for ground-state lasing. Hence, excited-state lasing is suppressed, despite the short cavity length of the laser. Short-cavity lasers have advantages such as operation as a high-repetition-rate mode-locked laser.

Fig. 3.16 Magnified spectrum around the lasing wavelength of the QD laser, which is approximately 1529 nm

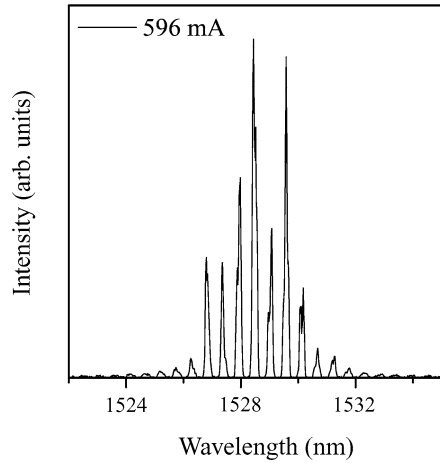


Fig. 3.17 Relationship between η_d and L . The internal optical loss (α_i) and internal quantum efficiency (η_i) are 43 % and 26.6 cm^{-1} , respectively

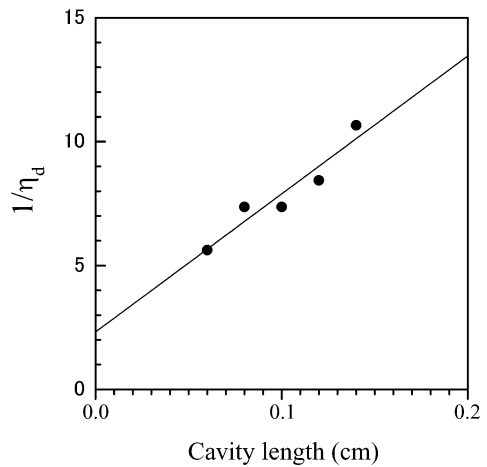


Figure 3.17 shows the relationship between the reciprocal of the external quantum efficiency (η_d) and the cavity length (L). The internal optical loss (α_i) and internal quantum efficiency (η_i) were determined on the basis of the relationship

$$\frac{1}{\eta_d} = \frac{1}{\eta_i} \left(\frac{\alpha_i L}{\ln\left(\frac{1}{R}\right)} + 1 \right)$$

where R denotes the reflectivity of the cavity mirror. The values of η_i and α_i are 43 % and 26.6 cm^{-1} , respectively. The large α_i value is attributed to the low optical confinement between the InGaAlAs waveguide layer and the InAlAs cladding layer, whose refractive indices differ slightly. In addition, the optimization of the number of stacked layers is important and should be investigated in the near future because excessive QD layers act as a loss.

Fig. 3.18 Temperature dependence of $L-I$ characteristics

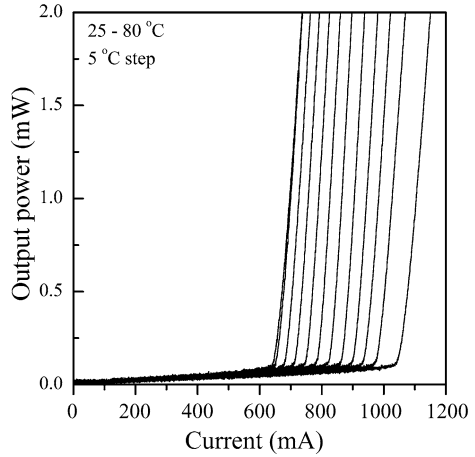


Figure 3.18 shows plots of the output power versus the current at various temperatures for a QD laser with a cavity length of 800 μm . This laser can be operated at temperatures up to 80 $^{\circ}\text{C}$ without any large decrease in the slope efficiency. Moreover, the increase in its threshold current is not as large as that of a 1.55- μm conventional semiconductor laser. Figure 3.19 shows the relationship between the threshold current density and the temperature. The characteristic temperature is described as:

$$J_{\text{th}} = J_0 \exp\left(\frac{T}{T_0}\right)$$

The value of T_0 for the QD laser was 113 K, which is greater than that of a 1.55- μm conventional edge-emitting semiconductor laser. (For example, for a GaInNAs quantum well LD it is 100 K [22], and for an InAs quantum dash LD it is 70 K [23].) This is because the QDs used as gain media have discrete energy levels. Moreover, even though numerous QD layers are stacked, the use of the strain compensation technique ensured that the crystal quality and strong QD confinement were maintained.

Next, we investigated the dependence of the diode parameters on the stacking layer number. We fabricated a QD laser using a stack of N InAs QD layers ($N = 5, 10, 15,$ and 20) and 18-nm-thick InGaAlAs spacer layers. The thickness of the active region was fixed at about 380 nm in each LD by adding lattice-matched InGaAlAs layers at the top and bottom of the stacked QD layers.

Figure 3.20 shows the dependence of the threshold current on the cavity length for QD lasers with different stacking layer numbers N ; the open circles, open squares, open triangles, and closed circles denote the $N = 5, 10, 15,$ and 20 samples, respectively. The threshold currents of the LDs with 15 and 20 QD layers decreased with a decrease in the cavity length. This implies that these LDs had sufficient gain. On the other hand, for the LDs with 5 and 10 QD layers, the threshold currents increased with a decrease in the cavity length, which implies that the gains in these LDs were insufficient. In our stacking structure, we can ignore the degradation in

Fig. 3.19 Relationship between threshold current density and temperature. The obtained T_0 value was 113 K

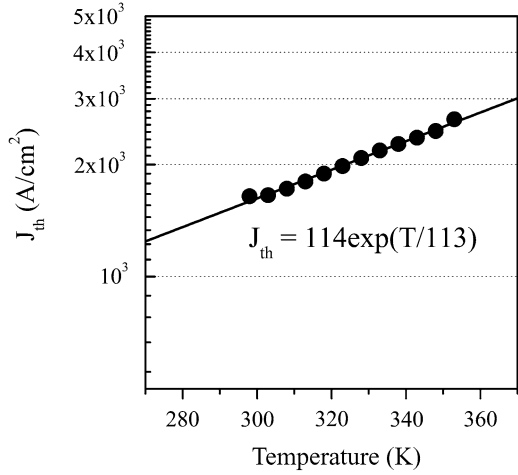
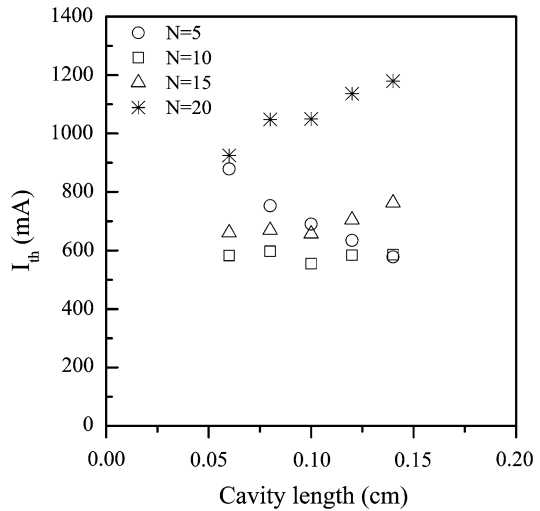


Fig. 3.20 Relationship between I_{th} and cavity length (L) for QD lasers with different stacking layer numbers N



the QD quality because a strain compensation technique was used to fabricate the stacking structure. Thus, the highly stacked structure in our laser is useful for fabricating high-gain LDs. This offers the advantage of fabricating a short-cavity laser that possesses high-speed-modulation LDs or high-repetition mode-locked LDs.

Figures 3.21 and 3.22 show the dependence of the internal loss (α_i) and internal quantum efficiency (η_i) on the QD layer stacking number. The values of α_i and η_i are 5.9 cm^{-1} and 17 % for $N = 5$, 16.9 cm^{-1} and 22 % for $N = 10$, 20.7 cm^{-1} and 25 % for $N = 15$, and 26.1 cm^{-1} and 28 % for $N = 20$. The internal loss and internal quantum efficiency increased with increasing N . The increase in the internal quantum efficiency associated with the increase in QD layers enhanced carrier recombination in the QDs. On the other hand, the internal loss also increased with

Fig. 3.21 Dependence of α_i on stacking layer number. The α_i values for each sample were 5.9 cm^{-1} for $N = 5$, 16.9 cm^{-1} for $N = 10$, 20.7 cm^{-1} for $N = 15$, and 26.1 cm^{-1} for $N = 20$

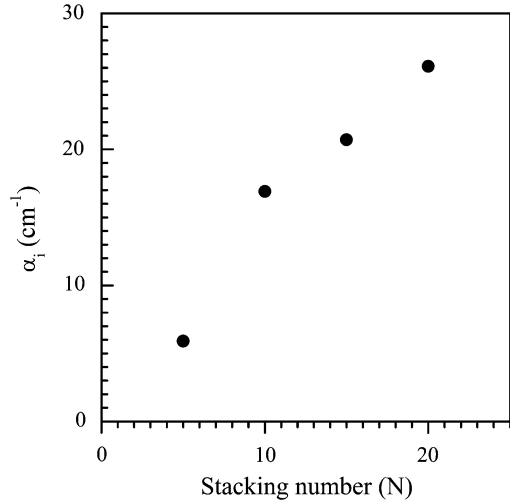
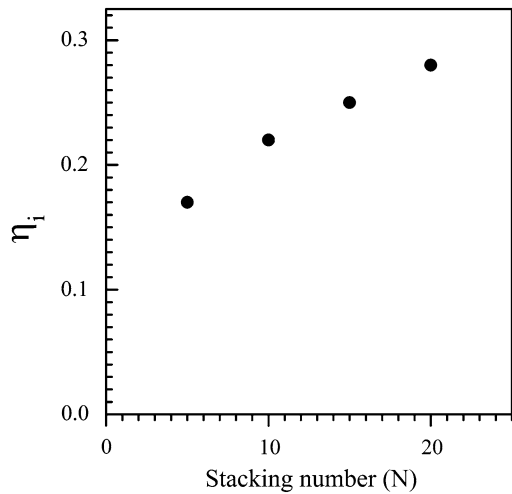


Fig. 3.22 Dependence of η_i on stacking layer number. The η_i values for each sample were 17 % for $N = 5$, 22 % for $N = 10$, 25 % for $N = 15$, and 28 % for $N = 20$



an increase in the QD layers. This could be attributed to imperfect coupling of the optical mode to the QD gain media. We used a layer of InAlAs, which has a larger refractive index than InP, for the upper cladding layer. Therefore, the center of the optical mode was pushed slightly upward to the InAlAs layer. Thus, the QDs located at the lower layer could not couple efficiently to the optical mode and acted as a loss. This large loss could be decreased by optimizing the device structure or changing the cladding layer material. However, the LD with 20 InAs QD layers achieved lasing with a relatively small threshold current, which means that a large gain was obtained in this laser by stacking 20 InAs QD layers. Therefore, the highly stacked InAs QD structure produced by using a strain compensation technique is

Table 3.2 Structural parameters of three 60-layer samples having different emission wavelengths

	Composition of spacer layer	d_{sp}	d_{QD}
sample 1	$\text{In}_{0.50}\text{Ga}_{0.21}\text{Al}_{0.29}\text{As}$	15 nm	3 ML
sample 2	$\text{In}_{0.51}\text{Ga}_{0.22}\text{Al}_{0.27}\text{As}$	15 nm	3 ML
sample 3	$\text{In}_{0.50}\text{Ga}_{0.25}\text{Al}_{0.25}\text{As}$	20 nm	4 ML

useful for obtaining a high gain, which can be applied to optical devices such as short-cavity lasers, including a high-repetition-rate mode-locked laser or SOA.

The advantage of the strain compensation technique is that we can change the QD and spacer layer thickness and the composition of the spacer layer as long as the strain compensation condition is satisfied. Therefore, it is expected that we can control the emission wavelength of InAs QDs by changing the growth parameters while maintaining the crystal quality of the highly stacked QDs. Thus, we fabricated and evaluated a QD laser consisting of highly stacked QD layers with different structural parameters using our strain compensation technique. Before fabricating the QD laser, we fabricated InAs QD stacked structures on InP(311)B substrates to confirm the change in the emission wavelength. After growing a lattice-matched $\text{In}_{0.52}\text{Al}_{0.48}\text{As}$ buffer layer 150 nm thick, we consecutively grew d_{QD} -ML InAs QDs and d_{sp} -nm-thick InGaAlAs spacer layers in stacks of up to 60 cycles. We controlled the emission wavelength of the QDs by changing d_{sp} , d_{QD} , and the composition of the spacer layer in three samples. The structural parameters of samples 1, 2, and 3 are summarized in Table 3.2.

Figure 3.23 shows the PL spectra of stacks of 60 InAs QD layers measured at room temperature. In these samples, we observed strong PL emission in which the peak wavelength of the QD ground state ranged from 1.47 to 1.64 μm . The small FWHM of around 30 meV indicates that the QDs were fabricated uniformly in this stacked structure. The shoulder structures of the PL spectrum correspond to emission in the excited states. The strong PL emission indicates that the generation of defects and dislocations was suppressed in these samples, even though 60 InAs QD layers were stacked.

Simple broad-area-stripe laser structures were fabricated under the conditions described above but containing different structures of highly stacked QDs (samples 1, 2, and 3 with 20 or 30 layers). Figure 3.24 shows the spectra before (dotted line) and after (solid line) lasing. The EL was measured under current injection below the lasing threshold. The EL spectrum is broad and is quite similar to the PL spectrum. Therefore, the change in the QD size and shape after growth can be ignored in our laser process. Lasing occurred at 1.47 (sample 1), 1.53 (sample 2), and 1.7 μm (sample 3) which were around the PL and EL peaks. Therefore, it corresponds to lasing at the ground state of the QDs. The controllable wavelength range was 230 nm, which covers the S, C, and L bands of fiber optic communication systems. In our structure, excited-state lasing is suppressed because the density of the QDs becomes very high as a result of the use of a strain compensation stack, which gives sufficient gain for ground-state lasing. An AFM image indicated that the total density of the stacked QDs increased to more than $1 \times 10^{12}/\text{cm}^2$ (not shown).

Fig. 3.23 PL spectrum of stacks of 60 InAs QD layers at room temperature

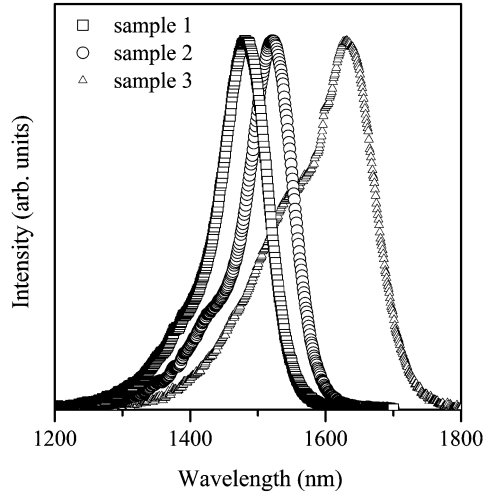
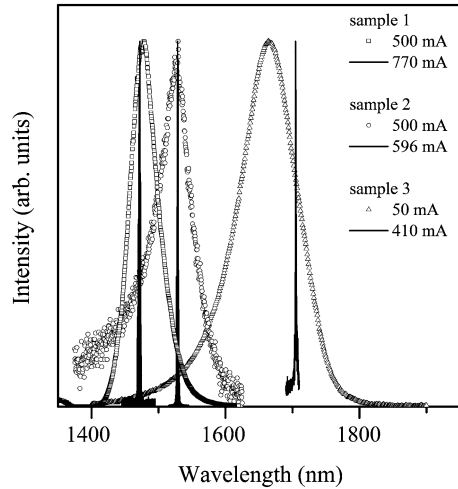
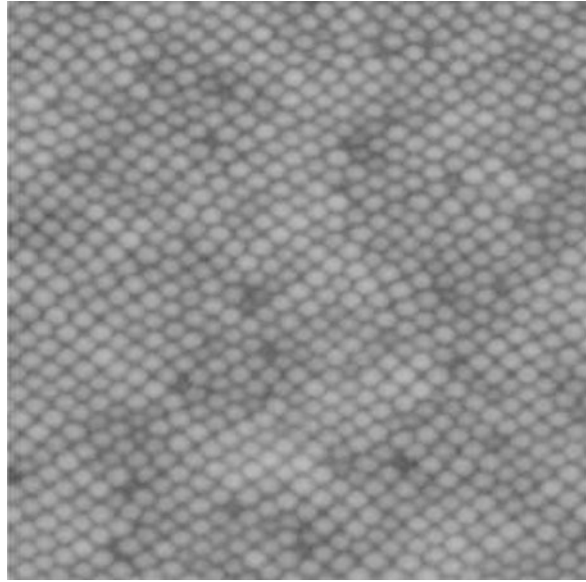


Fig. 3.24 EL and laser (*solid line*) spectra of QD lasers at room temperature



Control of the emission wavelength of highly stacked QDs was demonstrated above. If we grow different types of QDs in one sample, wider emission will be expected. In this case, strain compensation has an advantage because the strain energy can be canceled in one paired QD layer and spacer layer so that many QD layers with different structural parameters can be stacked in one sample. A wide-band optical gain is needed in high-performance wavelength-tunable LDs, SOAs for optical communication systems, and light sources for optical coherent tomography (OCT) for high-resolution mapping [22–25]. Thus, a modulated stacking structure based on the strain compensation technique is among the most promising candidates for achieving these devices. Three samples were fabricated with different stacked structures. In sample A, the 10 QD layer/spacer layer pairs ($d_{\text{QD}}\text{-ML}$ in bold/ $d_{\text{sp}}\text{-nm}$),

Fig. 3.25 AFM surface image of modulated stacking structure of InAs QDs (topmost two ML) in sample A ($1 \mu\text{m} \times 1 \mu\text{m}$)



starting from the buffer layer, had thicknesses of **4.5/22.5 / 4.0/20.0 / 3.5/17.5 / 3.0/15.0 / 2.5/12.5 / 2.0/10.0 ML/nm**; in sample B, the 3 QD layer/spacer layer pairs, starting from the buffer layer, had thicknesses of **4.5/22.5 / 4.0/20.0 / 3.5/17.5 / 3.5/17.5 / 3.0/15.0 / 3.0/15.0 / 3.0/15.0 / 2.5/12.5 / 2.5/12.5 / 2.5/12.5 / 2.5/12.5 / 2.5/12.5 / 2.0/10.0 / 2.0/10.0 / 2.0/10.0 / 2.0/10.0 / 2.0/10.0 / 2.0/10.0 ML/nm**; and in sample C, the 6 QD layer/spacer layer pairs, starting from the buffer layer, had thicknesses of **4.5/45 / 4.0/40 / 3.5/35 / 3.0/30 / 2.5/25 / 2.0/20 ML/nm**.

Figure 3.25 shows an AFM surface image of the stacked InAs QDs (topmost 2.0 ML) in sample A. Self-assembled QDs were fabricated even though the deposition thickness was less than that in the reference samples (for example, the sample with 4 ML-thick InAs as shown in Fig. 3.10). The average lateral size in the $[-233]$ direction and the height of the QDs were estimated to be 45.9 nm and 2.3 nm, respectively. The height of the QDs on the topmost layer was smaller than that of reference, in which the thickness of the QD layer was 4 ML. The density of the QDs in the topmost layer was $8.7 \times 10^{10}/\text{cm}^2$. In this sample, broad PL emission was observed at room temperature, as shown in Fig. 3.26. The peak wavelength and FWHM of this spectrum were 1624 nm and 143 nm, respectively. Although we obtained wider PL emission in sample A than in the reference sample, the broadening was not very large. The narrowing of the PL spectrum in sample A likely originates in carrier transfer from small QDs to large QDs, which is enhanced by the coupling of the QD state with thin spacer layers [26]. This QD state coupling was significant when the spacer layer thickness decreased to less than 20 nm. Therefore, the photo-excited carriers in the small QDs moved to large QDs in sample A. There are two ways to broaden the PL spectrum: increasing the number of QD layers that emit

Fig. 3.26 PL spectrum at room temperature for sample A

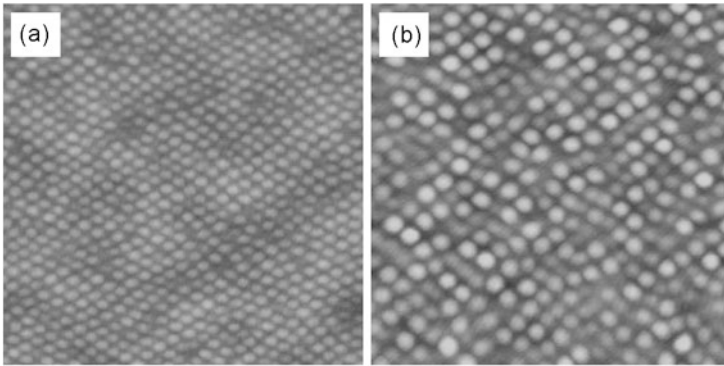
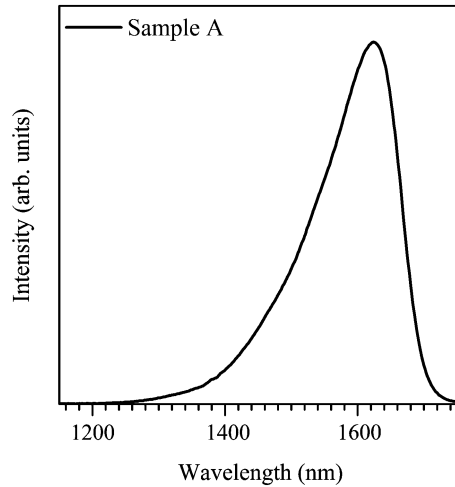
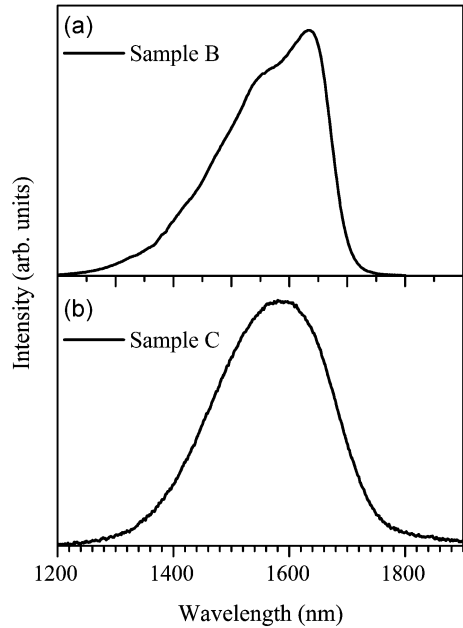


Fig. 3.27 AFM surface images of modulated stacking structure of InAs QDs (topmost 2 ML) for (a) sample B and (b) sample C ($1\ \mu\text{m} \times 1\ \mu\text{m}$)

at a shorter wavelength, and increasing the thickness of the spacer layer to prevent QD state coupling, i.e., preventing carrier transfer from small QDs to large QDs. Samples B and C were fabricated for these purposes.

Figures 3.27(a) and (b) show AFM surface images of the stacked InAs QDs (topmost layer) of samples B and C, respectively. In these AFM images, self-assembled QDs were also observed, even though the deposition thickness was less than in the reference samples. The average lateral size in the $[-233]$ direction and the height of the QDs were estimated to be 47.5 nm and 2.2 nm for sample B and 58.4 nm and 3.4 nm for sample C. Although the average size of the QDs in sample B is similar to that in sample A, that in sample C is slightly larger than that in sample A. The origin of the increase in QD size is not clear, but it is considered that the distribution of the strain field changed if thicker spacer layers were used.

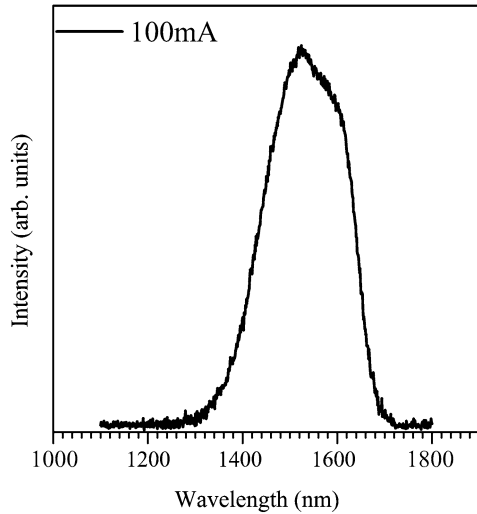
Fig. 3.28 PL spectra of modulated stacking structure of InAs QDs for (a) sample B and (b) sample C



Figures 3.28(a) and (b) show PL spectra for samples B and C, respectively. The peak wavelength and FWHM of the PL spectra for samples B and C are 1633 nm, 201 nm and 1581 nm, 241 nm, respectively. Compared to sample A, these samples showed wide-band PL emission over 200 nm, which is about two times wider than that for samples reported previously [20]. The PL spectrum of sample B is slightly narrower than that of sample C, indicating that the ratio of small QD layers and large QD layers is better optimized. Sample C shows a symmetrical PL spectrum, suggesting that coupling of the QD states is restricted in this sample. In this case, photo-excited carriers were distributed uniformly in each QD layer. However, the active layer became thicker in this structure because thicker spacer layers were used. Therefore, the appropriate method of the two mentioned above should be selected for each application, such as SOAs, which are the light sources in OCT. Although the integrated PL intensity is of the same order in sample C and the reference samples, the PL intensity is five times larger in samples A and B as a result of excitation transfer between the QD arrays [27]. The detailed mechanism of the enhanced PL intensity is now under investigation. Modulated stacking using this strain compensation technique is, however, a useful way to expand the gain wavelength because the strong emission at room temperature is attributed to the suppression of defect and dislocation generation due to strain compensation throughout the stack.

The EL spectrum of sample B was also measured with pulsed current injection into the same LD structure. As shown in Fig. 3.29, strong emission from the ground state appeared at around 1524 nm at an injection current of 100 mA, which is suitable for fiber optic communications, at room temperature. The FWHM was 213 nm, which is almost the same as in the PL spectrum. Modulated stacking using this

Fig. 3.29 EL spectrum for modulated stacked InAs QD structure (sample B) with an injection current of 100 mA in pulsed mode



strain compensation technique is thus a useful way to expand the gain wavelength. The strong emission at room temperature is attributed to the suppression of defect and dislocation generation due to strain compensation throughout the stack.

3.1.4 Summary

A fabrication technique for strain-compensated ultrahigh-density self-assembled InAs QDs was presented in this chapter. We successfully stacked up to 300 QD layers, and the total density of the stacked QDs was on the order of $10^{13}/\text{cm}^2$. High crystal quality was maintained throughout the stacking process, and no defects or dislocations were observed. This structure also exhibited good optical properties. Strong 1.55- μm emission was obtained from the InAs QDs at room temperature.

Some applications of highly stacked InAs QDs for LDs were also demonstrated and showed good LD properties. The lasing wavelength can be controlled from 1470 nm to 1700 nm. The controllable wavelength range was therefore 230 nm and covered the S, C, and L bands of fiber optic communication systems. Wide band emission (maximum bandwidth, 241 nm) was observed in the modulated stacking structure.

The various applications of highly stacked QD structures fabricated by the strain compensation technique include not only those mentioned in this chapter but also applications in other fields.

References

1. Y. Arakawa, H. Sakaki, *Appl. Phys. Lett.* **40**, 939 (1982)

2. T. Miyazawa, K. Takemoto, Y. Sakuma, S. Hirose, T. Usuki, N. Yokoyama, M. Takatsu, Y. Arakawa, *Jpn. J. Appl. Phys.* **44**, L620 (2005)
3. L. Goldstein, F. Glas, J.Y. Marzin, M.N. Charasse, G. Le Roux, *Appl. Phys. Lett.* **47**, 1099 (1985)
4. I.N. Stranski, L. Krastanow, *Akad. Wiss. Wien Math.-Nat. Iib* **146**, 797 (1937)
5. X.D. Huang, A. Stintz, C.P. Hains, G.T. Liu, J. Cheng, K.J. Malloy, *IEEE Photonics Technol. Lett.* **12**, 227 (2000)
6. A. Markus, J.X. Chen, C. Paranthoen, A. Fiore, C. Platz, O. Gauthier-Lafaye, *Appl. Phys. Lett.* **82**, 1818 (2003)
7. J.S. Wang, R.S. Hsiao, J.F. Chen, C.S. Yang, G. Lin, C.Y. Liang, C.M. Lai, H.Y. Liu, T.W. Chi, J.Y. Chi, *IEEE Photonics Technol. Lett.* **17**, 1590 (2005)
8. C.Y. Liu, S.F. Yoon, Q. Cao, C.Z. Tong, H.F. Li, *Appl. Phys. Lett.* **90**, 041103 (2007)
9. R. Kovsh, N.A. Maleev, A.E. Zhukov, S.S. Mikhrin, A.P. Vasil'ev, Yu.M. Shernyakov, M.V. Maximov, D.A. Livshits, V.M. Ustinov, Zh.I. Alferov, N.N. Ledentsov, D. Bimberg, *Electron. Lett.* **38**, 1104 (2002)
10. M. Ishida, N. Hatori, T. Akiyama, K. Otsubo, Y. Nakata, H. Ebe, M. Sugawara, Y. Arakawa, *Appl. Phys. Lett.* **85**, 4145 (2004)
11. M. Sugawara, N. Hatori, M. Ishida, H. Ebe, Y. Arakawa, T. Akiyama, K. Otsubo, T. Yamamoto, Y. Nakata, *J. Phys. D* **38**, 2126 (2005)
12. H. Saito, K. Nishi, A. Kamei, S. Sugou, *IEEE Photonics Technol. Lett.* **12**, 1298 (2000)
13. J. Brault, M. Gendry, O. Marty, M. Pitaval, J. Olivares, G. Grenet, G. Hollinger, *Appl. Surf. Sci.* **162**, 584 (2000)
14. H. Yang, X. Mu, I.B. Zotova, Y.J. Ding, G.J. Salamo, *J. Appl. Phys.* **91**, 3925 (2002)
15. K. Akahane, N. Yamamoto, N. Ohtani, Y. Okada, M. Kawabe, *J. Cryst. Growth* **256**, 7 (2003)
16. K. Akahane, T. Kawamura, K. Okino, H. Koyama, S. Lan, Y. Okada, M. Kawabe, *Appl. Phys. Lett.* **73**, 3411 (1998)
17. K. Akahane, H.Z. Xu, Y. Okada, M. Kawabe, *Physica E* **11**, 94 (2001)
18. G. Springholz, M. Pinczolits, V. Holy, S. Zerlauth, I. Vavra, G. Bauer, *Physica E* **9**, 149 (2001)
19. X.D. Huang, A. Stintz, C.P. Hains, G.T. Liu, J. Cheng, K.J. Malloy, *IEEE Photonics Technol. Lett.* **12**, 227 (2000)
20. K. Akahane, N. Ohtani, Y. Okada, M. Kawabe, *J. Cryst. Growth* **245**, 31 (2002)
21. K. Akahane, N. Yamamoto, T. Kawanishi, *Phys. Status Solidi A* **208**, 425 (2011)
22. S. Sudo, K. Mizutani, J. De Merlier, T. Okamoto, K. Tsuruoka, K. Sato, K. Kudo, *Electron. Lett.* **42**, 347 (2006)
23. T. Akiyama, M. Ekawa, M. Sugawara, K. Kawaguchi, H. Sudo, A. Kuramata, H. Ebe, Y. Arakawa, *IEEE Photonics Technol. Lett.* **17**, 1614 (2005)
24. D. Huang, E.A. Swanson, C.P. Lin, J.S. Schuman, W.G. Stinson, W. Chang, M.R. Hee, T. Flotte, K. Gregory, C.A. Puliafito, J.G. Fujimoto, *Science* **254**, 1178 (1991)
25. E. Swanson, D. Huang, M. Hee, J. Fujimoto, C. Lin, C. Puliafito, *Opt. Lett.* **17**, 151 (1992)
26. O. Kojima, H. Nakatani, T. Kita, O. Wada, K. Akahane, M. Tsuchiya, *J. Appl. Phys.* **103**, 113504 (2008)
27. K. Akahane, N. Yamamoto, M. Naruse, T. Kawazoe, T. Yatsui, M. Ohtsu, *Jpn. J. Appl. Phys.* **50**, 04DH05 (2011)

Chapter 4

Wavelength Up-Conversion Using a Phonon-Assisted Excitation Process and Its Application to Optical Pulse-Shape Measurement

Hiroyasu Fujiwara

Abstract This chapter describes experimental results for wavelength up-conversion using a phonon-assisted excitation process with degenerate beams and nondegenerate beams in dye grains. Optical pulse-shape measurement is also introduced as a new application of the phonon-assisted excitation process.

4.1 Introduction

Infrared light has been increasingly used in environmental and security applications, and there is a growing demand for infrared photodetectors. Among these, photodiodes using the inter-band transition due to light absorption have high industrial potential because of their relatively rapid response [1]. However, because an infrared photodetector utilizes material with a narrow band gap, which easily produces noise by thermal excitation, a device for cooling the photodetector is required in order to realize a sufficiently high signal-to-noise ratio (S/N) for detection. As a solution to these problems, there is a method in which the incident light is frequency up-converted (to a shorter wavelength), and a photodetector having detection sensitivity for visible light, with less noise, is used [2]. In using IR-phosphor for the frequency up-conversion, excitation to a triplet state from the ground state by another excitation method, such as ultraviolet excitation, is required, and thus, the slow response and unstable conversion efficiency of the measurement light become problematic [3].

In order to solve these problems, we have been investigating a novel frequency up-conversion method in which emission of visible light is obtained by multi-step excitation of a dye molecule's vibrational states using an optical near-field with a near-infrared frequency, thereby inducing transition of electrons into the electronically excited state [4]. Excitation of the molecular vibrational state is not possible with propagating light because it is optically forbidden. However, because an optical

H. Fujiwara (✉)

Central Research Laboratories, Hamamatsu Photonics K.K., Hirakuchi 5000, Hamakita-ku, Hamamatsu, Shizuoka 434-8601, Japan
e-mail: fujiwara@crl.hpk.co.jp

near-field is considered as a photon dressed with material excitations (a *dressed photon*), the optical near-field excites a coherent phonon at the molecular particle surface, creating a coupled state with the coherent phonon [5]. Therefore, molecules in the area where the optical near-field is present are excited by the phonon into higher vibrational states, via which they are electronically excited by the dressed photon. In contrast to the conventional optical excitation using propagating light, which is adiabatic and excites only the electronic system, the method described above is referred to as nonadiabatic because the optical near-field excites the molecular vibration. This nonadiabatic excitation process (*phonon-assisted excitation process*) has been applied to chemical vapor deposition [6–8], sputtering [9], lithography [10–12], and chemical etching [13].

In our previous work, we have discovered a novel light emission process using this phonon-assisted excitation [4]. We have observed emission of visible light through the near-infrared excitation of dye grains, such as 4-dicyanomethylene-2-methyl-6-(*p*-dimethylaminostyryl)-4H-pyran (DCM) and benzoic acid, 2-[6-(ethylamino)-3-(ethylimino)-2,7-dimethyl-3H-xanthen-9-yl]-ethyl ester, monohydrochloride (Rhodamine 6G). These dyes are transparent to near-infrared light; however, individual protrusions on the dye grains contribute to generating the optical near-field. Inside dye grains in the vicinity, dye molecules are excited to a higher vibrational state as an intermediate excited state due to the phonon-assisted excitation, giving rise to light emission from the dye.

However, detailed properties of the intermediate excited state in the phonon-assisted excitation process have not been elucidated. In addition, with these types of dyes, the wavelength conversion has been limited to that from approximately $\lambda = 805$ nm to 650 nm, that is, 0.37 eV in terms of the frequency up-shift. This is because the excitation wavelength and the fluorescence wavelength are close, and the excitation to electrically excited states occurs only by the one- and two-step phonon-assisted excitation processes. A larger up-shift is needed for detector applications, which would be effectively achieved by using a phonon-assisted excitation process involving two or more steps.

This chapter describes in detail phonon-assisted excitation processes with two or more steps for a larger up-shift with degenerate beams and phonon-assisted excitation processes with nondegenerate beams, as well as a new application: optical pulse-shape measurement.

4.2 Multi-step Phonon-Assisted Processes with Degenerate Beams

For a larger up-shift, we conducted experiments in which the dyes were changed to those having fluorescence properties toward shorter wavelengths. The dyes used were 2,3,5,6-1H,4H-tetrahydro-8-trifluormethylquinolizino-[9,9a,1-gh]-coumarin (Coumarin 153) and 2,3,5,6-1H,4H-tetrahydro-8-methylquinolizino-[9,9a,1-gh]-coumarin (Coumarin 102), materials that generate fluorescence of $\lambda = 570$ nm

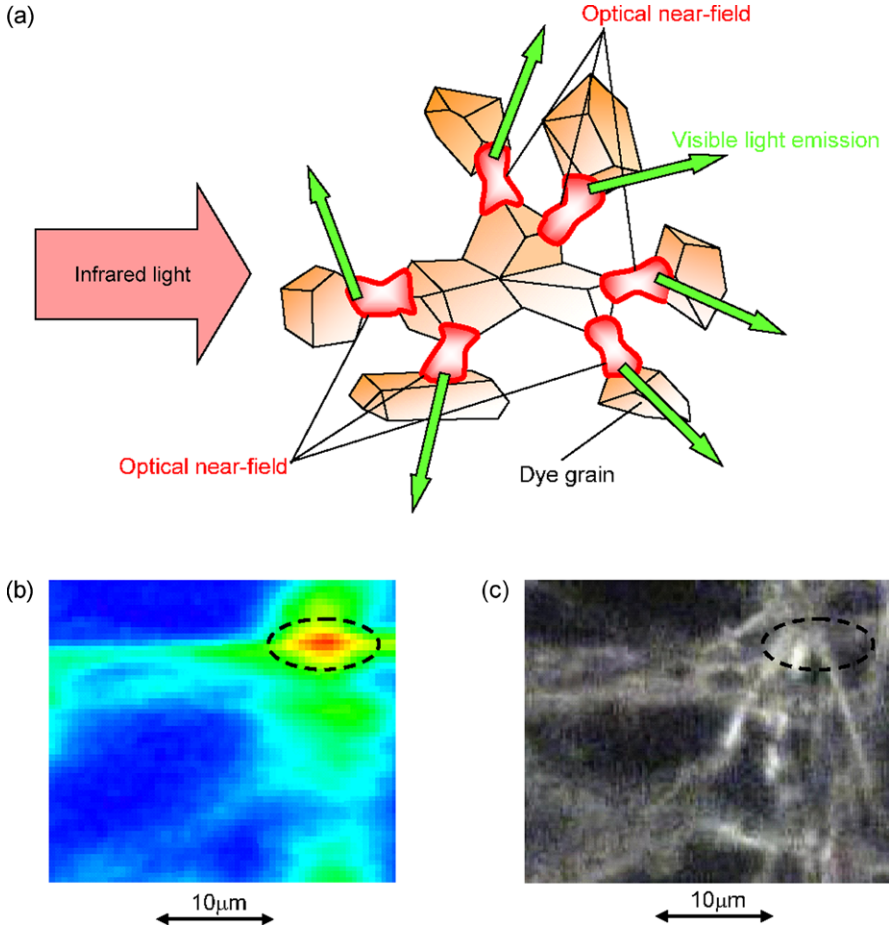


Fig. 4.1 (a) Overview of light emission from dye grains induced by the phonon-assisted excitation. (b) Optical microscopic image of visible emission light from dye grains excited by phonon-assisted process. (c) Optical microscopic image of dye grains at the same region of (b)

and 460 nm, respectively, when excited by light of a shorter wavelength than the absorption-edge wavelength used in the conventional adiabatic excitation [14]. Using these dye grains as samples, emission of visible light due to the near-infrared excitation was measured, and the excitation intensity dependence and lifetime of the intermediate excited state were investigated [15].

4.2.1 Principles of Multi-step Phonon-Assisted Process

We now describe the principles of light emission by phonon-assisted excitation of dye grains. Figure 4.1(a) is an overview of visible light emission from dye grains

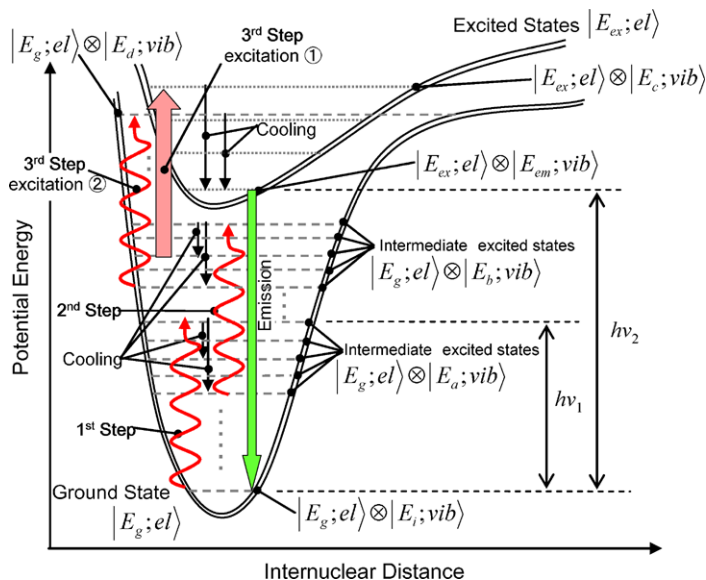


Fig. 4.2 Electronic potential curves in the configuration coordinates of the dye molecules. Illustration explaining the origin of the visible light emission by a two-step (excitation ①) and three-step (excitation ②) phonon-assisted excitation process

induced by the phonon-assisted excitation with an optical near-field. When infrared light whose wavelength is longer than the absorption-edge wavelength of the dye is incident on the dye grains, an optical near-field is generated at the surface of the dye grains, and it is especially pronounced at sharp protrusions. The generated optical near-field excites a coherent phonon at the surface of the dye grains, creating a coupled state with it [5]. As a result, dye molecules in the dye grains in the area in which the optical near-field is generated are excited into a higher energy state by a phonon of the dressed photon. Because the higher vibrational state serves as the intermediate excited state, the dye molecules are further excited by multiple phonons to an even higher energy state through multi-step excitation, eventually resulting in an electronically excited state. Subsequently, visible light is emitted by the electronic transition. Figure 4.1(b) shows an example of the visible light emission from dye grains (DCM) excited by near-infrared light. Figure 4.1(c) shows an optical microscopic image of dye grains at the same region as in Fig. 4.1(b). The dye grains take a rod-like shape, and the intensity of visible light emission is high at the tip of rod in particular.

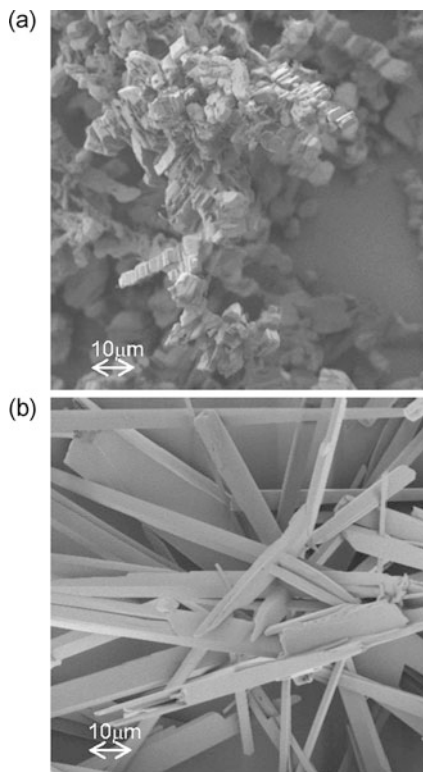
Figure 4.2 shows an overview of light emission by multi-step phonon-assisted excitation, resulting in transition of electrons in the dye molecules to an electronically excited state. In Fig. 4.2, a three-step excitation to the electronically excited state is shown; however, a light emission process involving two steps or four or more steps is possible, depending on the energy difference between the excitation wavelength and the dye absorption-edge wavelength. Figure 4.2 is an electronic potential curve

in the configuration coordinates of the dye molecules in the phonon mode coupled with the optical near-field. Here, $|E_\alpha; el\rangle$ and $|E_\beta; vib\rangle$ indicate the electronic state and molecular vibrational state, respectively. E_α denotes the energy of the electronic state, where the subscript α indicates the ground state ($\alpha = g$) and the excited state ($\alpha = ex$). E_β denotes the energy of the molecular vibrational state, where the subscript β indicates respective characteristic vibrational states ($\beta = i, a, b, c, d, em$).

- (1) **1st step:** The optical near-field is generated at the surface of the dye grains by the incident excitation light. The dye molecules in the nearby dye grains are excited by the phonon-assisted excitation process from the ground state, $|E_g; el\rangle \otimes |E_i; vib\rangle$, to a higher vibrational state, $|E_g; el\rangle \otimes |E_a; vib\rangle$ (indicated by the wavy arrow in Fig. 4.2). Because molecules in the excited vibrational state seek stable thermal equilibrium, they relax (cool) to a lower vibrational state.
- (2) **2nd step:** The vibrational state relaxing toward thermal equilibrium, following the 1st step, serves as the intermediate excited state, causing a second excitation by a phonon-assisted excitation process to an even higher energy state: a transition from $|E_g; el\rangle \otimes |E_a; vib\rangle$ to $|E_g; el\rangle \otimes |E_b; vib\rangle$ (indicated by the wavy arrow in Fig. 4.2). The molecules in the vibrational state resulting from the two steps of the phonon-assisted excitation process cool to a lower energy state.
- (3) **3rd step:** Excitation to the electronically excited state via the two transition routes described below is possible when the energy of the intermediate excited state is equal to or greater than 1.17 eV, i.e., the difference between the energy of the electronically excited state (for example, light emission wavelength of Coumarin 102; $h\nu_2 = 2.70$ eV, $\lambda = 460$ nm) and the photon energy of the excitation light (for example, $h\nu_1 = 1.53$ eV, $\lambda_{ex} = 808$ nm). The first route (excitation ①) is an excitation from $|E_g; el\rangle \otimes |E_b; vib\rangle$ to $|E_{ex}; el\rangle \otimes |E_c; vib\rangle$ by adiabatic excitation using propagating light (indicated by the thick arrow in Fig. 4.2). The other route (excitation ②) is an excitation to an even higher vibrational state, from $|E_g; el\rangle \otimes |E_b; vib\rangle$ to $|E_g; el\rangle \otimes |E_d; vib\rangle$ by the phonon-assisted excitation (indicated by the wavy arrow in Fig. 4.2). This energy is greater than the initial state $|E_{ex}; el\rangle \otimes |E_{em}; vib\rangle$ for light emission. Molecules relax from the states in these two transition routes, $|E_{ex}; el\rangle \otimes |E_c; vib\rangle$ or $|E_g; el\rangle \otimes |E_d; vib\rangle$, to the initial state for light emission, $|E_{ex}; el\rangle \otimes |E_{em}; vib\rangle$.

Following excitation by the above three steps, radiative relaxation occurs from the initial state for light emission, $|E_{ex}; el\rangle \otimes |E_{em}; vib\rangle$, to the ground state, $|E_g; el\rangle \otimes |E_i; vib\rangle$. Since the excitation in the 3rd step is an adiabatic excitation whose transition probability is about 10^6 times greater than that of the phonon-assisted excitation [4, 6], the probability of light emission that occurs in this transition route is limited by the phonon-assisted excitation probability, and the emitted light intensity I has a squared dependence on the incident light intensity E ($I \propto E^2$). This excitation process is referred to as a two-step phonon-assisted excitation process since two phonon-assisted steps contribute to the excitation. On the other hand, the phonon-assisted excitation ② in the third step has a probability equal to the phonon-assisted excitation probabilities of the first and second steps. The emitted

Fig. 4.3 SEM images of the dye grains. (a) Coumarin 153. (b) Coumarin 102

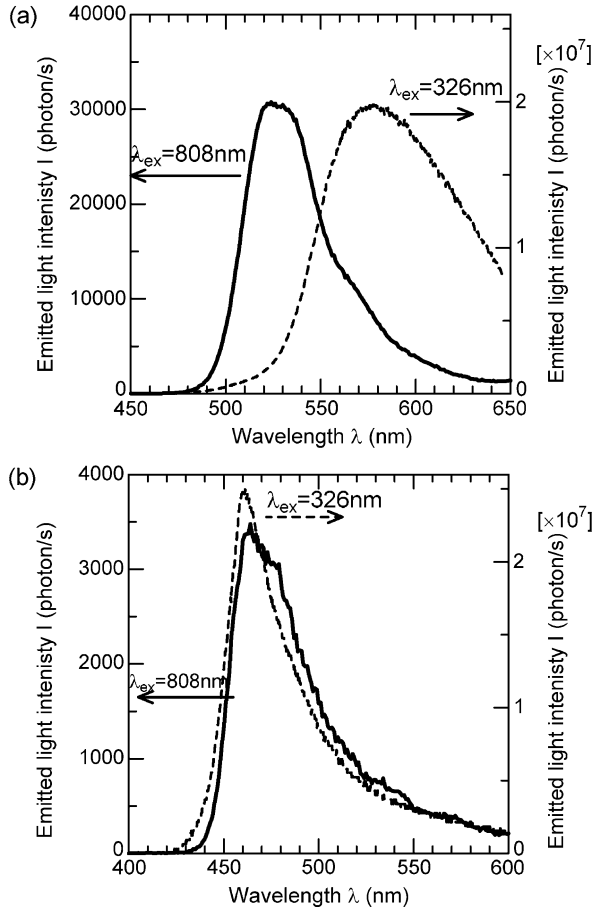


light intensity I of the dyes due to this excitation is the origin of the cubed dependence on the incident light intensity E ($I \propto E^3$). This excitation process is referred to as a three-step phonon-assisted excitation process since three phonon-assisted steps contribute to the excitation.

4.2.2 Sample Preparation

As experimental samples, two types of dyes (Coumarin 153 and 102) were prepared. When these dyes are dissolved in solution, the absorption-edge wavelengths are approximately 500 nm for Coumarin 153 and 440 nm for Coumarin 102, and they do not absorb near-infrared light of wavelengths around 808 nm [14]. These dyes were dissolved in acetone, and then dripped into water to crystallize [16]. The dye grains were obtained by evaporating the solution in quartz cells. The total thickness of the dye grains in the quartz cells was 1 mm. SEM images of the dye grains are shown in Fig. 4.3. Coumarin 153 dye grains take a granular shape with dimensions of approximately $5 \mu\text{m} \times 5 \mu\text{m} \times 5 \mu\text{m}$ (Fig. 4.3(a)). Coumarin 102 dye grains take a rod-like shape of approximately $2 \mu\text{m}$ in diameter and $50 \mu\text{m}$ in length (Fig. 4.3(b)). The optical near-field is generated at the surface of the dye grains by incident excitation

Fig. 4.4 Spectral profiles of the visible light emitted from (a) Coumarin 153 and (b) Coumarin 102. *Solid* and *broken* curves represent the spectra obtained with near-infrared and ultraviolet excitation, respectively



light, and it is especially pronounced at sharp protrusions. Coumarin 153 dye grains, which have smaller crystal grain size and a greater number of protrusions per unit volume, have a higher optical near-field generation efficiency, and thus are expected to show a higher light emission efficiency induced by the phonon-assisted excitation process.

4.2.3 Comparison Between Fluorescence and Emitted Spectra Induced by Phonon-Assisted Process

The solid curve in Fig. 4.4(a) indicates the emitted green light spectrum of Coumarin 153 dye grains obtained by near-infrared excitation. A CW laser diode (center wavelength $\lambda_{ex} = 808$ nm) was used as the near-infrared excitation light source. It was shifted about 54 nm toward shorter wavelengths as compared with the fluorescence

spectrum obtained by conventional adiabatic excitation using an ultraviolet light source (center wavelength $\lambda_{ex} = 326$ nm; the broken curve). The solid curve in Fig. 4.4(b) indicates the emitted blue light spectrum obtained by exciting Coumarin 102 dye grains using the same near-infrared light source as above. The broken curve in Fig. 4.4(b) indicates the fluorescence spectrum using an ultraviolet light source. Peak wavelengths of the two curves agree closely, suggesting that the light emission by near-infrared excitation is due to light emission from the electronically excited state. The frequency shift between the emitted light and the excitation light was approximately 1.17 eV.

Comparing peak intensities of the emission spectra in the cases of near-infrared excitation, the peak intensity of the light emitted from the Coumarin 153 dye grains was approximately 10 times greater than that of the Coumarin 102 dye grains. As shown in Figs. 4.3(a) and (b), comparing the shapes and sizes of the two dye grains, the phonon-assisted excitation process is suggested to be the origin of the observed difference in the emitted visible light intensities.

4.2.4 Excitation Intensity Dependence

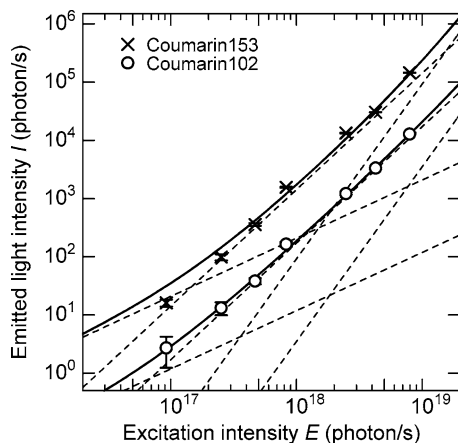
Figure 4.5 shows the dependence of emitted light intensity I on the excitation intensity E at $\lambda = 520$ nm (Coumarin 153) and 460 nm (Coumarin 102). The emitted light intensity I was least-squares fitted by the third-order function $I = aE + bE^2 + cE^3$. The values a , b , and c for the fitting obtained by the nonlinear Levenberg-Marquardt method [17] were as follows. For Coumarin 153: $a = (2.09 \pm 0.20) \times 10^{-16}$, $b = (1.42 \pm 0.02) \times 10^{-33}$, and $c = (9.20 \pm 0.39) \times 10^{-53}$. For Coumarin 102: $a = (1.19 \pm 0.85) \times 10^{-17}$, $b = (1.71 \pm 0.10) \times 10^{-34}$, and $c = (3.51 \pm 1.43) \times 10^{-54}$. The fitting results are shown by the solid curves in Fig. 4.5. In addition, the broken lines indicate the excitation intensity dependence of each order. The coefficient ratio c/b of the second and the third orders was approximately 2×10^{-20} to 6×10^{-20} .

According to the dressed photon model, the coefficient ratio c/b of the two-step and the three-step phonon-assisted excitation processes is represented by [6]

$$\frac{c}{b} = \frac{\hbar}{2\pi} \frac{I}{|\gamma_m|^2 E} \left(\frac{v_p^2}{u_p^2} \right) \left(\frac{\mu^{el}}{\mu^{nucl}} \right)^2. \quad (4.1)$$

The theoretical value of (4.1) was approximately 7×10^{-20} , when the measured value of Coumarin 153 at a low excitation intensity $I \approx aE = 14.8$ photons/s and the excitation light intensity $E = 9.2 \times 10^{16}$ photons/s were used, and additionally, $\mu^{nucl} = 1$ Debye, $\mu^{el} = 10^{-3}$ Debye (the electronic and lattice vibrational dipole moments), $\gamma_m = 10^{-1}$ eV (the linewidth of the electronic and vibrational states), and $v_p'/u_p' = 0.1$ (the conversion efficiency from the incident photon to a dressed photon) were used as other parameters. This theoretical value is nearly equal to the fitted value based on the experimental value; therefore, the dressed photon model is applicable to the excitation intensity dependence.

Fig. 4.5 Dependence of the emitted light intensity I on the excitation light intensity E



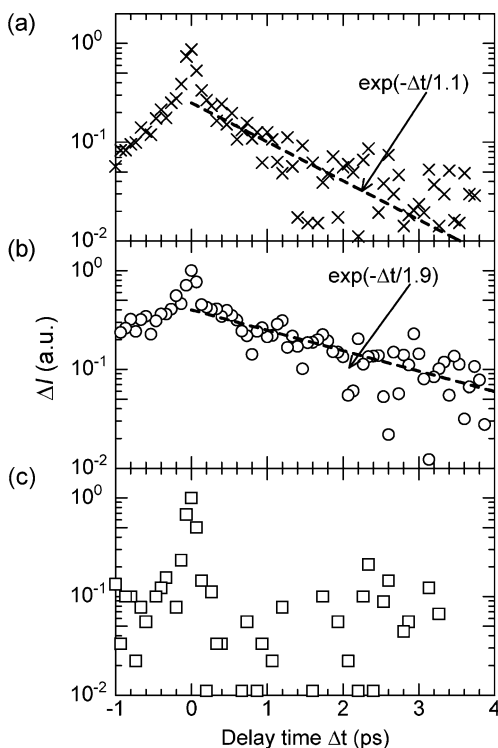
Only the coefficient a was larger than the theoretical value. This is likely caused by difficulties in estimating the first-order coefficient a . That is, the observed deviation of the coefficient a from the theoretical value is likely to be an experimental error, explained as follows: In the case of the dye samples used in this experiment, there is a large energy difference between the emitted light ($\lambda = 460\text{--}520$ nm) and the infrared excitation light ($\lambda = 808$ nm); therefore, the energy needed for excitation cannot be secured in the one-step phonon-assisted excitation process, resulting in a small proportional contribution to the light emission. As a result, the measured value aE becomes close to the detection limit (1 photon/s) of the photodetector.

Based on these experimental results and comparisons with theoretical values, it can be concluded that the visible light emission process in Coumarin 153 and 102 dye grains based on the near-infrared excitation was generated by the two- and three-step phonon-assisted excitation, with the excited vibrational level of the dye grains serving as the intermediate excited state. Light emission by the three-step phonon-assisted excitation was confirmed for the first time in this experiment.

4.2.5 Lifetime of the Intermediate Excited State

In the two- and three-step phonon-assisted excitation of Coumarin 153 and 102 dye grains, the intermediate excited state shown in Fig. 4.2 is the vibrational state of the dye grains. The lifetime of this intermediate excited state can be measured by pump-probe spectroscopy. More specifically, the measurement method was as follows. A femtosecond pulse from a mode-locked Ti:sapphire laser was used as the excitation light (center wavelength = 805 nm, pulse duration = 100 fs, repetition frequency = 80 MHz). The light pulse was split into two and made incident on a single point on a sample after passing along different optical paths. The length of one optical path was made variable to control the difference in the incident

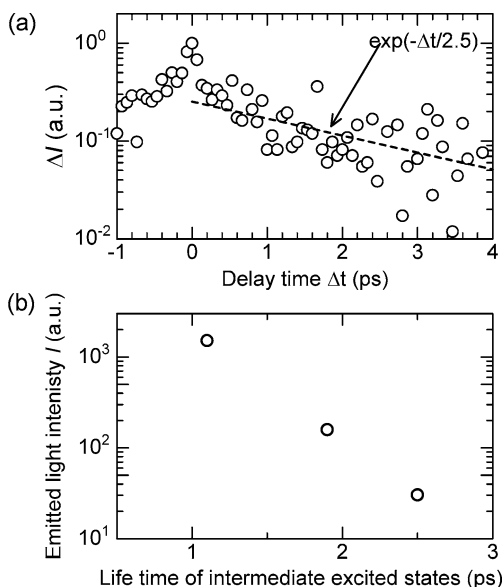
Fig. 4.6 Measured temporal behavior of the increment of the light intensity ΔI emitted from (a) grains of Coumarin 153, (b) grains of Coumarin 102, and (c) solution of Coumarin 153 in acetone



time of the two light pulses reaching the experimental sample. The relationship between the difference in the incident time for the two light pulses to reach the sample, the delay time Δt , and the emitted light intensity was examined.

The results are shown in Fig. 4.6. The vertical axis is the increment of the emitted light intensity ΔI , defined as follows: From the emitted light intensity due to phonon-assisted excitation obtained at $\Delta t = 0$, the sum of emitted light intensities obtained for the two light pulses when they were separately made incident on the sample was subtracted and the difference was normalized. The increment of the emitted light intensity ΔI at the delay time $\Delta t = t$ is proportional to $\exp(-t/\tau)$, where the time constant τ is the lifetime of the intermediate excited state, explained as follows: The number of dye molecules in the intermediate state excited by the pumping light pulse decreases with time constant τ because their vibrational energies are much higher than the thermal energy determined by the sample temperature [18–20]. Also, ΔI at $\Delta t = t$ is proportional to the number of dye molecules excited by the probing light pulse from this intermediate excited state to the electronically excited state for visible light emission. The probability of this excitation is proportional only to the number of the intermediately excited dye molecules at $\Delta t = t$, because it is proportional to both the probing light pulse intensity and the number of intermediately excited dye molecules. Therefore, the time constant τ , i.e., the lifetime of the intermediate excited state in the dye molecules, could be

Fig. 4.7 (a) Measured temporal behavior of the increment of the light intensity ΔI emitted from grains of Stilbene 3, and (b) the relations between the lifetime of the intermediate excited state and emitted light intensity for grains of Stilbene 3, Coumarin 102, and Coumarin 153



measured from the dependence ΔI on the delay time Δt , if the time constant τ is longer than the pumping light pulse duration. The decay time of ΔI was approximately 1.1 ps for Coumarin 153 dye grains (Fig. 4.6(a)), suggesting that the lifetime of their intermediate excited state was 1.1 ps. Figure 4.6(b) shows that the decay time was approximately 1.9 ps for Coumarin 102 dye grains, suggesting that the lifetime of their intermediate excited state is 1.9 ps.

For the purpose of comparison, the same measurements were carried out using a dye acetone solution (Coumarin 153) without dye grain precipitation. The results are shown in Fig. 4.6(c). With this sample, green light emission occurred only by the two-photon excitation using propagating light. The intermediate excited state of the two-photon excitation light emission is based on a two-step excitation via a virtual level; therefore, the emitted light intensity increases only when the two excitation light pulses show a temporal overlap. As a result, the profile of the temporal behavior of ΔI corresponds to the autocorrelation waveform of the excitation light pulse. Unlike Fig. 4.6(c), the results for the dye grains (Figs. 4.6(a) and (b)) suggest that their intermediate excited states are real levels whose lifetimes are longer than the duration of the light pulses.

Blue light emission by near-infrared excitation was observed from dye grains of 2,2'-([1,1'-biphenyl]-4,4'-diyl)-di-2,1-ethenediyl)-bis-benzenesulfonic acid disodium salt (Stilbene 3), prepared by the same method as for Coumarin 153 and 102. The emitted light wavelength was approximately 460 nm. The results of pump-probe spectroscopy are shown in Fig. 4.7(a). The lifetime of the intermediate excited state for Stilbene 3 was approximately 2.5 ps.

The cooling time for relaxing toward thermal equilibrium from an excited vibrational state ranges from a few ps to 10 ps for organic dye molecules and GaAs semiconductors [18–20], closely agreeing with our experimental results. Therefore,

it can be concluded that the lifetime of the intermediate excited state observed in this experiment is the lifetime of the intermediate excited state of the dye molecules that contributes to light emission induced by phonon-assisted excitation process. Figure 4.7(b) shows the relationships between emitted light intensities of Stilbene 3, Coumarin 102, and Coumarin 153 obtained under equal excitation conditions, and the lifetime of the intermediate excited states obtained in the experiment. The emitted light intensities decreased as the lifetime of the intermediate excited states became longer. The cooling time constant represents the phonon generation efficiency, and the smaller the cooling time constant is, the higher the phonon generation efficiency becomes. Therefore, the efficiency of the conversion from incident photon to dressed photon, v'_p/u'_p , is also likely higher, and it is speculated that dye grains whose intermediate excited state lifetime is shorter have a greater efficiency of light emission. The lifetime of the intermediate excited state is expected to be closely related to the dimensions and shapes of the grains.

As described above, the lifetime of the intermediate excited state of dye molecules excited by the phonon-assisted excitation was 1.1–2.5 ps, which is extremely short. Therefore, a frequency up-shifting mechanism using the phonon-assisted excitation process has great promise for photodetector applications since it can realize a very rapid response time. An application exploiting this characteristic is described in a later section. In addition, realizing blue-green light emission without using an ultraviolet light source or a pulse laser with a high peak intensity as excitation light [21] can be effective in such areas as display applications.

4.3 Multi-step Phonon-Assisted Process with Two Nondegenerate Beams

In the previous section, blue or green light emission of dye grains induced by the phonon-assisted excitation process was observed. These dyes are transparent to near-infrared light; however, individual protrusions on the dye grains serve as sources of optical near-fields. The energy of these optical near-fields is transferred to dye grains in the vicinity, and their dye molecules are nonadiabatically excited to a vibrational state of higher energy with the aid of the phonon energy in the grains (a two-step phonon-assisted excitation process is shown in Fig. 4.8). Because this intermediate excited state ($|E_g; el\rangle \otimes |E_a; vib\rangle$) is a real energy state, excitation to an even higher energy state ($|E_g; el\rangle \otimes |E_c; vib\rangle$) is possible with the subsequent transfer of the optical near-field energy. Eventually, the dye molecules are excited to an electronic excited state ($|E_{ex}; el\rangle \otimes |E_{em}; vib\rangle$), generating visible light. It has been speculated that phonon-assisted excitation is possible even if the excitation beam used to cause excitation to this intermediate excited state (indicated as 1st step in Fig. 4.2 or Fig. 4.8) and the second excitation beam (2nd step) differ from each other in terms of wavelength, etc. (i.e., mutually nondegenerate). This section describes the experimental results for the multi-step phonon-assisted process with two nondegenerate beams [22].

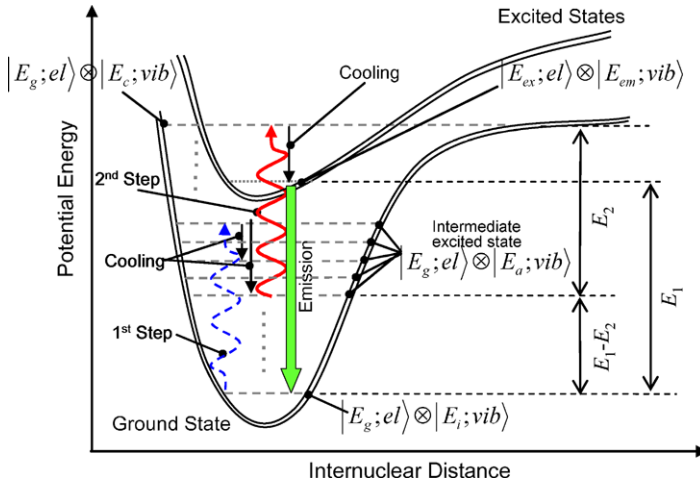


Fig. 4.8 Electronic potential curves in the configuration coordinates of the dye molecules. Illustration explaining the origin of the visible light emission by a two-step phonon-assisted excitation process

4.3.1 Emitted Spectra Induced by Phonon-Assisted Process with Nondegenerate Beams

Dye grains were obtained by dispersing DCM powder in ethanol solution, placing the solution in quartz cells, and evaporating the solution. The size of the dye grains was distributed between 10 nm and several micrometers. The resulting thickness of the dye grains in the quartz cells was 1 mm. DCM has an absorption edge wavelength of about 560 nm and does not absorb near-infrared light in the wavelength range of about 750–1350 nm [14]. However, our previous research has shown that, by irradiating the dye with near-infrared light at wavelengths of about 750–808 nm, the dye molecules are excited by a phonon-assisted process, generating visible light at wavelengths of about 650–700 nm [4].

Using two laser diodes that generated two beams of differing wavelengths as excitation light sources, the emitted light intensities obtained by irradiating the dye grains with the generated CW beams simultaneously or separately were measured and compared. The properties of the first beam (referred to as “signal beam” hereafter) were: wavelength $\lambda_1 = 1150$ nm; intensity $I_{ex(1150)} = 0.55\text{--}2.28$ W/cm²; and linear polarization. The properties of the second beam (referred to as “sampling beam” hereafter) were: wavelength $\lambda_2 = 808$ nm; intensity $I_{ex(808)} = 2.0\text{--}19.9$ W/cm²; and elliptical polarization. Emission spectra of the dye grains were measured using a CCD linear image sensor with a spectrometer.

The emission spectra are shown in Fig. 4.9. The dotted-line curve indicates the emitted light intensity, $I_{808}(\lambda)$, obtained when the sampling beam alone was radiated. The broken-line curve indicates the emitted light intensity, $I_{1150}(\lambda)$, obtained when the signal beam alone was radiated. The solid curve indicates the emitted light

Fig. 4.9 Emitted light spectra of visible light emission from the DCM dye grains due to near-infrared excitation. The *broken-line curve* $I_{1150}(\lambda)$ is the result for irradiation with the signal beam only. The *dotted-line curve* $I_{808}(\lambda)$ is the result for irradiation with the sampling beam only. The *solid-line curve* is the result for simultaneous irradiation with the signal beam and the sampling beam

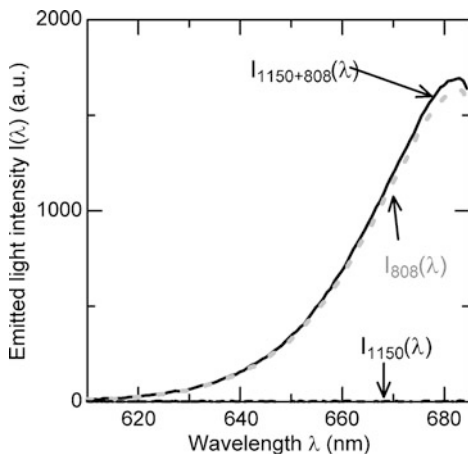
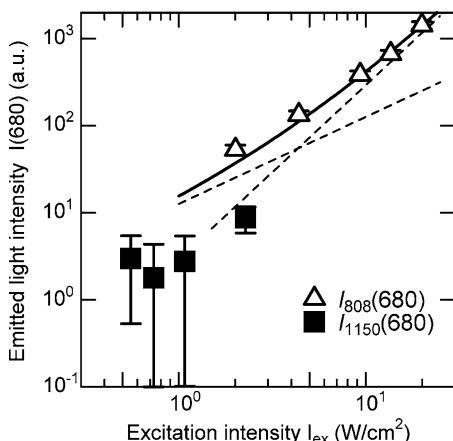


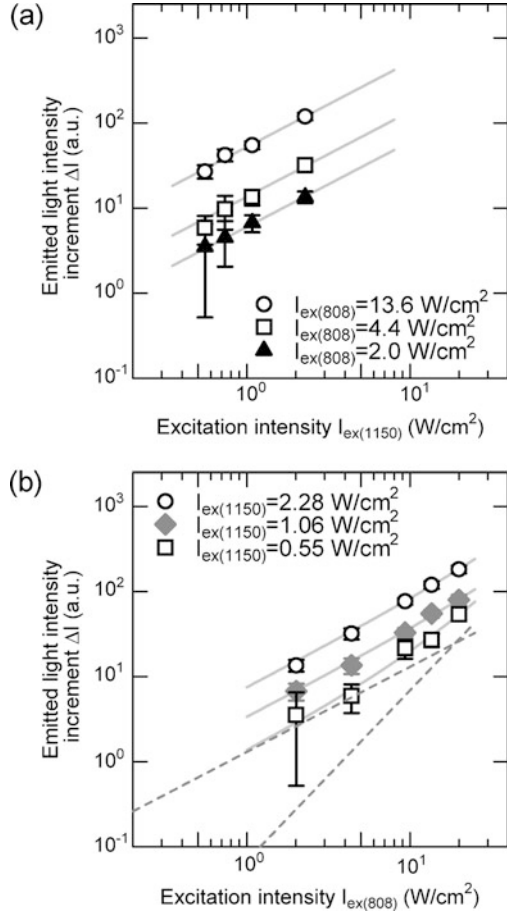
Fig. 4.10 The excitation intensity dependence of the emitted light intensity. *Triangles* indicate the excitation intensity $I_{ex(808)}$ dependence of the emitted light intensity $I_{808}(680)$. *Squares* indicate the excitation intensity $I_{ex(1150)}$ dependence of the emitted light intensity $I_{1150}(680)$. The *solid-line curve* is the result of curve fitting for $I_{808}(680)$ with a quadratic function



intensity, $I_{1150+808}(\lambda)$, obtained when the two beams were radiated simultaneously. The value of $I_{1150}(\lambda)$ was small, approximately equivalent to the noise level of the detector; nonetheless, the value of $I_{1150+808}(\lambda)$ was larger than the sum of the emitted light intensities obtained by separately radiating the signal beam or the sampling beam, i.e. $I_{1150}(\lambda) + I_{808}(\lambda)$. This result suggests that there is an excitation process induced by the simultaneous radiation of the signal beam and the sampling beam.

The triangles in Fig. 4.10 show the relationship between the emitted light intensity $I_{808}(\lambda)$ at $\lambda = 680$ nm (i.e., $I_{808}(680)$) and the excitation light intensity $I_{ex(808)}$ (sampling beam intensity). Similarly, the squares in Fig. 4.10 show the relationship between the emitted light intensity $I_{1150}(\lambda)$ at $\lambda = 680$ nm (i.e., $I_{1150}(680)$) and the excitation light intensity $I_{ex(1150)}$ (signal beam intensity). Because the values of $I_{1150}(680)$ were small, being approximately equivalent to the noise level of the detector, the relationship between $I_{1150}(680)$ and $I_{ex(1150)}$ is not clear. On the other hand, $I_{808}(680)$ was proportional to $I_{ex(808)}$ under weak excitation and proportional

Fig. 4.11 (a) The signal beam intensity $I_{ex(1150)}$ dependence of the emitted light intensity increment ΔI . (b) The sampling beam intensity $I_{ex(808)}$ dependence of the emitted light intensity increment ΔI



to $I_{ex(808)}^2$ under strong excitation. The solid-line curve in the figure was obtained by least squares fitting of a quadratic function, and the broken-line curves show components proportional to $I_{ex(808)}$ and $I_{ex(808)}^2$. These components correspond to the one-step and the two-step phonon-assisted excitation process, respectively [4, 15].

4.3.2 Excitation Intensity Dependence

The excitation process responsible for ΔI will now be discussed, where ΔI is the emitted light intensity increment caused by the simultaneous radiation of the signal beam and the sampling beam, defined as $\Delta I = I_{1150+808}(680) - \{I_{1150}(680) + I_{808}(680)\}$. Figure 4.11(a) shows the relationship between ΔI and the intensity of the signal beam used for excitation, $I_{ex(1150)}$, with the intensity of the sampling beam, $I_{ex(808)}$, as a parameter. The solid straight lines were obtained by least squares fit-

ting of linear functions, and their agreement with the experimental values indicates that one photon of the signal beam contributes to the excitation process. On the other hand, Fig. 4.11(b) shows the relationship between ΔI and the intensity of the sampling beam used for excitation, $I_{ex(808)}$, with the intensity of the signal beam $I_{ex(1150)}$ as a parameter. The solid-line curves in the figure were obtained by least squares fitting of quadratic functions, and the broken straight lines represent values proportional to $I_{ex(808)}$ and $I_{ex(808)}^2$ when $I_{ex(1150)} = 0.55 \text{ W/cm}^2$. These results show that ΔI was proportional to $I_{ex(808)}$ under weak excitation and proportional to $I_{ex(808)}^2$ under strong excitation. The components that are proportional to $I_{ex(808)}$ and $I_{ex(808)}^2$ correspond to the one-step and the two-step phonon-assisted excitation process, respectively.

The signal beam and the sampling beam were mutually nondegenerate, having no correlation in their phases, and they were also low-intensity CW beams. Therefore, the excitation process due to the simultaneous radiation of the signal beam and the sampling beam is likely a multi-step phonon-assisted excitation process brought about by the two mutually nondegenerate beams.

Considering the dependence of ΔI on the excitation intensities (i.e., $I_{ex(1150)}$ and $I_{ex(808)}$), seven potential excitation processes (Processes 1–7) were identified, as shown in Fig. 4.12. For all seven cases, the elapsed time after excitation of dye molecules from the ground state, i.e., $|E_g; el\rangle \otimes |E_i; vib\rangle$, is shown on the horizontal axes.

Process 1 Dye molecules are excited to an intermediate excited state, $|E_g; el\rangle \otimes |E_a; vib\rangle$, by phonon-assisted excitation due to the sampling beam, after which, they cool to a lower energy state, approaching thermal equilibrium, $|E_g; el\rangle \otimes |E_i; vib\rangle$. In this process, however, the molecules are adiabatically excited to an excited state, $|E_{ex}; el\rangle \otimes |E_b; vib\rangle$, by the signal beam, eventually transitioning to an electronic excited state, $|E_{ex}; el\rangle \otimes |E_{em}; vib\rangle$, which is the origin of visible light emission.

Process 2 This process is similar to Process 1 described above, but the 2nd step is the phonon-assisted excitation process due to the signal beam. In this case, the dye molecules are excited by the signal beam from the intermediate excited state, $|E_g; el\rangle \otimes |E_a; vib\rangle$, to an even higher vibrational state, $|E_g; el\rangle \otimes |E_c; vib\rangle$. Eventually, transition to $|E_{ex}; el\rangle \otimes |E_{em}; vib\rangle$ occurs by coupling of a higher vibrational state with an electronic excited state.

Process 3 Molecules are excited to an intermediate excited state by the phonon-assisted excitation by the signal beam, after which, they cool to a lower energy state; however, in this process, they are adiabatically excited by the sampling beam to $|E_{ex}; el\rangle \otimes |E_{em}; vib\rangle$.

Process 4 This process is similar to Process 3 described above, but the 2nd step is the phonon-assisted excitation by the sampling beam, causing an excitation to $|E_{ex}; el\rangle \otimes |E_{em}; vib\rangle$.

Process 5 Phonon-assisted excitation by the sampling beam is repeated twice in exciting the molecules to the intermediate excited state, after which, they cool to a lower energy state; however, in this process, they are adiabatically excited by the signal beam to $|E_{ex}; el\rangle \otimes |E_{em}; vib\rangle$.

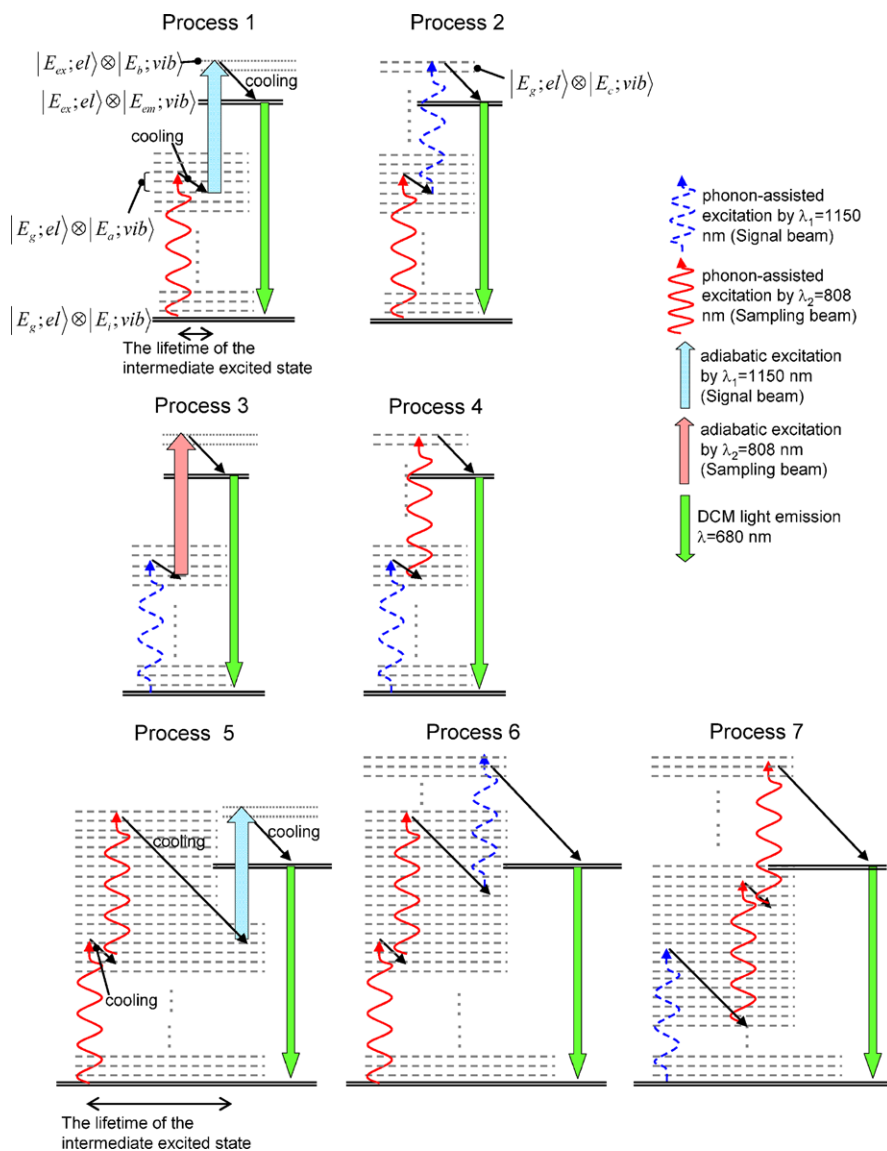


Fig. 4.12 Energy diagrams of phonon-assisted excitation process of the DCM dye grains by the sampling beam and the signal beam. The *broken lines* represent vibrational states of dye molecules at electronic ground states, the *dotted lines* represent the vibrational states of dye molecules at electronic excited states. The elapsed time from the initial excitation of dye molecules at the ground state $|E_g; el\rangle \otimes |E_i; vib\rangle$ is shown on the *horizontal axes*

Process 6 This process is similar to Process 5 described above, but the excitation by the signal beam is nonadiabatic (phonon-assisted), causing an excitation to $|E_{ex}; el\rangle \otimes |E_{em}; vib\rangle$.

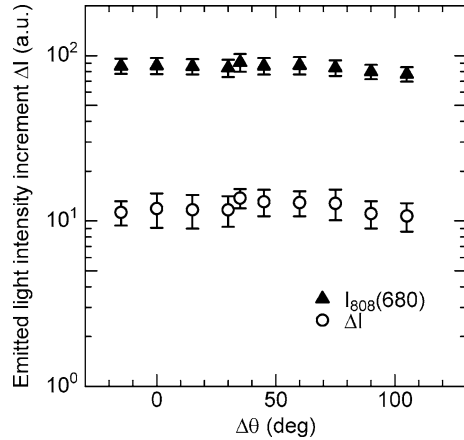
Process 7 The molecules are nonadiabatically excited to the intermediate excited state by the signal beam, after which they relax to a lower energy state and are then nonadiabatically excited by the sampling beam, twice in succession, to $|E_{ex}; el\rangle \otimes |E_{em}; vib\rangle$.

In Fig. 4.11(b), because ΔI has a primary dependency on the sampling beam intensity $I_{ex(808)}$ under weak excitation, the two-photon energy associated with Processes 1–4 is sufficient as the excitation energy required for visible light emission from the dye molecules. Nevertheless, Processes 5–7, involving three photons, appeared because there are dye molecules having low coupling efficiency between the electronic excited state and the molecular higher vibrational state of the ground state, and, in Processes 2 and 4, they do not cool to the electronic excited state $|E_{ex}; el\rangle \otimes |E_{em}; vib\rangle$ but approach thermal equilibrium by cooling. In these Processes 5–7, the time required to reach the electronic excited state, which is the origin of the light emission from dye grains, after the dye molecules in the ground state are excited (i.e., the lifetime of the intermediate excited state) is longer than it is in Processes 1–4.

4.3.3 Dependence of the Difference in Polarization Angle Between Two Nondegenerate Beams

In order to investigate the dependence of the difference in polarization angle between the sampling beam and the signal beam, $\Delta\theta$, on ΔI , the following experiment was conducted. A polarizer and a neutral density filter were placed in the optical path of the sampling beam, and the polarization direction of the linearly polarized sampling beam was controlled while keeping the intensity of a sampling beam incident on the sample constant, i.e., $I_{ex(808)} = 2.2 \text{ W/cm}^2$. The relationship between ΔI and $\Delta\theta$ is shown in Fig. 4.13. The values of ΔI showed nearly no change with respect to $\Delta\theta$. Fluctuations in the values are likely due to the precision in adjusting the sampling beam intensity $I_{ex(808)}$ with the neutral density filter. In support of this, when dye grains are singly irradiated with a sampling beam whose polarization direction is tilted from that of the signal beam by $\Delta\theta$, the resulting emitted light intensity $I_{808(680)}$ actually shows a fluctuation similar to ΔI . Therefore, ΔI is independent of the difference in polarization angle between the sampling beam and the signal beam. Possible reasons for this independence are that the orientation of the dye grains is random, and that the intermediate excited state is a real energy state and information about the polarization direction of the beam that excites the dye molecules to the intermediate excited state is lost. This non-dependence of the emitted light intensity on the difference in polarization angle between the two beams is a considerably different property from sum-frequency generation with nonlinear polarization, in which there is a dependence on the polarization angles of the sampling beam and the signal beam [23].

Fig. 4.13 The relationship between the emitted light intensity increment ΔI and the polarization angle difference $\Delta\theta$ between the signal beam and the sampling beam



The above experimental results showed, for the first time, the existence of a phonon-assisted excitation process by two mutually nondegenerate beams. In addition, unlike sum-frequency generation with nonlinear polarization, with this excitation process, the emitted light intensity did not change with respect to the difference in polarization angle between the two beams.

4.4 Application to Optical Pulse Shape Measurement

There is much demand for optical pulse measurement in the near infrared region at wavelengths of about 1–1.5 μm , which includes optical pulses used in optical fiber communication and pulses from fiber lasers [24–26]. However, the measurement is not easy because there is no photodetector with a high enough sensitivity and a high temporal resolution for this wavelength region. In order to measure optical pulse shapes in the picosecond/femtosecond regime in this wavelength band, sum-frequency generation with nonlinear crystals can be used to convert light of a certain wavelength to a shorter wavelength, whose intensity can then be measured with a photodetector that is sensitive to visible light [27–30]. Because the temporal resolution is determined by the width of the sampling pulse, a high temporal resolution can be obtained by using a short laser pulse. With this method, however, the signal beam (beam to be measured), the sampling beam, and the converted beam (to a short wavelength) must satisfy phase matching conditions [31–34]. As a result, depending on the wavelength of the beam to be measured, it is necessary to provide an optical element for polarization control, such as a wavelength plate, to adjust the angle of incidence to the nonlinear crystals; therefore, this method may not be suitable for measuring beams with a wide wavelength band or exhibiting polarization dependence.

As described in Sect. 4.2, because the energy of the intermediate excited state is greater than the thermal energy, which is determined by the sample temperature,

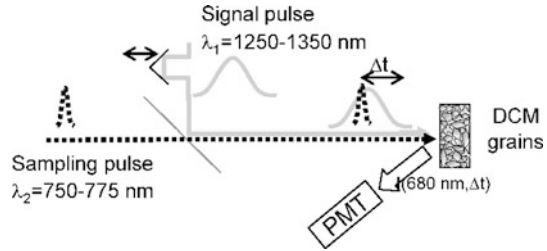
molecules excited by the phonon-assisted process cool to a lower energy state. In the case of dye grains, the amount of time that the dye molecules maintain the energy difference $E_1 - E_2$ (defined as the lifetime of the intermediate excited state, τ), where E_1 is the energy needed for excitation to the electronic excited state (i.e., the origin of visible light emission) and E_2 is the energy needed for the second excitation from the intermediate excited state, has been experimentally shown to be extremely short, at about 2.5 ps or less [15].

By exploiting this phonon-assisted excitation process, assuming the signal beam to be the beam for the first excitation, the sampling beam to be the beam for the second excitation, and visible light emission of the dye to be the resultant sampling signal, optical measurement with a temporal resolution of 2.5 ps should be possible. This optical measurement method does not use nonlinear polarization with polarization dependence but makes use of the vibrational level of molecules with a continuous energy distribution as an intermediate excited state. Therefore, an optical measurement device with a simple optical system, free of polarization dependence, and with a wide measurable wavelength band should be possible. In this section, we discuss the potential application of the phonon-assisted excitation process to optical pulse-shape measurement [22].

4.4.1 Experimental Setup

Pulse-shape measurement using the phonon-assisted excitation process with non-degenerate beams was attempted for the first time with the measuring device illustrated in Fig. 4.14. The signal pulse (center wavelength $\lambda_1 = 1250\text{--}1350$ nm; mean intensity $I_1 = 1.3$ W/cm²; repetition frequency = 80 MHz) to be measured was generated with a Ti:sapphire laser and an optical parametric oscillator (OPO). Also, the pump beam of the OPO was used as the sampling pulse (center wavelength $\lambda_2 = 750\text{--}775$ nm; intensity $I_2 = 3.2\text{--}5.1$ W/cm²; repetition frequency = 80 MHz). After passing along separate optical paths, the two pulses were directed to the same optical path using half mirrors and were made incident on DCM dye grains in a quartz cell at an identical position. Note that the polarization directions of the signal beam and the sampling beams were perpendicular to each other. The length of the optical path for the optical pulse to be measured was made variable to control the difference in time at which the two optical pulses were incident on the dye grains (i.e., delay time), Δt . Components of the emitted light intensity $I(\lambda, \Delta t)$ at the wavelength $\lambda = 680$ nm (i.e., $I(680, \Delta t)$) were extracted with a spectrometer, and the measurement was performed using a photomultiplier tube. When $\Delta t < 0$, the sampling beam reaches the dye grain before the signal beam does, making it possible to observe light emission by Processes 1, 2, 5, and 6 in Fig. 4.12. On the other hand, when $\Delta t > 0$, the sampling beam reaches the dye grains after the signal beam, making it possible to observe light emission by Processes 3, 4, and 7.

Fig. 4.14 Schematic representation of the optical pulse measurement system using the phonon-assisted excitation light emission induced by nondegenerate beams



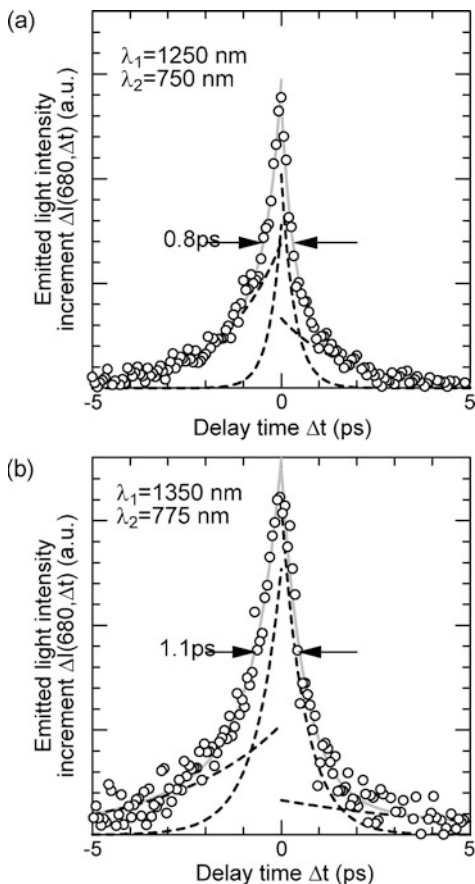
4.4.2 Experimental Results

Figure 4.15(a) shows the results of pulse-shape measurement for the signal beam (wavelength $\lambda_1 = 1250$ nm, intensity $I_1 = 1.3$ W/cm²), where the sampling beam had a wavelength $\lambda_2 = 750$ nm and intensity $I_2 = 3.2$ W/cm². The vertical axis in the figure shows the increment in emitted light intensity, $\Delta I(680, \Delta t)$, defined as: $\Delta I(680, \Delta t) = I(680, \Delta t) - I(680, -\infty)$. In the vicinity of $\Delta t = 0$, values of $\Delta I(680, \Delta t)$ can be clearly observed because of the light emission based on the phonon-assisted excitation process induced by the nondegenerate beams (i.e., the signal beam and the sampling beam). The full width at half maximum of this signal wave profile was about 0.8 ps, and its signal-to-noise ratio (S/N) was 34. The actual time interval of an incident optical pulse can be estimated from its spectral width, and the pulse widths for the signal beam and the sampling beam were estimated to be about 0.2 ps. These estimated widths are smaller than those determined by the measurements in this study. The reasons for this inconsistency were considered. Curve fitting for $\Delta I(680, \Delta t)$ was possible with use of the sum of two exponential functions for the time regions $\Delta t < 0$ and $\Delta t > 0$, respectively (i.e., $A \exp(-\Delta t/\tau_{fast}) + B \exp(-\Delta t/\tau_{slow})$ for $\Delta t > 0$ and $C \exp(\Delta t/\tau_{fast}) + D \exp(\Delta t/\tau_{slow})$ for $\Delta t < 0$). Solid-line curves in Fig. 4.15(a) are the results of least squares fitting. For the region $\Delta t > 0$, decay time constants τ_{fast} and τ_{slow} were 0.35 ps and 1.7 ps, respectively. The coefficient A of the decay component with the decay time constant τ_{fast} is about 4 times greater than the coefficient B of the decay component with the decay time constant τ_{slow} . On the other hand, for the region $\Delta t < 0$, the decay time constants τ_{fast} and τ_{slow} were 0.3 ps and 1.6 ps. There is no substantial difference between the coefficient C of the decay component with the decay time constant τ_{fast} and the coefficient D of the decay component with the decay time constant τ_{slow} . Also, as compared with the region $\Delta t > 0$, the decay component with τ_{slow} has a greater proportion with respect to $\Delta I(680, \Delta t)$. Consequently, the signal waveform profile shown in Fig. 4.15(a) is not symmetrical around $\Delta t = 0$, and compared with the region $\Delta t < 0$, the curve shows a steeper slope in the region $\Delta t > 0$.

The decay time constants τ_{fast} and τ_{slow} can be considered as the lifetime of the intermediate excited state, because the values of τ_{fast} and τ_{slow} (i.e., 0.3–1.7 ps) were approximately equivalent to the lifetime of the intermediate excited states obtained for Coumarin 153, Coumarin 102 and Stilbene 3 dye grains (i.e., 1.1–2.5 ps) in an experiment on phonon-assisted excitation light emission induced by degenerate beams [15]. Therefore, the temporal resolution of this measurement method (i.e.,

Fig. 4.15 (a) Signal wave profiles with $\lambda_1 = 1250$ nm and $\lambda_2 = 750$ nm. (b) Signal wave profiles with $\lambda_1 = 1350$ nm and $\lambda_2 = 775$ nm. The solid-line curves in (a) and (b) are the results of curve fitting ΔI with the sum of two exponential functions. The broken lines indicate the respective exponential functions:

$$A \exp(-\Delta t/\tau_{fast}) + B \exp(-\Delta t/\tau_{slow}) \text{ for } \Delta t > 0, \text{ and } C \exp(\Delta t/\tau_{fast}) + D \exp(\Delta t/\tau_{slow}) \text{ for } \Delta t < 0$$



full width at half maximum of 0.8 ps) is likely determined by the lifetime of the intermediate excited state. The presence of the two decay time constants, τ_{fast} and τ_{slow} , may be explained by the sampling beam contributing to $\Delta I(680, \Delta t)$ through both the two-step (Processes 1, 2 ($\Delta t < 0$), 3, and 4 ($\Delta t > 0$)) and the three-step (Processes 5, 6 ($\Delta t < 0$), and 7 ($\Delta t > 0$)) of the phonon-assisted nondegenerate excitation process.

The signal waveform profile shown in Fig. 4.15(a) is not symmetrical around $\Delta t = 0$ because the dye grains receive different levels of excitation energy from the beam that reaches them first, depending on the excitation routes (Processes 1, 2, 5, and 6 vs. Processes 3, 4, and 7 in Fig. 4.12), and because the lifetime of the intermediate excited states differ accordingly. When $\Delta t > 0$, a signal beam with a long wavelength reaches the dye grains first to excite them to the intermediate excited state, but the photon energy of this excited state is lower than that of the sampling beam with a short wavelength. Therefore, because the lifetime of the intermediate excited state is short, the waveform profile in the $\Delta t > 0$ region is steeply sloping downward.

Figure 4.15(b) shows the results of pulse-shape measurement for the signal beam (wavelength $\lambda_1 = 1350$ nm, intensity $I_1 = 1.3$ W/cm²) where the sampling beam had a wavelength $\lambda_2 = 775$ nm and intensity $I_2 = 5.1$ W/cm². Keeping the incident angle to the sample identical to the case shown in Fig. 4.15(a), a signal waveform with a full width at half maximum of about 1.1 ps and an S/N of 19 was measured. As with Fig. 4.15(a), curve fitting for the signal waveform $\Delta I(680, \Delta t)$ is possible with use of the sum of two exponential functions for the time regions $\Delta t < 0$ and $\Delta t > 0$, respectively. For the region $\Delta t > 0$, decay time constants τ_{fast} and τ_{slow} were 0.62 ps and 5.2 ps, respectively, and, for the region $\Delta t < 0$, decay time constants τ_{fast} and τ_{slow} were 0.69 ps and 3.0 ps, respectively. Similarly to Fig. 4.15(a), the signal waveform profile is not symmetrical around $\Delta t = 0$, and, compared with the region $\Delta t < 0$, the curve is steeply sloping downward in the region $\Delta t > 0$.

As shown by the above experimental results, the signal waveform obtained by the optical pulse-shape measurement using phonon-assisted excitation light emission from the DCM dye grains induced by nondegenerate beams had a measurement wavelength range of 1250–1350 nm and an S/N of about 19–34. The full width at half maximum was about 0.8–1.1 ps, which is likely constrained by the lifetime of intermediate excited state. With this measurement method, there is no restriction on angular correlation between the polarization directions of the signal beam and the sampling beam, nor is there any need for a device for controlling the polarization direction before the beam reaches the dye grains, such as a wavelength plate. In addition, a wide wavelength region can be measured with this method because the incident angle to the dye grains can be fixed independent of the wavelength of the signal beam.

4.5 Summary

Blue–green light emission from dye grains, Coumarin 153, Coumarin 102 and Stilbene 3, by near-infrared excitation was observed. This phenomenon was based on phonon-assisted excitation. A maximum frequency up-shift of 1.17 eV was confirmed. Based on the excitation intensity dependence, manifestation of a light emission mechanism by three-step phonon-assisted excitation was confirmed. The lifetime of the intermediate excited state was shown to be 1.1–2.5 ps. The frequency up-shifting mechanism based on the phonon-assisted excitation in the dye grains is very promising for application to fast-response infrared photodetectors.

Using DCM dye grains and mutually nondegenerate beams generated by two CW laser diodes, visible light emission from the dyes by near-infrared excitation based on a phonon-assisted, nondegenerate excitation process was observed. This principle was applied to optical sampling as a measurement method. As a result, the optical pulse shape in the wavelength band of $\lambda = 1250$ –1350 nm, which is close to the wavelength range used for optical fiber communications, was measured with a temporal resolution of 0.8–1.1 ps.

Acknowledgements This chapter is a reconstituted document based on Refs. [4, 15], and [22]. This work was partially supported by a New Energy and Industrial Technology Development Organization (NEDO) project on a comprehensive activity for personal training and industry-academia collaboration.

References

1. A. Rogalski, M. Razeghi, Proc. SPIE **3287**, 2 (1998)
2. H.J. Baker, J.J. Bannister, T.A. King, E.S. Mukhtar, Appl. Opt. **18**, 2136 (1979)
3. P.W. Atkins, J. Paula, Molecular spectroscopy 2: electronic transitions, in *Physical Chemistry*, 9th edn. (Oxford University Press, Oxford, 2010), p. 489
4. T. Kawazoe, H. Fujiwara, K. Kobayashi, M. Ohtsu, IEEE J. Sel. Top. Quantum Electron. **15**, 1380 (2009)
5. M. Ohtsu, K. Kobayashi, T. Kawazoe, T. Yatsui, M. Naruse, *Principles of Nanophotonics* (CRC Press, Boca Raton, 2008)
6. T. Kawazoe, K. Kobayashi, S. Takubo, M. Ohtsu, J. Chem. Phys. **122**, 024715 (2005)
7. T. Kawazoe, Y. Yamamoto, M. Ohtsu, Appl. Phys. Lett. **79**, 1184 (2001)
8. T. Kawazoe, K. Kobayashi, M. Ohtsu, Appl. Phys. B **84**, 247 (2006)
9. W. Nomura, T. Yatsui, Y. Yanase, K. Suzuki, M. Fujita, A. Kamata, M. Naruse, M. Ohtsu, Appl. Phys. B **99**, 75 (2010)
10. H. Yonemitsu, T. Kawazoe, K. Kobayashi, M. Ohtsu, J. Lumin. **122–123**, 230 (2007)
11. T. Kawazoe, M. Ohtsu, Y. Inao, R. Kuroda, J. Nanophotonics **1**, 011595 (2007)
12. T. Kawazoe, T. Takahashi, M. Ohtsu, Appl. Phys. B **98**, 5 (2010)
13. T. Yatsui, K. Hirata, W. Nomura, Y. Tabata, M. Ohtsu, Appl. Phys. B **93**, 55 (2008)
14. U. Brackmann, *Lambdachrome Laser Dyes*, 3rd edn. (Lambda Physik, Fort Lauderdale, 2000)
15. H. Fujiwara, T. Kawazoe, M. Ohtsu, Appl. Phys. B **98**, 283 (2010)
16. F.M. Lee, C.E. Stoops, L.E. Lahti, J. Cryst. Growth **32**, 363 (1976)
17. D.W. Marquardt, SIAM J. Appl. Math. **11**, 431 (1963)
18. F. Laermer, T. Elsaesser, W. Kaiser, Chem. Phys. Lett. **156**, 381 (1989)
19. H.-J. Polland, W.W. Rühle, K. Ploog, C.W. Tu, Phys. Rev. B **36**, 7722 (1987)
20. Y. Rosenwaks, M.C. Hanna, D.H. Levi, D.M. Szymd, R.K. Ahrenkiel, A.J. Nozik, Phys. Rev. B **48**, 14675 (1993)
21. G.S. He, R. Signorini, P.N. Prasad, Appl. Opt. **37**, 5720 (1998)
22. H. Fujiwara, T. Kawazoe, M. Ohtsu, Appl. Phys. B **100**, 85 (2010)
23. K. Kato, IEEE J. Quantum Electron. **QE-22**, 1013 (1986)
24. A. Takada, M. Saruwatari, Electron. Lett. **24**, 1406 (1988)
25. H. Lobentanzer, H.-J. Polland, W.W. Rühle, W. Stolz, K. Ploog, Appl. Phys. Lett. **51**, 673 (1987)
26. M.E. Fermann, A. Galvanauskas, M.L. Stock, K.K. Wong, D. Harter, L. Goldberg, Opt. Lett. **24**, 1428 (1999)
27. C. Dorrer, IEEE J. Sel. Top. Quantum Electron. **12**, 843 (2006)
28. H. Ohta, S. Nogiwa, Y. Kawaguchi, Y. Endo, Electron. Lett. **36**, 737 (2000)
29. H. Ohta, N. Banjo, N. Yamada, S. Nogiwa, Y. Yanagisawa, Electron. Lett. **37**, 1541 (2001)
30. H. Takara, S. Kawanishi, A. Yokoo, S. Tomaru, T. Kitoh, M. Saruwatari, Electron. Lett. **32**, 2256 (1996)
31. A. Yariv, W.H. Louisell, IEEE J. Quantum Electron. **QE-2**, 418 (1966)
32. S. Umegaki, S. Yabumoto, S. Tanaka, Appl. Phys. Lett. **21**, 400 (1972)
33. S. Umegaki, S. Tanaka, Jpn. J. Appl. Phys. **16**, 775 (1977)
34. G.C. Bhar, U. Chatterjee, Jpn. J. Appl. Phys. **29**, 1103 (1990)

Chapter 5

Micro and Extended-Nano Fluidics and Optics for Chemical and Bioanalytical Technology

Kazuma Mawatari, Yuriy Pihosh, Hisashi Shimizu, Yutaka Kazoe, and Takehiko Kitamori

Abstract Integrated chemical systems on microfluidic chips are further downscaling to 10^1 – 10^3 nm scale, which we call extended-nano space. The extended-nano space is a transient space from single molecules to bulk condensed phase, and new liquid properties can be expected in fluidics and chemistry. Actually, many unique liquid properties are increasingly reported which are quite different with microspace. In addition, development of new chemical devices is in progress by utilizing the unique characteristics of extended nanospace. Although new research area is being formed, there exist many challenges in fundamental technologies (nanofabrication, fluidic control, detection, partial surface modification, etc.) due to the extremely small size. Optical near field (ONF) technology is one promising solution because the size of ONF is comparable with extended-nano space and also has unique optical properties such as non-adiabatic optical transitions. In this chapter, we introduce our approach to construct a new micro and extended-nano chemical systems by utilizing the unique characteristics of ONF.

5.1 Introduction

In a past half century, electronics technologies progressed rapidly. Electronic components such as transistors, capacitors and resistance were integrated to a circuit by micro/nano fabrication technologies, and the device technologies were established. In addition, the integration technologies allowed higher performance of the information processing. Due to the development, general people can use the miniaturized electronic systems (e.g. laptop computer and cell phone) without any significant difficulties. However, if we look at chemical and biological field, the available technologies have not been changed significantly. For example, if we consider solvent extraction experiments which are used to analyze target molecules by extracting the molecules to organic or aqueous phase, traditional apparatus such as a flask, shaker and pipette has been utilized. Device technology in chemistry and biotechnology

K. Mawatari (✉)

Department of Applied Chemistry, School of Engineering, The University of Tokyo,
7-3-1 Hongo, Bunkyo, Tokyo 113-8656, Japan
e-mail: kmawatari@icl.t.u-tokyo.ac.jp

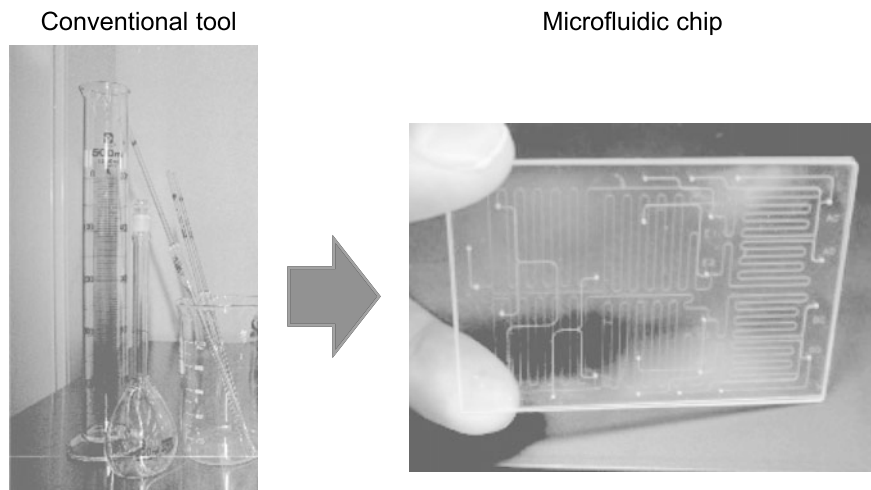


Fig. 5.1 Traditional apparatus for chemical experiments and microfluidic chip

also has not been developed. In developing a chemical plant, the volumes of the traditional apparatus were scaled up with much effort to realize uniform mixing and temperature control.

In 1990s, integrated micro chemical systems on a chip have been developed (Fig. 5.1) [1, 2]. Microfabrication technologies were applied, and microfluidic channels with a size of 10–100 μm were fabricated on silicon, glass and plastic substrates. In the microspace, many chemical operations were integrated in microspace as micro unit operations (MUOs) [3]. These chemical operations include mixing, reaction, detection, separation, extraction, distillation, concentration. The fundamental technologies were also developed, which were pressure-driven microfluidics, surface control methods, detection technologies and fabrication methods. Those methods allowed varieties of analysis, synthesis and biochemical systems integrated on microchips, and their superior performances such as rapid, simple, and high efficient processing have been proved. Currently, practical microsystems are being developed in clinical diagnosis, environmental analysis, food analysis, drug synthesis and basic research for biology, pharmaceutical, tissue engineering.

Recently, micro fluidic technologies were applied to 10^1 – 10^3 nm scale space which we call extended-nano space to distinguish from nanospace or nanotechnology dealing with 10^0 – 10^1 nm space (Fig. 5.2). The extended-nano space bridges between single molecules in nanospace and normal condensed phase in bulk, and the liquid properties and chemistry in extended-nano space have not been clarified. One main reason is that the space is 2–3 orders smaller than microspace, and the technologies developed for microspace cannot be utilized. In order to solve these problems, the basic research tools for extended-nano space were rapidly developed in a recent few years. In particular, optical technologies play significant roles for detection in chemistry and fluidics. Due to the technical development, new specific

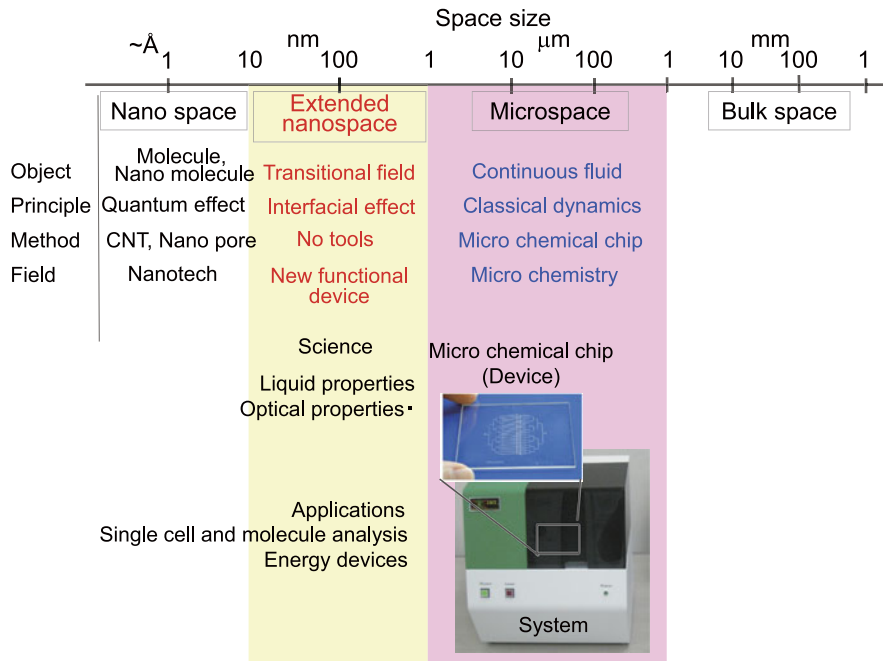


Fig. 5.2 Size hierarchy and micro and extended-nano space

phenomena in fluidics and chemistry were clarified, which were quite different with the liquid properties in micro or bulk space [4, 5]. From a view point of photonics, the extended-nano scale is comparable or smaller than light wavelength. Therefore, nanophotonics will play an important role to understand the phenomena. For application, by combining fluidics, chemistry, photonics, new device technologies can be expected. Ohtsu's group proposed a new concept of phonon-polariton, which is generated by illuminating a light for extended-nano objects [6]. The phonon-polariton allows optical excitation pathways which are usually prohibited by utilizing phonon energy. As a consequence, the phonon-polariton apparently behaves as a higher energy photon than incident photon energy. These characteristics were applied to TiO₂ water splitting by visible light.

In this chapter, we will introduce micro and extended-nano fluidics and its applications. Because this book focusing on nanophotonics, several optical technologies were selected, which were used for detection and reaction.

5.2 Technology and Applications by Microfluidics

5.2.1 Integration Methods

For realizing various chemical processes, we should utilize many chemical operations. These chemical operations can usually be divided to unit operations. As the

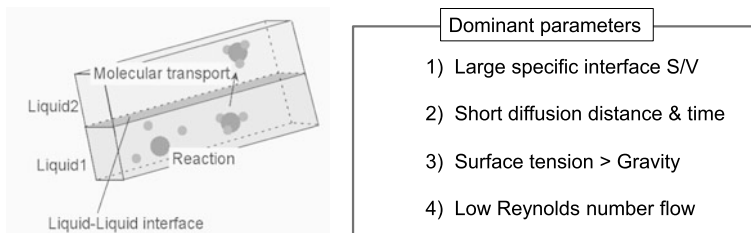


Fig. 5.3 Characteristics of liquid in microspace

► Stabilization of multiphase microflow

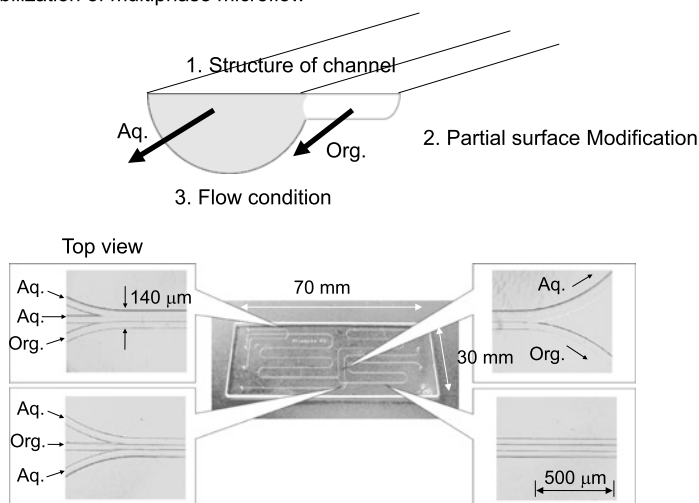


Fig. 5.4 Stabilization of multiphase laminar flow

bulk chemical processing plant, the bulk scale operations could include multiphase reaction, mixing, separation, detection, etc. However, direct miniaturization of bulk scale unit operation cannot be applied in microspace. For the integration, unique characteristics of microspace should be considered as shown in Fig. 5.3. For example, surface or interfacial force is several orders larger than gravity force. Therefore, conventional chemical operations using gravity force cannot be scaled down in the same format. Rather, surface properties should be carefully adjusted to control the liquid flow. For multiphase laminar flow, wall of the microfluidic channels is partially modified with chemical reagent such as hydrophobic molecules. By controlling the surface properties, multiphase flows can easily formed (Fig. 5.4), which was quite difficult to form in bulk. Then, MUOs that perform similar functions can be achieved, and the MUOs are in place of resistor, capacitor, and diode in an integrated circuit. In particular, multiphase laminar flow is an important fluidic format to realize MUOs. In Fig. 5.5, bulk scale unit operations for solvent extraction were converted to MUOs by multiphase laminar flow. Then, the MUOs can be combined

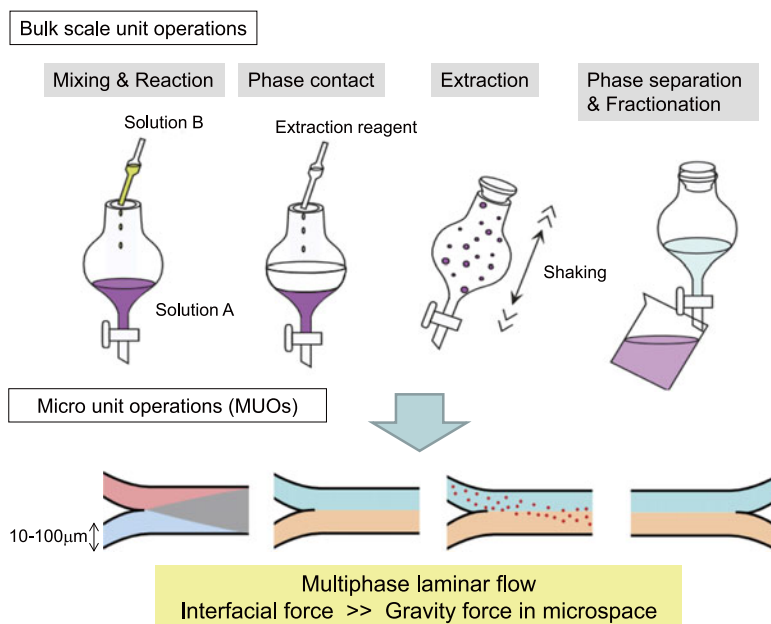


Fig. 5.5 Stabilization of multiphase laminar flow

in parallel and serial like an electric circuit by continuous flow chemical processing (CFCP) as shown in Fig. 5.6. The function of the integrated microfluidic chips is analogous to that of a chemical central processing unit.

The combination of MUOs and its arrangement are dependent on specific applications. Usually, for specific chemical processes, a national standard procedure is settled. For example of cobalt ion analysis, the procedure is illustrated in Fig. 5.7 (left). Standard procedures consist of a complex formation reaction, solvent extraction, and decomposition and removal of the coexisting metal complex. For each chemical operation, aqueous solution is wasted, and organic phase are utilized and transferred to the next process. The standard analytical procedure is decomposed to unit operations, which are mixing, reaction, phase contact, extraction, phase separation and determination as shown in Fig. 5.7 (middle). Finally, the corresponding MUOs are assigned to each unit operation. The MUOs are connected in parallel and serial, and microfluidic chip can be realized (Fig. 5.8), which works as a chemical device [7]. These are general designing process of microfluidic chip. The channel size and length can be also designed when the bulk scale reaction and diffusion time is known. Computational fluid dynamics (CFD) software will be helpful for the design.

These process are established general integration procedures and can be applied various chemical processes in analytical and chemical synthesis fields. The application fields are wide from medical diagnosis, environmental analysis, food analysis, process analysis, cell biology, tissue engineering, cosmetics, pharmaceutical, and

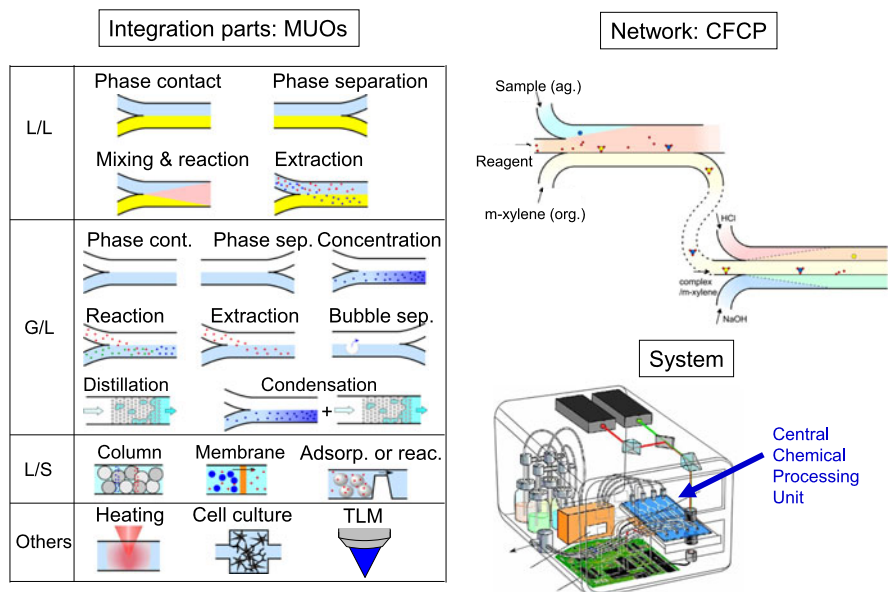


Fig. 5.6 Stabilization of multiphase laminar flow

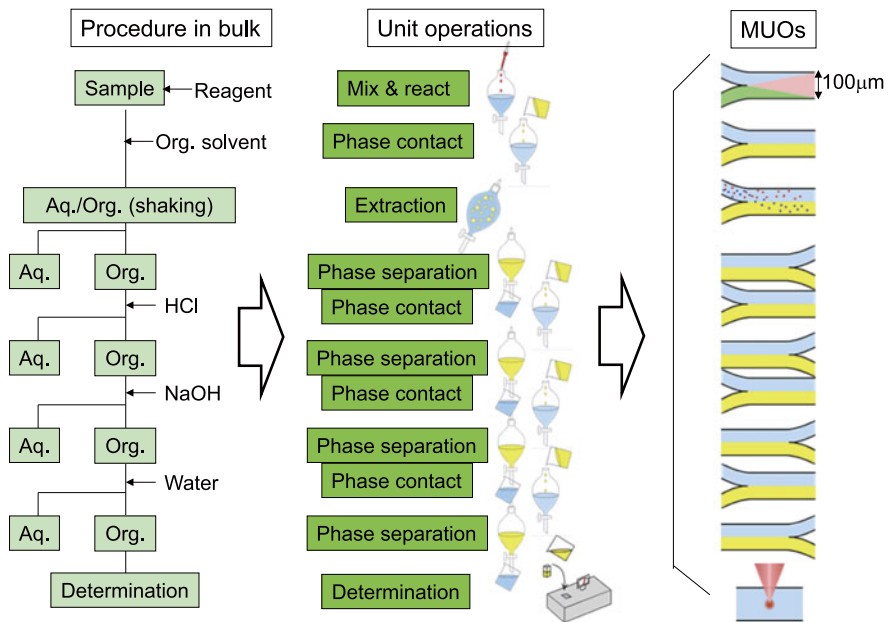
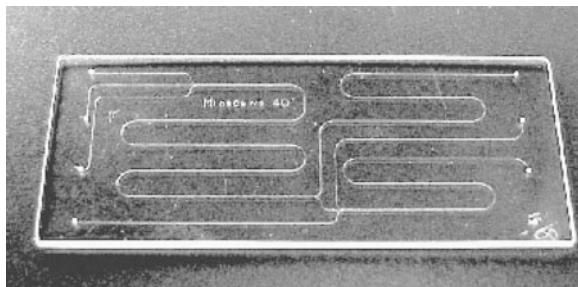


Fig. 5.7 Conversion of bulk procedures to MUOS (example of solvent extraction)

Fig. 5.8 Co ion analysis chip in which MUOs are integrated in parallel and serial

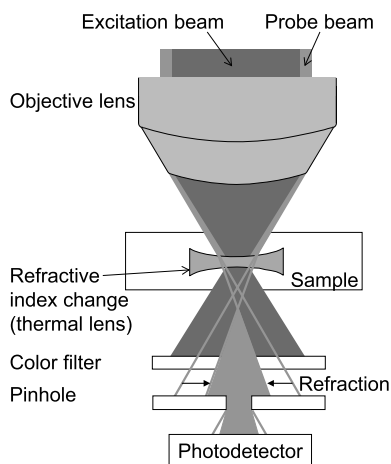


production of fine chemicals. In conventional methods, the procedures are quite troublesome because washing processes by hydrochloric acid, water, and sodium hydroxide solution are repeated step-by-step. In addition, the conventional procedures need a long analysis time (e.g. 6 hours for cobalt ion analysis). In microfluidic chips, chemical reaction and molecular transport can be realized in continuous flow chemical process. It provides advantages of small sample and reagent volume, short process time, simplicity and omission of troublesome operations. These integration approaches allowed device technology in chemistry and biotechnology for the first time.

5.2.2 Optical Detection Method for Single Molecule Detection

Single molecule detection is the largest landmark in the history of analytical chemistry as an achievement of the ultimate sensitivity in analysis. Furthermore, single molecule detection has great influences in various fields such as physics, chemistry, biology and medicine since it allowed us direct, real-time investigations of molecular dynamics, enzymatic activities of single enzymes and intra- and intermolecular interactions of biomolecules [8]. In particular, single molecule detection is strongly required in micro- and nanospace because the number of analyte molecules is reduced with decreasing detection volume [9]. For example, if 1 nM solution is filled in a 1 μm cube, the expected number of analytes is 0.6, which represents the necessity of single molecule detection.

Laser spectroscopy has been frequently used to detect single molecules in microspace because laser can be tightly focused and increase sensitivity dramatically. The most successful single molecule detection method is laser induced fluorescence (LIF) combined with a confocal microscope or total internal reflection microscope. The well-established setups of LIF can decrease background signal of solvent to distinguish fluorescence signal of analyte from the background. However, LIF can detect only fluorescent molecules, while most of molecules have no fluorescence. Therefore, single molecule detection method for nonfluorescent molecules is strongly required for further applications of microfluidics. To date, some other single molecule detection methods have been proposed such as scanning electrochemical microscope (SECM) and surface enhanced Raman spectroscopy (SERS), although the analytes are still limited to a small range of molecules.

Fig. 5.9 Principle of TLM

In order to detect a wide range of nonfluorescent molecules, an absorption-based method is desirable. Among the absorption-based methods, photothermal spectroscopy is known to be the most sensitive method. Photothermal spectroscopy detects nonfluorescent molecules based on light absorption and nonradiative relaxation of analyte molecules. When a molecule in a ground state is excited by light, the molecule in an excited state relaxes via a radiative or nonradiative process. Here, almost all molecules produce thermal energy with nonradiative processes because few molecules have fluorescence quantum efficiencies of nearly 1. Therefore, measurements of the thermal energy make it possible to detect a wide range of molecules. The detection methods using the light-to-heat conversion are called photothermal spectroscopy. Photothermal spectroscopy is known to be much more sensitive than other absorption spectroscopies because a use of high-brightness laser can dramatically increase the intensity of the photothermal effects. In particular, thermal lens spectroscopy (TLS) is well-known as a very sensitive method which can detect small amount of molecules in solutions [10]. However, TLS could not be performed under an optical microscope, which led to difficulties of measurements.

The problem was solved by a development of thermal lens microscope (TLM) [11]. The principle of TLM is illustrated in Fig. 5.9. A sample is heated by an excitation laser through absorption and nonradiative relaxation. Then, a local change in refractive index is induced in the sample medium. This change in refractive index is called thermal lens because its distribution is similar to a concave lens. As a result, a probe laser introduced coaxially is refracted by the thermal lens and a change of light density is detected by a pinhole and photodetector. In order to realize this principle, the focal points of the excitation and probe beam must be mismatched along z axis. If the focal point of the excitation beam is lower than that of the probe beam, the probe beam is diverged as Fig. 5.10(a). Contrary, if the excitation focus is in upper side, the probe beam is converged as Fig. 5.10(c). Although the both configurations make the probe beam refracted, the probe beam is not refracted if the two beams are

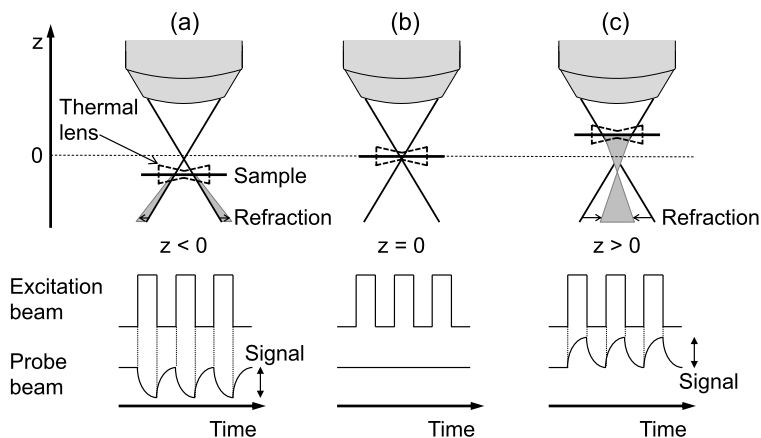


Fig. 5.10 Relationship of focal points configurations and thermal lens signal

focused at the same point as Fig. 5.10(b). Therefore, for thermal lens microscope, an objective lens with a chromatic aberration (not apochromatic one) is used, or the two focal points are intentionally mismatched using uncollimated beams. The output of the photodetector is finally fed into a lock-in amplifier to obtain a thermal lens signal. When the excitation beam is intensity-modulated at a certain frequency, the intensity of the refracted probe beam also oscillates at the frequency as shown in Fig. 5.10 (bottom). Then, the amplitude of the oscillation is extracted as the thermal lens signal which is proportional to the absorbance of the analyte solution.

Figure 5.11 is an example of calibration curve obtained by a TLM [12]. The analyte is aqueous solution of a nonfluorescent dye. In this experiment, the volume of detection area was estimated as the confocal volume (1.3 fL). Then, the amount of detected molecules was calculated to be 0.13–2.6 zmol and the limit of detection was 85 ymol (50 molecules). Thus, an ultrasensitive measurement of a nonfluorescent molecule could be realized using the TLM. In addition, the thermal lens signal can be enhanced by some kinds of organic solvents due to their large temperature gradient of refractive index (dn/dT) and low thermal conductivity. This tells that more sensitive, single molecule level measurement might be possible using a TLM. Figure 5.12 is a calibration curve of a nonfluorescent metal porphyrin complex dissolved in benzene [13]. The calibration curve was linear in a range of countable number of molecules and the LOD reached to 0.34 molecules in 7.2 fL. The physical meaning of this subsingle molecule detection is explained as following. If the number of molecules is such a low level, the probability of the molecule becomes Poisson distribution. The distribution tells us that there is no molecule in most cases, and sometimes one molecule in the detection volume. From Debye-Einstein-Stokes theory, the analyte molecule goes through the detection volume in several milliseconds by diffusion. On the other hand, a time constant of lock-in amplifier, that is an integration time of signal, is several seconds to determine the low concentration. Therefore, thousands of molecules enter and leave the detection volume and their probability is averaged as an expected number of molecules.

Fig. 5.11 Calibration curve of a nonfluorescent dye in water

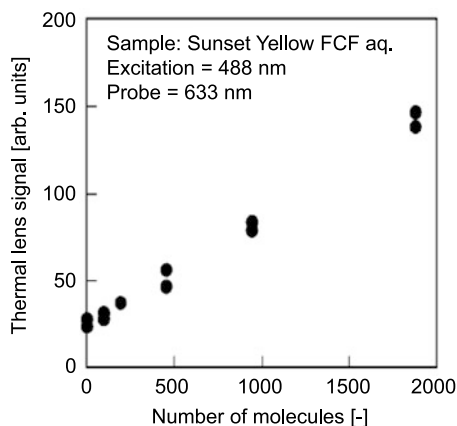
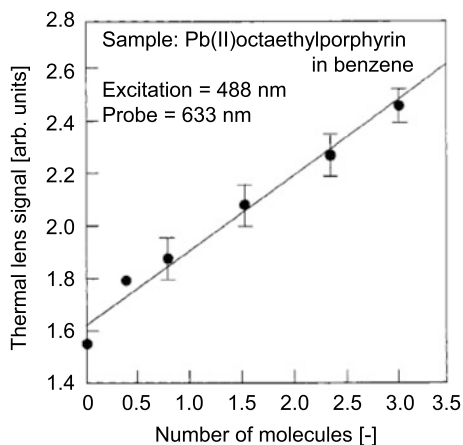


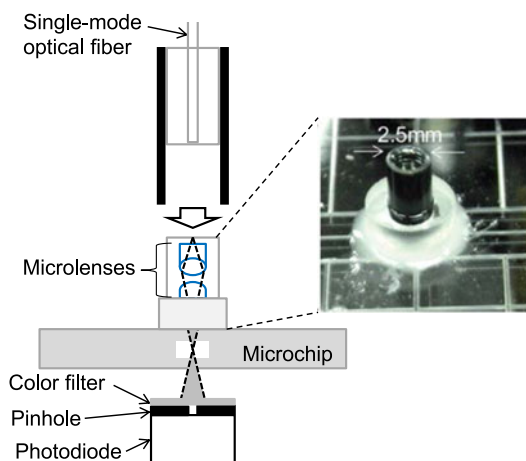
Fig. 5.12 Calibration curve of a metal porphyrin complex in organic solvent



The TLM which has such a splendid detection performance for nonfluorescent molecules has already been commercialized. For example, a standard TLM was developed as a product by incorporating laser optics into an optical microscope. In addition, the TLM was also miniaturized as a built-in detection device for microfluidic analysis systems such as immunoassay and ammonia detection. Figure 5.13 shows a structure of the thermal lens detection device [14]. An optical fiber is used to guide the excitation and probe lasers and connected with three microlenses fixed on a microchip to focus the lasers. Owing to this technical development, various microfluidic devices with sensitive absorptometric detection entered into the market.

As explained before, TLM can determine a concentration of subsingle molecule level, although thousands of molecules are involved in the measurement with an averaging time of several seconds. Contrary, a transit of single molecule can be detected with an averaging time of milliseconds which is same time scale as Brownian diffusion. However, such single molecule counting measurement has a difficulty deriving from the principle of TLS. In the principle of conventional TLS, a small

Fig. 5.13 Components of thermal lens detection device



intensity change by refraction of a probe beam is detected as a signal (S). On the other hand, the original intensity of the probe beam becomes optical background (B), which leads to a very small signal-to-background (S/B) ratio of 10^{-5} . In case of concentration determination, the small signal can be recovered by averaging signal for several seconds using a lock-in amplifier. However, in case of counting, the single molecule signal is buried in the large optical background because the signal cannot be time-averaged. Subsequently, a reduction of the optical background is indispensable to single molecule counting by TLM.

In order to solve this problem, a principle realizing background-free detection, differential interference contrast (DIC) method was introduced into TLM [15]. Figure 5.14 illustrates the principle of differential interference contrast thermal lens microscope (DIC-TLM). A probe beam is separated by a DIC prism and mixed again by another DIC prism to make interference. Due to the interference, the probe intensity becomes zero and background-free is achieved. On the other hand, the excitation beam is not separated, by controlling its polarization plane. Then, the excitation beam is absorbed by an analyte and a local refractive index change is induced for one of the two probe beams. This produces phase contrast between the two probe beams to be detected by the interference. Since the transmitted probe beam is detected only when the analyte is in the detection volume, this principle realizes background-free detection of photothermal effects.

Figure 5.15 shows results of single gold nanoparticle (5 nm) counting using conventional TLM and DIC-TLM. In the results, many pulse signals were observed when the particles transited the detection volume. The pulse signals were confirmed to be generated not by scattering, but by photothermal effect of nanoparticles. The signal-to-noise (S/N) ratio of the pulse signal was dramatically improved by DIC-TLM. This was because the optical background was reduced by the interference to decrease the baseline noise. Thus, DIC-TLM realized ultrasensitive detection of single metallic nanoparticles, which suggests the possibility of single molecule counting. Considering absorption coefficients of porphyrin molecules and the sig-

Fig. 5.14 Principle of DIC-TLM

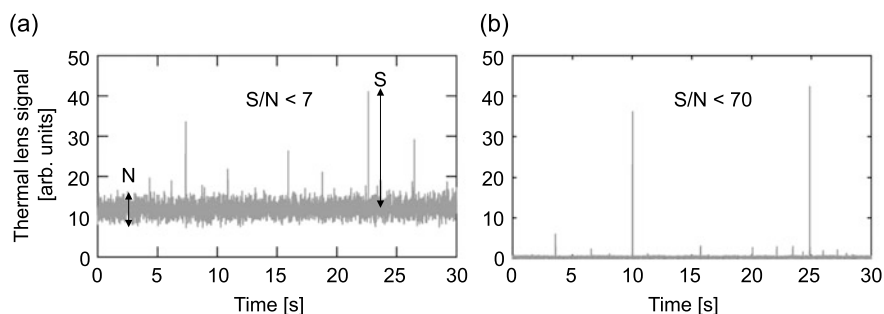
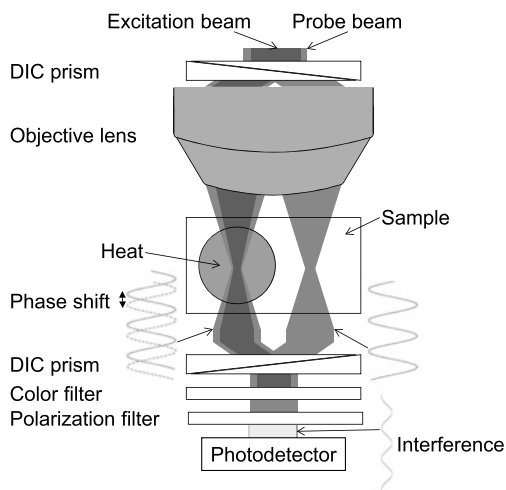


Fig. 5.15 Results of single gold nanoparticle counting by (a) conventional TLM and (b) DIC-TLM

nal enhancement by organic solvents, S/N ratios of single porphyrin molecules are detectable. Moreover, large protein molecules could be also detected if a UV excitation beam is used. If the detection of single nonfluorescent molecule is realized, targets of single molecule chemistry would be expanded largely.

5.2.3 Applications

After proposal of general integration methods utilizing MUOs and CFCP, the application field of microfluidic technology was rapidly expanded from DNA separation/detection to general chemistry and biochemistry. The fundamental technologies have been established, and practical systems are currently realized. In the system, optical technologies are one of breakthrough to detect very small amount of analyte molecules. Several companies commercialized practical microsystems. Some examples are illustrated in Fig. 5.16.

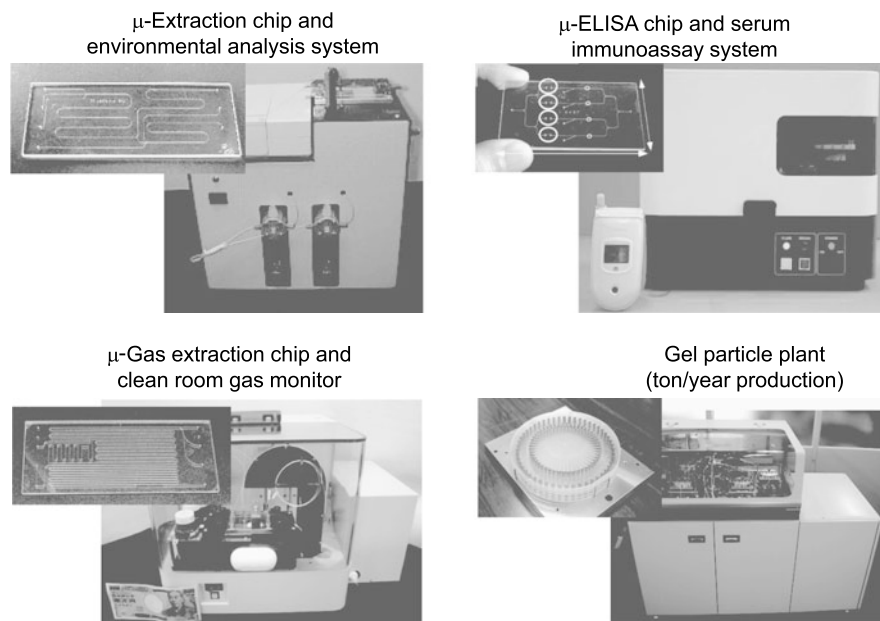


Fig. 5.16 Practical microsystems for analytical and chemical synthesis fields

Among the practical systems, a blood analysis system using immunoassay is introduced here. Immunoassays are important analytical methods for clinical diagnosis (cancer, virus infection, allergy, cardiovascular, etc.) and can be used for quantitative or qualitative analysis of proteins in blood. The immunoassay utilized immunoreaction between antigen and antibody. There are several methods to realize the immunoassay. The most popular method is enzyme-linked immunosorbent assay (ELISA). In ELISA, antibody or antigen was immobilized on a solid support, and analyte molecules are captured by the immunoreaction. In order to determine the amount of captured analyte molecules, enzyme-labeled antibody was introduced and captures the analyte molecules. After introduction of substrate, the substrate reacts with the enzyme, and colored products (dyes) are generated. The concentration of the dyes is determined by absorption photometry. As shown in a previous section, the immunoassay can be converted to MUOs as shown in Fig. 5.17. The procedure includes (1) immunoreaction of antigen (analyte) and antibody, (2) washing, (3) immunoreaction of antigen and enzyme-labeled antibody, (4) washing, (5) enzymatic reaction of substrate and enzyme and (6) concentration determination. These processes can be decomposed to unit operations, and almost all the unit operations can be realized by same MUOs (immunoreaction on microbeads). Then, an integrated microfluidic chips can be designed and fabricated (Fig. 5.18). A dam structure was used to trap microparticles inside the microfluidic channel. Based on the chip design and fabrication, a miniaturized automated system was realized. The fluidic components such as a syringe pump, micro-valve, dispenser and connector were integrated into a system together with a sensitive optical detection component (TLM device)

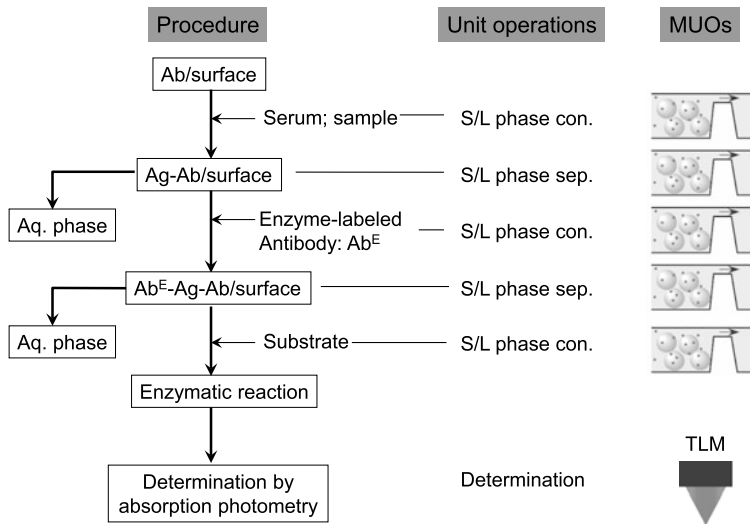
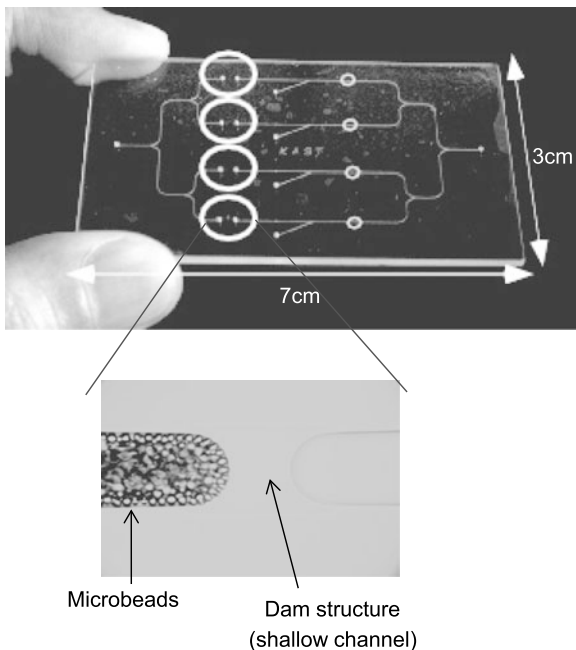


Fig. 5.17 Conversion immunoassay procedure to MUOs

Fig. 5.18 A photograph of microELISA chip



as shown in Fig. 5.19. The data showed very good correlation with conventional method for allergy diagnosis [16]. The reliability of the system was verified with patient serum. The superior performance was also verified in shortening analysis

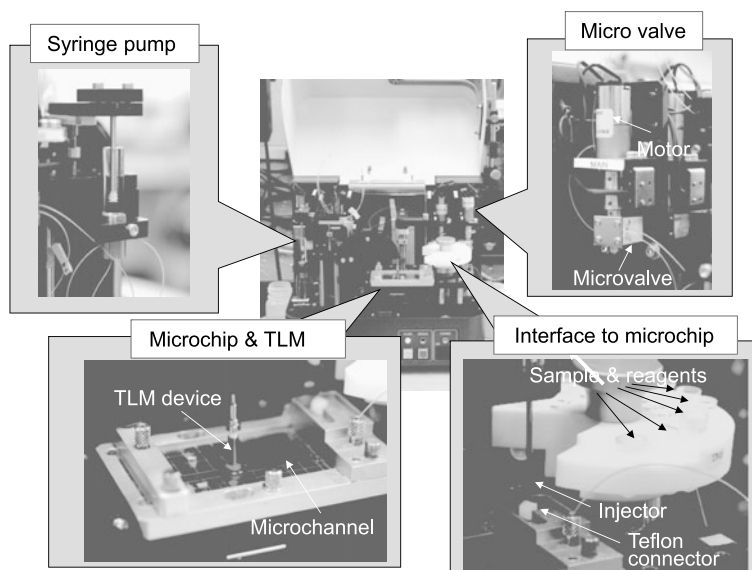


Fig. 5.19 Developed automated microELISA system

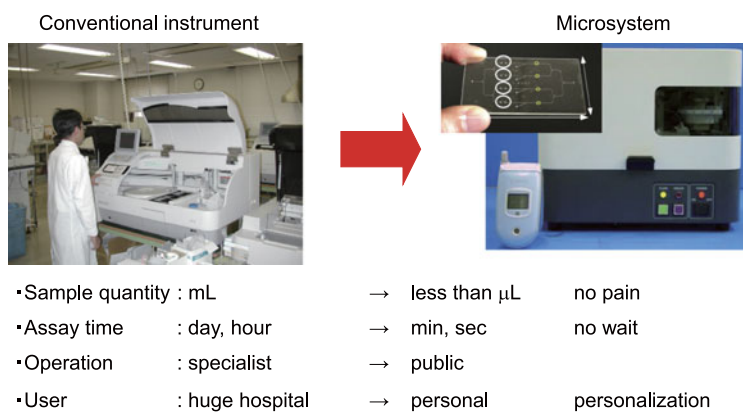


Fig. 5.20 Comparison of conventional ELISA and microELISA

time, smaller volume of serum, easy-to-use as shown in Fig. 5.20. The miniaturized rapid diagnosis system will be very promising for point-of-care diagnosis in clinics and health check at home.

The size is still large compared with an electronic device such as a cellular phone. In near future, by integrating nanophotonic devices, fluidic devices and electronic devices, the hand-held microfluidic devices will be realized and new analytical field utilizing the mobility are opened.

5.3 Extended-Nano Fluidics and Optics

5.3.1 Introduction

As micro/nanotechnologies have been rapidly developed, integrated chemical systems are downscaling to 10–1000 nm (extended nanoscale), which bridges the gap between single molecules and condensed phase, in order to achieve manipulation and sensing of individual molecules for biology, analytical chemistry and reaction chemistry. One of final goals of extended-nanofluidics is single cell analysis for basic biological study and medical applications, by extracting ultra small-volume analyte molecules into an extended nanochannel from a cell in microspace. However, in such small space with extremely increased surface-to-volume ratio, physics and chemistry are different from the bulk space due to dominant surface effects, and the space itself is often shorter than the optical wavelength. Therefore, extended-nanofluidics and optics are fundamental components for the integrated chemical systems, as well as fabrication and surface chemistry.

In order to establish extended-nanofluidics, physics and chemistry of liquids confined in nanospaces must be explored. Hence study of liquid behavior in nanospaces, which traditionally has been interested to understand porous medium in chemistry, biology and geology, has been more important in the past decades. A number of experimental and theoretical studies have investigated liquids confined in single nm-sized space, e.g., carbon nanotubes, porous silica, biological macromolecules and clay minerals [17, 18]. These studies have revealed unique liquid properties of water including ice-like structure, slower molecular motions, and depression of the freezing point, due to oriented behavior of confined molecules. On the other hand, the extended nanospace (10–1000 nm) is a transitional regime of molecular behavior, from single molecules to condensed phase (size of water molecule is approximately 3 Å). Also this space is comparable to well known electric double layer in an aqueous solution, an ion screening layer to cancel the surface electric charge with 1–100 nm thicknesses determined by the Debye length. The extended nanospace is more suitable for fluidic systems with collective behavior of liquid molecules. Although the regime of extended nanospace is relatively condensed liquid compared to single-nm space, various unique properties also have been reported by recent studies, such as higher viscosity, lower permittivity and higher conductivity [4]. Especially, Tsukahara et al. studied water confined in fused-silica extended nanochannels by nuclear magnetic resonance analysis (NMR) and revealed that the proton exchange rate in water increases with decreasing the channel size, suggesting loosely coupled water molecules by hydrogen bond in the vicinity of the wall within 50 nm [19, 20]. From these results, a hypothesis of three phase model for water confined in micro/nanospace has been proposed, where the water in closed space consists of adsorption phase of ice-like bilayer structure within 10 nm on the surface, proton transfer phase of loosely coupled water molecules within 50 nm, and bulk phase of ordinary liquid structure, as illustrated in Fig. 5.21. These unique water properties in nanospaces are expected to play an important role in chemical

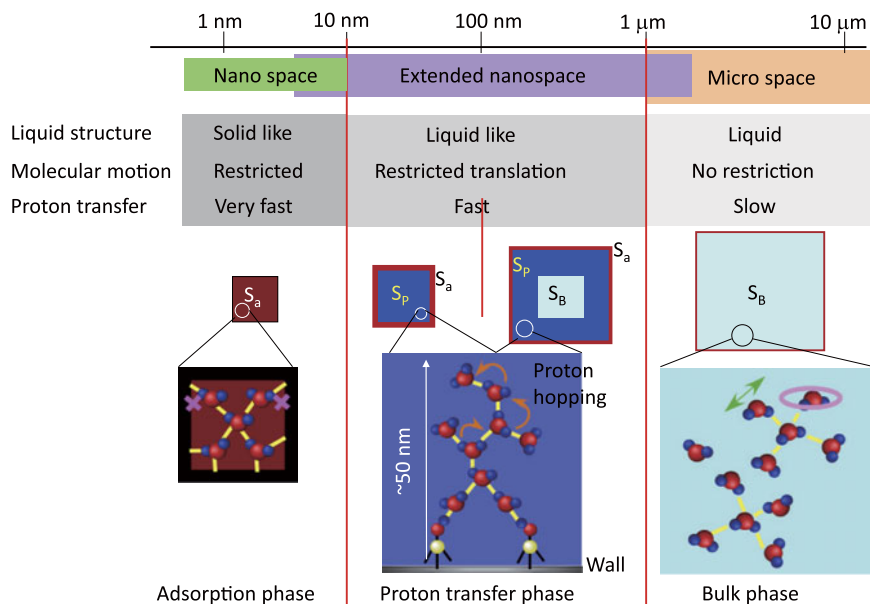


Fig. 5.21 A schematic illustration of the three-phase model. In the bulk phase, S_B , the water molecules have an ordinary liquid structure and free translation and rotation. In the proton transfer phase, S_p , the water molecules keep a four-coordinated H_2O structure, and have slower translational motion and higher proton transfer due to proton hopping along a linear $O \cdots H-O$ hydrogen bonding chain. In the adsorption phase, S_a , the water has an ice-like bilayer structure, with both translation and rotation inhibited

and biological functions, including chromatography separation of molecules, cell signaling mechanism, and stability of protein hydration.

Since extended nanospace is small volume and short length, sophisticated detection technologies are strongly required. Optical detection allows *in situ* and non-invasive detection with very small sample volume on microchips made of transparent materials. For 100 nm detection volume, single molecule detection is required even for 1 μM solutions, which is a typical concentration in analytical chemistry. Laser induced fluorescence, which uses fluorescent molecules releasing absorbed energy by radiative decay processes from the electronic excited state, is a broadly used because of very high sensitivity [21]. However, since the radiative decay is rather rare process, almost all species of molecule release the adsorbed energy as heat by non-radiative decay process. On the other hand, Kitamori et al. has developed a method for nonfluorescent molecules based on heat generation, i.e., thermal lens microscopy (TLM), and achieved high sensitivity for microspace [13]. Recently, TLM was further improved for extended nanospace by coupling with differential interference contrast optics (DIC-TLM) [22]. DIC-TLM could achieve detection of several-hundred nonfluorescent molecules in aqueous solution in extended nanochannel for the first time.

In addition, spatial resolution of the optical detection is important especially for basic studies to reveal spatial liquid structure and distribution of properties. Based on the three phase model as illustrated in Fig. 5.1, 10 nm-order spatial resolutions are required for studies of extended nanospace. However, it is difficult to achieve such sub-wavelength resolution by normal far-field optics owing to the Abbe's diffraction limit. Recently, several methods to achieve super resolution over the diffraction limit, including total internal reflection microscopy (TIRM), scanning near-field optical microscopy (SNOM) and stimulated emission microscopy (STED) [23–25]. These optical technologies can greatly contribute to extended-nanofluidics.

On the other hand, another approach is to use optics as a unit operation in integrated chemical systems. One of applications of nanophotonics is optical near-field (ONF) based reactions using nanostructured materials. Our group has been developed a unit operation of TiO₂-based photocatalytic reaction for water splitting using ONF [26]. In order to fabricate well-controlled TiO₂ nanostructure, a fabrication method of nanorods, i.e., glancing angle deposition (GLAD), has been developed.

In this chapter, extended-nanofluidics and optics important for integrated chemical systems are provided. Optical detection methods of single molecule sensitivity and super resolution are described. Then, recent results for liquid and optical properties in extended nanospace are described. Finally, we introduce an application of extended-nanofluidics and optics. Nanochromatography, which uses extended nanochannel as a separation column for very high efficient separation, is combined with the high sensitive detection method, for future application of single cell analysis.

5.3.2 *Optical Detection Methods*

5.3.2.1 DIC-TLM

Since the field of nanofluidics emerged, the importance of detection techniques has been rapidly increasing. For detection in nanospace, high sensitivity is firstly required because the number of analyte molecules is very small due to the extremely small detection volume. Laser induced fluorescence (LIF) is the most commonly used detection method for nanofluidics. However, there is almost no method to detect nonfluorescent molecules in nanochannels. As explained in a previous section, thermal lens microscope (TLM) is a strong detection tool of nonfluorescent molecules for microfluidic applications. Nevertheless, conventional TLMs have not been applied to detection in nanochannel. This is because the size of thermal lens becomes as small as the size of nanochannel. On the other hand, the principle of conventional TLM is based on refraction that is a phenomenon of geometric optics. Geometric optics, which deals with problems whose optical systems are larger than wavelengths of light, is not available in nanospace. That is the reason why conventional TLMs could not be used in nanochannels. Contrary, differential interference contrast thermal lens microscope (DIC-TLM) explained in a previous

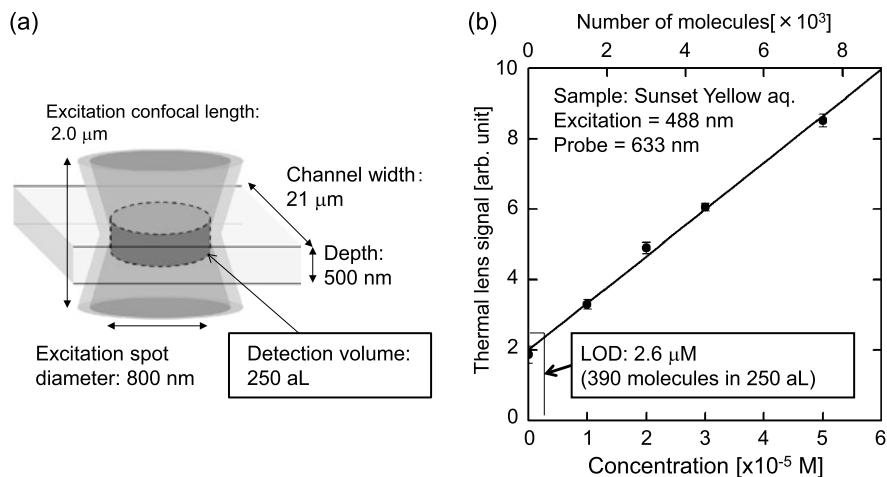


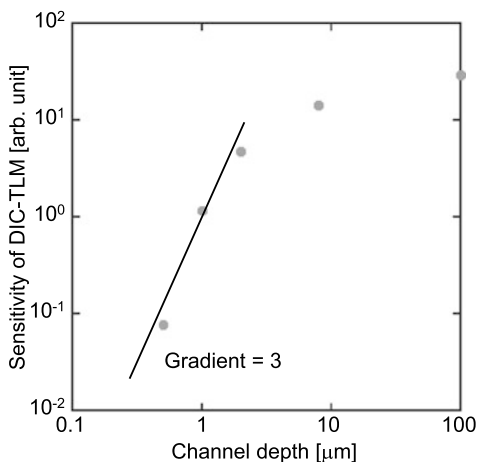
Fig. 5.22 (a) Optical configuration of laser spots and nanochannel and (b) calibration curve of nonfluorescent dye in determination of concentration using DIC-TLM

section is based on phase contrast and interference that are phenomena of wave optics. Wave optics, which can deal with problems that geometric optics is not valid, is available in nanospace. Therefore, the DIC-TLM can become a strong detection tool for nanofluidics.

Figure 5.22(a) illustrates an optical configuration of laser spots and a 500-nm deep nanochannel in a measurement using DIC-TLM [22]. The detection volume can be accurately calculated using an excitation spot size and confocal length because the nanochannel depth is smaller than the confocal length. Figure 5.22(b) is a calibration curve of a nonfluorescent dye solution obtained by DIC-TLM. The calibration curve was linear in μM range and the limit of detection (LOD) was 2.6 μM . This concentration corresponds to 390 molecules in the detection volume of 250 aL. This is the first result of sensitive measurement of nonfluorescent molecules in a thin nanochannel whose scale is same as wavelength of light.

Figure 5.23 shows a characteristic of sensitivity for nanochannel depth. The sensitivity initially decreased gradually and rapidly from 2 μm in proportion to the cube of depth. This tendency is accountable for three reasons as following. Firstly, the sensitivity decreases gradually due to a decrease of the number of excited molecules. Secondly, a part of generated heat transfers from water to silica by thermal diffusion with decreasing depth. Thirdly, the heat transfer causes an increase in refractive index of silica, while refractive index of water decreases with rising temperature. As a result, the changes in refractive index of water and silica canceled out with each other, which decreases the sensitivity rapidly. Owing to these problems, the sensitivity of DIC-TLM is partly lost in case of nanochannel. If this problem is solved, single molecule measurement in nanochannel using DIC-TLM could be realized.

Fig. 5.23 Relationship of sensitivity and channel depth



5.3.2.2 Stimulated Emission Depletion Microscopy

Fluorescence microscopy has been a promising tool in various fields including microchemistry and biology. Recently, engineering fields of chemistry are further downscaling to extended nanospace, and scientific interests of biology are shifting to nanoscale bio-organisms such as organelles, neurons and proteins. However, normal far-field optical microscopy, even confocal microscopy, cannot be applied because the spatial resolution is restricted by the Abbe's optical diffraction limit of similar order to optical wavelength. On the other hand, near-field optical methods, total internal reflection microscopy (TIRM) and scanning optical near-field microscopy (SNOM), can achieve sub-wavelength resolution. However, TIRM is only available to measurement in the vicinity of a flat surface, and SNOM cannot be used in closed space such as micro/nanochannels and intracellular spaces.

Therefore, a far-field optical microscopy with a spatial resolution higher than the optical diffraction limit is desired for general observation for nanopspaces. In recent advances, several kinds of super resolution microscopy of 10–100 nm resolution have been developed, including stimulated emission depletion (STED) microscopy, stochastic optical reconstruction microscopy (STORM) and saturated structured-illumination microscopy (SSIM) [25, 27, 28]. Among these methods, STED microscopy, which enables to achieve fluorescence excitation spot smaller than 100 nm, is considered to be most applicable because of similarity of its principle as normal fluorescence microscopic methods. STED microscopy has recently used for observation of bio-organisms and measurement of flows in a nanocapillary [29, 30].

STED microscopy decreases the size of fluorescence excitation spot by using two laser beams and effect of STED. Figure 5.24 shows a schematic of the energy-level diagram for a fluorophore. In the normal fluorescence, when the fluorophore is excited by light, an outer electron jumps from the ground state to the singlet state. From the singlet state, de-excitation to the ground state by fluorescence emission

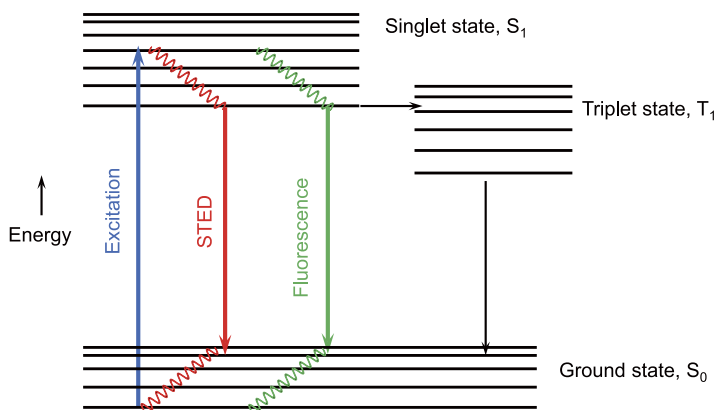


Fig. 5.24 Schematic of energy-level diagram of fluorescence and STED

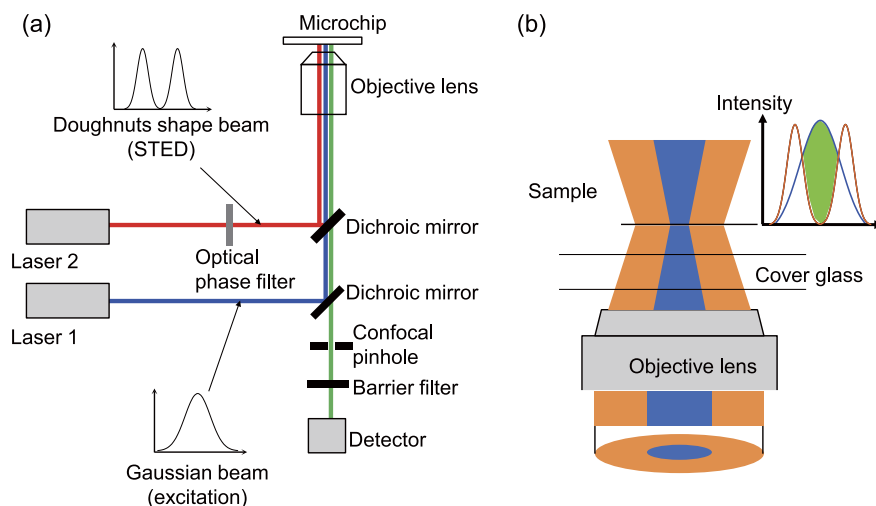


Fig. 5.25 Schematics of (a) STED microscope and (b) excitation of fluorescent molecules with STED effect

or by radiationless collision or crossing to the triplet state can occur. On the other hand, in STED, the de-excitation to the ground state is alternatively enforced by light illumination of longer wavelength than wavelengths of fluorescence absorption spectrum. This process is applied to realize the super resolution.

Figure 5.25(a) illustrates a schematic of a STED microscope. Two laser beams are used: one is for fluorescent excitation of a Gaussian intensity profile, and another is for STED of a doughnut shape intensity profile, i.e., STED beam by an optical phase filter. The two laser beams are completely aligned, and focused to fluorescent molecules through dichroic mirrors and an objective lens (Fig. 5.25(b)).

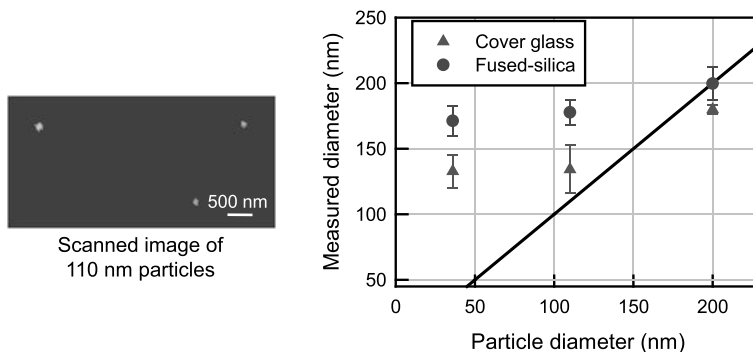


Fig. 5.26 (a) 20-averaged fluorescence image of particles stuck on the fused-silica plate. (b) The diameter of particle image estimated from the 2D Gaussian fitting as function of the actual diameter of particle

The fluorescent molecules in the center of the focal spot are excited to the singlet state and emit fluorescence. However, those in the periphery of the focal spot, where the STED beam is illuminated, are forced to return to the ground state without fluorescence emission. As a result, only the fluorescence emitted from the molecules in the doughnuts hole is detected. Therefore a spatial resolution of 10–100 nm can be realized, which is narrower than a width of the Gaussian focal spot of the excitation beam under the optical diffraction limit. The spatial resolution of the STED microscopy δx is described as [31]

$$\delta x = \frac{\lambda}{2n \sin \theta \sqrt{1 + I/I_{sat}}} \quad (5.1)$$

Where λ is the wavelength of the laser beam, n is the refractive index, q is the half aperture angle of the lens, I is the STED beam intensity, and I_{sat} is the saturation intensity where half of the excited molecules are stimulated to the ground state. This indicates the detection spot can be narrowed by increasing the STED beam intensity. Although the STED laser narrows the focal spot, a depth-wise resolution determined by the focal depth is still under the optical diffraction limit.

The STED microscopy was demonstrated for imaging of nanoparticles stuck on a glass surface to evaluate a spatial resolution [32]. A STED microscope was composed of Ar laser of 458 nm/488 nm wavelengths for the excitation, a fiber laser of 592 nm wavelength for STED, an oil immersion objective lens (100 \times , $NA = 1.4$, refractive index of immersion oil $n = 1.52$) and an avalanche photo diode (APD). The fluorescence was detected by a confocal pinhole. The scanning at an interval of 33.7 nm was conducted by galvanometer mirrors. 36 nm, 110 nm and 200 nm fluorescent polystyrene particles stuck on a cover glass of 0.17 mm were imaged. Then the particle image diameter was determined from a 2D Gaussian fitting, and then compared to the actual diameter, as shown in Fig. 5.26. When the diameter is 200 nm, the measured diameter is approximately equal to the actual size. For the 36 nm and 110 nm particles, the values are almost constant and larger than the actual diameters: approximately 134 nm. These results show the spatial resolution

limited by the width of the fluorescence excitation spot. Therefore, the spatial resolution, i.e., the minimal distance to resolve two separate points, was estimated to be $134/2 = 66$ nm. On the other hand, the depth-wise resolution for the imaging is under the diffraction limit. The depth-wise resolution was estimated to be 655 nm based on the principle of the confocal microscopy [33].

The above measurement system was used to reveal proton concentration in a fused-silica nanochannel, as mentioned in later section. For the fused-silica, owing to the optical aberration, the spatial resolution of STED microscope in the image plane was reduced to 87 nm.

5.3.2.3 Nano-Particle Image Velocimetry

Understanding fluid flows in micro/nanospace is important to develop novel integrated chemical systems. Recent studies for liquids confined in extended nanospace have suggested a possibility of spatially-distributed liquid structure and properties, especially near the surface, considering the electric double layer and the three phase model as described in Fig. 5.21. Also, due to dominant surface effects by extremely increased surface-to-volume ratio, studying behavior of substrates including colloids, macromolecules and bio-materials is fundamental for applications such as nanochromatography and nanoimmunoassay. These suggest importance of study for fluid flow and substrate behavior near the surface within several hundred nanometers. Therefore, spatially-resolved measurement methods for near-wall flow and substrates, which have a spatial resolution higher than the optical diffraction limit, are strongly required.

Particle image velocimetry (PIV) has been a broadly used method in fields of fluid mechanics [34]. The tracer particles are seeded into fluid, and images of flowing particles are captured. Then velocity distribution of fluid is obtained from the displacement of tracer particles during a time interval. Since this method uses particles, both fluid flow and particle motion can be investigated. Santiago et al. developed PIV for microchannel flows by applying fluorescence microscopy, i.e., micro-particle image velocimetry (μ PIV) [35]. Normal procedure to obtain the velocity distribution includes ensemble averaging to eliminate an error owing to the Brownian diffusion of tracers, which is significant in small scale. Although μ PIV has been broadly used for visualization of microscale flows [36, 37], it is difficult to apply this method to studies of interfacial dynamics owing to spatial resolutions under the optical diffraction limit and size of tracer particles typically 1 μ m.

In order to realize spatial resolution higher than the diffraction limit, near-field optics has been applied to PIV. Evanescent wave-based particle image velocimetry using total internal reflection microscopy (TIRM), nano-particle image velocimetry (nPIV), has been developed to measure the velocities within the first several hundred nanometers next to the wall. The evanescent wave is used as an excitation light for fluorescent tracers as illustrated in Fig. 5.27(a). When the light is totally reflected at an interface between two media of different refractive indices ($n_1 > n_2$), the incident

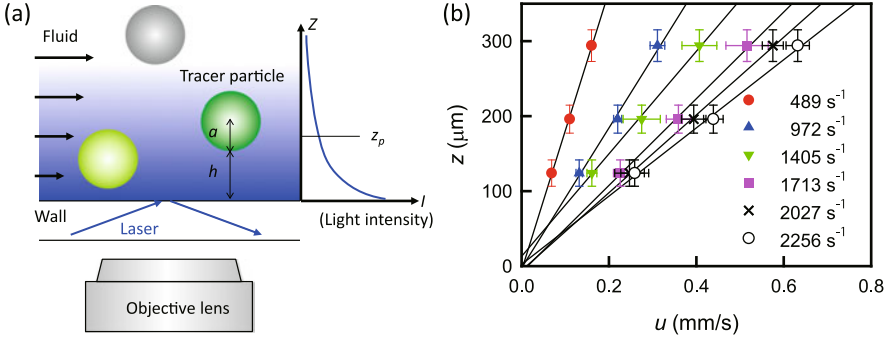


Fig. 5.27 (a) Schematic of nano-particle image velocimetry. (b) Velocity profiles of Poiseuille flows near the microchannel wall for different shear rates. The *solid lines* indicate a linear fitting to the experimental data

light partially penetrates into the medium of lower refractive index propagating parallel to the interface. The light intensity has an exponential decay with a penetration depth z_p as follow:

$$z_p = \frac{\lambda}{4\pi\sqrt{n_1^2\sin^2\theta_i - n_2^2}} \quad (5.2)$$

where θ_i is the incident angle. Typically $z_p \approx 100$ nm for total internal reflection of light of $\lambda = 488$ nm at an incident angle of θ_i exceeding a critical angle $\theta_c = \sin^{-1}(n_2/n_1)$ by a few degrees.

Many efforts have been made to develop nPIV for measurement of near-wall fluid flows in microchannels. Zettner and Yoda demonstrated nPIV using 300 nm and 500 nm tracer particles [38]. Smallest tracer of visible quantum dot of 11 nm hydrodynamic diameter was applied to nPIV by Pouya et al. [39]. Guasto et al. developed statistical particle tracking method for small particle images of low signal-to-noise ratio [40]. In these methods, only an averaged near-wall velocity in the evanescent wave field can be obtained. Hence it has been difficult to measure near-wall velocity profile in the depth-wise direction by spatially resolving the evanescent wave field.

Yoda et al. has further developed nPIV to obtain the near-wall flow profile, which is called multilayer nano-particle tracking velocimetry (MnPTV) [41]. A method to determine the separation distance between the particle edge and the wall h , which has been established in colloid science [42], was introduced. Since the fluorescent intensity excited by the evanescent wave also has the exponential decay, the particle center position z can be determined as follow:

$$z = a + h = a + z_p \ln\left(\frac{I_0}{I}\right) \quad (5.3)$$

where a is the particle radius and I_0 is the intensity of particle touching the wall ($h = 0$). By using this developed method, near-wall distribution of velocity, particle number density and diffusion coefficient can be measured simultaneously.

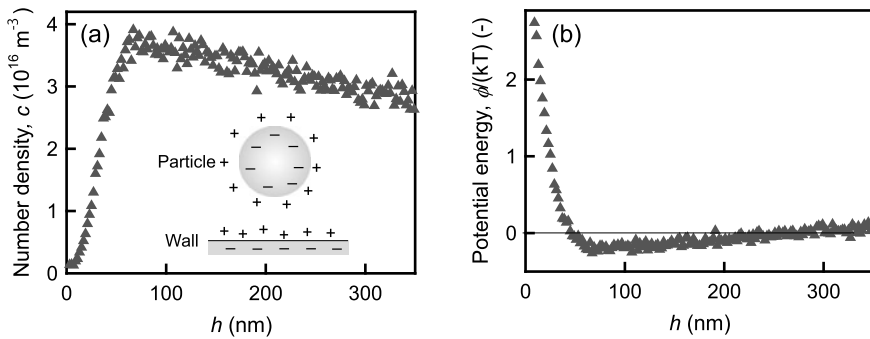


Fig. 5.28 Profiles of (a) number density and (b) potential energy of 220 nm fluorescent polystyrene particles as function of the separation distance, h

Near-wall velocity profile of Poiseuille flows in a fused-silica microchannel was measured by MnPTV [43]. Experiments were conducted for the channel of 469 μm width and 41 μm depth. 100 nm fluorescent polystyrene particles were used as tracer. Particles were illuminated by the evanescent wave of 488 nm wavelength, and the images were captured by a time interval of 1.5 ms. After determining particle position, the particle image in the evanescent wave field of 300 nm thickness was divided into three layers depending on z . The velocities in the layer were ensemble-averaged to eliminate the error by the Brownian fluctuation. Representative position of averaged velocity for each layer (z) was defined to be an average z -position sampled by the particles in the layer based on number densities $c(h)$

$$\langle z \rangle = a + \langle h \rangle = a + \frac{\sum hc(h)}{\sum c(h)} \quad (5.4)$$

Figure 5.27(b) shows near-wall velocity profiles of Poiseuille flow of 10 mM NH_4HCO_3 in the microchannel at shear rates of 486 s^{-1} to 2255 s^{-1} . The velocity profile in agreement with the analytical solution of Poiseuille flow could be obtained.

Near-wall particle distribution in microchannel flows also was evaluated for study of interactions between the particle and surface [44, 45]. From the particle positions, profile of the number density of particles was obtained. Figure 5.28(a) shows near-wall distribution of 220 nm polystyrene particles. The particles nonuniformly distributes in the vicinity of the wall. The result shows typical particle distribution with a potential energy described by the Derjaguin-Landau-Verwey-Overbeek (DLVO) theory. In case of polystyrene particle of almost similar density as aqueous solution, the potential energy is mainly governed by electrostatic and van der Waals effects. The electrostatic interaction is due to the electric double layer with 1–100 nm length scale, and repulsive in this case because both the particle and wall surfaces are negatively charged. On the other hand, the van der Waals interaction is attractive and significant in a region within 50 nm of the surface. Since the particles

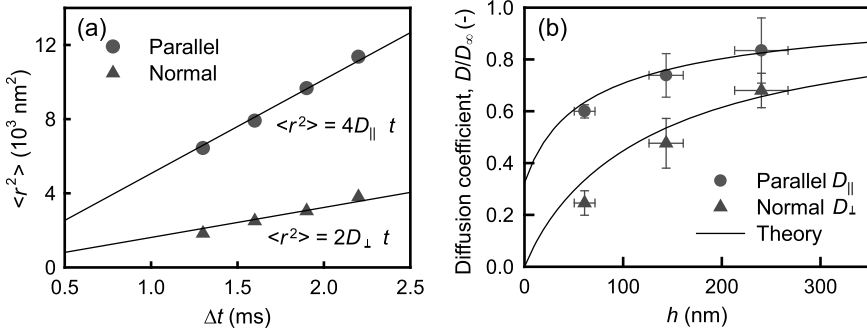


Fig. 5.29 (a) The means square of the displacements $\langle r^2 \rangle$ as function of the time interval Δt and (b) normalized diffusion coefficients D/D_{∞} as function of the separation distance h , for the Brownian motion of 220 nm fluorescent polystyrene particles parallel and normal to the wall

have the Boltzmann distribution, the potential energy $\phi(h)$ can be obtained from the particle distribution as shown in Fig. 5.28(b), given by

$$\frac{\phi - \phi_0}{kT} = \ln \left\{ \frac{c(h)}{c_0} \right\} \quad (5.5)$$

where k is the Boltzmann constant and T is the temperature. In most recent studies, the near-wall particle distribution in electrokinetically driven flows was investigated, and additional repulsive force acting on the particle due to the Maxwell stress was revealed [45].

Since the near-wall displacements of particle include components of the Brownian fluctuation, near-wall diffusion coefficients can be estimated [46]. Measurements were conducted for 220 nm polystyrene particles for time intervals Δt of 1.3 ms, 1.6 ms, 1.9 ms and 2.2 ms. The variance of the displacements $\langle r^2 \rangle$ was determined from the probability density function of the displacements by a least-square fitting with a Gaussian function. The diffusion coefficients parallel D_{\parallel} and normal to the wall D_{\perp} were obtained from a linear relationship between $\langle r^2 \rangle$ and Δt as shown in Fig. 5.29(a), considering $\langle r^2 \rangle = 4D_{\parallel} \Delta t$ and $\langle r^2 \rangle = 2D_{\perp} \Delta t$. Figure 5.29(b) shows diffusion coefficients as function of the separation distance h , which are normalized by that in the bulk by the Stokes-Einstein relation $D = kT/(6\pi\mu a)$. Classical hydrodynamic theory describes that, when the particles are in the near-wall region, Brownian diffusion becomes anisotropic by hindrance effects owing to the hydrodynamic drag due to the wall. The hindrance factors for the diffusion coefficients are expressed for component parallel to the wall [47]

$$\frac{D_{\parallel}}{D_{\infty}} = 1 - \frac{9}{16} \left(\frac{a}{z} \right) + \frac{1}{8} \left(\frac{a}{z} \right)^3 - \frac{45}{256} \left(\frac{a}{z} \right)^4 - \frac{1}{16} \left(\frac{a}{z} \right)^5 \quad (5.6)$$

and for component normal to the wall [48, 49]

$$\frac{D_{\perp}}{D_{\infty}} = \frac{6h^2 + 2ah}{6h^2 + 9ah + 2a^2} \quad (5.7)$$

as shown in Fig. 5.29(b). The results well agrees with the theoretical values, and the diffusion coefficient normal to the wall decreases to less than 30 % at $h = 60$ nm.

Since nPIV can measure fluid flow and substrate behavior with 10 nm-order spatial resolution, this method has possibility for study of extended nanochannel after further developments.

5.3.3 *Liquid and Optical Properties*

5.3.3.1 Proton Behavior in Extended Nanospace

Overview of Specific Properties in Extended Nanospace Recent studies of extended nanospace have reported various specific properties of liquid, phase transition and chemical reaction [4]. These results suggest possibilities for novel fluidic devices using specific properties of extended nanospace for analytical applications, chemical synthesis and energy production. In order to explain the specific phenomena in extended nanospace, Tsukahara et al. proposed the three phase model, where the aqueous liquid has specific structure due to surface effects: adsorbed water phase of several-molecules thickness next to the surface, proton transfer phase of loosely coupled water molecules by hydrogen bond within 50 nm, and bulk water phase as illustrated in Fig. 5.21 [19, 20]. On the other hand, a classical model for the aqueous liquids, the electric double layer, is also considered to be dominant due to its thickness of 1–100 nm. Herein, we describe various physicochemical properties of extended nanospace.

Viscosity of liquid confined in extended nanospace has been studied by several methods. Hibara et al. observed capillary filling into a fused silica extended nanochannel of a 330 nm hydrodynamic diameter [50]. The filling speed was slower showing few times higher water viscosity than the bulk. Similar results for slower capillary filling for hydrophilic extended nanospace has been reported, which can be explained considering hydrogen bond between silanol surface and water molecules, and electroviscous effect by the electric double layer [51, 52]. In addition, results of time-resolved fluorescence measurement showed higher viscosity and lower permittivity, which are strongly related to the specific structure of confined water [50]. On the other hand, measurement of pressure-driven flows in hydrophobic extended-nano carbon pore showed faster flow rate than the bulk, suggesting interactions between hydrophobic surface and liquid [53].

Electrical conductivity in extended nanospace, which is strongly related to ion behavior, has been studied. Electric conductance of KCl solution filled in a plate type extended nanochannel of 50 nm height (and microscale width) was estimated from AC impedance measurement, using platinum electrodes embedded in microchannels interfaced with the nanochannels [54]. The conductivity was obtained from the resulting Cole-Cole plots. The conductivity decreased with decreasing KCl concentration, reaching a plateau for low ion concentration below 10^{-4} M. This conductivity plateau could be explained by overlap of the electric double layer mainly

formed by excess protons, with the Debye length comparable to the channel height. Liu et al. measured the proton conductivity of HClO_4 solution in a plate extended nanochannel from the electric current [55]. The proton conductivity increased in extended nanospace, and the authors concluded that the enhanced conductivity is due to the electric double layer overlap. On the other hand, Tsukahara et al. conducted AC impedance measurement for KCl solution in square type extended nanochannels (nanoscale width and depth) using a nanofluidic chip equipped with two microchannels containing mercury microelectrodes directly interfaced with the nanochannels [56]. From the Cole-Cole plots, the electric conductivity and the capacitance were estimated. The results suggested increased viscosity and decreased dielectric constant of the solution, and a conductivity plateau below 10^{-4} M corresponding to the results of plate nanochannels. It was confirmed that, in extended nanospace, the density of dissociated silanols (SiO^-) on a surface was reduced and the proton concentration is greater than that expected from a initial solution.

The surface charge plays an important role for liquid properties in extended nanospace because it induces the electric double layer formed by mobile counter ions. A streaming potential/current measurement is one of the most useful methods for evaluating the effects of surface charge on liquid properties. When the counter ions in electric double layer are transported in nanospaces by pressure driven flow, the streaming potential/current relating to the surface charge, flow rate and ion strength is induced. van der Heyden et al. conducted streaming current measurements for various ion solutions in silica plate nanochannels with 10–1000 nm height [57]. Morikawa et al. developed a streaming potential/current measurement system for square extended nanochannels and proved their performance using KCl solutions [58]. By using this method, isoelectric points in extended nanochannels fabricated by fused-silica were measured [59]. Since the streaming current is flow of mobile counter ions by pressure driven flow, dissociation of silanol groups on the surface: $\equiv \text{SiO}^- + 2\text{H}^+ \leftrightarrow \equiv \text{SiOH}_2^+$, which has been reported to be 2.6–3.2 in the bulk, can be estimated. The isoelectric point in a 2720 nm channel was almost similar to the reported values, however, that in extended nanochannel (580 nm) was decreased to less than 2.0. The results suggest enhancement of proton dissociation in extended nanospace.

When the electric double layer is overlapped in extended nanospace, ions are spatially distributed, resulting in electrical polarization of the channel. Cations are enriched near the negatively charged surface, while anions are localized to the center of the nanospaces or excluded from the nanospaces due to the electrostatic repulsive/attractive forces. Ion enrichment/depletion in external electric field in a plate nanochannel was demonstrated using fluorescent dye molecules [60]. Kato et al. investigated a relationship between the thickness of electric double layer and the velocity of 50 μM fluorescent solutes in square extended nanochannel (width; 270 nm, depth; 280 nm), and clarified that the more negatively charged solute such as fluorescein with negative divalent produced higher velocity compared with sulforhodamine B with monovalent or rhodamine B with neutral [61]. This is evidence that negatively charged ions could be localized to the center of the extended nanospaces, because of the Debye length of about 50 nm for a 50 μM solution comparable to the extended nanospace.

It has been unclear at the molecular level about how the properties of water molecules are affected by size-confinement. Tsukahara et al. studied molecular structure and dynamics of water and non-aqueous solvents confined in fused-silica extended nanospaces using nuclear magnetic resonance (NMR) [19, 20]. The results of size dependency of the ^1H -NMR spin-lattice relaxation rate ($^1\text{H}-1/T_1$) suggested that size-confinement in extended nanospace produces slower translational motion of water, but does not affect the hydrogen-bonding structure and rotational motion. Only the translational motion change of H_2O can be attributed to protonic diffusion invoking excess proton hopping pathway along a linear $\text{O}\cdots\text{H}-\text{O}$ hydrogen bonding chain between adjacent water molecules than hydrodynamic translational diffusion. By measuring ^1H -NMR spin-spin relaxation rate ($^1\text{H}-1/T_2$) and rotating-frame spin-lattice relaxation rate ($^1\text{H}-1/T_{1\rho}$) values, the proton exchange rate of water molecules confined in extended nanospace was determined to be larger by a factor of more than 10 from that of bulk water because of chemical exchange of protons between water and SiOH groups on glass surfaces. From these results, the three phase model, considering the proton transfer phase of loosely coupled water within about 50 nm of the surface, was proposed as illustrated in Fig. 5.21.

Generally, when water is in confined geometries, the saturated vapor pressure is lower than that at the flat surface due to the Laplace pressure, as described by the Kelvin equation. Tsukahara et al. developed an experimental system for the water evaporation, which can strictly control equilibrium vapor pressure and temperature in extended nanochannels, and studied size dependency of water for capillary evaporation by optical microscope observation [62]. The water evaporated in microchannels at 22 °C, while did not evaporate in extended nanospaces. The water in 120 nm extended nanospace started to evaporate at 22.2 °C. Furthermore, the vapor pressures in extended nanospace were found to be lower than those calculated from a model based on Kelvin's equation. By using the lower vapor pressure in extended nanospace, distillation of an aqueous solution containing 9.0 wt% ethanol and capillary condensation of ethanol vapor were succeeded to demonstrate in 270 nm extended nanoscale pillar structures [63].

The unique water properties in extended nanospace are expected to affect reaction properties. Tsukahara et al. demonstrated the enzyme reaction, in which the fluorogenic substrate TokyoGreen- β -galactoside is hydrolyzed to fluorescein derivative TokyoGreen and β -galactose by β -galactosidase enzyme acting as a catalyst in a Y-shaped extended nanochannel by using pressure driven flow control system [64]. The results suggested that the enzyme reaction rate is increased by a factor of about 2 compared with those in the bulk. The acceleration of the reaction kinetics is attributed to the enhancement of proton mobility of water in extended nanospace.

Measurement of Proton Concentration and Diffusion Study of proton behavior in extended nanospace is important, because the specific water layer of loosely coupled water molecules is considered to enhance proton hopping through hydrogen bonding network and the electric double layer is a dissociated ion layer near the surface. Most recently, our group has studied proton diffusion and distribution by optical detection methods using fluorescein as a pH indicator [32, 65]. Figure 5.30

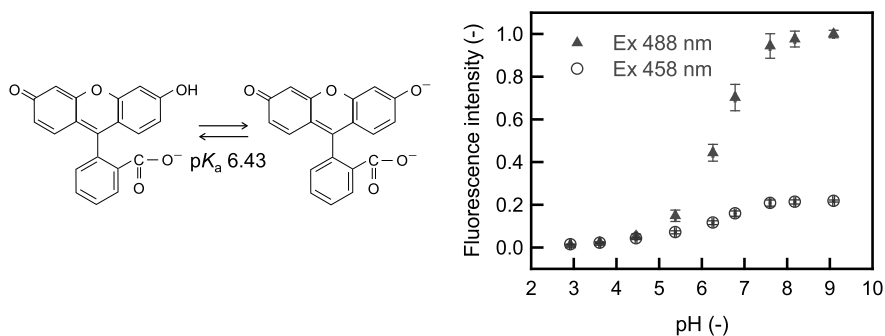


Fig. 5.30 Chemical structure and fluorescent intensities of fluorescein with excitation by 458 nm and 488 nm wavelengths, as function of pH of electrolyte solution

shows chemical structure and fluorescent intensities of fluorescein, which is dependent on pH of electrolyte solution. The fluorescent intensity of fluorescein excited by a laser beam of 488 nm wavelength significantly varies with pH around 6.4 due to a chemical equilibrium constant of $pK_a = 6.43$.

Recent studies of water in extended nanospace suggest effects of proton concentration on the electrical conductivity. It is considered that the electric double layer is overlapped in extended nanospace, however, there is no report for direct observation of electric double layer. Kazoe et al. have developed super-resolution laser-induced fluorescence for measuring proton distribution in extended nanochannel, using stimulated emission depletion (STED) microscopy, as described in previous Sect. 5.32. STED microscopy realized the super-resolution measurement of 87 nm resolution in the image plane, and 655 nm resolution in the depth-wise direction, for fused-silica nanochannels. The ratiometric measurements were conducted using the property of molar absorption coefficient of fluorescence, which is strongly dependent on the pH at wavelength around 490 nm, while almost independent at wavelength at 460 nm. By the ratiometric method, error by nonuniform distribution of fluorescein was eliminated. Figure 5.31 shows proton distribution in a nanochannel of 410 nm width and 405 nm depth, for solutions of water, 10^{-4} M KCl and 10^{-2} M KCl, where 8.6 μ M fluorescein was dissolved. The proton distribution was resolved by 33.7 nm interval of 87 nm resolution in the spanwise direction, while averaged over the depthwise direction owing to the spatial resolution of 655 nm. When the water was flown through the nanochannel, whole region of the channel is filled by overlapped electric double layers formed by protons to cancel the negative charge of glass surface, and the average proton concentration was 19.1 times higher than the bulk. The concentration in the near-wall region of 30 nm was 6 times larger than the channel center. However, the Debye length seemed to be approximately 100 nm, much shorter than 311 nm predicted from the bulk pH of 6.04. It was considered that the silanol group itself provides excess protons by dissociation ($\equiv \text{SiOH} \leftrightarrow \equiv \text{SiO}^- + \text{H}^+$), and makes the Debye length shorter. With shorter Debye length by increasing KCl concentration, the pH in the channel became close

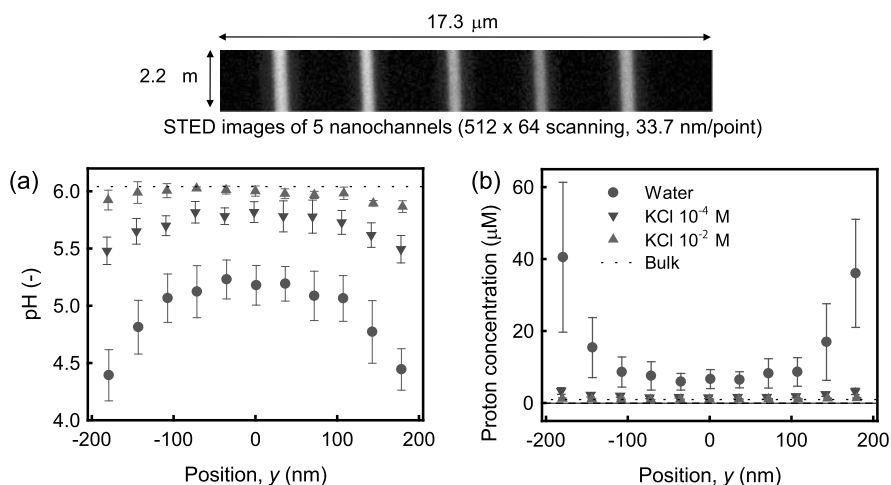


Fig. 5.31 Profile of pH and proton concentration in the extended nanochannel of 410 nm width and 405 nm depth, compared with the bulk value measured in a microchannel

to the bulk value and the distribution became relatively uniform except the region very close to the wall, in agreement with the classical theory.

According to NMR results, an increase of the diffusion coefficient and ion mobility can be expected in the proton transfer phase. Therefore, effects of accelerated proton exchange through water molecules in extended nanospace on the actual proton transfer have been studied by measuring the proton diffusion coefficients [65]. Measurements were conducted for square extended nanochannels of various hydrodynamic diameters, interfaced with two microchannels, as shown in Fig. 5.32. Firstly, 10⁻⁴ M fluorescein and 10⁻² M HCl solution was introduced into the left microchannel at 10 kPa, and 10⁻⁴ M fluorescein and 10⁻⁴ M phosphate buffer solution (PBS) was introduced into right microchannel. In this condition, nanochannels were filled with the fluorescein and PBS. Then, after switching off the pressures, protons were diffused to the right microchannel and the fluorescent intensity decreased owing to pH decrease. The moving front of protons was clearly observed as Fig. 5.32, and quantitatively measured as shown in Fig. 5.33(a). From a linear relationship between the square displacement $\langle X^2 \rangle$ and the time showing the correlation coefficient of 0.98, diffusion coefficients could be estimated because of $\langle X^2 \rangle = 2D\Delta t$. Figure 5.33(b) shows the diffusion coefficients of protons as function of the channel size. The diffusion coefficient was decreased for channel sizes of below 1580 nm, and then enhanced for smaller channels from 330 nm. The enhancement factor at 180 nm was almost 4 compared with the bulk value. It is known that the proton diffusion is dependent on the Grotthuss mechanism, and is expressed by the Stokes-Einstein relation and proton hopping, with weighting parameters of χ_S and χ_H

$$D = \chi_S \frac{kT}{6\pi\mu a} + \chi_H \frac{kT\lambda_{H+}}{z^2 F^2} \quad (5.8)$$

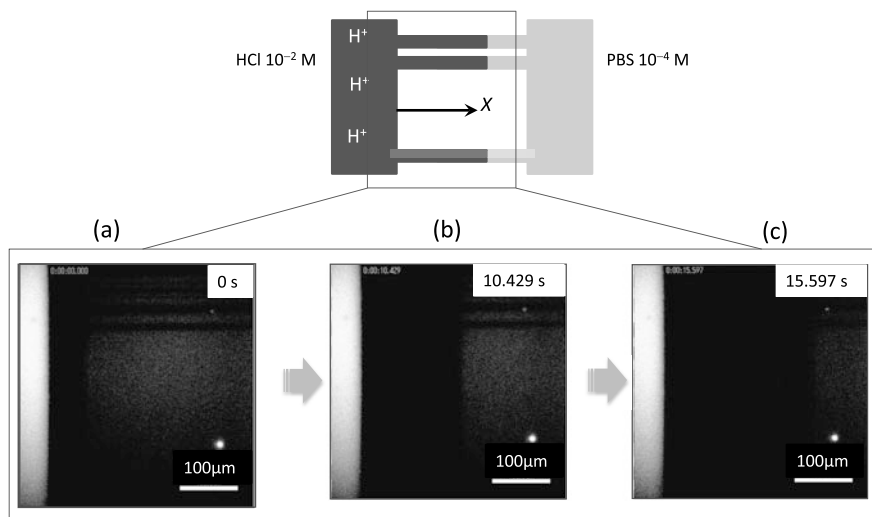


Fig. 5.32 Proton diffusion across nanochannels of hydrodynamic diameter of 737 nm at (a) $t = 0$ s, (b) $t = 10.429$ s, and (c) $t = 15.597$ s

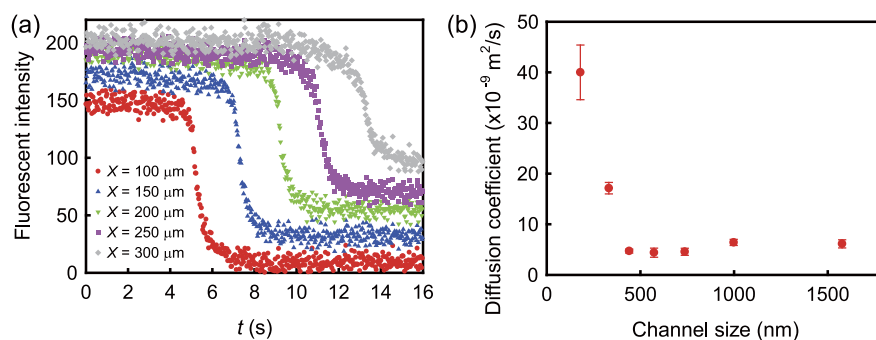


Fig. 5.33 (a) Fluorescent intensity measurement at $X = 100, 150, 200, 250,$ and $300\mu\text{m}$. $t = 0$ s denotes the measurement starting point. (b) Proton diffusion coefficient as function of the channel size

where z is the proton charge, F is the Faraday's constant and λ_{H^+} is the proton mobility. Considering the water properties in extended nanospace, it was suggested that the decrease of diffusion coefficients from 1580 nm to 570 nm is due to the increase of the viscosity, and the increase of diffusion coefficients from 570 nm and 180 nm is dominated by the increased proton mobilities corresponding to the results by our NMR studies [19, 20]. The results for the first time proved that the specific water structure increasing viscosity and proton exchange rate significantly affects the proton transport by diffusion. The conductance of the nanochannel at 330 nm was $6.4 \times 10^{-3} \text{ S cm}^{-1}$, assuming that proton concentration is 10^{-2} M , which is

comparable with the Nafion membrane well used as proton exchange membrane in fuel cells. This calculation shows that the fused-silica nanochannels can be an alternative to the Nafion membrane with advantages of low crossover by glass substrates and large mechanical strength.

5.3.3.2 TiO₂ Nanorod Fabrication and Water Splitting by Visible Light

Using sunlight to perform water splitting (the photocatalysis process) to produce hydrogen is one the most important human aims in the production of cheap energy, since both water and sunlight are vastly abundant. This process requires a material which, during the light absorption, could generate a transient state decaying at least partially to form some chemical species. TiO₂ has proved itself as a very popular and a promising functional material in the recent years. The main role of TiO₂ is addressed at the challenges in the field of energy applications, particularly in photochemistry to perform efficient water splitting for hydrogen production [66–71], in photocatalysis [72–74] and photovoltaics [75], respectively, because this material has a good stability, is non-toxic and is attained at low cost. The performance of the applications mentioned above depends not only on the bulk properties of TiO₂ or their modification by doping or sensitizing with inorganic and organic dyes, but also on the morphology of the TiO₂ material on the nanometer scale.

Many kinds of experimental techniques have been employed for the preparation of TiO₂ films, such as pulsed laser deposition [76], reactive evaporation [77] and chemical vapor deposition [78]. However, with the help of these techniques, the TiO₂ deposits usually have a low specific surface area which results in a weaker photocatalytic activity; and they are not subjected to serious practical problems typical for TiO₂ powders or nanoparticles, which are associated with synthesis, annealing and immobilization. Compared to nanoparticles, such dimensional nanostructures as nanowires or nanorods have much better transport properties and also a bigger surface area in comparison with the bulk or two dimensional nanostructures. Thus, TiO₂ nanorods or well-defined based nanorods structures are highly considered for both photoelectrochemical and photovoltaics applications. However, the photocatalytic activity of TiO₂ is the most active in the anatase phase under UV light irradiation due to its wide band gap energy (3.2 eV; ~350 nm). So, there is a very big interest in expanding the photoresponse of to the longer wavelength for the reason that most of solar light corresponds to visible light and TiO₂ can harvest the UV light which takes only ~5 % of sunlight, resulting in low energy conversion efficiency.

There has been an interest research strategy aimed at expanding the photoresponse in TiO₂ in the visible region. One of the well-reported strategies consists in doping TiO₂ with a transition metal [79, 80] or the main group of elements like carbon [68, 81, 82] or nitrogen [83]. Another promising approach involves the plasmon-induced enhancement of the visible response in TiO₂ loading metal nanoparticles (Au, Ag, etc.), yet these materials need a large applied bias or the addition of electron donor in order to obtain hydrogen generation. The stability of the metal also still remains a problem [84, 85].

To obtain a good material, that would meet the requirements in both the band gap energy and stability, is the main issue not only for photoelectrochemistry, but also for materials science, as it still has limitations and cannot be solved only by chemical modification.

On the other hand, nanotechnology allows preparing many kinds of nanostructured semiconductors which have unique optical and electronic properties. Although the nanostructured TiO₂ enhances the photocatalytic performance in UV region by improving the charge separation and better transport properties, but the visible response of nanostructured TiO₂ resulting from nanostructures has not been investigated yet.

Recently, prof. Ohtsu's group reported that optical near-field (ONF) generated at nanostructures can excite the coherent phonons in the nanostructures, together with the ONF these excited coherent phonons form a coupled state which is called virtual exciton-phonon-polariton. This coupled state contributes to the so-called phonon-assisted process, which excites an electron in the valence band of a semiconductor to the conduction band via energy of phonon [86, 87]. Although this excitation is an electric-dipole forbidden, it is allowed by the ONF which can couple with phonons to generate a quasi-particle of exciton-phonon-polariton in a nanometric space. That is, this quasi-particle can excite the electron to the phonon level and successively to the conduction band. This two-step excitation process is possible even though the incident photon energy is lower than the band gap energy.

This chapter provides a detailed description of a new physical approach to induce the visible response of TiO₂ by introducing favorable nanostructures to generate ONF on which we have recently reported [26]. It is found that the generation of ONF strongly depends on the nanometric structures; hence, the fabrication of favorable TiO₂ nanostructures is crucial to induce the ONF effect. Among the techniques for fabrication of nanostructures, glancing angle deposition (GLAD) allows a viable way to fabricate aligned nanorods with a well-controlled diameter, density and shape [74, 88].

Controllable Fabrication of Nanorods Structures The experimental set-up for the glancing angle deposition (GLAD) is quite simple, and usually consists of collimated evaporation or deposition source beam which has a large incident angle (bigger than 80°) with respect to the substrate normal (see Fig. 5.34). Originally this technique is different from traditional physical vapor deposition (PVD) techniques because it utilizes highly oblique deposition angles.

During the deposition of a thin film onto a flat substrate, initially impinging atoms will randomly form islands on the substrate, and these nucleated islands will act as shadowing centers and shield that area from other incident atoms. The shadowing effect and limited adatom diffusion eventually produce a micro- or nanostructure of small isolated columns slanting toward the incident beam (see Fig. 5.34 (right part)). In GLAD configuration, the substrate is manipulated by two stepper motors: one motor controls the incident angle α , and the other motor controls the azimuthal rotation φ of the substrate with respect to the substrate surface normal. During the GLAD process, the substrate can rotate azimuthally at a fixed incident angle α , rotate back and forth changing the incident angle α , or rotate azimuthally and polarly

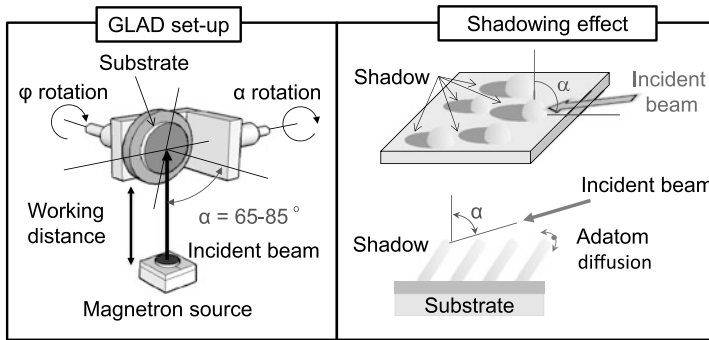


Fig. 5.34 The basic schematic illustration of the GLAD process

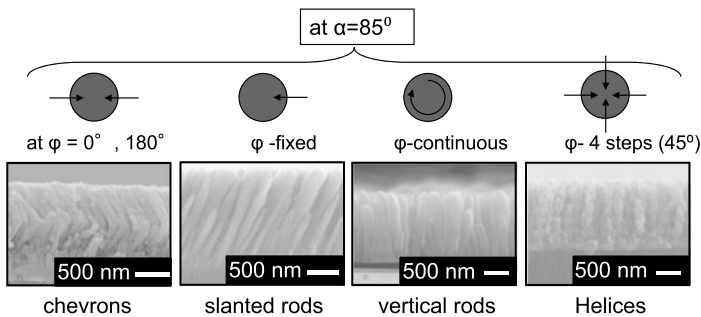


Fig. 5.35 Cross-sectional SEM images of TiO_2 nano-sculptured films fabricated on flat glass substrates at constant incident angle α : chevrons—when the azimuthal rotation φ is set on two opposite positions; slanted rods—when φ is set in one position; vertical rods—when φ is set in continuous rotation and helices—when φ is set in continuous rotation, but stops for a while every 45°

simultaneously. The driving of the both step motors is controlled by a computer. By changing the speed and the phase of φ rotation, polar rotation or the combination of two rotations with respect to the deposition rate, we can produce many kinds of nano-sculptured shapes of deposits: chevrons, slanted rods, simple vertical rods and helices [74] (see Fig. 5.35).

In continuation of this chapter, we will focus on describing our efforts to fabricate simple vertical TiO_2 nanorods by the GLAD technique, and will provide some discussion on the possibility to control the diameter and the shape of TiO_2 nanorods by changing experimental parameters (such as working distance, incident angle α and the speed of azimuthal substrate rotation φ) during the GLAD process.

For the fabrication of TiO_2 vertical nanorods, the custom-built radio frequency magnetron sputtering system was used as the deposition source. The deposition was performed using the Ti target (50 mm in diameter, thickness 5 mm, and purity 99.99 %, purchased from Furuuchi Chemical Corporation). The sputtering of Ti in the Ar/ O_2 mixture was performed at relative low pressure 0.1 Pa and at long throw 80–120 mm (the distance from the substrate center to the deposition source) to re-

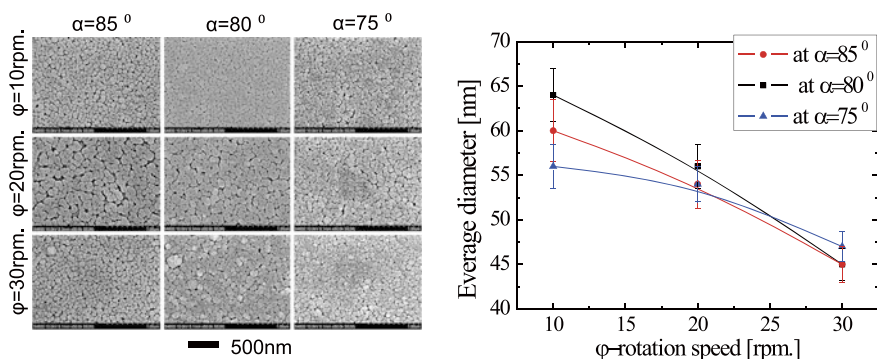


Fig. 5.36 SEM top view images of TiO_2 nanorods samples prepared by GLAD on the ITO substrate at various incident angles and rotation speed. The results of the average diameter of nanorods were estimated from SEM images

duce the scattered components of flux from the magnetron source. A shutter placed between the magnetron and the special rotated substrate holder (GLAD configuration) allowed pre-sputtering of the materials for at least 5 min before deposition. The deposition rate from the magnetron flux was controlled by quartz crystal microbalance (QCM) and the thickness of all deposited films was controlled at 300 nm for comparative study.

From the beginning of this work, we have been studying the influence of the substrate rotation regime ϕ and the incident angle α deposition on the morphology of deposited columnar structures of the TiO_2 material at the constant deposition rate and fixed working distance ~ 120 mm. The TiO_2 nanorods structured films were deposited onto the transparent conducting substrate ITO (Sigma-Aldrich, surface sheet resistance $\sim 10\text{--}15 \text{ } \Omega/\text{sq}$ and roughness factor of $\sim 1.6 \pm 0.1$) and were photoelectrochemically (PEC) characterized afterwards. Before the deposition, all the ITO substrates were cleaned with ethanol in the ultrasound bath for 15 min and dried under a stream of argon to avoid any contamination on the surface, because the morphology and the surface energy of the substrates play a significant factor for the growth of nanorods due to their self-organization nature during the GLAD process. Figure 5.36 shows SEM images of the TiO_2 nanocolumnar structure deposited on ITO with a different rotation speed of 10–30 rpm at three different incident deposition angles. All the nanocolumns are aligned vertically with respect to the substrate, and the location of the columns is random with well-separated from each other individual nanorods with different diameters as revealed by the top view of SEM images (Fig. 5.36). Taking into account that all deposits correspond to films with a constant film thickness, we estimated the mean average nanorods diameter from SEM images with the help of image analysis software Image J. These results, also described in Fig. 5.36 (right part), indicate that, in fact, the nanorods diameter will decrease monotonically with the substrate rotation speed ϕ for all investigated incident deposition angles α . There is a clear variation of nanorods diameter, which depends on two parameters, and the mean nanorods diameter was found to vary from 45 to

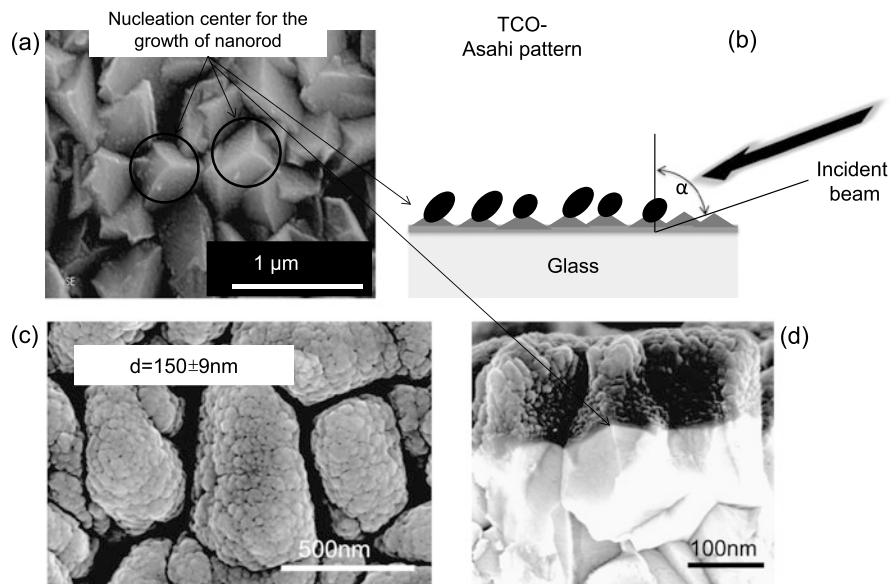


Fig. 5.37 Top view SEM image of a pyramid-like patterned F-doped Tin Oxide (TCO) coated glass (a); (b) shows how the pyramid shape of the TCO substrate works as a nucleation site for the growth of nanorods; SEM images of (c) the top view and (d) the side view of TiO_2 nanorods deposited on the TCO patterned substrate

65 nm. The formations of the vertical nanorods are expected, if we consider the direction of the sputtered flux (or atoms) as it is shown in Fig. 5.34. Subsequently the substrate rotates azimuthally (φ) so each part of the surface has an equal chance to receive the same amount of deposited atoms from the magnetron source. This is a good evidence that the purpose of the azimuthal rotation φ is to constantly adjust the columns' tilting direction to make them straight.

In order to achieve a larger diameter of TiO_2 nanorods (larger than 100 nm), a pyramid-like patterned F-doped tin oxide coated glass substrate (TCO) was used (Asahi-Glass, surface resistivity 8–12 Ω/sq). In this case, the nano-pattern plays as nucleation site for the growth of nanorods, as shown in Fig. 5.37.

All the as-deposited TiO_2 nanostructures showed the preferred amorphous phase and it was converted to the single-phase anatase by annealing at 550 under oxygen flow (400 sccm) in 4 hours, which was confirmed by the XRD analysis. The oxygen flow was used during the annealing process to reduce the oxygen defects in the film.

PEC Characterization and Water Splitting The solar photoelectrochemical process is one of the most attractive methods for conversion of solar to chemical energy fuel by means of water splitting, with hydrogen as the energy carrier. The simplest photoelectrochemical cell usually consists of a semiconductor photoanode and a metal counter electrode (for example, Pt) immersed in the electrolyte solution. According to the classical theory, the photoanode (usually n-type TiO_2 film)

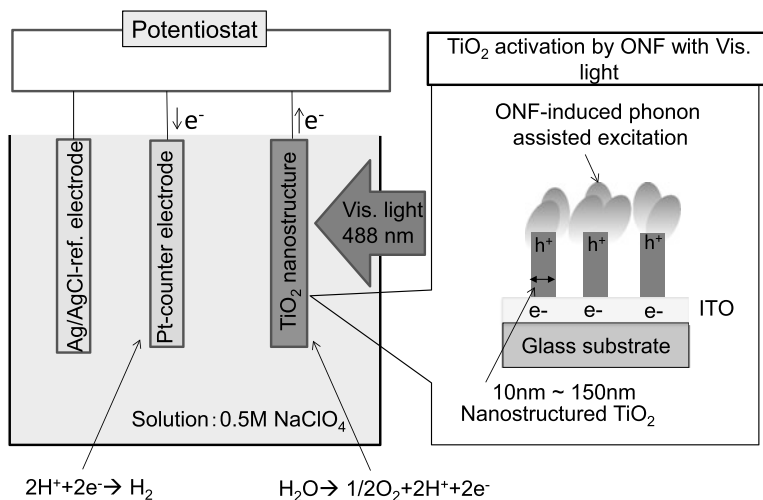
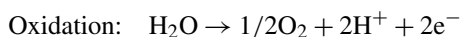


Fig. 5.38 Simple schematic diagram of a photoelectrochemical cell, which includes a photoanode, cathode and the reference electrode. The *inset figure* corresponds to the principle of the ONF-induced excitation of TiO₂ by the visible light

under incident UV-light irradiation absorbs light, and this absorption creates excited photoelectrons in the conduction band and holes in the valence band of the semiconductor. The photoelectrons and holes reduce and oxidize water to produce the stoichiometric 2:1 mixture of H₂ and O₂ by the following reactions:



However, the photocatalytic activity is low, because the TiO₂ material has a wide band gap 3.2 eV and can harvest the UV light which takes only ~5 % of sunlight, as it has been mentioned above.

Our ability to fabricate nanostructured TiO₂ films by GLAD is significant, because this method allows to make a precise design and to control the geometrical features. This allows achieving a TiO₂ nanostructured material with specific light properties to generate the ONF, and the generated ONF is utilized to excite TiO₂ with visible light. The photocatalytic activity of the TiO₂ nanostructured films prepared by GLAD was characterized by standard photoelectrochemical measurement in a custom-built 3-electrode cell (Pt wire counter electrode, Ag/AgCl reference electrode, and nanostructured TiO₂ thin film as a working electrode) with an equipped quartz window of 15 mm in diameter. The simple schematic diagram of this process is shown in Fig. 5.38. For visible irradiation, the 488 nm Argon ion laser was used, and the irradiation spot diameter was changed in the range of 1–15 mm to vary the power density. The power was calibrated and measured using the ADCMT 8230E optical power meter. All the power dependence measurements under visible irradiation were acquired at 0.5 V vs. Ag/AgCl external bias voltage.

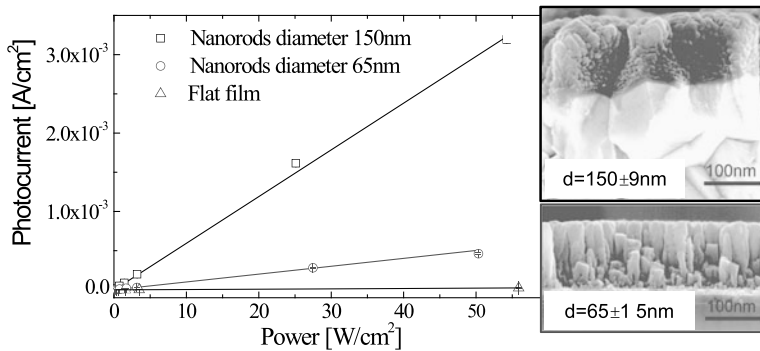


Fig. 5.39 The photoresponse of GLAD fabricated TiO₂ nanorods sample under visible light irradiation (488 nm), compared with the P-25 flat reference film

The photocurrent was acquired by the ALS electrochemical analyzer Model 814B, and the photocurrent density was calculated from the $I-t$ curves after 6 s when the light-on and the $I-t$ curves reach the steady state.

Figure 5.39 shows the PEC performance of 300 nm thick nanostructured TiO₂ films under visible light (488 nm) irradiation. The enhancement of the photocurrent in 150 nm nanorods was observed, which is more than two orders of magnitude compared to the reference P-25 flat film. This linear dependence in a wide range of light power density (from 10 to 50 E/cm⁻²) excludes the possibility of the excitation of TiO₂ by non-linear multi-photon absorption. As it has been described above, the phonon-assisted excitation is possible through the two-steps, and since the second step transition from the energy levels of phonon to the conduction band is a conventional adiabatic transition, the probability of this transition is more than 10⁶ times larger than that of the first transition step from the valence band to phonon levels [87, 89]. In addition, the second step transition of a conventional adiabatic transition easily saturates, which results in the linear power dependence as shown in Fig. 5.39.

It is necessary to add that the photocurrent has been also acquired in the range of 10⁻⁵ A at the lowest irradiation power, which excludes the factors of thermal effect or background noise during the PEC measurements.

We measured the absorption spectra of nanorods samples to exclude the possibility of absorption due to impurity of samples. The absorbance spectra show clear interference patterns in the visible region which can be attributed to the interference in the thickness of the films 300 nm. The slight absorption in the visible region has been observed, and this absorption strongly enhances in nanorod samples. The enhancement of the visible absorption can be ascribed to the scattering effect on complex nanorod structures. A strong gain of optical absorption in nanorod samples is in good agreement with previous reports on the decrease of refraction index and the consequent increase of light trapping and nanocavity effect in nanostructures [90, 91].

In conclusion, this result confirmed a novel physical approach to excite TiO₂ with visible light by utilizing the ONF, generated at nanostructures via the phonon-

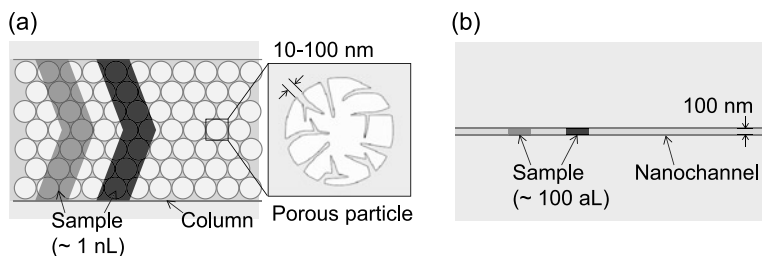


Fig. 5.40 Comparison of (a) conventional HPLC with (b) extended-nano chromatography

assisted excitation on the surface of TiO_2 prepared by GLAD. This study opens a new perspective for the development of visible-light driven nanostructured materials.

5.3.4 Applications

Recently, comprehensive analyses of biochemical processes are performed at single cell level to elucidate differences of gene expression for each cell [92]. This movement requires novel technologies of handling and analysis of ultralow volume sample. Therefore, extended-nano space has been proposed as a platform of single cell analysis. Since the volume of extended-nano space (aL-fL) is smaller than the volume of single cell (pL), an efficient single cell analysis is expected.

High-performance liquid chromatography (HPLC) has an important role in so-called omics technologies. Therefore, chromatographic separation of minute volume sample has been one of the principal targets of micro- and nanofluidics [93]. Exploiting the strong surface effects of nanochannel, a chromatography using an extended-nano channel was proposed. Figure 5.40 is a comparison of conventional HPLC and the extended-nano chromatography. Conventional HPLC uses a separation column packed with porous particles. Contrary, the extended-nano chromatography uses an extended-nano nanochannel itself as a separation column. The merits of using nanochannel are explained in principle as following. Separation efficiency of chromatography is evaluated using plate height H which is expressed as following equation.

$$H = A + B \cdot u + C/u \quad (5.9)$$

Here, smaller H means better separation efficiency and the A , B and C term come from eddy diffusion, longitudinal dispersion and radial dispersion as shown in Fig. 5.41, respectively. Firstly, in case of packed column, the separation efficiency decreases due to the A term which is caused by random pathways of molecules. In contrast, the A term can be eliminated in the extended-nano chromatography. Next, the C term could be also negligible because diffusion of molecules in radial direction is much faster than diffusion in longitudinal direction. Thus, the extended-nano

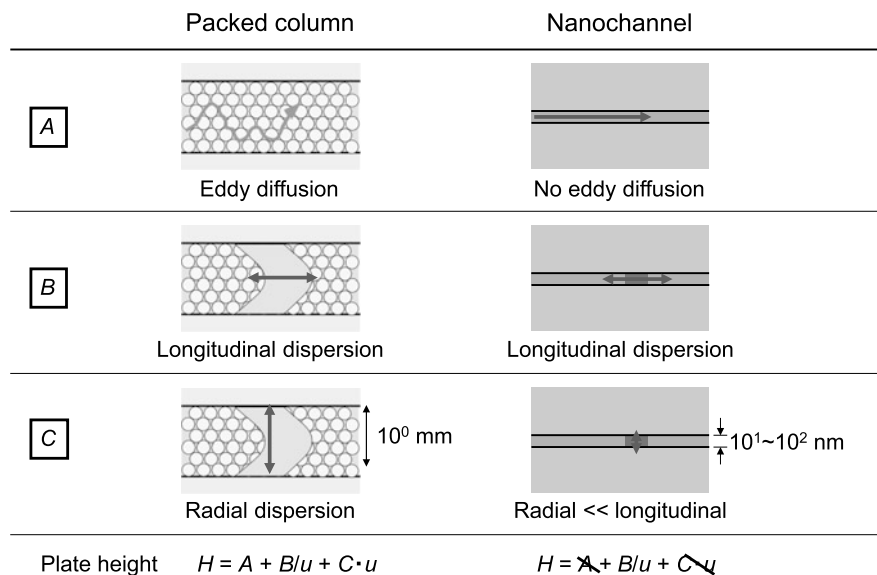


Fig. 5.41 Comparison of packed column and nanochannel for separation efficiency

chromatography has a potential of high separation efficiency which overcomes the limitation of conventional HPLC.

Figure 5.42(a) is an example of chromatogram obtained by the extended-nano chromatography [94]. Two fluorescent dyes with different emission wavelengths were separated reproducibly and detected separately. The injected sample volume was ~ 1 fL, which indicated that the scale of analysis was 9 orders of magnitude smaller compared to a capillary chromatography reported previously. Figure 5.42(b) is a van Deemter plot of the separation. The experimental and theoretical values of plate height were well accorded with each other. The lowest plate height was $2.3 \mu\text{m}$ and the plate number reached $440,000/\text{m}$, which realized a separation efficiency one order higher than conventional HPLC. The largest advantage of chromatography as a separation method is that various separation modes are available. To date, normal-phase, reversed-phase and HILIC mode were developed for the extended-nano chromatography using a pressure-driven nanofluidic control system [95]. Therefore, the extended-nano chromatography has a prospect as a universal separation technique in chemistry and biochemistry.

One of the largest issues on the future development of the extended-nano chromatography is a detection method. The differential interference contrast thermal lens microscope (DIC-TLM) would be a solution for this problem. Previously, a conventional TLM with a UV excitation laser was successfully used as a detector of chromatography [96]. In addition, the detection performance of DIC-TLM was verified as a detector of the extended-nano chromatography [97]. Combining the UV excitation, DIC-TLM and extended-nano chromatography, an integrated sys-

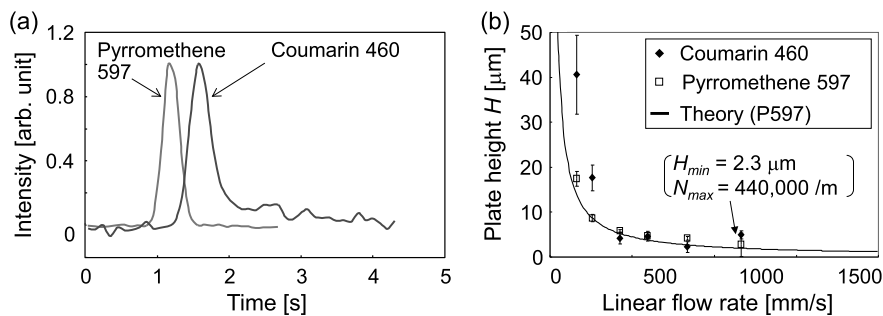


Fig. 5.42 Comparison of packed column and nanochannel for separation efficiency

tem could be developed to realize quantitative analyses of proteins, secretions and metabolites in a single cell.

5.4 Summary

In this chapter, microfluidic and extended-nano fluidic technologies were briefly introduced. As a fundamental technology, optical technologies played important roles for ultrasensitive detection and photochemical reaction. In extended-nano space, the space size becomes smaller than the wavelength. Therefore, nanophotonics will be a key technology. Many unique properties were discovered in microscopic chemical properties and fluidic properties. In addition, by combining with nanophotonic and nanofluidics, quite unique applications can be expected. For this purpose, fundamental research will be dispensable. Currently, there are still many unknown phenomena both in chemistry and optics.

Acknowledgements This work was supported by Core Research for Evolutionary Science and Technology (CREST) of Japan Science and Technology Agency (JST), Specially Promoted Research and Core-to-Core Program of Japan Society for the Promotion of Science (JSPS).

References

1. D.R. Reyes, D. Lossifidis, P.A. Auroux, A. Manz, *Anal. Chem.* **74**, 2623 (2002)
2. P.A. Auroux, D. Lossifidis, D.R. Reyes, A. Manz, *Anal. Chem.* **74**, 2637 (2002)
3. T. Kitamori, M. Tokeshi, K. Sato, A. Hibara, *Anal. Chem.* **76**, 52A (2004)
4. T. Tsukahara, K. Mawatari, T. Kitamori, *Chem. Soc. Rev.* **39**, 1000 (2010)
5. K. Mawatari, T. Tsukahara, T. Kitamori, *Analyst* **136**, 3051 (2011)
6. M. Ohtsu, *Progress in Nanophotonics I* (Springer, Berlin, 2011)
7. M. Tokeshi, T. Minagawa, K. Uchiyama, A. Hibara, K. Sato, H. Hisamoto, T. Kitamori, *Anal. Chem.* **74**, 1565 (2002)
8. A. Ishijima, T. Yanagida, *Trends Biochem. Sci.* **26**, 438 (2001)
9. P. Dittrich, A. Manz, *Anal. Bioanal. Chem.* **382**, 1771 (2005)

10. R.D. Snook, R.D. Lowe, *Analyst* **120**, 2051 (1995)
11. K. Uchiyama, A. Hibara, H. Kimura, T. Sawada, T. Kitamori, *Jpn. J. Appl. Phys.* **39**, 5316 (2000)
12. K. Sato, H. Kawanishi, M. Tokeshi, T. Kitamori, T. Sawada, *Anal. Sci.* **15**, 525 (1999)
13. M. Tokeshi, M. Uchida, A. Hibara, T. Sawada, T. Kitamori, *Anal. Chem.* **73**, 2112 (2001)
14. K. Mawatari, T. Ohashi, T. Ebata, M. Tokeshi, T. Kitamori, *Lab Chip* **11**, 2990 (2011)
15. H. Shimizu, K. Mawatari, T. Kitamori, *Anal. Chem.* **81**, 9802 (2009)
16. T. Ohashi, K. Mawatari, K. Sato, M. Tokeshi, T. Kitamori, *Lab Chip* **9**, 991 (2009)
17. V. Buch, J.P. Devlin, *Water in Confining Geometries* (Springer, Berlin, 2003)
18. P. Ball, *Chem. Rev.* **108**, 74 (2008)
19. T. Tsukahara, A. Hibara, Y. Ikeda, T. Kitamori, *Angew. Chem., Int. Ed. Engl.* **46**, 1180 (2007)
20. T. Tsukahara, W. Mizutani, K. Mawatari, T. Kitamori, *J. Phys. Chem.* **113**, 10808 (2009)
21. J.L. Kinsey, *Annu. Rev. Phys. Chem.* **28**, 349 (1977)
22. H. Shimizu, K. Mawatari, T. Kitamori, *Anal. Chem.* **82**, 7479 (2010)
23. D. Axelrod, *Annu. Rev. Biophys. Bioeng.* **13**, 247 (1984)
24. L. Novotny, S.J. Sranick, *Annu. Rev. Phys. Chem.* **57**, 303 (2006)
25. S.W. Hell, *Nat. Biotechnol.* **21**, 1347 (2003)
26. T.H. Le, K. Mawatari, Y. Pihosh, T. Kawazoe, T. Yatsui, M. Ohtsu, M. Tosa, T. Kitamori, *Appl. Phys. Lett.* **99**, 213105 (2011)
27. M.J. Rust, M. Bates, X. Zhuang, *Nat. Methods* **3**, 793 (2006)
28. M.G.L. Gustafsson, *Proc. Natl. Acad. Sci. USA* **102**, 13081 (2005)
29. B. Hein, K.I. Willing, S.W. Hell, *Proc. Natl. Acad. Sci. USA* **105**, 14271 (2008)
30. C. Kuang, G. Wang, *Lab Chip* **10**, 240 (2010)
31. G. Donnert, J. Keller, R. Medda, M.A. Andrei, S.O. Rizzoli, R. Lührmann, R. Jahn, C. Eggeling, S.W. Hell, *Proc. Natl. Acad. Sci. USA* **103**, 11440 (2006)
32. Y. Kazoe, K. Mawatari, Y. Sugii, T. Kitamori, *Anal. Chem.* **83**, 8152 (2011)
33. J.S. Park, C.K. Choi, K.D. Kihm, *Exp. Fluids* **37**, 105 (2004)
34. R.J. Adrian, *Annu. Rev. Fluid Mech.* **23**, 261 (1991)
35. J.G. Santiago, S.T. Wereley, C.D. Meinhart, D.J. Beebe, R.J. Adrian, *Exp. Fluids* **25**, 316 (1998)
36. R. Lindken, M. Rossi, S. Groß, J. Westerweel, *Lab Chip* **9**, 2551 (2009)
37. S.T. Wereley, C.D. Meinhart, *Annu. Rev. Fluid Mech.* **42**, 557 (2010)
38. C.M. Zetter, M. Yoda, *Exp. Fluids* **34**, 115 (2003)
39. S. Pouya, M. Koochesfahani, P. Snee, M. Bawendi, D. Nocera, *Exp. Fluids* **39**, 784 (2005)
40. J.S. Guasto, P. Huang, K.S. Breuer, *Exp. Fluids* **41**, 869 (2006)
41. M. Yoda, Y. Kazoe, *Phys. Fluids* **23**, 111301 (2011)
42. D.C. Prieve, *Adv. Colloid Interface Sci.* **82**, 93 (1999)
43. H. Li, M. Yoda, *J. Fluid Mech.* **662**, 269 (2010)
44. H. Li, M. Yoda, *Meas. Sci. Technol.* **19**, 075402 (2008)
45. Y. Kazoe, M. Yoda, *Langmuir* **27**, 11481 (2011)
46. Y. Kazoe, M. Yoda, *Appl. Phys. Lett.* **99**, 124104 (2011)
47. H. Faxén, *Ann. Phys.* **373**, 89 (1922)
48. H. Brenner, *Chem. Eng. Sci.* **16**, 242 (1961)
49. M.A. Bevan, D.C. Prieve, *J. Chem. Phys.* **113**, 1228 (2000)
50. A. Hibara, T. Saito, H.B. Kim, M. Tokeshi, T. Ooi, M. Nakao, T. Kitamori, *Anal. Chem.* **74**, 6170 (2002)
51. N.R. Tas, J. Haneveld, H.V. Jansen, M. Elwenspoek, A. van der Berg, *Appl. Phys. Lett.* **85**, 3274 (2004)
52. J. Haneveld, N.R. Tas, N. Brunets, H.V. Jansen, M. Elwenspoek, *J. Appl. Phys.* **104**, 014309 (2008)
53. M. Whitby, L. Cagnon, M. Thanou, N. Quirke, *Nano Lett.* **8**, 2632 (2008)
54. D. Stein, M. Kruithof, C. Dekker, *Phys. Rev. Lett.* **93**, 035901 (2004)
55. S. Liu, Q. Pu, L. Gao, C. Korzeniewski, C. Matzke, *Nano Lett.* **5**, 1389 (2005)

56. T. Tsukahara, T. Kuwahara, A. Hibara, H.B. Kim, K. Mawatari, T. Kitamori, *Electrophoresis* **30**, 3212 (2009)
57. F.H.J. van der Heyden, K. Besteman, S.G. Lemay, C. Dekker, *Phys. Rev. Lett.* **96**, 224502 (2006)
58. K. Morikawa, K. Mawatari, M. Kato, T. Tsukahara, T. Kitamori, *Lab Chip* **10**, 871 (2010)
59. K. Morikawa, K. Mawatari, Y. Kazoe, T. Tsukahara, T. Kitamori, *Appl. Phys. Lett.* **99**, 123115 (2011)
60. Q. Pu, J.S. Yun, H. Temkin, S.R. Liu, *Nano Lett.* **4**, 1099 (2004)
61. M. Inaba, M. Kato, T. Tsukahara, K. Mawatari, A. Hibara, T. Kitamori, *Anal. Chem.* **82**, 543 (2010)
62. T. Tsukahara, T. Maeda, K. Mawatari, A. Hibara, T. Kitamori, in *Proc. microTAS* (2008), p. 1311
63. A. Hibara, K. Toshin, T. Tsukahara, K. Mawatari, T. Kitamori, *Chem. Lett.* **37**, 1064 (2008)
64. T. Tsukahara, K. Mawatari, A. Hibara, T. Kitamori, *Anal. Bioanal. Chem.* **391**, 2745 (2008)
65. H. Chinen, K. Mawatari, Y. Pihosh, K. Morikawa, Y. Kazoe, T. Tsukahara, T. Kitamori, *Angew. Chem., Int. Ed. Engl.* **51**, 3573 (2012)
66. A. Fujishima, K. Honda, *Nature* **238**, 37 (1972)
67. G.K. Mor, K. Shankar, M. Paulose, O.K. Varghese, C.K. Grimes, *Nano Lett.* **5**, 191 (2005)
68. S.U.M. Khan, M. Al-Shahry, W.B. Ingler, *Science* **297**, 2243 (2002)
69. Y.J. Hwang, A. Boukai, P.D. Yang, *Nano Lett.* **9**, 410 (2009)
70. J.H. Park, S. Kim, A. Bard, *Nano Lett.* **6**, 24 (2006)
71. G. Wang, H. Wang, Y. Ling, Y. Tang, X. Yang, R.C. Fitzmorris, C. Wang, J.Z. Zhang, Y. Li, *Nano Lett.* **11**, 3026 (2011)
72. U. Diebold, *Surf. Sci. Rep.* **48**, 53 (2003)
73. I. Turkevych, Y. Pihosh, M. Goto, A. Kasahara, M. Tosa, S. Kato, K. Takehana, T. Takamasu, G. Kido, N. Koguchi, *Thin Solid Films* **516**, 2387 (2008)
74. Y. Pihosh, I. Turkevych, J. Ye, M. Goto, A. Kasahara, M. Kondo, M. Tosa, *J. Electrochem. Soc.* **156**, K160 (2009)
75. M. Grätzel, *Nature* **414**, 338 (2001)
76. S. Yamamoto, T. Sumita, T. Sugiharuto, A. Miyashita, H. Naramoto, *Thin Solid Films* **401**, 88 (2001)
77. P. Zeman, S. Takabayashi, *Surf. Coat. Technol.* **153**, 93 (2002)
78. A. Watanabe, T. Tsuchiya, Y. Imai, *Thin Solid Films* **406**, 132 (2002)
79. M. Anpo, *Pure Appl. Chem.* **72**, 1787 (2000)
80. A. Di Paola, G. Marci, L. Palmisano, M. Schiavello, K. Uosaki, S. Ikeda, B. Ohtani, *J. Phys. Chem. B* **106**, 637 (2002)
81. M. Janus, B. Tryba, M. Inagaki, M.A.W. Morawski, *Appl. Catal. B, Environ.* **52**, 61 (2004)
82. S. Sakthivel, H. Kisch, *Angew. Chem., Int. Ed. Engl.* **42**, 4908 (2003)
83. R. Asahi, T. Morikawa, T. Ohwaki, K. Aoki, Y. Taga, *Science* **293**, 269 (2001)
84. Y. Tian, T. Tatsuma, *Chem. Commun.* **2004**, 1810 (2004)
85. Y. Tian, T. Tatsuma, *J. Am. Chem. Soc.* **127**, 7632 (2005)
86. K. Kobayashi, S. Sangu, H. Ito, M. Ohtsu, *Phys. Rev. A* **63**, 013806 (2001)
87. T. Kawazoe, K. Kobayashi, S. Takubo, M. Ohtsu, *J. Chem. Phys.* **122**, 024715 (2005)
88. K. Robbie, M.J. Brett, *J. Vac. Sci. Technol. A* **15**, 1460 (1997)
89. T. Kawazoe, H. Fujiwara, K. Kobayashi, M. Ohtsu, *IEEE J. Sel. Top. Quantum Electron.* **15**, 1380 (2009)
90. Z.P. Yang, L. Ci, J.A. Bur, S.Y. Lin, P.M. Ajayan, *Nano Lett.* **8**, 446 (2008)
91. W. Han, L. Wu, R.F. Klie, Y. Zhu, *Adv. Mater.* **19**, 2525 (2007)
92. D. Wang, S. Bodovitz, *Trends Biotechnol.* **28**, 281 (2010)
93. K. Faure, *Electrophoresis* **31**, 2499 (2010)
94. R. Ishibashi, K. Mawatari, T. Kitamori, *Small* **8**, 1237 (2012)
95. R. Ishibashi, K. Mawatari, K. Takahashi, T. Kitamori, *J. Chromatogr. A* **1228**, 51 (2012)
96. S. Hiki, K. Mawatari, A. Hibara, M. Tokeshi, T. Kitamori, *Anal. Chem.* **78**, 2859 (2006)
97. H. Shimizu, K. Mawatari, T. Kitamori, *J. Sep. Sci.* **34**, 2920 (2012)

Index

A

Abbe's diffraction limit, 138
Absorption coefficient, 131, 150
Absorption spectra, 50, 51, 55–57
Adiabatic local density approximation, 11
Adsorption phase, 136, 137
Aharonov-Bohm effect, 43
Aid of the phonon energy, 108
Anatase phase, 153
Antibody, 133
Antigen, 133
Auger recombination, 60, 64, 66

B

Back reaction, 25
Band gap energy, 153, 154
Biology, 122, 125, 127, 136, 140
Blue light, 104
Boltzmann distribution, 54, 55
Bright exciton, 40, 42, 44–48, 50–52, 54, 55, 59, 67
Brillouin zone, 34–36
Bulk phase, 136, 137

C

Capacitance, 148
Cavity mode, 85
Characteristic temperature, 87
Charged exciton, 33, 67
Chemical equilibrium constant, 150
Chemical vapor deposition, 153
Chiral index, 33–36, 45, 51, 55, 62
Chiral vector, 33, 34
Chirality, 33, 46, 51, 56
Chromatic aberration, 129
Clinical diagnosis, 122, 133
Closely packed structure, 75, 76, 79

Coefficient ratio, 104
Coherence length, 55, 58–60, 67
Coherent phonon, 100
Concentration, 122, 129–131, 133, 137, 139, 143, 147, 148, 150–152
Confocal length, 139
Confocal microscope, 127
Continuous flow chemical processing, 125
Cooling time, 107
Coulomb interactions, 34, 38, 43, 63, 65
Coumarin 102, 98
Coumarin 153, 98
Critical angle, 144

D

Dark exciton, 40, 42, 44–48, 52–55, 58, 59, 67
DCM, 98, 109
DCM dye grain, 116
Debye length, 136, 148, 150
Debye-Einstein-Stokes theory, 129
Decay time constant, 117
Density of states, 36, 59, 71, 72, 82
Dependence of emitted light intensity, 104
Dephasing process, 58
Derjaguin-Landau-Verwey-Overbeek (DLVO) theory, 145
Diffraction limit, 1
Diffusion, 125, 129, 130, 139, 143, 144, 146, 147, 149, 151, 152, 154, 160
Dipole acceleration, 16
Dipole approximation, 1, 4
Dipole radiation, 9
Display, 108
Dissociation, 148, 150
Distillation, 122, 149
Dressed photon, 98
Dressed photon model, 104

- Drug synthesis, 122
Dye grain, 100, 102, 119
- E**
Effective core pseudopotentials, 12
Effective potential, 24
Elapsed time, 112
Electric double layer, 136, 143, 145, 147–150
Electrical conductivity, 147
Electrokinetically driven flow, 146
Electron density, 10
Electron-hole pair, 33, 38–40, 65, 67
Electronic state, 101
Energy conversion efficiency, 153
Ensemble averaging, 143
Environmental analysis, 122, 125
Enzyme-linked immunosorbent assay, 133
Evanescent wave, 143–145
Exchange interaction, 48, 52, 67
Exchange-correlation (XC) potential, 11
Excitation ①, 101
Excitation ②, 101
Excitation process, 111
Exciton binding energy, 38, 39, 51
Exciton Bohr radius, 60, 67
Exciton multiplication, 62, 64–66
Exciton population, 45, 52, 54, 57, 65
Exciton-exciton annihilation, 56, 57, 64, 65
Excitons, 33, 38–40, 46, 49–56, 59–67
Extended nanospace, 121, 136–138, 140, 143, 147–152
Extended-nano chromatography, 160, 161
External quantum efficiency, 86
Extremely short, 116
- F**
Family pattern, 51
Far-field, 1
Far-field optics, 138
Faraday, 42, 43
Fermi level, 35
Fluorescence microscopy, 140
Fluorescent molecule, 127–130, 132, 137–139, 141, 142
Fluorophore, 140
Food analysis, 122, 125
Freezing point, 136
Frequency up-conversion, 97
Fuel cell, 153
Full-multipole effects, 22
Fullerene, 33
Fused-silica, 136, 142, 143, 145, 148–150, 153
- G**
Geometric optics, 138, 139
Glancing angle deposition, 138, 154
Gradient force, 21
Graphene, 33–35, 48
Green light, 103
Grid-based method, 12
Grotthuss mechanism, 151
- H**
Harmonic-generation (HG) spectra, 16
High-performance liquid chromatography, 160
Higher vibrational state, 101
HILIC mode, 161
Homogeneous linewidth, 58, 60–64
Hydrogen bond, 136, 137, 147, 149
- I**
Immunoassay, 130, 133, 134, 143
Immunoreaction, 133
Impedance, 147, 148
Increment of the emitted light intensity, 106
Induced dipole moments, 15
Inelastic exciton scattering, 62
Infrared light, 97
Inhomogeneous broadening, 41
Inhomogeneous electron dynamics, 14
Instantaneous, 9
Integrated chemical system, 121
Interference, 131, 137–139, 159, 161
Intermediate excited state, 100, 101
Intermolecular Coulomb interaction, 5
Internal quantum efficiency, 86, 88
Inversion symmetry, 16
Ionic background, 24
Isoelectric point, 148
- J**
Jellium model, 24
- K**
Kelvin equation, 149
Kleinman-Bylander separable form, 11, 24
Kohn-Sham, 9
- L**
Laplace pressure, 149
Larger up-shift, 98
Laser induced fluorescence, 127
Laser spectroscopy, 127
Lifetime, 105, 108
Lifetime of the intermediate excited state, 114, 119
Light-to-heat conversion, 128

- Limit of detection, 129, 139
- Local density approximation, 24
- Lorentzian function, 42, 60, 61
- M**
- Magnetic flux, 42–44
- Magneto optical spectroscopy, 42
- Maxwell stress tensor, 21
- Maxwell-Schrodinger coupled equation, 25
- MBE, 73–76, 84
- Micro unit operations, 122
- Micro-particle image velocimetry, 143
- Microchannel, 143–145, 147–149, 151
- Microfluidics, 122, 127
- Microspace, 121, 122, 124, 127, 136, 137
- Minimal coupling Hamiltonian, 4
- Modulated stacking structure, 91–95
- Molecular beam epitaxy, 73
- Molecular vibrational state, 101
- Multi-step excitation, 100
- Multiphase flow, 124
- Multipolar Hamiltonian, 4, 5
- N**
- Nafion membrane, 153
- Nano-optics, 21
- Nano-particle image velocimetry, 143, 144
- Nanochannel, 136–140, 143, 147–153, 160–162
- Nanofluidic, 136, 138, 139, 148, 160–162
- Nanoparticle, 131, 132, 142, 153
- Nanophotonics, 21, 123, 138, 162
- Nanorod, 138, 153–157, 159
- Nanotechnology, 122, 154
- Nanowire, 153
- Near-field, 2
- Near-field optics, 143
- Near-infrared excitation, 103
- Nine-point difference formula, 12
- Non-dependence, 114
- Non-propagating wave, 2
- Non-radiative decay process, 137
- Nondegenerate beam, 108, 112, 115, 116
- Nonuniform light-matter interaction, 3
- Norm-conserving pseudopotential, 11, 24
- Normal-phase, 161
- Nuclear magnetic resonance, 136, 149
- Number of the intermediately excited dye molecules, 106
- O**
- Octapole, 5, 6
- One-step, 112
- Optical fiber, 130
- Optical loss, 86
- Optical measurement, 116
- Optical near field, 121
- Optical near-field, 97, 101
- Optical nonlinearity, 60
- Optical pulse measurement, 115
- Optical pulse shape, 119
- Optical pulse-shape measurement, 98
- Optical trapping, 21
- Optical tweezers, 21
- Oscillating dipole, 23
- Oscillating dipole radiation, 7
- Oscillator strength, 52, 54, 55, 58–60
- P**
- Particle image velocimetry, 143
- Particle tracking, 144
- Penetration depth, 144
- PH indicator, 149
- Pharmaceutical, 122, 125
- Phase contrast, 131, 139
- Phase matching condition, 115
- Phonon generation efficiency, 108
- Phonon sideband, 46, 47, 49, 51
- Phonon-assisted, nondegenerate excitation process, 119
- Phonon-assisted excitation process, 98
- Phonon-assisted process, 154
- Phonon-polariton, 123, 154
- Photocatalytic reaction, 138
- Photoluminescence, 37, 82
- Photoresponse, 153, 159
- Photothermal effect, 128, 131
- Photothermal spectroscopy, 128
- Photovoltaics, 153
- Physical vapor deposition, 154
- Plate height, 160, 161
- Plate number, 161
- Poiseuille flow, 144, 145
- Polarization, 4
- Polarization angle, 114
- Polarization charges, 26
- Polarization control, 115
- Polarization operator, 5
- Power spectra, 16
- Pressure-driven flow, 147
- Processes 1, 2, 5, and 6, 116
- Processes 3, 4, and 7, 116
- Proton exchange membrane, 153
- Proton exchange rate, 136, 149, 152
- Proton hopping, 137, 149, 151
- Proton transfer phase, 136, 137, 147, 149, 151
- Pseudowavefunctions, 11

Pulsed laser deposition, 153
 Pump-probe spectroscopy, 105

Q

QD array, 78, 79, 81, 82, 94
 QD laser, 71, 72, 74, 83, 84, 86–88, 90, 91
 Quadrupole, 5, 6
 Quadrupole moment, 17
 Quantum dot, 71, 73, 144
 Quantum electrodynamics theory, 21
 Quantum yield, 55, 57
 Quartz crystal microbalance, 156

R

Radiative decay processes, 137
 Radiative lifetime, 55, 58, 59, 64, 67
 Random, 114
 Rapid response time, 108
 Ratio problem, 39
 Ratiometric measurement, 150
 Reactive evaporation, 153
 Real energy state, 108, 114
 Real level, 107
 Refraction, 131, 138, 159
 Refractive index, 128, 129, 131, 139, 142, 144
 Result of pulse-shape measurement, 117
 Retarded, 9
 Reversed-phase, 161
 Rod-like shape, 102

S

S-K mode, 74, 75, 83
 Sampling beam, 109
 Saturated structured-illumination microscopy, 140
 Scanning electrochemical microscope, 127
 Scanning near-field optical microscopy, 138
 Screening charges, 26
 Self-assembled, 71, 73–75, 83, 93, 95
 Self-consistent interaction, 2
 Self-interaction term, 8
 SERS, 2
 Seven potential excitation processes, 112
 Sharp protrusion, 103
 Shockley-Queisser limit, 65
 Signal beam, 109
 Signal waveform profile, 118
 Signal-to-background (S/B) ratio, 131
 Signal-to-noise ratio, 117
 Silanol group, 148, 150
 Simultaneous radiation, 110, 111
 Single carbon nanotube spectroscopy, 41
 Single molecule chemistry, 132
 Single molecule detection, 127

Single-walled carbon nanotube, 33, 34, 49
 Singlet-triplet splitting, 52
 Solar photoelectrochemical process, 157
 Spin-orbit coupling, 48
 Stilbene 3, 107
 Stimulated emission microscopy, 138
 Stochastic optical reconstruction microscopy, 140
 Stokes shift, 51
 Stokes-Einstein relation, 146, 151
 Stranski-Krastanov mode, 74
 Streaming potential/current, 148
 Strong excitation, 111
 Surface enhanced Raman spectroscopy, 127
 Surface-to-volume ratio, 136, 143
 Symmetry-breaking, 14

T

Theoretical value, 104
 Thermal conductivity, 129
 Thermal equilibrium, 101
 Thermal lens microscope, 128, 129, 131, 138, 161
 Thermal lens spectroscopy, 128
 Thermalization, 54, 58
 Three phase model, 136, 138, 143, 147, 149
 Three-step phonon-assisted excitation process, 102
 Threshold current density, 84, 87, 88
 Tight-binding approximation, 34
 Time-averaged force, 27
 Time-dependent density functional theory, 4
 Time-dependent Hartree potential, 11
 Time-dependent Kohn-Sham approach in real space, 10
 Time-resolved spectroscopy, 33, 54, 67
 TiO₂, 123, 138, 153–160
 Tissue engineering, 122, 125
 Total internal reflection microscope, 127
 Transverse part of the electric field, 5
 Trion, 33, 51, 52, 67
 Tube diameter, 43, 44, 46–48, 51, 52, 55–59
 Two transition routes, 101
 Two- and three-step phonon-assisted excitation, 105
 Two-dimensional fast Fourier transform, 79
 Two-step phonon-assisted excitation process, 101, 112

V

Van Deemter plot, 161
 Vapor pressure, 149
 Virtual level, 107

Viscosity, [147](#)
Visible light, [97](#)
Visible light emission, [100](#)
Visible light emission process, [105](#)
Voigt, [42–44](#)
Von-Hove singularity, [36, 38](#)

W
Water splitting, [123, 138, 153, 157](#)
Wave optics, [139](#)
Weak excitation, [110](#)
Wide wavelength region, [119](#)
Wide-band optical gain, [91](#)